THERMO-STRUCTURAL ANALYSIS OF 3D COMPOSITES

A THESIS

Submitted by

SANTHOSH B

for the award of the degree

of

DOCTOR OF PHILOSOPHY

DEPARTMENT OF SHIP TECHNOLOGY
COCHIN UNIVERSITY OF SCIENCE AND TECHNOLOGY
KOCHI – 682 022

DECEMBER 2010

CERTIFICATE

I here by certify that to the best of my knowledge, the thesis entitled ***'THERMO-STRUCTURAL ANALYSIS OF 3D COMPOSITES'*** *is a record of bonafide research work carried out by* ***Sri. Santhosh. B****, Part time research student, Reg. No. 3160 under my supervision and guidance, as the partial fulfillment of the requirement for the award of the Ph.D degree in the faculty of technology. The results presented in this thesis or parts of it have not been presented for the award of any other degree.*

Kochi-22
9-12-2010

Dr. C. G. Nandakumar
Research Guide,
Dept. of Ship Technology,
Cochin University of Science
and Technology,
Kochi - 22.

DECLARATION ABOUT THE AUTHENTICITY OF THE RESEARCH WORK BY THE RESEARCH STUDENT

I here by declare that the thesis entitled ***'THERMO-STRUCTURAL ANALYSIS OF 3D COMPOSITES'*** *is an authentic record of research work carried by me under the supervision and guidance of* ***Dr. C. G. Nandakumar****, Department of Ship Technology, in the partial fulfillment of the requirement for the award of the Ph.D degree in the faculty of technology and no parts thereof has been presented for the award of any other degree.*

Kochi-22
9-12-2010

Santhosh B
Part time Research Student
Reg. No: 3160
Dept. of Ship Technology
CUSAT
Kochi - 22.

TABLE OF CONTENTS

ACKNOWLEDGEMENTS

I would like to express my gratitude and sincere thanks to my guide and mentor Dr. C G Nandakumar without whose help this work would not have been materialized. The pleasure of learning from him will remain in my memory forever. Words cannot match the debt I owe in this regard. I would like to thank Shri. S Sundararajan, Brahmaprakash Scientist, Composites Entity for his valuable guidance, advice and encouragement through out my studies, without which I would not have reached this milestone.

I would like to thank Dr. K P Narayanan, Head, Department of Ship Technology for his support in carrying out this work. I am thankful to departmental research committee members for their support and valuable suggestions during the review meetings.

I express my extreme gratitude to VSSC, ISRO for permitting me to carryout doctoral studies at Cochin University of Science and Technology and providing the necessary data and computational environment. I would like to thank Shri. M Enamuthu, Deputy Director, Composites Entity and Shri. S Sridhar, Head, Composite Launch Vehicle Structures Division for giving me an opportunity to carry out my higher studies and sincerely thank them for the encouragement and support provided by them.

I would like to thank my friends and colleagues for the many discussions we had. Most importantly, I would like to express my deep gratitude and sincere appreciation to my family members for their dedication and inspiration that enabled me for this achievement in my life. I would like to make a special mention about my wife Smt. Priyadarsini R S and our son Harigovind whose support, encouragement and sacrifices have enabled me to reach this milestone.

ABSTRACT

KEYWORDS: 3D Woven, 3D Braided, Thermomechanical properties, Thermo-structural analysis, Carbon-Carbon composites, Analytical modelling, CCA model, Representative Unit Cell, Nonlinear finite element analysis, Nosecap.

Three dimensional (3D) composites are strong contenders for the structural applications in situations like aerospace, aircraft and automotive industries where multidirectional thermal and mechanical stresses exist. The presence of reinforcement along the thickness direction in 3D composites, increases the through the thickness stiffness and strength properties. The 3D preforms can be manufactured with numerous complex architecture variations to meet the needs of specific applications. For hot structure applications Carbon-Carbon (C-C) composites are generally used, whose property variation with respect to temperature is essential for carrying out the design of hot structures.

The thermomechanical behavior of 3D composites is not fully understood and reported. The methodology to find the thermomechanical properties using analytical modelling of 3D woven, 3D 4-axes braided and 3D 5-axes braided composites from Representative Unit Cells (RUC's) based on constitutive equations for 3D composites has been dealt in the present study. High temperature Unidirectional (UD) Carbon-Carbon material properties have been evaluated using analytical methods**,** viz., Composite Cylinder Assemblage Model and Method of Cells based on experiments carried out on Carbon-Carbon fabric composite for a temperature range of 300^{o}K to 2800^{o}K. These properties have been used for evaluating the 3D composite properties. From among the existing methods of solution sequences for 3D composites, "3D Composite Strength Model" has been identified as the most suitable method. For the generation of material properties of RUC's of 3D composites, software has been developed using MATLAB. Correlation of the analytically determined properties with test results available in literature has been established. Parametric studies on the variation of all the thermomechanical constants for different 3D preforms of Carbon-Carbon material have been studied and selection criteria have been formulated for their applications for the hot structures.

Procedure for the structural design of hot structures made of 3D Carbon-Carbon composites has been established through the numerical investigations on a Nosecap. Nonlinear transient thermal and nonlinear transient thermo-structural analysis on the Nosecap have been carried out using finite element software NASTRAN. Failure indices have been established for the identified preforms. Identification of suitable 3D composite based on parametric studies on strength properties and recommendation of this material for Nosecap of RLV based on structural performance have been carried out in this study. Based on the 3D failure theory the best preform for the Nosecap has been identified as 4-axis 15^{o} braided composite.

LIST OF TABLES

LIST OF FIGURES

ABBREVIATIONS

ASTM	American Standards for Testing Methods
CA	Compliance Averaging
CR	Crimp Reduction
C-C	Carbon-Carbon
CCA	Composite Cylinder Assemblage (model)
CFD	Computational Fluid Dynamics
CFRP	Carbon Fibre Reinforced Plastics
CTE	Coefficient of Thermal Expansion
DERA	Defence Evaluation and Research Agency
el	Element
expt.	Experimental
FEM	Finite Element Model
G1, G2, G3	Geometrical configurations
GCS	Global Coordinate System
ILSS	Interlaminar Shear Strength
LCS	Local Coordinate System
LLAW	Layer to Layer Angle Interlock Weave
LLOW	Layer to Layer Orthogonal Weave
max	Maximum
min	Minimum
NASTRAN	NASA Structural Analysis
NISA	Numerically Integrated Elements for System Analysis
NPL	National Physical Laboratory
OA	Orientation Averaging (model)
RLV	Reusable Launch Vehicle
RT	Room Temperature
RTM	Resin Transfer Moulding
RUCA	Repeating Unit Cell for Analysis
RUC	Representative Unit Cell / Geometrically Repeating Unit Cell
sel	subelement
sec	section
ssec	subsection
SA	Stiffness Averaging
Ti	Titanium
TMA	Thermal Mechanical Analyzer
TS	Transverse Strains
TT	Through the Thickness

TTAW	Through the Thickness Angle Interlock Weave
TTOW	Through the Thickness Orthogonal Interlock Weave
TTOW-1, LLOW-1	Warp weaver passes around a single filler before reversing the direction
TTOW-2, LLOW-2	Warp weavers passes around two fillers before reversing the direction
TTOW-1-1, LLOW-1-1, TTOW-2-1, LLOW-2-1	If only one warp weaver between adjacent stuffers.
TTOW-1-2, LLOW-1-2, TTOW-2-2, LLOW-2-2	If there are two warp weavers between adjacent stuffers.
UD	Unidirectional
wrt	With respect to
WF	Woven Fabric
1D, 2D, 3D	One, Two, Three Dimensional
3DCSM	3D Composite Strength Model

NOTATIONS

Mathematical symbols

[ ]	Rectangular or square matrix
{ }	Column, row and diagonal matrices
$[\ ]^T$	Matrix transpose
$[\ ]^{-1}$	Matrix inverse

Latin symbols

a_{ij}	Extensional compliance matrix
$\overline{a}_{ij}$	Extensional compliance matrix for RUCA/RUC/3D Composite
A_{ij}	Extensional stiffness matrix
$\overline{A}_{ij}$	Extensional stiffness matrix for RUCA/RUC/3D Composite
C_p	Dynamic Pressure
C_{ij}	Material stiffness matrix
$\overline{C}_{ij}$	Transformed stiffness matrix
d_s	Diameter of stuffer
d_f	Diameter of filler
d_w	Diameter of warp weaver
$E_L, E_T, \nu_{LT}, G_{LT}, G_{TT}, \alpha_L, \alpha_T$	UD composite thermoelastic properties along the fiber and transverse directions
E	Young's modulus
E_{11}, E_{22}, G_{12}, ν_{12}	Elastic properties
E_X, E_y, G_{xy}, ν_{xy}	Elastic properties
G_{12}, G_{23}, G_{31}	Shear Modulus
[G]	Stress transformation matrix
k_a, k_t	Axial and transverse effective thermal conductivities of a matrix impregnated yarn
k_{fa}, k_{fr}	Axial and transverse thermal conductivities of fiber
k_m	Matrix thermal conductivity
K_1, K_2, K_3	Thermal conductivities in orthotropic directions
L, $L^{'}$, L^{*}	Length of a side of RUCA
n_x	Number in x direction
n_y	Number in y direction
n_z	Number in z direction
n_x	Number of layers of stuffers

n_y	Number of layers of fillers
N_x	Applied stress resultant
N_{xy}, N_{yz}, N_{zx}	Shear Loads
N^T	Thermal force resultant
q	Heat flux
[Q]	Strain transformation matrix
S_{xx}, S_{yy}, S_{zz}	Tensile stresses
S_{xy}, S_{yz}, S_{zx}	Shear stresses
[T]	Transformation matrix
T_{amp}	Ambient temperature
T_g	Flow parameter
V_f	Fiber volume fraction
V^o_f	Overall fiber volume fraction
x, y, z	Cartesian coordinates
X_T^f	Tensile strength of fiber along longitudinal direction
X_T, Y_T, S	Strengths of UD lamina/strand
X_c	Compressive strength
X_T, Y_T, Z_T	Tensile strength properties along X, Y, Z axes

Greek symbols

α	Coefficient of thermal expansion
$\bar{\alpha}$	Average coefficient of thermal expansion
$\beta, \beta_x, \beta_y, \beta_z$	Azimuth angles with respect to x, y, z directions
γ	Shear strain / Inplane shear strain
Δ_{pz}	Deformation due to P in z direction
ΔT	Change in temperature
η	Stiffness knock down factor
ν	Poisson's ratio
Φ	Angle made by braider yarn diameter at jamming condition
$\varepsilon_x, \varepsilon_y, \varepsilon_z$	Normal tensile strain in x, y and z directions
$\varepsilon_{xy}, \varepsilon_{zx}, \varepsilon_{yz}$	Shear strains
ε_c	Compressive normal strain along x axis
ε	Strain / Normal strain
ρ	Density
σ	Stress / Normal stress
σ_x	Normal tensile stress in x direction

τ_{12}	Shear stress in xy or 12 plane
τ	Shear stress

Superscripts

e	Effective properties
el	Refers to an element
f	Quantities of fiber
f	Fillers
m	Quantities of matrix
o	Overall / overall properties
sec	Refers to a section perpendicular to loading direction
sel	Refers to a subelement
ssec	Refers to a subsection
s	Stuffer
w	Warp weaver

Subscripts

a	Refers to axial yarn
b	Refers to braider yarn
f	Quantities in fill direction / refers to fiber
m	Refers to matrix
n	Number of iterations
w	Quantities in warp direction
x, y, z	Global coordinates
1, 2, 3	Local coordinates

CHAPTER 1

INTRODUCTION

1.1 General

Laminated composites made of unidirectional layers are used in high technology applications because of their high inplane specific stiffness and specific strength. These potential properties are realized only if the composite structure is loaded primarily in the plane of the reinforcement. If a composite structure is subjected to loading along other directions, the location of primary structural failure would be at the fiber / resin interface. This has necessitated the development of fiber reinforced textile composites which possess significant fibrous interconnectivity between adjacent planes of fibers to supplement the relatively weak fiber / resin interface. This interconnectivity would enhance the damage tolerance of composite structures.

Weaving, Braiding, Knitting and Through the Thickness Stitching are the main processes used for making textile preforms. The textile preforms are planar or three dimensional. The interconnectivity is mainly in the plane of the preform for the planar textile preforms. The 3D textile preforms for the structural composites are fully integrated continuous fiber assemblies having multi-axial inplane and out of plane fiber orientations. Normally the 3D composites are made using the 3D textile preforms and Resin Transfer Molding (RTM). Such composites are characterized by enhanced through the thickness mechanical properties, fracture / impact resistance, damage tolerance and dimensional stability. Near net shape manufacturing of structural components with complex shapes is also facilitated by the use of textile preforms and RTM. But the inplane mechanical properties of the textile composites are lower than the laminated composites made of Unidirectional (UD) layers.

One of the advantages of the 3D textile preforms is the formation of integral structure to the near net shape. This has led to their usage in structural applications in aerospace, aircraft and automotive industries. The 3D textile preforms can be manufactured with numerous complex architecture variations to meet the needs of specific applications. The 3D textile composite structures consist of continuous reinforcement yarns arranged along multiple directions. In 3D composites, reinforcement is present along the thickness direction

leading to an increase in the through the thickness stiffness and strength properties. They possess high value of failure strain in both tension and compression. Such composite structures are ideal materials for structural applications where multidirectional mechanical and thermal stresses are experienced. Advanced composites usually consist of high performance fibres as reinforcement phases and polymers or metals as matrices. Carbon-Carbon (C-C) composites consist of fibres embedded in a carbonaceous matrix.

Eventhough the textile composites are finding increasing applications in several structural applications, their failure behavior and stress distribution under different loading condition are not well understood. For the effective use of textile composites, their mechanical behavior needs to be clearly understood.

The 3D orthogonal interlock woven composites are a class of materials finding increasing use in structural applications. Orthogonal interlock woven 3D preforms have reinforcement yarns arranged in an orthogonal geometry, with all yarns intersecting at 90^0. The yarns can be introduced uniformly in each of the three directions to provide quasi isotropic properties or yarns can be provided in unbalanced amounts when design considerations require directional properties. The orthogonally woven 3D preforms generally have a finer geometrical repeating unit cell. If fibres are inclined the preforms are called angle interlock woven composites, and these preforms consist of three set of yarns. The stuffers (s) are oriented along the longitudinal direction. The fillers (f) are oriented transverse to the longitudinal direction. The stuffers and fillers form an orthogonal array. The warp weavers (w) crisscross the weave thickness at 90^0 or at an angle with the axis. Various weave geometrical parameters are fibre size, fibre spacing, fibre distribution, interlock lengths and depths. There are four main types of interlock preforms: Through the Thickness Orthogonal Weave (TTOW), Through the Thickness Angle Interlock Weave (TTAW) and Layer to Layer Orthogonal Weave (LLOW) and Layer to Layer Angle Interlock Weave (LLAW).

Braiding is a process of interconnecting yarns to form two dimensional (2D) and three dimensional (3D) fabrics. The 2D braided preforms are essentially planar with the fibrous interconnectivity mainly in the plane of the preform. The 3D braided preforms are fully integrated continuous fiber assemblies with multiaxial inplane and out of plane fibre orientations.

The 3D braided preforms can be made by 2-step braiding, 4-step braiding or solid braiding. The fabric is constructed by intertwining of yarn systems to form an integral preform structure. Using the braided preforms and the RTM, the braided composites of a variety of architectures can be made. The 3D braided composite structures / preforms consist of continuous reinforcement yarns arranged along multiple directions. Such composite structures are ideal materials for structural applications where multidirectional mechanical and thermal stresses are experienced.

Designing and developing 3D braided composites is more complicated compared to the conventional laminated composites. Braided preform configuration can be designed to enhance typical mechanical properties for a given application. The exact distribution and orientation of the fibres depends upon braiding procedure used and the consolidation of braided composites. One of the important requirements is to increase the overall fiber volume fraction of the braided composites. This requires exact fulfillment of the jamming condition. For the mechanical property characterization, knowledge of the precise fibre structure is an essential requirement. Textile preform configuration can be designed to enhance typical mechanical properties for a given application.

Such composite materials are generally used for high temperature applications where multidirectional stress state exists in the structure, generally defined as hot structures. Reusable Launch Vehicles (RLV) used in aerospace engineering is the best example for hot structure. The RLV's are subjected to severe aerodynamic loads and thermal loads during flights. The control surfaces have to withstand high heat flux and elevated temperatures along with the pressure loads during the different regimes of the vehicle mission.

Since these hot structures experience multidirectional thermal and stress pattern and has complicated geometries for the aerodynamic profile, classical solutions are unavailable. Finite element method has generally been employed for such problems for performing nonlinear transient thermal analysis and nonlinear transient thermo-structural analysis. The structural behaviour is manifested with nonlinearity arising from time dependent thermal and structural strains. Experimental determination of 3D orthotropic thermomechanical properties of composites are required for carrying out thermal and thermo-structural analysis.

1.2 Scope and Objective

The objectives of the present study have been set as,

- The determination of high temperature material properties of unidirectional Carbon-Carbon material using analytical methods from the Carbon-Carbon fabric properties.
- The generation of 3D composite thermomechanical properties at room temperature and at elevated temperature from Representative Unit Cells (RUC's) based on constitutive equations for 3D composites.
- Identification of the best suitable 3D composite for RLV Nosecap through parametric studies involving the stress analysis of Nosecap by finite element method.

Various investigations and activities that constitute the scope of the study have been depicted schematically in fig 1.1.

1.3 Content of the Thesis

The first chapter of the thesis contains the introduction to 3D woven and braided composites and its application to hot structure applications. In the second chapter the literature survey carried out on woven, braided and thermo-structural analysis has been explained. In the third chapter the generation of unidirectional properties from the tested Carbon-Carbon fabric properties has been explained. The mathematical formulations for 3D composites, the details of the mathematical codes generated and the properties generated for different preform architectures has been given in fourth chapter. In the fifth chapter the thermo-structural analysis of a Nosecap which is a hotstructure has been carried out using the selected preforms and the selection of the best preform using the 3D failure theory has been explained. The sixth chapter gives the summary and conclusions.

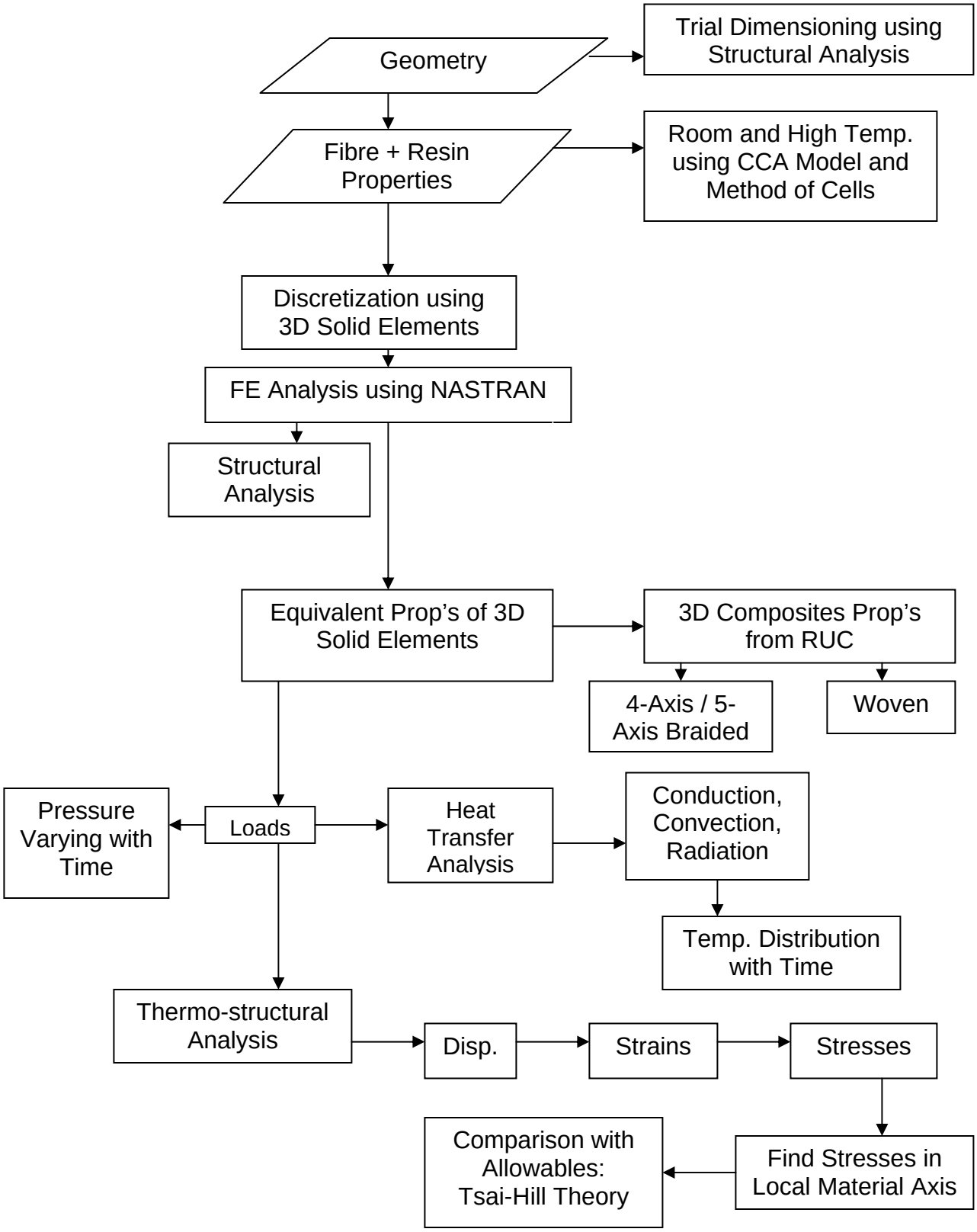

Fig 1.1 Schematic Representation of the Scope of Hot Structure Design

CHAPTER 2

LITERATURE REVIEW

Analytical methods are necessary for the evaluation of the thermal and mechanical properties of 3D composites. Survey of the literature has been carried out to find the proposed methods to obtain the elastic, thermal and strength properties of 3D composites. The scope of the survey has been extended to application of these properties in designing and developing hot structures and the review is given under three subheadings subsequently.

2.1 3D Woven Composites

Thermomechanical behavior of 3D woven composites (and under various loading directions) by employing various methods has been reported. One of the common models used in the literature for the determination of elastic properties of 3D woven composites is the Orientation Averaging (OA) model (Yang *et al.* 1986, Ko 1989, Whitney and Chou 1989, Tarnopolskii *et al.* 1992, Nagai *et al.* 1994, Cox 1995[1], Hartranft *et al.* 1995, Kuo 1995, Sankar and Marrey 1997[1], Tan *et al.* 1997, 1998, 1999, Naik and Thuruthimattam 1998[2], 1999). In this model, the 3D composite is assumed to be made up of small discrete volumes in which the fibers are aligned and treated as UD composites. Yarn waviness effects are generally not considered in the model. Using the isostress or isostrain assumptions, the response of a characteristic volume is averaged to obtain the macroscopic properties. This method is referred as the Volume Averaging method or Homogenization method, as well.

Based on the OA approach, Cox (1995[2]) presented a model for the elastic properties of 3D composite. Ko (1989) presented the fabric geometry model for finding out the elastic and strength properties of a 3D composite. In this approach, geometric unit cells defining the fabric architecture have been identified and quantified. The fractional volume in all the fibre directions has been calculated geometrically. A 6x6 stiffness matrix has been formed for a system of resin impregnated yarns using the stiffness matrix for a comparable UD composite and transforming it to the fibre orientation. The stiffness matrix for each system of yarns has been superimposed in proportion to their contributing volumes. Maximum strain energy criterion has been used to determine the properties for each system of yarns. The composite

has been said to have failed when all the yarns have failed. However, the failure of the average medium representing the composite need not be same as the failure of the weakest section in the unit cell.

Nagai *et al.* (1994) presented a model based on the stress analysis of a unit cell of 3D composite. The method involved the discretization of the unit cell into transversely isotropic sections, which are defined transverse to the loading direction and have been termed as volume elements. Expressions have been derived for the elastic properties of the unit cell as a whole. The failure strain for the unit cell has been defined as that of the weakest section. An attempt has been made to predict the tensile failure stress and strains under the assumption that failure of a section can be obtained from knowledge of the amount of fibre and matrix in a section which consists of longitudinal and transverse impregnated strands and pure matrix regions. Hence, the failure should be considered only at the elemental level consisting only of longitudinal or transverse resin impregnated strands and at pure matrix regions. In this paper, the failure is considered at section level, which represents the gross properties of the unit cell. This implies that the secondary failures and the effect of the failed elements on further stress-strain behavior had not been considered in their approach.

The thermal conductivity of the 3D orthogonal composite can be found by thermal electrical analogy which is based on similarity between the partial differential equations governing the thermal potential (temperature), T, and electrical potential distributions (electromotive force) E, (Clayton 1971, Dasgupta and Agarwal 1992, Ning and Chou 1995, 1998). The thermal resistance R, and heat flow $q = \Delta T/R$, in a thermal system are analogous to the electrical resistance r, and current flow $I = \Delta E/r$, in an electrical system. Here ΔT and ΔE are respectively the temperature difference and electrical potential difference, the fourier law governing the heat flow is mathematically equivalent to the ohms law governing the current flow. On the basis of this analogy, the effective thermal conductivity of a composite material has been determined by analysing the equivalent electrical resistance using ohms law.

Similar but limited studies are available on the prediction of stress and failure of 3D woven composites (Tarnopolskii *et al.* 1992, Cox *et al.* 1994[1], Cox 1995[2], Kuo 1995, Naik and Thuruthimattam 1998[1]). The failure of the average medium, but not the failure of the weakest region has been considered in these models. However, failure of average medium

representing the composite need not be the same as the failure of the weakest region in the 3D woven composites. This implies that the secondary failures and the effect of the failed regions on further stress-strain behavior have not been considered in these models.

Sankar and Marray (1997[1], 1997[2]) have presented an analytical method for two dimensional 2D plain weave and satin weave fabric composites. They have determined inplane and through the thickness thermoelastic properties. Ishikawa *et al.* (1997) have presented a closed form method for the thermomechanical properties of 3D orthogonal woven composites. In their analysis, actual 3D composite architecture has not been considered. Only a single layer consisting of stuffers, fillers and warp weavers with rectangular cross sections had been analyzed. The geometry considered for their analytical method does not really refer to a 3D woven composite. Tan *et al.* (1997, 1998, 1999) have presented two models for thermoelastic analysis of 3D woven composites. Their analysis is based on gross properties at element level. Rectangular cross sections were considered for the elements. The geometry of 3D woven composites has not been truly represented in their study. In all the above studies on thermoelastic behavior, mixed stiffness averaging and compliance averaging technique has been considered.

Cox *et al.* (1994[2], 1995) have presented the Binary Model (BM) for 3D composites based on finite element analysis. He has performed Monte Carlo simulations of failure under monotonic and fatigue loading. Micromechanical models of observed failure events have been used to determine the constitutive properties of the model elements. The two elements of the model have been the reinforcing tows representing only the axial properties of the individual resin impregnated strands and the effective medium elements representing all other properties of the strands, resin pockets, voids etc., in an average sense. The constitutive laws for the elements had been nonlinear with plasticity and local failure incorporated. The effective medium and tow elements have been coupled by imposing constraints between nodes. In the undamaged state, the elements shared the same nodes, while in the damaged state, relative displacements have been specified. Also the strands had no transverse properties; instead they have been included in the average properties of the effective medium elements.

The angle interlock woven composites, Through the Thickness Angle interlock Weave (TTAW) and Layer to Layer Angle interlock Weave (LLAW) have been explained in detail by

Naik and Azad (2001) and by Naik and Sridevi (2001). Even though, the assumptions are the fibres as straight, due to actual geometric undulations, certain knock down factors are introduced to get the effective properties. In reality the stuffers, fillers and warp weavers may not be straight. The predicted values are higher than the experimental values because the predictions are based on the ideal geometry.

Different weave geometries have been studied by Cox *et al.* (1994[2], 1995) and by Cox and Dadkhah (1995) for carbon/epoxy and its comparison with the test data have been presented for room temperature. It has been seen that the predictions are higher than the experimental results, since the predictions have been based on the ideal geometry.

Considering the above aspect, Cox and Dadkhah (1995) introduced the concept of Stiffness Knockdown Factors (SKNF) based on tow waviness in actual 3D composites. He developed experimental methods for characterizing the waviness of nominally straight tows. They have quantified out of plane waviness by statistical analysis of digitized images of cross sections. Digital image analysis has been used to reduce the images of stuffers and fillers to one dimensional curves representative of their centers. The axial stiffness properties of the 3D composites along the stuffer and filler directions have been knocked down by a factor in OA model. The stiffness knock down factors have been estimated from the tow waviness, i.e., from the distribution of out of plane misalignment angles. The Young's modulus in the fibre direction and Poisson's ratio have been reduced as E_1^{α}, $v_{12}^{\alpha} \rightarrow \eta^{\alpha} E_1^{\alpha}$, $\eta^{\alpha} v_{12}^{\alpha}$, where $\eta^{\alpha} \leq 1$and α = s, f. For the orthogonally woven composite (TTOW / LLOW) that has been studied, the SKNF have been $\eta^s = 0.86 (\pm 0.06)$ and $\eta^f = 0.98 (\pm 0.05)$. The waviness in the stuffers and fillers has been different. A lower KNF indicates higher waviness. For the TTAW that has been studied, the SKNF's were $\eta^s = 0.82 (\pm 0.07)$ and $\eta^f = 0.45 (\pm 0.04)$ and for LLAW, $\eta^s = 0.84 (\pm 0.05)$ and $\eta^f = 0.64 (\pm 0.05)$.

Tow waviness leads to reduction of the effective axial modulus of a straight tow. Cox *et al.* (1994[1]) has made a simple estimate of this softening and has incorporated in the model of the 3D composite, where spatially averaged composite properties have been estimated by averaging the properties of constituent tows of different orientations. They observed some inplane misalignment of stuffers and fillers. However, their fluctuations have been considerably smaller than the out of plane misalignments. They suggested a modification to the analytical model by reducing the longitudinal property due to warp weaver crimp via the

extreme assumption that the axial properties E_1^w, v_{12}^w of the warp weavers be reduced to the transverse properties E_2^w, v_{23}^w. The property reduction due to this has been termed as Crimp Reduction (CR). In their study the experimental failure strain is significantly higher than the predicted value. This is because the stuffers were initially undulated, as indicated by a low knockdown factor. As the load is increased, these undulated stuffers tend to straighten. Thus, the total experimental strain indicated is due to the combined effect of straightening and elongation of the stuffers during loading.

Naik and Thuruthimattam (1998[1]) analyzed typical architectures of TTAW and LLAW composites. They observed that the warp weavers had a stair step path through the thickness resulting from debulking of the weave preform during consolidation. The two portions of the warp weaver yarns have been roughly straight, with both the segments nearly oriented along the through the thickness direction. Stuffers have been nearly straight for both the cases whereas the fillers were wavy. During the processing and consolidation of the preforms into 3D composites, the thickness of the composite panel would decrease, and the stuffers, fillers and warp weavers would become wavy. Extend of yarn waviness and reduction in thickness would depend on the processing condition. It would vary for different products. The reduction in thickness of the 3D composite during consolidation would lead to an increase in V_f^o, in turn would lead to an increase in the mechanical properties. On the other hand, the waviness of the yarn would lead to a decrease in the mechanical properties. UD composite / impregnated strand properties have been derived by them using the 3D Composite Strength Model (3DCSM), considering the filler and warp weaver dimensions to be tending to zero. These UD composite properties match well with properties obtained using the composite cylinder assemblage model developed by Hashin (1972) and the method of cells developed by Aboudi (1991). Balanced symmetric crossply laminate properties are obtained using the 3D composite strength model considering the warp weaver dimensions to be tending to zero. Also, the fiber distribution along the stuffer and filler directions has been considered to be the same for the crossply laminate. There is a wide range of elastic and strength properties of bidirectional woven fabric composites, depending upon the extent of fibre undulation with optimum geometries have been presented by the following authors (Ganesh and Naik 1994, 1996[1], 1996[2], 1996[3], Naik 1994). The predicted properties by the authors match well with the reported properties.

2.2 3D Braided Composites

Braiding technology and braid geometry have been studied extensively by various authors (Stuart 1990, Chou 1992, Du and Ko 1993, Wang and Wang 1995[1], 1995[2], Pandey and Hahn 1996[1], 1996[2], Kumar and Wang 1997, Kuo and Chin 1997, Kuo *et al.* 1998, Mohajerjasbi 1998, Chen *et al.* 1999[1], 1999[2], Kamiya *et al.* 2000, Tang and Postle 2000, 2001, 2002). Thermomechanical analysis of 2D braided composites has been reported in literature (Naik[b] *et al.* 1994, Naik[b] 1995, Falzon and Herszbergl 1998, Byun 2000, Huang 2000). The analytical predictions are based on 2D homogenization technique. Such composites have lower through the thickness properties. The thermomechanical analysis has been carried out using 3D homogenization technique for 3D braided composites by various authors (Shanahan and Hearle 1978, Wang and Wang 1995[1], 1995[2], Glaessgen *et al.* 1996, De *et al.* 1998, Boisse *et al.* 2001, Wang and Sun 2001, Sagar *et al.* 2003).

In modeling the preform geometry, the effects of the braiding parameters on the generation of initial preform microstructure requires a detailed analysis. Several assumptions have been made on the yarn path traces and the yarn cross sections to simplify mathematical modeling by Wang and Wang (1995[1], 1995[2]). In their study, the effect of the interaction and friction between the yarns has not been considered. Wang and Sun (2001) considered the effect of interaction and friction between the yarns, but the change of yarn cross sections owing to the interaction has not been considered. Geometrical models which consider the interaction effects have been developed based on the principle of stationary potential energy (Shanahan and Hearle 1978, Glaessgen *et al.*1996, Sagar *et al.* 2003).

The deformed final configuration owing to the loads coming on the preform due to various processing conditions like draping etc., has been obtained from the initial preform by various investigators. De *et al.* (1998), Boisse *et al.* (2001) and Hofstee and Van (2001) have used FEM to deal with the fiber reorientation resulting from draping fabrics over a product mould. Further, the effect of compaction and resin flow has been integrated in determining the final geometry (Hu and Newton 1997, Robitaille and Gauvin 1998, Chen and Chou 1999, 2000, Chen *et al.* 2001). These studies have provided a general relationship between lateral pressure due to resin flow and geometric parameters like volume fraction or thickness of the final product. Lomov et al (2001) determined the permeability of the preform for resin transfer or injection processes. They have also presented review on preform modelling strategies.

Lei *et al.* (1992) have considered the 3D braid architecture assuming straight strand within individual braid steps. They have considered the so obtained geometry as a space structure for analysis. Bigaud *et al.* (2005) have considered an initial geometry based on the motion of the bobbin carriers. They have arrived at the final realistic geometry based on the yarn interactions and the consolidation process by assuming a known thickness of the final product.

There exist a relationship between the manufacturing process and the resulting preform architecture which should be analytically obtainable. Based on the braiding procedure, Ko (1982) has made a study on the yarn architecture in the preforms. In the case of a rectangular preform braided by the 4-step 1 x 1 procedure, he has identified a unit cell like substructure which represents the fiber architecture of the entire preform. Li (1990) has used rectangular preforms braided by the 4-step 1 x 1 procedure which is topologically different from the unit cell obtained by Ko. He observed that the surface and interior unit cells have different configurations. Lei *et al.* (1992) and Kostar and Chou (1992) have further observed that corner unit cells are different than surface and interior unit cells. Wang and Wang (1995[1]) have described the topology of the 3D braided structure and differentiated central (interior), side (surface) and corner unit cells using the braiding procedure alone. They have observed that the general topology remains the same for identical braiding procedures.

Li and Shiekh (1988) have made a comparison on the process, structure and mechanical properties of the preforms for 2-step braids and 4-step braids. Du *et al.* (1991) have identified a process based on the yarn jamming condition of the preform using a detailed analysis of 2-step braided preforms. A systematic analysis has been performed for studying the effect of various preform geometric and process parameters on the microstructures of 2-step and 4-step braided composites by Byun and Chou (1996). Pandey and Hahn (1996[2]) have developed a solid model from the traces of the yarn path and then retrieved the unit cells by sectioning the integrated solid model and further predicted the elastic properties using isostrain condition. A review on the application of 3D composites has been presented by Mouritz *et al.* (1999).

Yang *et al.* (1986) have presented fiber inclination model for the elastic analysis of 3D braided composites. The analysis has been based upon the classical laminated plate theory.

In order to predict the tensile modulus of 3D braided composites, Ko (1986) has proposed a model based on average cosine concept. Byun and Chou (1989) and Chou and Ko (1989) have reviewed various models to predict the response of homogenized equivalents of textile composites. Wang and Wang (1995[1]) have presented microstructure property relationships in 3D braided composites. Wu (1996) has proposed a three cell model to determine the mechanical properties of braided composites. In his model the unit cell has been subdivided into three cells for analysis. Sun and Qiao (1997) have proposed a modified laminate theory to predict elastic properties for 3D braided composites.

Zuorong *et al.* (1999) have evaluated the elastic properties of braided composites using the homogenization method. They observed a good match between the experimental and predicted results. Chen *et al.* (1999[1]) have presented a unit cell geometrical model on the basis of fibre movement in braiding processes. Further, Chen *et al.* (1999[2]) have proposed the finite multiphase element method to predict the elastic properties of braided composites. Tao *et al.* (2004[1], 2004[2]) have developed finite element model to predict the local stress and strength within 3D braided composites under the three dimensional mechanical loading. They also studied the nonlinear response and damage evolution. Tang and Postle (2000, 2001, 2002) have simulated the fabric structure and derived the fiber volume fraction of the braided composites. They have carried out simulation and developed mathematical model to establish tensile and shear moduli for 3D 4-step braiding process. Further, they used the nonlinear finite element approach to simulate and analyse the 3D braided structures for deformation. Miravete *et al.* (2006) have proposed an analytical mesomechanical approach which is based on a unit cell scheme taking into account the geometry and the mechanical properties of phases, the fiber and the matrix. Different aspects of braided composites behavior, i.e., energy absorption characteristics, damage mechanisms and the behavior under compressive loading have been studied by various authors (Chou 1992, Bogdanovich and Pastore 1996, Kalidindi and Abusafieh 1996, Kuo *et al.* 1998, Ko 1999, Kostar and Chou 1999, Harte and Fleck 2000).

Comparison of analytical and experimental results and difference between these has been investigated by many authors. Naik and Thuruthimattam (1998[1], 1998[2], 1999) have used the 3D Composite Strength Model for generating the 3D woven composites and their method of evaluating the properties satisfactorily meets the tested properties, so the above method has been used in the present study for the evaluation of properties. Braid

architecture has been considered with an extension of 3D Composite Strength Model for the property evaluation of 3D braided composites by Lei *et al.* (1992). Sun and Qiao (1997) and Zuorong *et al.* (1999) have evaluated the elastic properties based on similar homogenization method has been adopted in the present study.

2.3 Thermo-structural Analysis of Composite Structures

Heat transfer, thermal stresses, and thermal buckling analyses have been performed on the unconventional wing structure of a Hyper-X hypersonic flight research vehicle designated as X-43 subjected to nominal Mach 7 aerodynamic heating by William and Leslie (2001). A wing mid span cross section has been selected for the heat transfer and thermal stress analyses. Thermal buckling analysis has been performed on three regions of the wing skin (lower or upper); 1) fore wing panel, 2) aft wing panel, and 3) unit panel at the middle of the aft wing panel and thermal buckling analysis has been performed on a mid span wing segment. The unit panel region is identified as the potential thermal buckling initiation zone. Therefore, thermal buckling analysis of the Hyper-X wing panels has been reduced to the thermal buckling analysis of that unit panel. “Buckling temperature magnification factors” has been established. Structural temperature versus time histories has also been presented. The results show that the concerns of shear failure at wing and spar welded sites, and thermal buckling of Hyper-X wing panels may not arise under Mach 7 conditions.

An alternative design for variable sweep wings have been investigated by Mattioni *et al.* (1998), which consists of a two spar, CFRP (Carbon Fiber Reinforced Plastics) wing, with truss like ribs. The spar web is a shell structure laminated using an unsymmetric stack sequence in order to take advantage of the residual stress field developed during the curing process, resulting in increased transverse curvature of the spar. The effect of this curvature is two fold: to increase the moment of inertia to withstand bending stresses and under certain loading conditions, to behave like an elastic hinge to allow the sweep angle of the wing to change.

Finite element thermal stress analysis has been performed by William and Raymond (1991) on a rectangular titanium honeycomb core sandwich panel, which is subjected to thermal load with a temperature gradient across its depth. The distributions of normal stresses in the face sheets and the face sheet / sandwich core interfacial shear stresses are

presented. The thermal buckling of the heated face sheet was analyzed by assuming the face sheet to be resting on an elastic foundation representing the sandwich core. Thermal buckling curves and thermal buckling load surface has been presented for setting the limit for temperature gradient across the panel depth.

Thermo-structural analyses of passive and active hot composite structures considering temperature depended material properties under thermal and mechanical loads has been carried out by Ramesh (2004). The behaviour of the composite material under thermal and thermochemical loads and how it is translated into the modeling of thermo-structural analysis, general approaches to carry out such analysis has been briefly discussed. Thermo-structural analysis shows that thermal stresses are very much predominant when compared to stresses due to mechanical loads. A parametric study on variation of coefficient of thermal expansion ***(α)*** due to change in fiber orientation of 2D Carbon-Carbon cap type structure has been studied and it is concluded that one of the critical design variables identified is the ***α*** value across the thickness of the laminate.

A Structural Performance and Resizing (SPAR) finite element thermal analysis computer program has been used in heat transfer analysis of the space shuttle orbiter subjected to reentry aerodynamic heating by William *et al.* (1986). Three wing cross sections and one mid fuselage cross section have been selected for the thermal analysis. The predicted thermal protection system surface temperatures has been found to agree well with flight measured temperatures. The calculated Aluminium structural temperatures also have agreed reasonably well with the flight data from reentry to touch down. The effects of internal radiation and internal convection have been found to be significant. The SPAR finite element solutions have been found to agree reasonably well with those obtained from the conventional finite difference method.

Thermo-structural analysis has been performed on a heated titanium honeycomb core sandwich panel by William (1997). The sandwich panel has been supported at its four edges with spar like substructures that acted as heat sinks, which are generally not considered in the classical analysis. One side of the panel has been heated to high temperature to simulate aerodynamic heating during hypersonic flight. Two types of surface heating have been considered, where flat temperature profile, which ignores the effect of edge heat sinks is the first case and the latter case is dome shaped temperature profile,

which approximates the actual surface temperature distribution associated with the existence of edge heat sinks. The finite element method has been used to calculate the deformation field and thermal stress distributions in the face sheets and core of the sandwich panel. The detailed thermal stress distributions in the sandwich panel have been presented, and critical stress regions are identified. The study shows how the magnitudes of those critical stresses and their locations change with different heating and edge conditions. The paper presents comprehensive, three dimensional graphical displays of thermal stress distributions in every part of a titanium honeycomb core sandwich panel subjected to hypersonic heating on one side. The plots offer quick visualization of the structural response of the panel and are very useful for hot structures designers to identify the critical stress region.

Mechanical and thermal buckling analyses have been performed on rectangular plates with central cutouts by William (1998). The cutouts are either circular holes or square holes. The finite element structural analysis method was used to study the effects of plate support conditions, plate aspect ratio, hole geometry, and hole size on the mechanical and thermal buckling strengths of the perforated plates. By increasing the hole size, thermal buckling strengths of the plates has been enhanced. The compressive buckling strengths of the plates could also be increased considerably only under certain boundary conditions and aspect ratios. The plate buckling mode can be symmetrical or antisymmetrical, depending on the plate boundary conditions, aspect ratio, and the hole size. For the same cutout areas, the buckling strengths of the same sized plates with square holes generally surpass those of the plates with circular holes over the range of hole sizes. The results and illustrations provide vital information for the efficient design of aerospace structural panels.

A lighter composite design which is thermomechanically compatible to the primary structure of the satellite has been presented by Harri and Helsinki (1998). Carbon composite electronics housing has been designed according to the requirements set for an existing Aluminum housing. The various aspects considered in the thermal and structural analysis have been presented. Based on the design and analysis results, a breadboard model has been manufactured and tested. The correlation between analysis and test results has been discussed in short.

An analytical solution has been presented for three dimensional thermomechanical deformations of a simply supported Functionally Graded (FG) rectangular plate subjected to

time dependent thermal loads on its top and/or bottom surfaces by Senthil (2002). Material properties have been taken to be analytical functions of the thickness coordinate. The uncoupled quasi static linear thermoelasticity theory has been adopted in which the change in temperature, if any, due to deformations is neglected. A temperature function that identically satisfies thermal boundary conditions at the edges and the Laplace transformation technique has been used to reduce equations governing the transient heat conduction to an Ordinary Differential Equation (ODE) in the thickness coordinate which is solved by the power series method. The elasticity problem for the simply supported plate for each instantaneous temperature distribution has been analyzed by using displacement functions that identically satisfy boundary conditions at the edges. The analytical solution is applicable to a plate of arbitrary thickness. Results have been given for two constituent metal ceramic FG rectangular plates with a power law for through the thickness variation of the volume fraction of the constituents. The effective elastic moduli at a point have been determined either by using the Mori-Tanaka or the self consistent scheme. The transient temperature, displacements and thermal stresses at several critical locations has been presented for plates subjected to either time dependent temperature or heat flux prescribed on the top surface. Results are also given for various volume fractions of the two constituents, volume fraction profiles and the two homogenization schemes.

Thermal buckling of antisymmetric cross ply laminates has been investigated by Thomas *et al.* (1992). Thermal critical load parameter and mechanical critical load parameter in the case of isotropic and composite laminates has been discussed.

2.4 Comments

From among the reported analytical and experimental investigations the 3D Composite Strength Model proposed by Naik and Thuruthimattam (1998[1], 1998[2], 1999) for generating the thermomechanical properties of 3D woven composites has been identified for the present study. They have analyzed various architectures of preforms, considering the variation of fibre orientations which includes the changes in configurations due to processing and consolidation of preforms into 3D composites. Orientation Averaging model (OA) used by various authors (Cox and Dadkhah 1995, Naik and Thuruthimattam 1998[1], 1998[2], 1999, Tan et al. 1998) is used to solve the mathematical formulation of RUC to find the average properties and failure stresses. The properties generated by using the above model with

carbon/epoxy at room temperature data compare very well with the experimental investigations. The UD properties have been established based on Composite Cylinder Assemblage Model by Hashin (1972) and the Method of Cells by Aboudi (1991), which are well validated in literature. The experimental data generated by Cox et al. (1994[1] and 1995), Cox and Dadkhah (1995) for 3D composites has been used to validate the code developed based on the analytical methodology.

Recommendations made by Ishikawa et al. (1997) for using Compliance Averaging scheme for determination of modulus of elasticity and CTE and Stiffness Averaging scheme for moduli of rigidity and Poisson's ratio have been adopted in the present study. The thermal conductivity of the 3D composite is estimated using thermal electrical analogy used by various authors (Clayton 1971, Dasgupta and Agarwal 1992, Ning and Chou 1995, 1998) has been adopted in the present study.

The 3D Composite Strength Model used for generating the woven composite properties has been extended by Lei et al. (1992) for braid architecture and was further extended by Sun and Qiao (1997) and Zuorong et al. (1999) based on similar homogenization method. Unit cell geometry for 3D braided composites is explained in detail by Du and Ko (1993). These procedures have been adopted at relevant stages in the present study.

CHAPTER 3

DETERMINATION OF HIGH TEMPERATURE MATERIAL PROPERTIES OF UD C-C MATERIAL

3.1 Experimental Determination of Material Properties of C-C Fabric

Design and development of thermo-structural products capable of withstanding the stringent flight conditions is a major task. C-C composites are the state of the art material and C-C composite products are important breakthrough as far as materials are concerned. Testing and characterization of engineering materials are mandatory for quality control, thermo-structural product design, prediction and evaluation of product performance. Eventhough composites are heterogeneous and anisotropic, for complete characterization it is assumed to be 3D orthotropic and subsequently the properties are evaluated in three mutually perpendicular directions. Material properties of C-C fabric are determined from experimental investigations. From these known properties of C-C fabric, unidirectional material properties are determined analytically. These properties will become the input for generating the properties for 3D composites and from among these all the elastic, thermal and strength constants need to be evaluated for their analysis. The test methodology to be adopted for complete characterization is explained under subsequent headings.

3.2 Test Methodology

The physical properties, mechanical and thermal properties at Room Temperature (RT) and elevated temperatures which are required for design purpose are listed out in table 3.1. Inplane testing methods are unsuitable for adaptation to Through Thickness (TT) mechanical testing due to manufacturing difficulties of the specimen and costs associated with producing thick composite sections (i.e. 20 mm, or greater). ASTM standard specimens for the determination of TT properties have dimensions much more than the product thickness. Special techniques developed by National Physical Laboratory (NPL), UK have been resorted to evaluate TT mechanical properties.

Table 3.1 Properties of Carbon-Carbon Composite (for carrying out thermo-structural analysis)

Physical Properties	
1	Volume fraction of fibre in x, y and z directions
2	Volume fraction of matrix
3	Volume fraction of void
4	Density
Mechanical Properties	
1	Tensile strength and modulus in x, y and z directions
2	Compressive strength and modulus in x, y and z directions
3	Shear strength and modulus in xy, yz and xz planes
4	Poisson's ratio in xy, yz and xz planes
Thermal Properties	
1	Coefficient of thermal expansion in x, y and z directions
2	Thermal conductivity in x, y and z directions
3	Specific heat

3.2.1 Physical properties

The physical properties and the testing standards are shown in table 3.2. The mechanical and thermal properties of composites strongly dependent on the fibre volume fraction and this parameter constitute an important quality measure. There are three methods for determining the fibre volume fraction viz., matrix digestion, the burn off technique and photo micrographic technique. The first two methods are ASTM standard but not applicable for C-C composites as the matrix and the reinforcement are composed of the same element (carbon). The photo micrograph is not an ASTM standard, but it provides an independent estimate of fibre volume fraction. The method requires a photograph of a polished cross section of a composite and many such samples to produce reliable results, because the area viewed is only about a hundredth of a square millimeter whereas it is possible to obtain an image of the distribution of fibres and to detect voids in the other methods. ASTM methods are available for the determination of density and void fraction.

Table 3.2 Physical Properties and Testing Standards

Sl. No.	Property	Procedure	Specimen dimensions l x b x t (mm)
1	Fibre volume fraction	Non-ASTM Method	5x5x5
2	Density	ASTM D 505	25x12.5x10
3	Void fraction	ASTM D 2734	25x12.5x10

3.2.2 Mechanical properties

The ASTM procedure or the procedure followed by M/s. Kompozit, Russia has been adopted for inplane mechanical properties. The specimen dimensions and test procedure are shown in table 3.3. Procedures developed exclusively for TT mechanical properties evaluation by NPL, and Defense Evaluation and Research Agency (DERA), UK are used in the present study. Square cross section specimens (15 mm square) with TT dimensions ranging from 18 to 40 mm have proved satisfactory for measuring TT elastic properties. Specimen dimensions specified by DERA method are shown in table 3.4.

Table 3.3 Standard Specimen Dimensions for Inplane Mechanical Properties

Sl. No.	Property	Procedure	Specimen dimensions (mm)
1	Tensile strength & Modulus (x, y)	ASTM D 638M	150x 25x 10
2	Compressive strength & Modulus (x, y)	Russian std	30x15x15
3	Shear strength & Modulus (xy plane)	Russian std	66x33x18
4	Poisson's ratio (xy plane)	Russian std	170x10x15
5	Interlaminar Shear Strength (ILSS)	Russian std	50x15x10
6	Flexural strength & Modulus	Russian std	300x 15x10

The sample for tension test and compression test at RT are shown in fig 3.1 and 3.2 respectively. The sample for ILSS and Poisson's ratio are shown in fig 3.3 and 3.4 respectively.

Table 3.4 Standard Specimen Dimensions for TT Mechanical Properties

Sl. No.	Property	Specimen dimensions (mm)
1	Tensile strength & Modulus (z)	12.5x12.5x19
2	Compressive strength & Modulus (z)	12.5x12.5x19
3	Shear strength & Modulus (xz, yz)	20x10x2
4	Poisson's ratio (xz, yz)	12.5x12.5x19

3.2.3 Thermal properties

Coefficient of Thermal Expansion (CTE) in all the three directions can be determined using Thermo Mechanical Analyzer (TMA). The sample size is small and can be realized from the standard laminates. Sample diameter requirement is 12 mm for the Russian method using A-26M instrument. The standards and the specimen dimensions for all the thermal properties are shown in table 3.5.

Table 3.5 Standard Specimen Dimensions for Thermal Properties

Sl. No.	Property	Procedure	Specimen Dimensions lxbxt(mm)
1	Coefficient of thermal expansion	ASTM 3386	4x4x6
2	Thermal conductivity	ASTM C177	50ϕ x 6
3	Specific heat	ASTM E 794	10-15

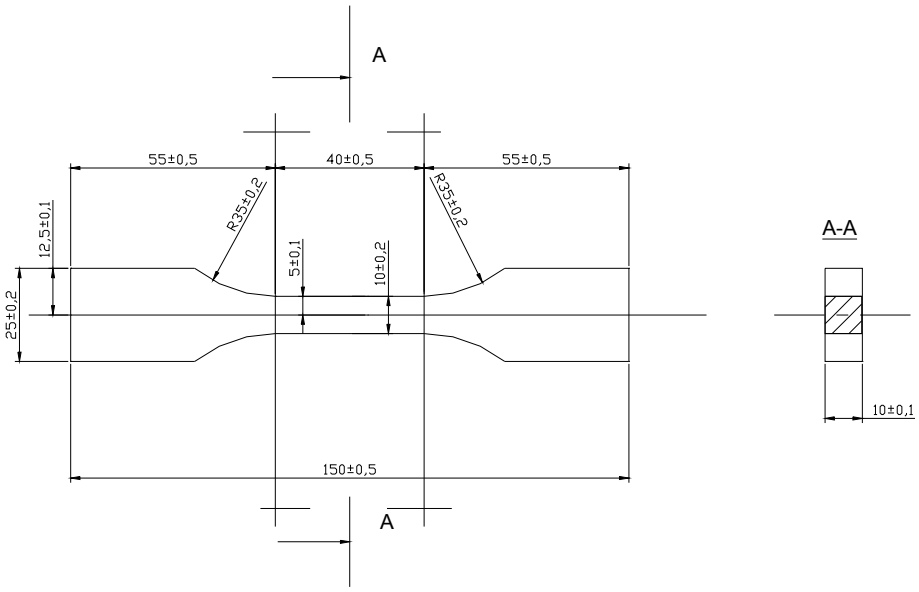

Fig 3.1 Specimen for Tension Test at Room Temperature

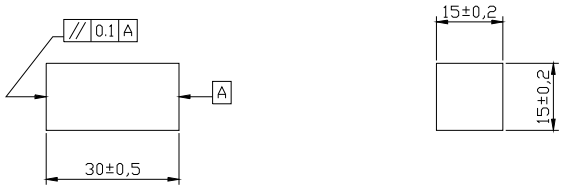

Fig 3.2 Specimen for Compression Test at Room Temperature

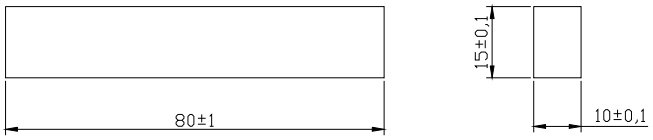

Fig 3.3 Specimen for Out of plane Shear Test

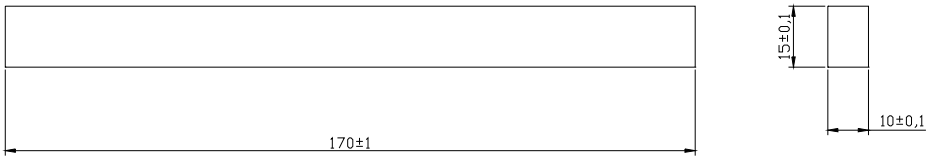

Fig 3.4 Specimen for Determination of Poisson's ratio

3.3 Tested Properties of C-C Fabric

Specimens are made and tested at M/s Kompozit, Russia using the test methodology and standards specified in sections 3.2.1, 3.2.2 and 3.2.3 and the properties (i.e; elastic, strength and thermal) are shown in table 3.6, 3.7 and 3.8.

Table 3.6 Carbon-Carbon Fabric Elastic Properties

Property / Temperature in deg. K	**293**	**773**	**1273**	**1773**	**2273**	**2773**
Longitudinal tensile modulus in warp direction (N/mm^2)	70000	70000	70000	70000	66000	64000
Longitudinal tensile modulus in weft direction (N/mm^2)	70000	70000	70000	70000	66000	64000
Transverse tensile modulus (N/mm^2)	2400	2400	2400	2400	2400	2400
Poisson's ratio v_{12} v_{23} v_{31}	0.05	0.05	0.05	0.05	0.05	0.05
Inplane shear modulus G_{12} (N/mm^2)	2000	2000	2000	2000	2000	2000
Out of plane shear modulus G_{13}, G_{23} (N/mm^2)	1200	1200	1200	1200	1200	1000

Table 3.7 Carbon-Carbon Fabric Strength Properties

Property / Temperature in deg. K	**293**	**773**	**1273**	**1773**	**2273**	**2773**
Tensile strength in warp direction (N/mm^2)	120	120	120	140	130	120
Tensile strength in weft direction (N/mm^2)	120	120	120	140	130	120
Compressive strength in warp direction (N/mm^2)	90	90	90	110	100	90
Compressive strength in weft direction (N/mm^2)	90	90	90	110	100	90
Tensile strength in transverse direction (N/mm^2)	6	6	6	7	7	
Compressive strength in transverse direction (N/mm^2)	100	100	100	110	100	
Inplane shear strength (N/mm^2)	25	25	25	30	25	
ILSS (N/mm^2)	8	8	8	10	12	

Table 3.8 Carbon-Carbon Fabric Thermal Properties

Property / Temperature in deg. K	**293**	**773**	**1273**	**1773**	**2273**	**2773**
CTE in warp direction (/^{o}K)	-3.50E-07	5.50E-07	1.00E-06	1.30E-06	1.80E-06	2.00E-06
CTE in weft direction (/^{o}K)	-3.50E-07	5.50E-07	1.00E-06	1.30E-06	1.80E-06	2.00E-06
CTE in TT direction (/^{o}K)	2.50E-06	4.00E-06	5.00E-06	6.00E-06	7.00E-06	7.00E-06
Thermal conductivity in warp direction (W/m^{o}K)	8.5	10	11.5	13.25	14.85	15.9
Thermal conductivity in weft direction (W/m^{o}K)	8.5	10	11.5	13.25	14.85	15.9
Thermal conductivity in transverse direction (W/m^{o}K)	5.1	6.4	7.8	9.2	10.5	11.6
Specific heat (J/Kg.^{o}K)	650	1590	1920	2020	2090	2130

3.4 Determination of UD Properties from Fabric Properties

Unidirectional properties of impregnated C-C strand and basic carbon matrix properties are necessary for determining the 3D composite mechanical and thermal properties since they form the basic building blocks of the representative unit cell (RUC). The fabric geometry and UD fibre geometry described by Ganesh and Naik (1996[1], 1996[2], 1996[3]) have been used in the present study for the analytical estimation of the UD properties from fabric. The volume fractions of the fabric and UD fibre can easily be determined from the above geometries. The impregnated fibre is assumed to be transversely isotropic and its elastic properties are evaluated from the transversely isotropic fibre and matrix properties at fibre volume fraction, V_f. The properties of the fibres and the matrix used for making the textile composite need to be evaluated for different volume fractions for evaluating the overall properties of the textile composites. Different methods are employed for determining these properties. They are Composite Cylinder Assemblage model (CCA) by Hashin (1972), which gives the mechanical properties and Aboudi's method of cells by Aboudi (1991) and by Paley and Aboudi (1992) which give all the thermomechanical properties required for the estimation of equivalent textile composite properties. The description of CCA model and Aboudi's method are given in Appendix A and Appendix B of the thesis.

For the evaluation of UD properties, the methodology adopted is validated using tested T-300 carbon fabric properties to tested T-300 UD properties which are shown in table 3.9. Once the T-300 material properties are validated, the same is extended for C-C as well.

Table 3.9 Prediction and Correlation of T-300 UD from Fabric Properties

Property	T-300 Fabric (Experimental)	T-300 UD (Experimental)	T-300 UD (Analytical)	% Variation
E_x (N/mm^2)	44223.48	128020.5	126902.2	0.87
E_y (N/mm^2)	43899.75	9074.25	8819.19	2.8
v_{xy}	0.102	0.286	0.292	2.09
G_{xy} (N/mm^2)	3433.5	4757.85	4532.22	4.7
σ_x (N/mm^2)	470.88	1393.02	1353.78	2.8
τ_{xy} (N/mm^2)	85.1508	88.7805	85.16	4.0

3.5 Results and Discussions

UD properties of impregnated Carbon fibre with 0.66 volume fraction have been evaluated based on the assumptions explained in section 3.4. Similarly the properties of carbon matrix are also evaluated. Through the thickness properties of the fabric is dominated by the matrix and transverse properties of fibre which are very close to matrix values, being matrix and fibre made out of carbon material. Hence assuming the same as matrix properties is a valid assumption, which also closely resembles the fabrication process adopted for making C-C. The results of these investigations are described below.

The elastic properties for UD fibre and matrix are evaluated and the properties are given in table 3.10 and 3.11. The modulus of elasticity varying with temperature along fibre and transverse direction is given in fig 3.5. The variation of shear modulus for UD fibre varying with temperature is given in fig 3.6.

Table 3.10 Elastic Properties of Impregnated Carbon Fibre

Property / Temperature in deg. K	**293**	**773**	**1273**	**1773**	**2273**	**2773**
Longitudinal tensile modulus in fibre direction (N/mm^2)	200869.6	200869.6	200869.6	200869.6	189391.3	183652.2
Transverse tensile modulus (N/mm^2)	6952.399	6952.399	6952.399	6952.399	6946.052	6942.586
Poisson's ratio $v_{12} = v_{13}$	0.143478	0.143478	0.143478	0.143478	0.143478	0.143478
Poissons ratio v_{23} (assumed)	0.3	0.3	0.3	0.3	0.3	0.3
Inplane shear modulus G_{12}, G_{13} (N/mm^2)	2678.09	2678.09	2678.09	2678.09	2678.09	2678.09
Out of plane shear modulus G_{23} (N/mm^2)	2674.00	2674.00	2674.00	2674.00	2671.56	2670.23

Table 3.11 Elastic Properties for Carbon Matrix

Property / Temperature in deg. K	293	773	1273	1773	2273	2773
Modulus of elasticity (N/mm^2)	2400	2400	2400	2400	2400	2400
Poisson's ratio	0.05	0.05	0.05	0.05	0.05	0.05
Shear modulus (N/mm^2)	1142.857	1142.857	1142.857	1142.857	1142.857	1142.857

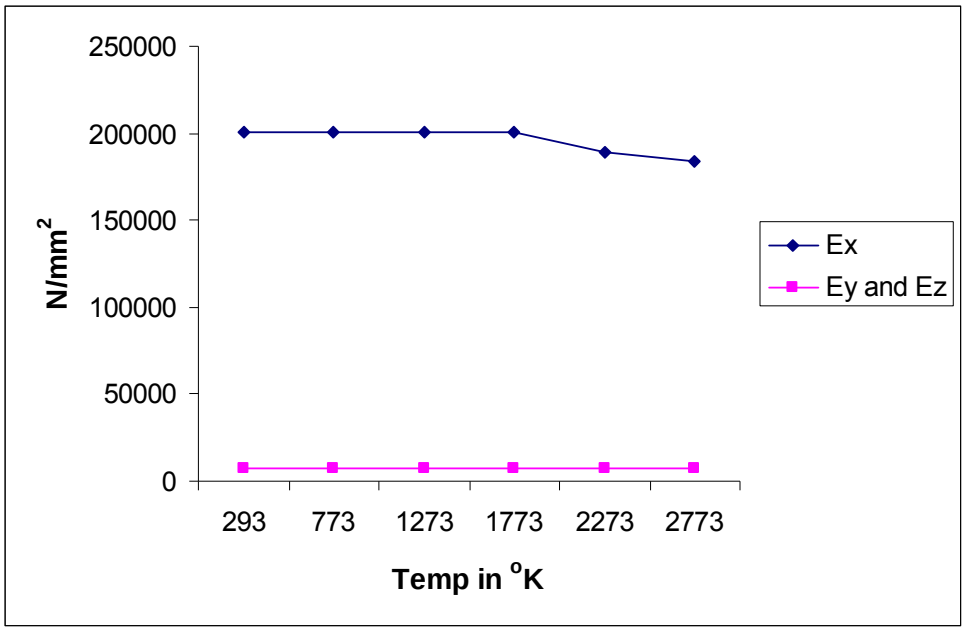

Fig 3.5 Modulus of Elasticity along Fibre and Transverse Direction

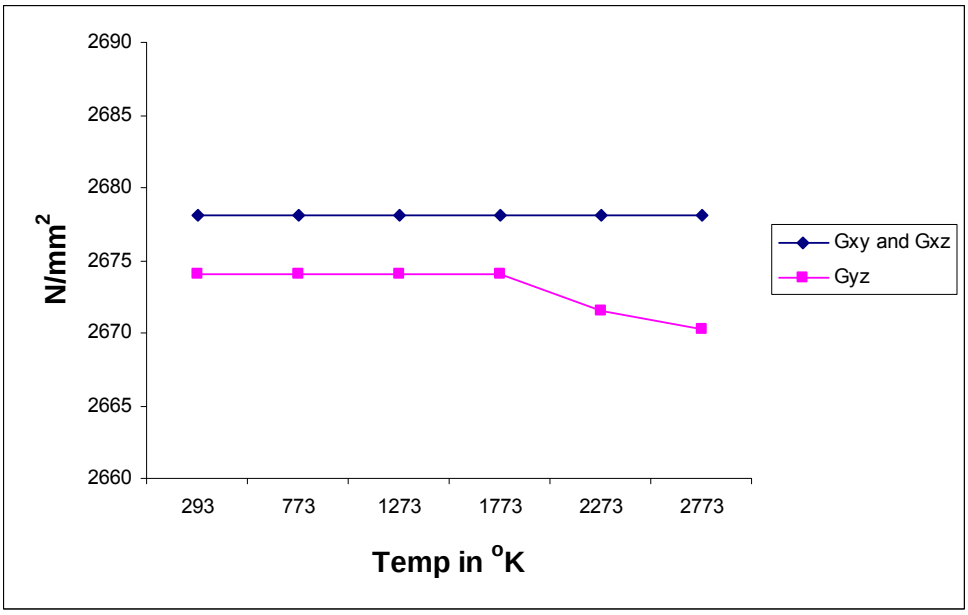

Fig 3.6 Shear Modulus of UD

The thermal properties are evaluated for UD fibre and matrix varying with temperatures and are shown in tables 3.12 and 3.13. The CTE along fibre and transverse direction is shown in fig 3.7. The same for the cabon matrix is shown in fig 3.8. The thermal conductivity in the fibre direction and transverse direction is shown in fig 3.9. The same for the carbon matrix is shown in fig 3.10. The specific heat for the UD fibre and matrix is shown in fig 3.11.

Table 3.12 Thermal Properties of Impregnated Carbon Fibre

Property / Temperature in deg. K	**293**	**773**	**1273**	**1773**	**2273**	**2773**
CTE in fibre direction (/^{o}K)	-1.0E-06	1.58E-06	2.87E-06	3.73E-06	5.17E-06	5.74E-06
CTE in transverse direction (/^{o}K)	7.17E-06	1.15E-05	1.43E-05	1.72E-05	2.01E-05	2.01E-05
Thermal conductivity in fibre direction (W/m^{o}K)	24.39	28.70	33.00	38.02	42.61	45.63
Thermal conductivity in transverse direction (W/m^{o}K)	14.63478	18.36522	22.38261	26.4	30.13043	33.28696
Specific heat (J/Kg.^{o}K)	650	1590	1920	2020	2090	2130

Table 3.13 Thermal Properties for Carbon Matrix

Property / Temperature in deg. K	**293**	**773**	**1273**	**1773**	**2273**	**2773**
CTE (/^{o}K)	2.50E-06	4.0E-06	5.0E-06	6.0E-06	7.0E-06	7.0E-06
Thermal conductivity (W/m ^{o}K)	5.1	6.4	7.8	9.2	10.5	11.6
Specific heat (J/Kg. ^{o}K)	650	1590	1920	2020	2090	2130

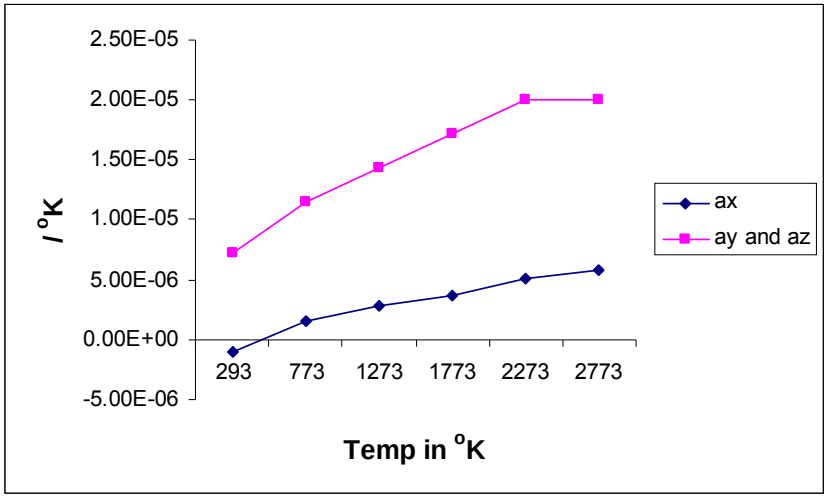

Fig 3.7 CTE along Fibre and Transverse Directions

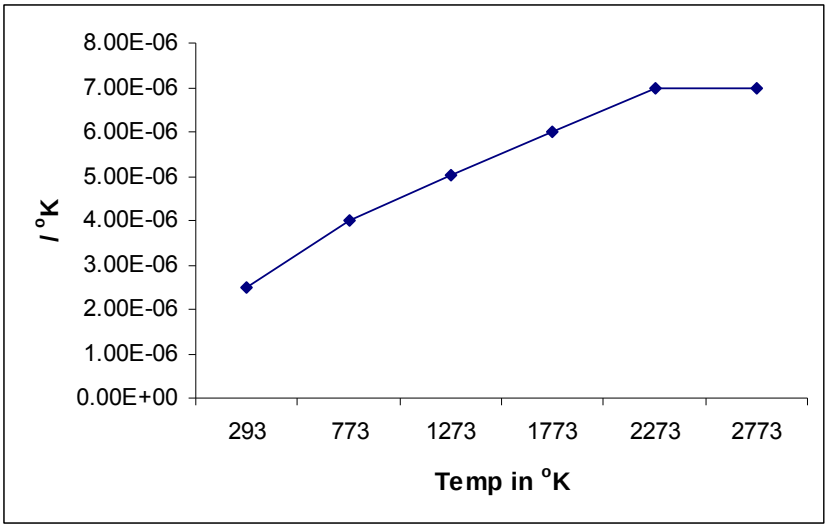

Fig 3.8 CTE for Carbon Matrix

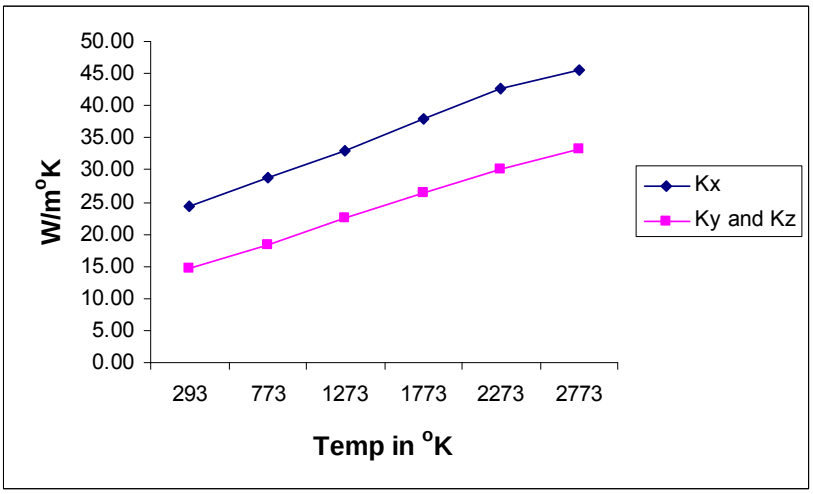

Fig 3.9 Thermal Conductivity along Fibre and Transverse Directions

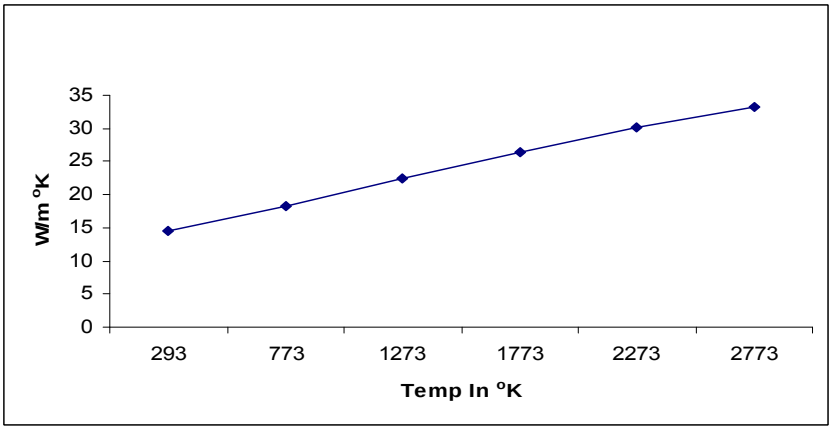

Fig 3.10 Thermal Conductivity for Carbon Matrix

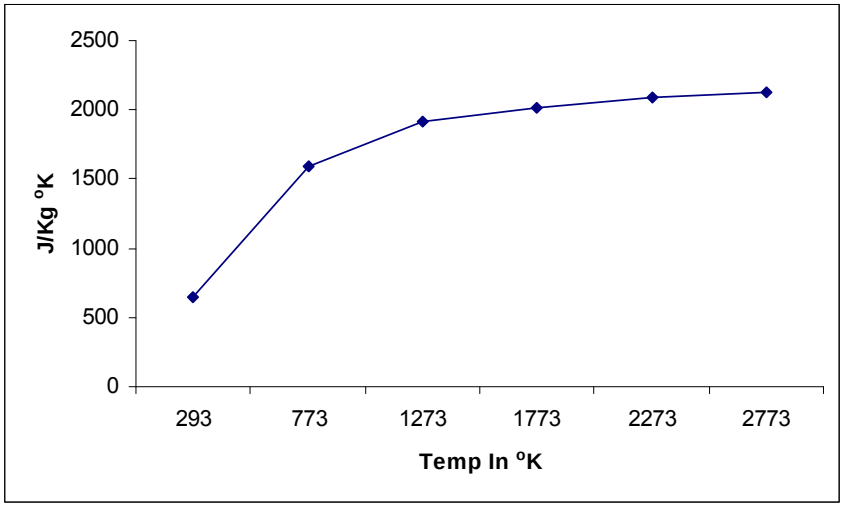

Fig 3.11 Specific Heat of UD and Matrix

The strength properties are evaluated for UD fibre and matrix varying with temperature and are shown in tables 3.14 and 3.15. The tensile strength along fibre direction and transverse direction are given in fig 3.12 and 3.13. The same for the carbon matrix is given in fig 3.14. The compressive strength along fibre direction and transverse direction is shown in fig 3.15 and 3.16. The inplane shear strength for UD is given in fig 3.17 and that for the matrix is given in fig 3.18.

Table 3.14 Strength Properties of Impregnated Carbon Fibre

Property / Temperature in deg. K	**293**	**773**	**1273**	**1773**	**2273**	**2773**
Tensile strength in fibre direction (N/mm^2)	344.3478	344.3478	344.3478	401.7391	373.0435	344.3478
Compressive strength in fibre direction (N/mm^2)	258.2609	258.2609	258.2609	315.6522	286.9565	258.2609
Tensile strength in transverse direction (N/mm^2)	6	6	6	7	7	7
Compressive strength in transverse direction (N/mm^2)	100	100	100	110	100	100
Inplane shear strength (N/mm^2)	25	25	25	30	25	25
Out of plane shear strength (N/mm^2)	8	8	8	10	12	12

Table 3.15 Strength Properties for Carbon Matrix

Property / Temperature in deg. K	**293**	**773**	**1273**	**1773**	**2273**
Tensile strength (N/mm^2)	6	6	6	7	7
Shear Strength (N/mm^2)	8	8	8	10	12

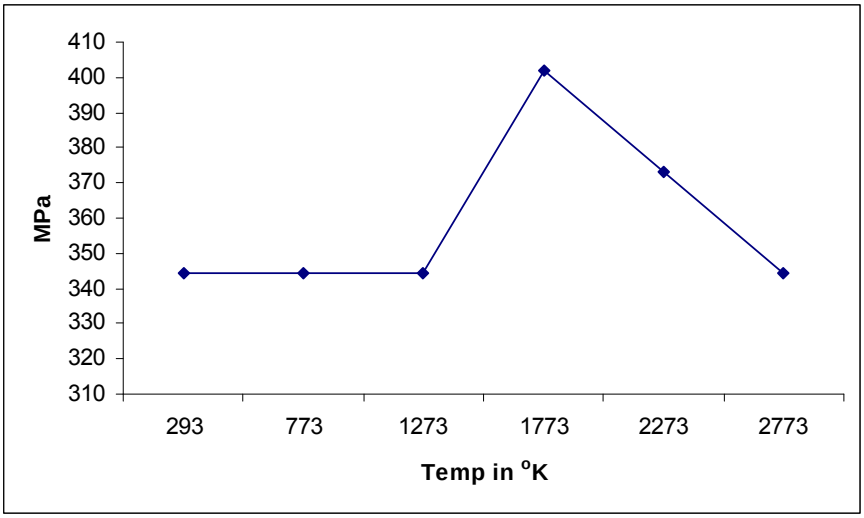

Fig 3.12 Tensile Strength along Fibre Direction

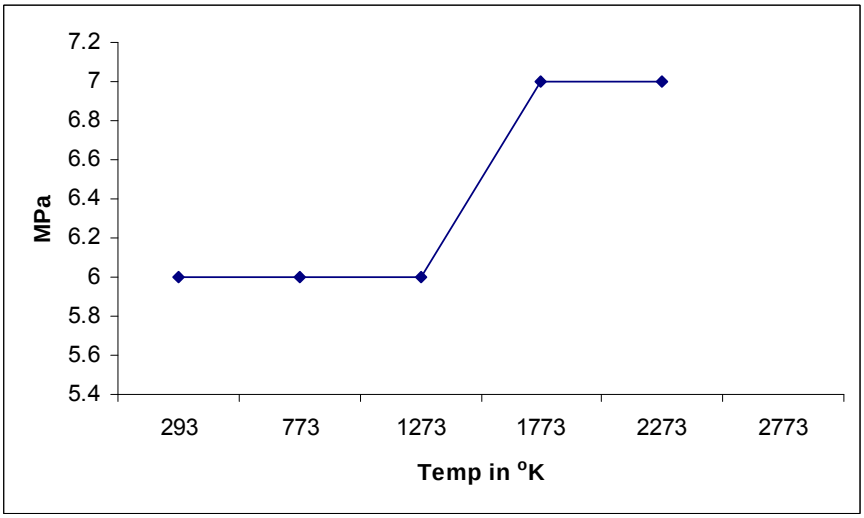

Fig 3.13 Tensile Strength along Transverse Direction

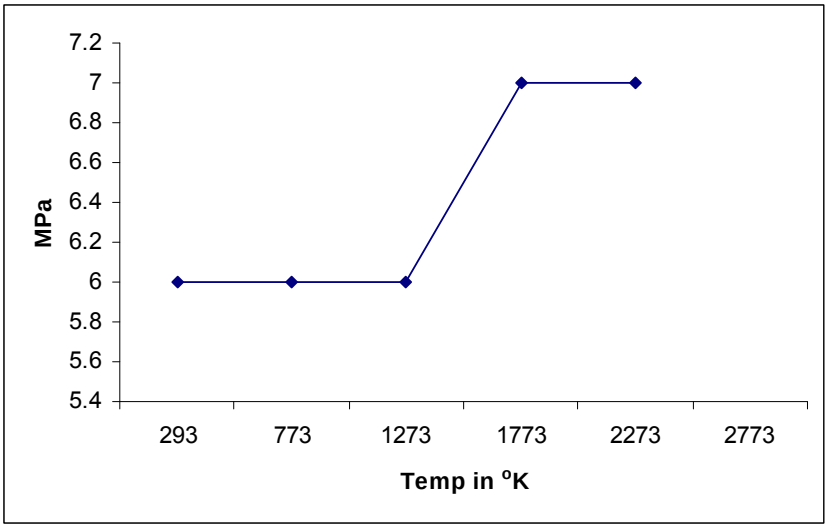

Fig 3.14 Tensile Strength of Carbon Matrix

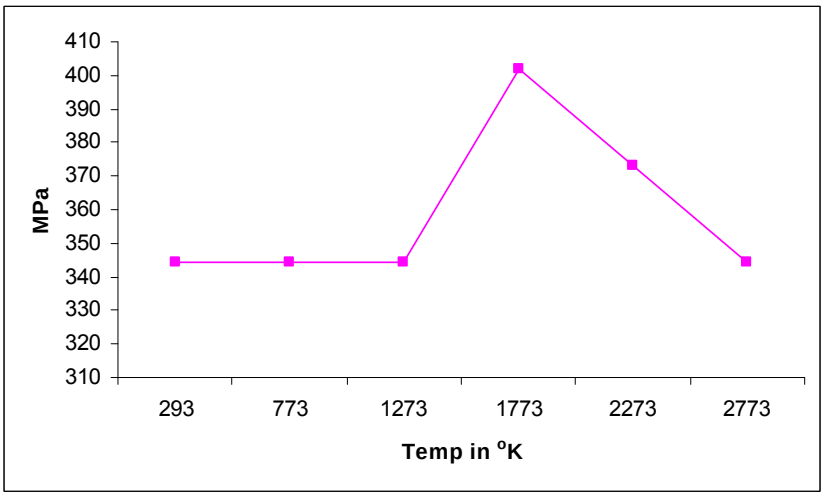

Fig 3.15 Compressive Strength along Fibre Direction

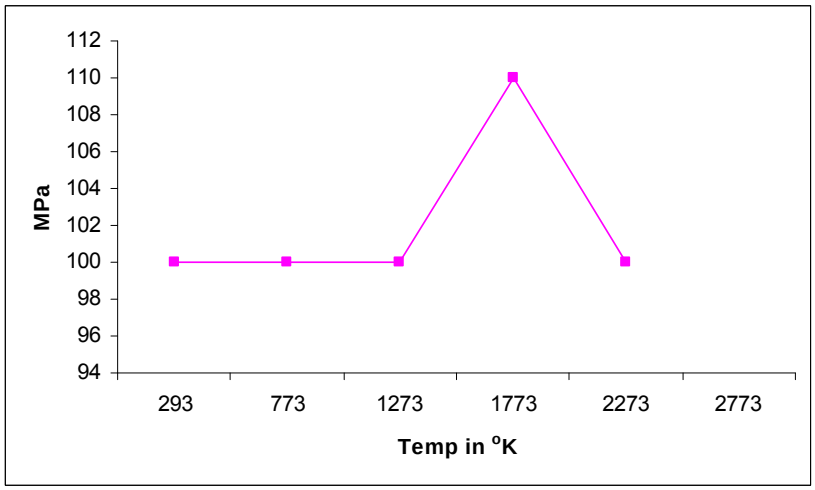

Fig 3.16 Compressive Strength along Transverse Direction

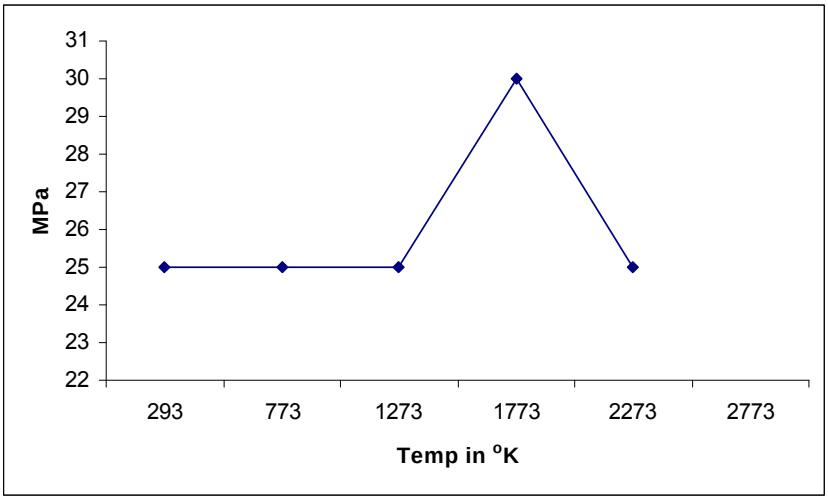

Fig 3.17 Inplane Shear Strength of Carbon Fibre

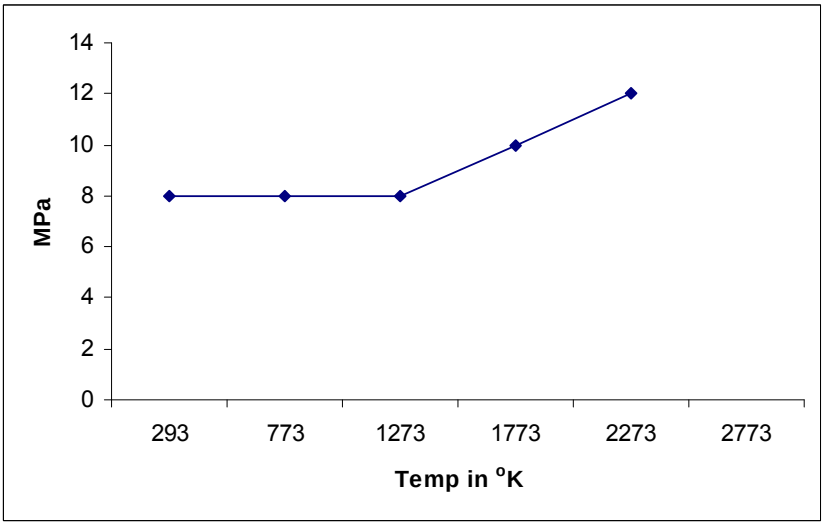

Fig 3.18 Shear Strength of Carbon Matrix

It can be observed that the CTE of carbon fibre is negative at RT and the sign changes as temperature increases. This is a basic material property of carbon fibres. The strength increases at 1773°K and then further decreases which is attributed to the alignment of carbon atoms when it is further carbonized from its forming temperature. It is quite interesting to note that the elastic properties start decreasing after 1773°K. The magnitude of reduction in elastic properties and increase of strength properties are not much significant. The above properties

form the input for generating the 3D composite properties from RUC. The variation of properties with respect to temperature will be used for generating 3D composite properties for its use in designing a hot structure which will be experiencing varying temperature during different instants of its mission.

CHAPTER 4

ANALYTICAL INVESTIGATIONS ON GENERATION OF 3D COMPOSITE MATERIAL PROPERTIES

4.1 Introduction

3D woven and 3D braided composites have fibres oriented in the out of plane directions (ie; in three or more orientations). The elastic, strength and thermal properties of such 3D composites vary according to material and orientation characteristics of fibre. Evaluation of the above properties using test methods is very expensive and the need arise for analytical methods for calculating such properties from the generic material properties. RUC's are developed for different configurations for generating the 3D composite properties. RUC is a unit cell which repeats its characteristics in all the three mutually perpendicular directions, which can be used to evaluate all the orthotropic properties of 3D composites. 3D composites and formulation of RUC are described subsequently based on the mathematical formulations. "3D Woven Composite Strength Model" developed and presented by Naik and Thuruthimattam (1998[1], 1998[2], 1999) has been used for the 3D woven composites and the same has been extended for the 3D braided composites. Orientation Averaging model (OA) as mentioned elsewhere (Cox and Dadkhah 1995, Naik and Thuruthimattam 1998[1], 1998[2], 1999, Tan *et al.* 1998) is used to solve the mathematical formulation of RUC to find the average properties and failure stresses. Isostress / Isostrain assumptions are used to find the response characteristic of the volume to obtain the macroscopic properties. Software that has been generated for evaluating properties has also been described.

4.2 Analysis of 3D Woven Composites

The potential properties of 3D orthogonal interlock woven composites can be realized by the designer only if various architectural variations can be evaluated using simple and accurate analytical tools. In the present study, analytical models have been developed for stress and failure analysis of 3D woven composites based on two level discretization. This can be used to predict the stiffness and strength properties of 3D orthogonal interlock woven

composites under various loading conditions on the model. Stress and failure studies have been carried out at subelement level consisting of only pure matrix regions or impregnated strand regions. The strand subelements are either along, across or inclined with respect to reference directions. In the subelements of RUC, fibres are aligned and treated as UD composites and fibres are considered straight along the fibre direction.

4.2.1 Dimensions of the RUC

The 3D orthogonal weave is made out of fibres in three orthogonal directions, viz., stuffers (s) which are oriented along the longitudinal direction (Loom feed direction), fillers (f) which are transverse to the loom feed direction (between layers of stuffers) and warp weavers (w) which are 90 degrees to stuffers and fillers direction. There are two types of orthogonal weaves, viz., Through the Thickness Orthogonal interlock Weave (TTOW) and Layer to Layer Orthogonal interlock Weave (LLOW).

Dimensions of the unit cell for analysis have been defined as follows.

For TTOW and LLOW,

$$L_x = d_f + d_w \quad \text{for TTOW-1 and LLOW-1} \tag{4.1}$$

$$L_x = 2(d_f + d_w) \quad \text{for TTOW-2 and LLOW-2} \tag{4.2}$$

$$L_y = d_s + d_w \quad \text{with one warp weaver between adjacent stuffers} \tag{4.3}$$

$$L_y = d_s + 2d_w \quad \text{with two warp weavers between adjacent stuffers} \tag{4.4}$$

$$L_z = n_x\, d_s + (n_x + 1)\, d_f + 2d_w \tag{4.5}$$

Where d_f, d_s and d_w are the diameter of the respective fibres, L_x, L_y and L_z are the basic dimensions of the RUC and n_x is the number of stuffers.

The RUC is defined as shown in fig 4.1 and 4.2. The RUC is divided into sections, elements, subsections, and subelements in the order. Since the final subdivision is at subelement level the secondary failure as well as the ultimate failure can be predicted.

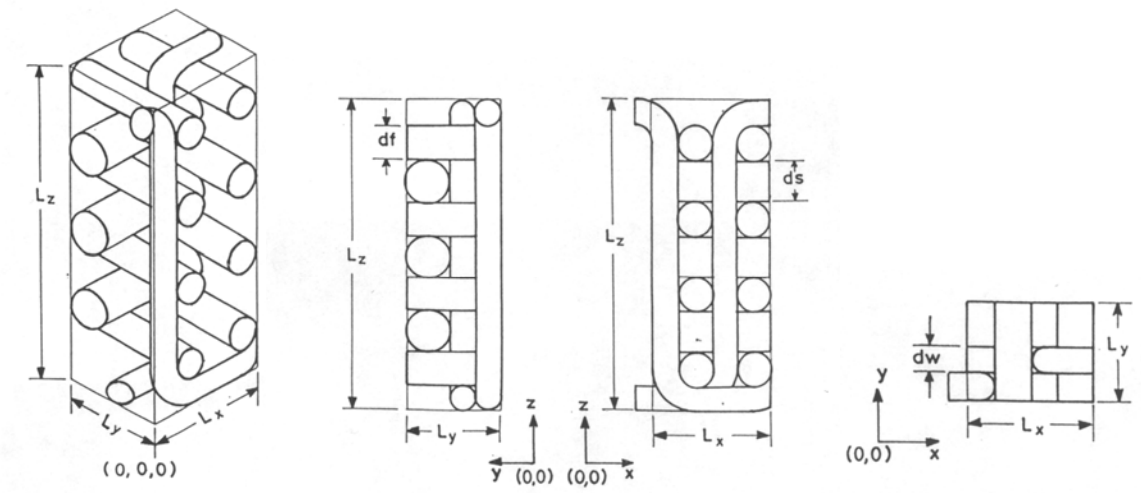

Fig 4.1 RUC for 3D Orthogonal Case (TTOW-2-2) (Naik and Thuruthimattam 1998[1], 1998[2], 1999)

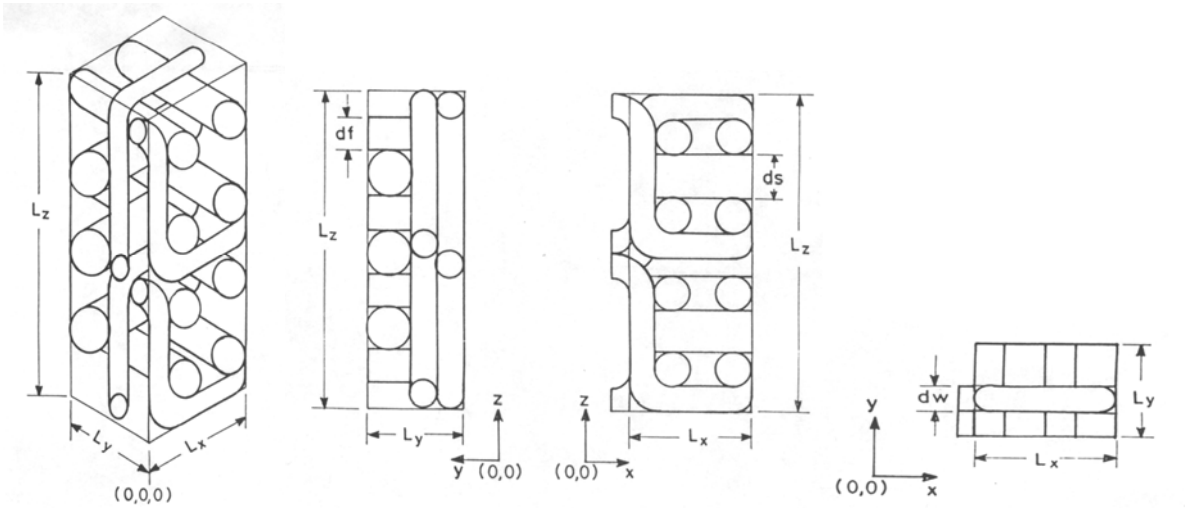

Fig 4.2 RUC for 3D Orthogonal Case (LLOW-2-2) (Naik and Thuruthimattam 1998[1], 1998[2], 1999)

4.2.2 Elastic properties of the RUC

The impregnated strands in a RUC are assumed to be transversely isotropic. The RUC is discretized into sections and elements (fig 4.3 and 4.4). Elements consist of stuffer, filler, warp weaver and pure matrix regions as shown in fig 4.5. The elements are divided into subsections and subelements as shown in fig 4.6. The mathematical formulations are worked out for evaluating the average mechanical properties and the failure analysis is carried out.

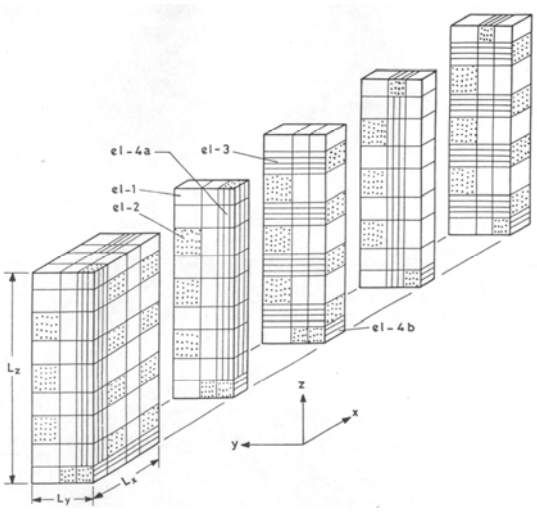

Fig 4.3 Discretization of RUC: (TTOW-2-2)

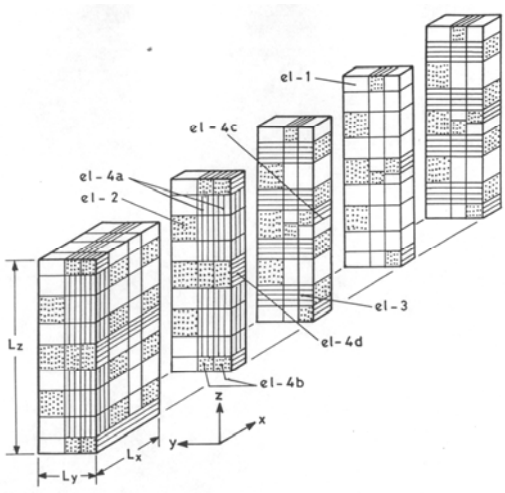

Fig 4.4 Discretization of RUC: (LLOW-2-2)

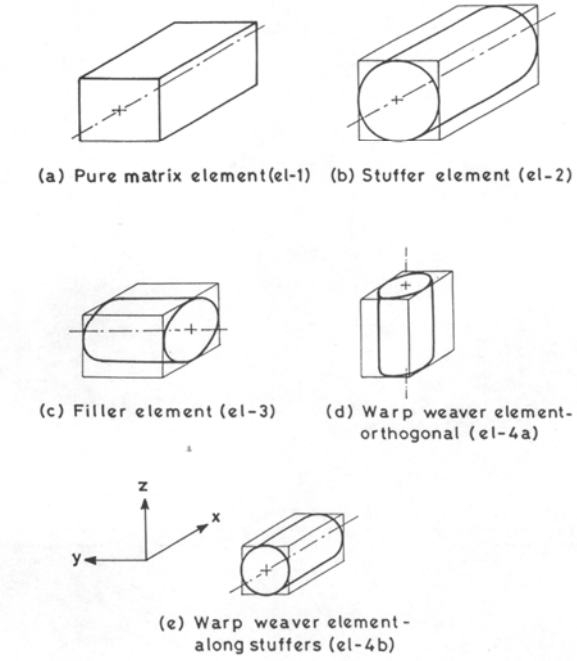

Fig 4.5 Elements of the RUC

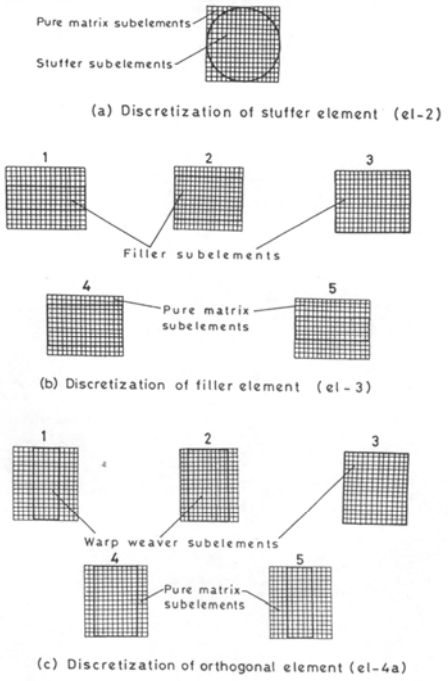

Fig 4.6 Subelements of Elements in RUC

The analytical model of RUC is called Representative Unit Cell for Analysis (RUCA) and the cross section of the fibers can be quasi square or quasi rectangle. Elements which defines the RUCA can be of four types viz., pure matrix elements, elements with reinforcement along loading direction, elements with reinforcement transverse to loading direction and elements with warp weavers. The methodology used here is Orientation

Averaging of 3D composites for TTOW or LLOW. If the number of stuffers are n_x where x = 1 to n, then the number of fillers are $n_y = n_x + 1$. Once the number and cross sectional properties of stuffers, fillers and warp weavers are finalised, the RUC dimensions can be found out besides the overall fibre volume fraction for the RUC.

The properties of the elements are found in their local coordinate system and inturn the stiffness matrix of elements (at room and at higher temperatures). After the determination of stiffness matrix of each element in its local coordinates, it is transformed to the global coordinate system. The fibre path is exactly traced based on the RUC and integrated within the RUC to obtain the equivalent orthotropic properties for the RUC. The structure is assumed to be assembled as a number of RUC's joining together; it is assumed to be quasi orthotropic / quasi homogenous. All the elastic, strength and thermal properties for the 3D orthogonal composites have been arrived at assuming Knock Down Factors (KNF) and Crimp Reductions (CR). Knock down factors are introduced to calculate the effective properties, since the fibres possess geometric undulations in reality. Stiffness knockdown factor (KNF) based on yarn waviness has been suggested by Cox *et al* (1994[1], 1994[2], 1995), where the properties are found in an averaged way. Through the thickness direction properties gets reduced due to warp weaver crimp. For accounting the warp weaver Crimp Reduction (CR), E_1^W *and* ν_{12}^W of warp weavers are reduced to its transverse direction properties E_2^W *and* ν_{23}^W. The above KNF's and CR's have been used in the formulations for property generation in the present study.

Using the fibre and matrix properties as well as the fibre volume fraction of the subelement, elastic properties can be determined using Composite Cylinder Assemblage model (Hashin 1972). The stiffness matrix [C] for the subelement can be determined using eqn. 4.6, where E_i is the moduli of elasticity, ν_{ij} and G_{ij} are the Poisson's ratio and shear moduli for the respective subelements.

$$
\begin{aligned}
&C_{11}^{sel} = E_1\frac{(1-\nu_{23}\nu_{32})}{\Delta} \quad C_{12}^{sel} = E_1\frac{(\nu_{21}+\nu_{23}\nu_{31})}{\Delta}\\
&C_{22}^{sel} = E_2\frac{(1-\nu_{13}\nu_{31})}{\Delta} \quad C_{23}^{sel} = E_2\frac{(\nu_{32}+\nu_{12}\nu_{31})}{\Delta}\\
&C_{13}^{sel} = E_1\frac{(\nu_{31}+\nu_{21}\nu_{32})}{\Delta} \quad C_{33}^{sel} = E_3\frac{(1-\nu_{12}\nu_{21})}{\Delta}\\
&C_{44}^{sel} = G_{23},\ C_{21}^{sel} = C_{12}^{sel},\ C_{55}^{sel} = G_{13},\ C_{32}^{sel} = C_{23}^{sel},\ C_{66}^{sel} = G_{12},\ C_{31}^{sel} = C_{13}^{sel}\\
&\text{where, } \Delta = 1-\nu_{12}\nu_{21}-\nu_{23}\nu_{32}-\nu_{31}\nu_{13}-2\nu_{21}\nu_{32}\nu_{13}
\end{aligned}
\qquad (4.6)
$$

Assuming impregnated strands as transversely isotropic, stiffness matrix of the subelement can be expressed as $\left[C_{ij}^{sel}\right]$ i, j = 1.....6 , where $C_{22}^{sel} = C_{33}^{sel}$, $C_{12}^{sel} = C_{13}^{sel}$, $C_{55}^{sel} = C_{66}^{sel}$.

After determining C_{ij}^{sel} of each subelement in the Local Coordinate System (LCS), it is transformed to the Global Coordinate System (GCS) using the transformation matrix [T] given in Appendix C. Transformation is not required for pure matrix subelements, the matrix being isotropic.

Transformed stiffness matrix of the subelements can be expressed using the following equation.

$$\left[\overline{C}_{ij}^{sel}\right] \quad i,\ j = 1.....6 \ . \tag{4.7}$$

Extensional stiffness matrix of each subsection is given by eqn. 4.8 and 4.9.

$$A_{ij}^{ssec} = {}^{1}\!/_{ly^{el}} \int_{0}^{ly^{el}} \int_{0}^{lz^{el}} \overline{C}_{ij}^{sel}\, dy\, dz \qquad i,\ j = 1.....6 \tag{4.8}$$

$$A_{ij}^{ssec} = {}^{1}\!/_{ly^{el}} \sum_{1}^{ny^{sel}} \sum_{1}^{nz^{sel}} \overline{C}_{ij}^{sel}\, ly^{sel}\, lz^{sel} \qquad i,\ j = 1.....6 \tag{4.9}$$

where, ny^{sel} & nz^{sel} are the number of subelements along y and z directions.

Extensional stiffness matrix of the element can be determined using following equations.

$$A_{ij}^{el} = {}^{1}\!/_{lx^{el}} \int_{0}^{lx^{el}} A_{ij}^{ssec}\, dx \qquad i,\ j = 1.....6 \tag{4.10}$$

$$A_{ij}^{el} = {}^{1}\!/_{lx^{el}} \sum_{1}^{nx^{ssec}} A_{ij}^{ssec}\, lx^{ssec} \qquad i,\ j = 1.....6 \tag{4.11}$$

where, nx^{ssec} is the number of subsection along x direction.

Extensional compliance matrix $\left[a_{ij}^{el}\right] = \left[A_{ij}^{el}\right]^{-1}$

The elastic properties of the elements can be determined using eqn. 4.12.

$$\left.\begin{aligned}
&E_x^{el} = {}^{1}\!/_{lz^{el}\, a_{11}^{el}} \quad E_y^{el} = {}^{1}\!/_{lz^{el}\, a_{22}^{el}} \quad E_z^{el} = {}^{1}\!/_{lz^{el}\, a_{33}^{el}} \\
&G_{xy}^{el} = {}^{1}\!/_{lz^{el}\, a_{66}^{el}} \quad G_{yz}^{el} = {}^{1}\!/_{lz^{el}\, a_{44}^{el}} \quad G_{xz}^{el} = {}^{1}\!/_{lz^{el}\, a_{55}^{el}} \\
&\nu_{xy}^{el} = -\frac{a_{12}^{el}}{a_{11}^{el}}, \ \nu_{zx}^{el} = -\frac{a_{31}^{el}}{a_{33}^{el}}, \ \nu_{zy}^{el} = -{}^{a_{32}^{el}}\!/_{a_{33}^{el}} \\
&\nu_{yz}^{el} = -{}^{a_{23}^{el}}\!/_{a_{22}^{el}}, \ \nu_{yx}^{el} = -{}^{a_{21}^{el}}\!/_{a_{22}^{el}}, \ \nu_{xz}^{el} = -{}^{a_{13}^{el}}\!/_{a_{11}^{el}}
\end{aligned}\right\} \tag{4.12}$$

Using isostress, isostrain conditions the element stiffness matrix $\left[C_{ij}^{el}\right]$ i, j = 1.....6 can be obtained by substituting the properties derived using eqn. 4.12 in eqn. 4.6.

Extensional stiffness matrix of the section can be determined using eqn. 4.13 and 4.14.

$$A_{ij}^{sec} = {}^{1}\!/_{Ly} \int_{0}^{Ly} \int_{0}^{Lz} C_{ij}^{el}\, dy\, dz \qquad i, j = 1.....6 \tag{4.13}$$

$$A_{ij}^{sec} = {}^{1}\!/_{Ly} \sum_{1}^{ny^{el}} \sum_{1}^{nz^{el}} C_{ij}^{el}\, ly^{el}\, lz^{el} \qquad i, j = 1.....6 \tag{4.14}$$

Where, ny^{el} *and* nz^{el} are elements in the section along y and z directions.

Extensional stiffness matrix of RUC can be obtained using eqn. 4.15 and 4.16.

$$\overline{A}_{ij} = {}^{1}\!/_{Lx} \int_{0}^{Lx} A_{ij}^{sec}\, dx \qquad i, j = 1.....6 \tag{4.15}$$

$$\overline{A}_{ij} = {}^{1}\!/_{Lx^{el}} \sum_{1}^{nx^{sec}} A_{ij}^{sec}\, lx^{sec} \qquad i, j = 1.....6 \tag{4.16}$$

where, nx^{sec} is the number of sections along x direction.

Compliance matrix $\left[\bar{a}_{ij}\right] = \left[\overline{A}_{ij}\right]^{-1}$ i, j = 1.....6 (4.17)

Properties of the RUC can be derived from $\left[\bar{a}_{ij}\right]$ where,

$$E_x = {}^{1}\!/_{Lz\bar{a}_{11}}, \quad E_y = {}^{1}\!/_{Lz\bar{a}_{22}}, \quad E_z = {}^{1}\!/_{Lz\bar{a}_{33}} \tag{4.18}$$

$$G_{yz} = {}^{1}\!/_{Lz\bar{a}_{44}}, \quad G_{xz} = {}^{1}\!/_{Lz\bar{a}_{55}}, \quad G_{xy} = {}^{1}\!/_{Lz\bar{a}_{66}}$$

$$\nu_{xy} = -\frac{\bar{a}_{12}}{\bar{a}_{11}}, \nu_{yz} = -\frac{\bar{a}_{23}}{\bar{a}_{22}}, \nu_{yx} = -\frac{\bar{a}_{21}}{\bar{a}_{22}}, \nu_{zx} = -\frac{\bar{a}_{31}}{\bar{a}_{33}}, \nu_{zy} = -\frac{\bar{a}_{32}}{\bar{a}_{33}}, \nu_{xz} = -\frac{\bar{a}_{13}}{\bar{a}_{11}}$$

For finding the properties along stuffer, filler and warp weaver directions, sections are considered along the respective fibre directions.

4.2.3 Thermal expansion properties of the RUC

In the Composite Cylinder Assemblage model, Coefficient of Thermal Expansion (CTE) of subelements are given by $\left\{\alpha_i^{sel}\right\}$ i=1 to 6. The above values are transformed to GCS by the transformation matrix [T] using eqn. 4.19.

$$\left\{\overline{\alpha}_i^{sel}\right\}=[T]^{-1}\left\{\alpha_i^{sel}\right\} \tag{4.19}$$

The thermal force resultants and CTE's can be determined using Stiffness Averaging (SA) and Compliance Averaging (CA) methods.

In **Stiffness Averaging (SA) scheme** the thermal force resultants for each subsections can be determined using eqn. 4.20, where $\overline{C}_{ij}^{sel}$ are known from eqn. 4.7.

$$\left\{N_i^{T\,ssec}\right\}=\frac{\Delta T}{l_y^{el}l_z^{el}}\left[\sum_1^{n_y^{sel}}\sum_1^{n_z^{sel}}\left[\overline{C}_{ij}^{sel}\right]\left\{\overline{\alpha}_i^{sel}\right\}l_y^{sel}l_z^{sel}\right] \quad \text{i=1 to 6} \tag{4.20}$$

Summing up $\left\{N_i^{T\,ssec}\right\}$ along x direction, the thermal force resultant for an element can be expressed as eqn. 4.21.

$$\left\{N_i^{T\,el}\right\}=\frac{1}{l_x^{el}}\sum_1^{n_x^{sec}}\left\{N_i^{T\,ssec}\right\}l_x^{ssec} \quad \text{i=1 to 6} \tag{4.21}$$

CTE's of the element can be written using eqn. 4.22.

$$\left\{\alpha_i^{el}\right\}=\frac{1}{\Delta T}\left[a_{ij}^{el}\right]\left\{N_i^{T\,el}\right\} \quad \text{i=1 to 6} \tag{4.22}$$

Using C_{ij}^{el} from eqn. 4.12 and α_i^{el} from eqn. 4.22 and integrating them in the yz plane the thermal force resultant for a section $\left\{N_i^{T\,sec}\right\}$ can be evaluated and the expression is given as eqn. 4.23.

$$\left\{N_i^{T\,sec}\right\}=\frac{\Delta T}{l_y l_z}\left[\sum_1^{n_y^{el}}\sum_1^{n_z^{el}}\left[\overline{C}_{ij}^{el}\right]\left\{\alpha_i^{el}\right\}l_y^{el}l_z^{el}\right] \quad \text{i=1 to 6} \tag{4.23}$$

The thermal force resultant for the RUC $\left\{N_i^{T}\right\}$ can be determined by integrating $\left\{N_i^{T\,sec}\right\}$ along x direction and can be written as eqn. 4.24.

$$\left\{N_i^{T}\right\}=\frac{1}{L_x}\sum_1^{n_x^{sec}}\left\{N_i^{T\,sec}\right\}l_x^{sec} \quad \text{i=1 to 6} \tag{4.24}$$

The coefficients of thermal expansions for the RUC can be expressed as eqn. 4.25.

$$\{\alpha_k\}=\frac{1}{\Delta T}\left[\overline{a}_{ij}\right]\left\{N_i^{T}\right\} \quad \text{i=1 to 6} \tag{4.25}$$

where, α_k, i.e; $\alpha_x,\alpha_y,\alpha_z,\alpha_{xy},\alpha_{xz}$ and α_{yz} are the coefficients of thermal expansion of the 3D woven composite.

Eventhough the CTE's are obtained using SA method, the transverse direction CTE's α_y and α_z can be better approximated using CA scheme, owing to the fact that in CA method, the compliance matrices are used for estimating CTE's which takes into account the effects of transverse terms. In the present analysis both CA and SA are used to evaluate the elastic and thermal properties.

Using the **Compliance Averaging (CA) scheme** the thermal expansion properties of each subsection, element, section and RUC / 3D woven composite can be evaluated from eqn. 4.26, 4.27, 4.28 and 4.29 respectively.

$$\left\{\alpha_i^{ssec}\right\} = 1/\Delta T\left[a_{ij}^{ssec}\right]\left\{N_i^{Tssec}\right\} \quad i,j = 1 \text{ to } 6 \tag{4.26}$$

$$\left\{\alpha_i^{el}\right\} = 1/l_x^{el} \sum_{1}^{n_x^{ssec}} \left\{\alpha_i^{ssec}\right\} l_x^{ssec} \quad i = 1 \text{ to } 6 \tag{4.27}$$

$$\left\{\alpha_i^{sec}\right\} = 1/\Delta T\left[a_{ij}^{sec}\right]\left\{N_i^{Tsec}\right\} \quad i = 1 \text{ to } 6 \tag{4.28}$$

$$\left\{\alpha_k\right\} = 1/l_x \sum_{1}^{n_x^{sec}} \left\{\alpha_i^{sec}\right\} l_x^{sec} \quad i = 1 \text{ to } 6 \tag{4.29}$$

Here, α_k , i.e; $\alpha_x, \alpha_y, \alpha_z, \alpha_{xy}, \alpha_{xz}$ and α_{yz} are the CTE's of the 3D woven composite.

The flow sequence for estimating the thermomechanical properties of the 3D orthogonal composite is given in fig 4.7.

4.2.4 Thermal conductivity properties of the RUC

The thermal conductivity of the 3D orthogonal composite has been found by the thermal electrical analogy. In each sections perpendicular to the loading direction, the resistance of each fibre and matrix is calculated and assembled in parallel and its equivalent resistance is found for each section for the load applied along the x direction. The thermal conductivity of the RUC is found by assembling these in series along the loading direction. The same procedure is repeated along 'y' and 'z' axis to get the equivalent thermal conductivity in the respective directions (Clayton 1971, Dasgupta and Agarwal 1992, Ning and Chou 1995, 1998).

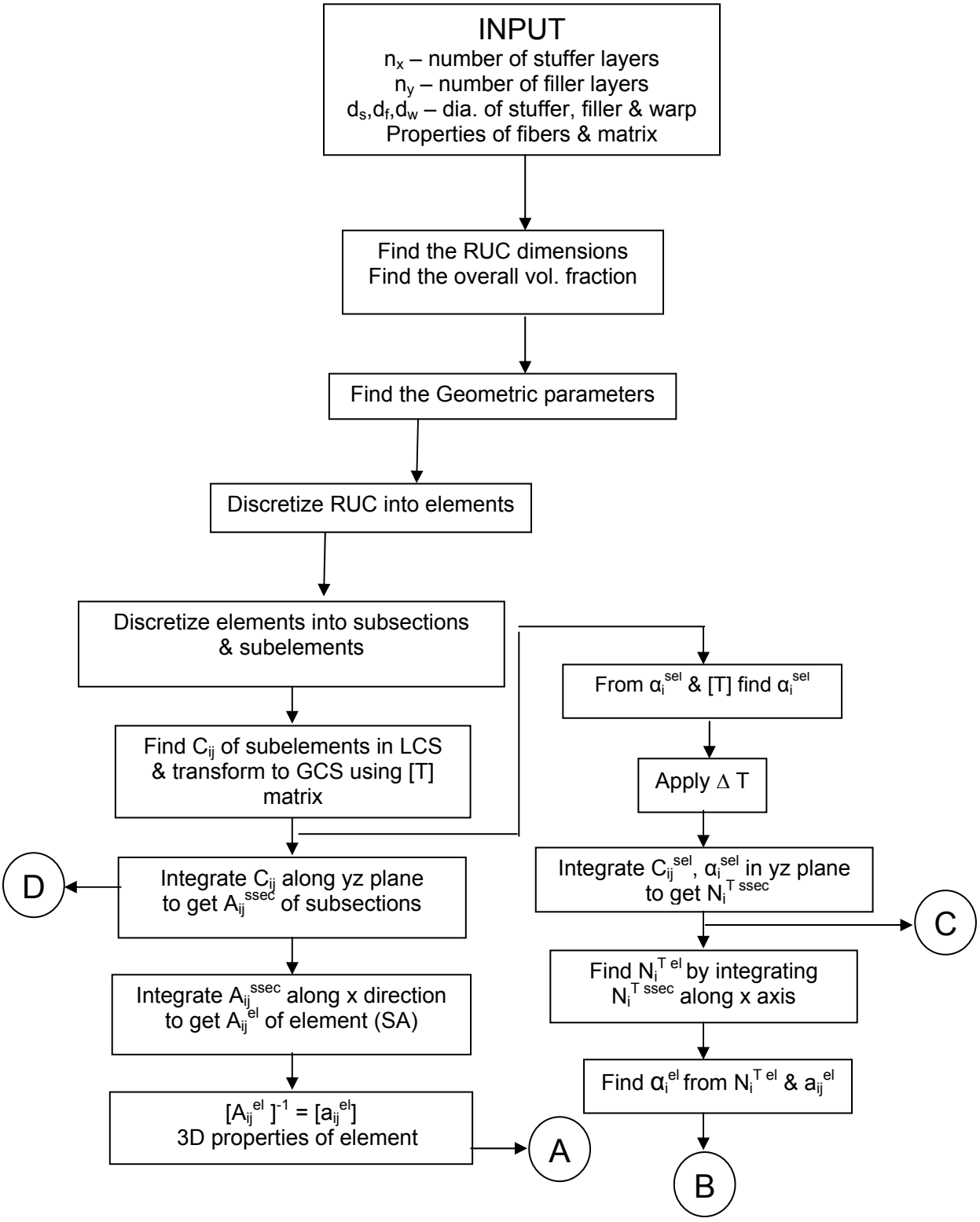
INPUT
n_x – number of stuffer layers
n_y – number of filler layers
d_s, d_f, d_w – dia. of stuffer, filler & warp
Properties of fibers & matrix
Find the RUC dimensions
Find the overall vol. fraction
Find the Geometric parameters
Discretize RUC into elements
Discretize elements into subsections & subelements
Find C_{ij} of subelements in LCS & transform to GCS using [T] matrix
Integrate C_{ij} along yz plane to get A_{ij}^{ssec} of subsections
Integrate A_{ij}^{ssec} along x direction to get A_{ij}^{el} of element (SA)
$[A_{ij}^{el}]^{-1} = [a_{ij}^{el}]$
3D properties of element
A
D
From α_i^{sel} & [T] find α_i^{sel}
Apply Δ T
Integrate C_{ij}^{sel}, α_i^{sel} in yz plane to get $N_i^{T\ ssec}$
C
Find $N_i^{T\ el}$ by integrating $N_i^{T\ ssec}$ along x axis
Find α_i^{el} from $N_i^{T\ el}$ & a_{ij}^{el}
B

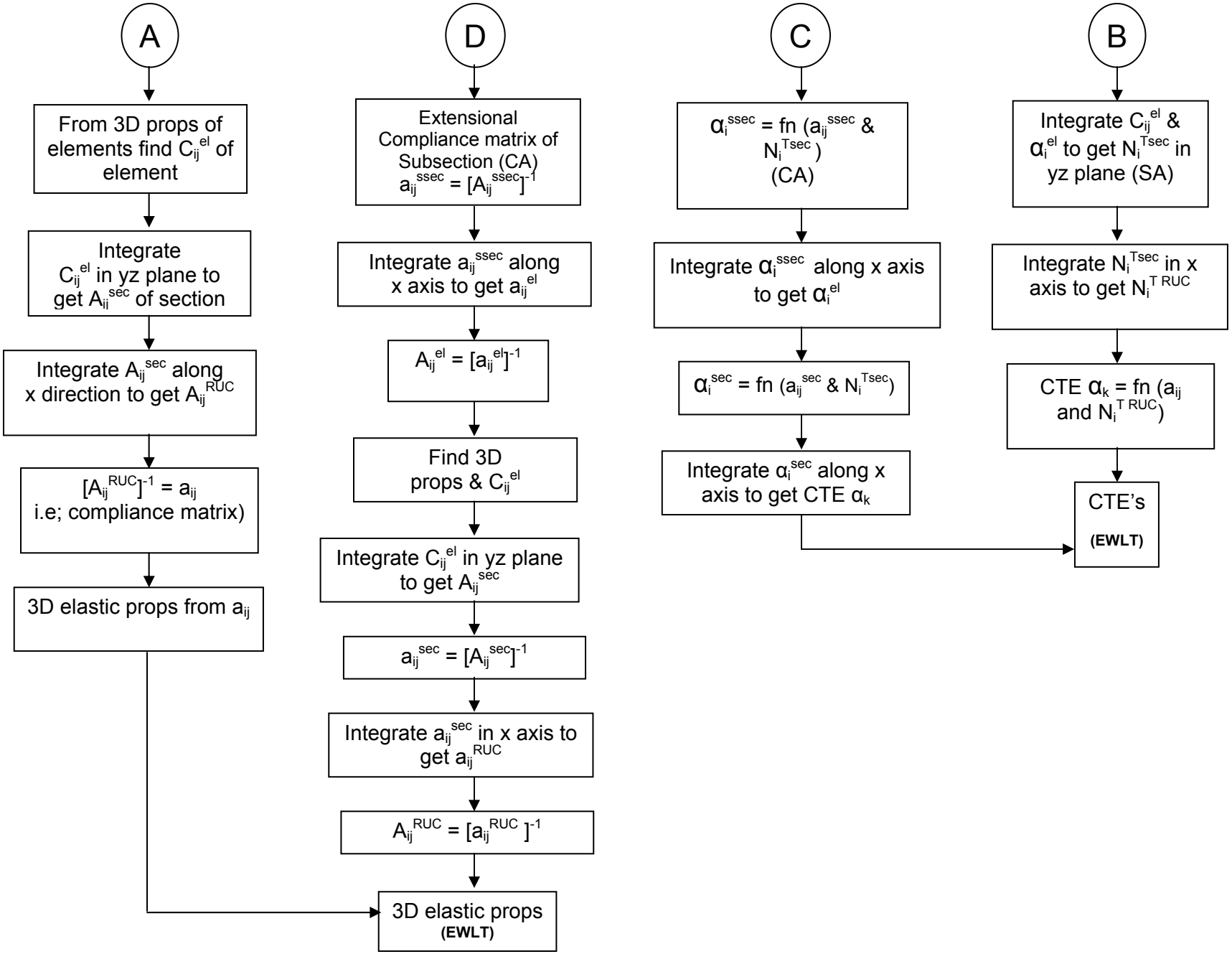

Fig 4.7 Schematic Diagram of Determination of Thermomechanical Properties

4.2.5 Strength analysis of the RUC

Generation of tensile strength and shear strength from RUC is described in the following sections.

4.2.5.1 Tensile strength

The RUCA is divided into sections perpendicular to the loading direction. Isostress assumption is made for calculating stresses in each section. Sections are further divided into elements. Isostrain assumption is made for calculating stresses in the elements. Elements are divided into subsections and uniform isostress condition is assumed within subsections. Subsections are further divided into subelements where uniform isostrain conditions are assumed.

The directions are assigned in such a way that the axis 1 is along the loading direction (stuffer direction) and axis 2 and 3 transverse to the loading direction. For the analysis a unit load is acting along 1 axis. Transverse strains for RUCA can be determined using eqn. 4.30, where $\overline{a}_{21}$ and $\overline{a}_{31}$ are obtained from eqn. 4.17.

$$\varepsilon_y = \overline{a}_{21} N_x ,\ \varepsilon_z = \overline{a}_{31} N_x \tag{4.30}$$

Where, $\mathrm{N_x}$ is the load applied in x direction on unit cell per unit width.

Transverse strains for all sections, elements, subsections and subelements are assumed to be the same as the average transverse strains for RUCA.

i.e; $\varepsilon_i^{sec} = \varepsilon_i \qquad i = y, z$ (4.31)

$\varepsilon_y^{el} = \varepsilon_y$ and $\varepsilon_z^{el} = \varepsilon_z$ (4.32)

Since isostrain assumption is made within each section the strain along the loading direction within the section and all the corresponding elements would be same. Strains of each section along loading direction can be determined from eqn. 4.33 using eqn. 4.13.

$$\varepsilon_x^{sec} = \frac{N_x - A_{12}^{sec}\varepsilon_y - A_{13}^{sec}\varepsilon_z}{A_{11}^{sec}} \tag{4.33}$$

Average strain of RUCA along loading direction is,

$$\varepsilon_x = {}^{1}\!/_{L_x} \int_0^{L_x} \varepsilon_x^{\sec} d_x \tag{4.34}$$

$$\text{i.e; } \varepsilon_x = {}^{1}\!/_{L_x} \sum_{1}^{n_x^{\sec}} \varepsilon_x^{\sec} dx \tag{4.35}$$

where, $\mathrm{n}_{\mathrm{x}}^{\mathrm{sec}}$ is the number of sections along x direction.

Similarly, for loading along y and z directions, the corresponding strains are determined. From the strains on each element and the extensional stiffness matrix, the load on this can be determined using eqn. 4.36.

$$\left\{N_i^{el}\right\} = \left[A_{ij}^{el}\right]\left\{\varepsilon_i^{el}\right\} \qquad \text{i, j} = 1.....6 \tag{4.36}$$

Strain along the loading direction within a subsection of each element can be expressed using eqn. 4.37.

$$\varepsilon_x^{s\,\sec} = \frac{N_x^{el} - A_{12}^{s\,\sec}\varepsilon_y - A_{13}^{s\,\sec}\varepsilon_z}{A_{11}^{s\,\sec}} \tag{4.37}$$

Here, $\varepsilon_y^{el} = \varepsilon_y^{s\,\sec} = \varepsilon_y$ and $\varepsilon_z^{el} = \varepsilon_z^{s\,\sec} = \varepsilon_z$

Since isostrain assumption is made within each subsection, the strain along the loading direction within each subsection and all corresponding subelements would be the same and can be expressed using eqn. 4.38.

$$\varepsilon_{\mathrm{x}}^{\mathrm{sel}} = \varepsilon_{\mathrm{x}}^{\mathrm{ssec}} \tag{4.38}$$

The subelement strains are transformed back to the subelement local coordinate system using transformation matrix [T] and described in eqn. 4.39.

$$\{\bar{\varepsilon}\} = [T]\{\varepsilon\} \tag{4.39}$$

Subelement is assumed to have failed when the strain due to the applied load exceeds the failure strain of the corresponding subelement. When a subelement fails, degradation analysis is carried out i.e; the contribution of this subelement is not considered for further analysis. After all the subelements have failed in a subsection, the element is assumed to have failed. RUCA/RUC is assumed failed when all the elements in a section have failed. The load at which the entire section fails corresponds to the failure strength and the corresponding strain is the failure strain. Similarly the failure strength for ‘y’ and ‘z’ directions (Ny and Nz) by loading RUC in the respective axis can be estimated.

4.2.5.2 Shear strength

Shear strain is assumed to be constant within RUCA and is evident in eqn. 4.40. Shear strain can be obtained for a given shear load $(\mathrm{N_{xy}})$ using eqn. 4.41.

$$\varepsilon_{xy}^{\sec} = \varepsilon_{xy},\ \ \varepsilon_{xy}^{el} = \varepsilon_{xy}^{\sec},\ \ \varepsilon_{xy}^{s\sec} = \varepsilon_{xy}^{el},\ \ \varepsilon_{xy}^{sel} = \varepsilon_{xy}^{s\sec} \tag{4.40}$$

i.e., $\varepsilon_{xy}^{sel} = \varepsilon_{xy}$

$$\varepsilon_{xy} = \bar{a}_{66}\, N_{xy} \tag{4.41}$$

It can be further deduced that $\varepsilon_{yz} = \bar{a}_{44}\, N_{yz},\ \varepsilon_{zx} = \bar{a}_{55}\, N_{zx}$ (4.42)

The failure philosophy adopted for estimating tensile strength is adopted to estimate the failure shear strength of RUCA / RUC. Similarly loading in xz and yz planes gives the corresponding shear strengths.

The flow sequence for estimating the strength properties of the 3D orthogonal composite is given in fig 4.8.

4.2.6 Development of computer code

For generating the elastic, strength and thermal properties for woven composites, five separate codes have been written using MATLAB and the details of subroutines are described in subsequent subsection. The description and the source codes generated are described elsewhere (Santhosh 2010).

4.2.6.1 *EWLT*

This code generates the elastic and CTE constants for the woven composites for layer to layer and through the thickness composites. The inputs required for the code are fibre details, elastic properties (nine elastic constants) and CTE's (three constants) of the fibre and matrix with respect to temperature and the geometrical parameters of the RUC's. The outputs from the code are the equivalent elastic properties (9 elastic constants) and CTE's (3 constants) for all the respective RUC's.

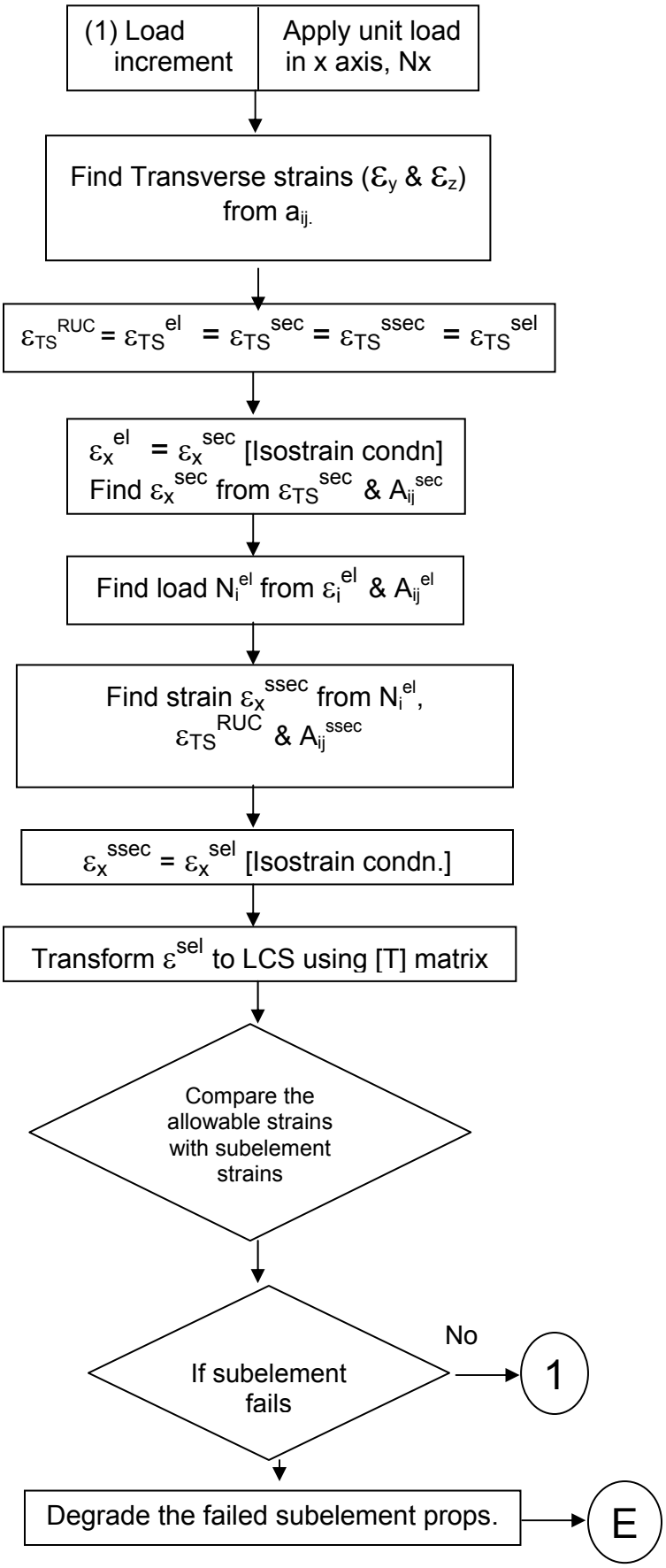
(1) Load increment
Apply unit load in x axis, Nx
Find Transverse strains ($\mathcal{E}_y$ & $\mathcal{E}_z$) from $a_{ij.}$
$\varepsilon_{TS}^{RUC} = \varepsilon_{TS}^{el} = \varepsilon_{TS}^{sec} = \varepsilon_{TS}^{ssec} = \varepsilon_{TS}^{sel}$
$\varepsilon_x^{el} = \varepsilon_x^{sec}$ [Isostrain condn]
Find ε_x^{sec} from ε_{TS}^{sec} & A_{ij}^{sec}
Find load N_i^{el} from ε_i^{el} & A_{ij}^{el}
Find strain ε_x^{ssec} from N_i^{el}, ε_{TS}^{RUC} & A_{ij}^{ssec}
$\varepsilon_x^{ssec} = \varepsilon_x^{sel}$ [Isostrain condn.]
Transform ε^{sel} to LCS using [T] matrix
Compare the allowable strains with subelement strains
If subelement fails
No
1
Degrade the failed subelement props.
E

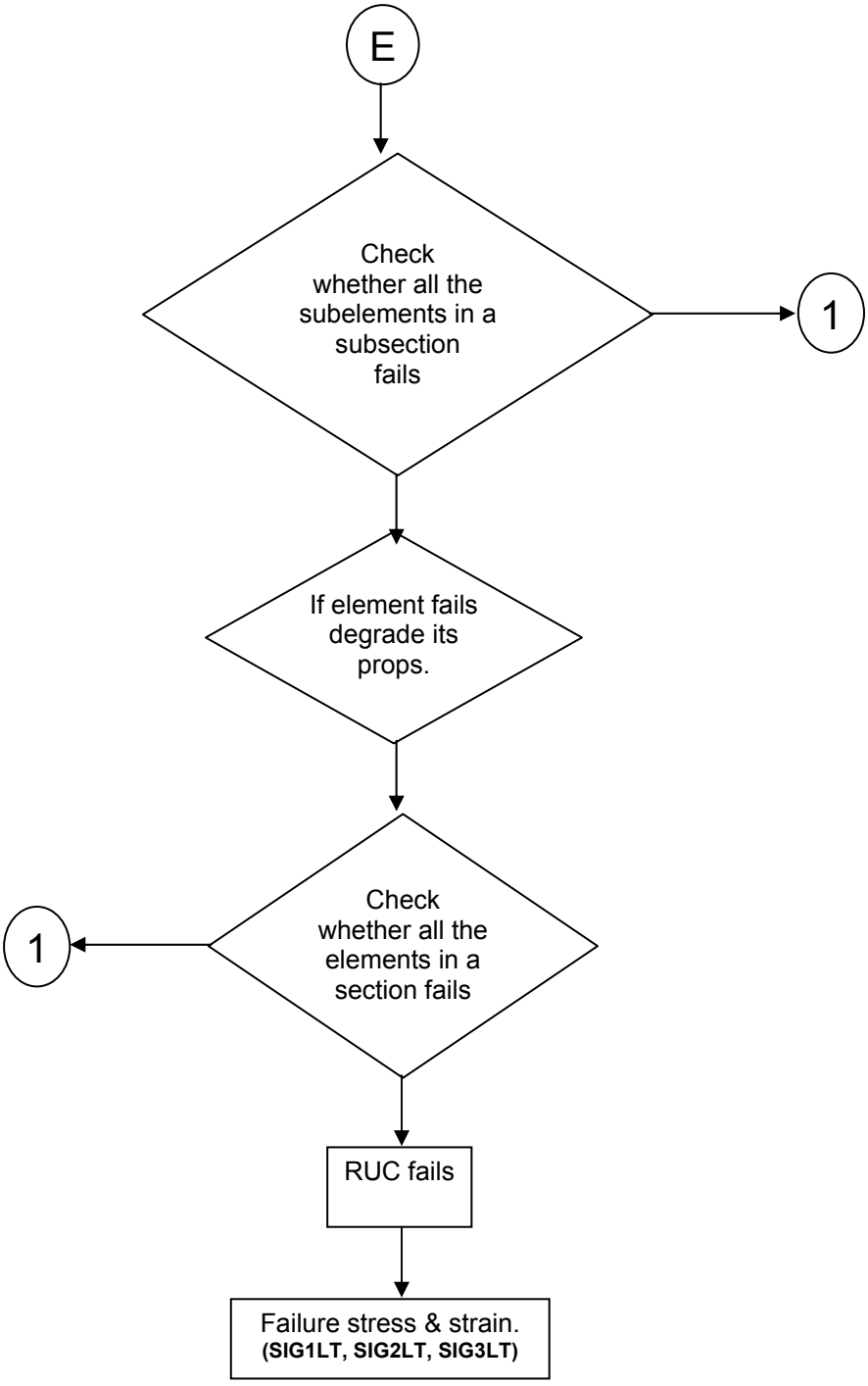

Fig 4.8 Schematic Diagram of Determination of Strength Properties

4.2.6.2 *KLT*

This code generates the thermal conductivity constants for the woven composites for layer to layer and through the thickness composites. The inputs required for the code are fibre details, thermal conductivity properties (three constants) of the fibre and matrix with respect to temperature and the geometrical parameters of the RUC's. The outputs from the code are the equivalent conductivity properties (3 constants) for all the respective RUC's.

4.2.6.3 *SIG1LT*

This code generates the strength constants like σ_x and τ_{xy} for the woven composites for layer to layer and through the thickness composites. The inputs required for the code are fibre details, elastic properties (nine constants), strength properties (six constants) of the fibre and matrix with respect to temperature and the geometrical parameters of the RUC's. The outputs from the code are the equivalent strength properties (σ_x and τ_{xy}) for all the respective RUC's.

4.2.6.4 *SIG2LT*

This code generates the strength constants like σ_y and τ_{yz} for the woven composites for layer to layer and through the thickness composites. The inputs required for the code are fibre details, elastic properties (nine constants), strength properties (six constants) of the fibre and matrix with respect to temperature and the geometrical parameters of the RUC's. The outputs from the code are the equivalent strength properties (σ_y and τ_{yz}) for all the respective RUC's.

4.2.6.5 *SIG3LT*

This code generates the strength constants like σ_z and τ_{zx} for the woven composites for layer to layer and through the thickness composites. The inputs required for the code are fibre details, elastic properties (nine constants), strength properties (six constants) of the fibre and matrix with respect to temperature and the geometrical parameters of the RUC's. The outputs from the code are the equivalent strength properties (σ_z and τ_{zx}) for all the respective RUC's.

4.3 Analysis of 3D Braided Composites

4.3.1 Introduction

Understanding the geometry of the braided preform is important for the thermomechanical analysis of 3D braided composites. The overall fibre volume fraction of braided composites is normally low, in the range of 30 to 40%. The mechanical performance of 3D braided composites can be enhanced by increasing the fibre volume fraction. This requires clear understanding of the jamming condition. With an ideal geometry of the 3D braided preform, perfect jamming condition would give the maximum fibre content. Additionally, introduction of axial yarns leads to an increase in the fiber content. These aspects are not clearly dealt in the studies available on literature on 3D braided composites. In the present study an accurate thermomechanical model has been generated for predicting the thermomechanical behavior of 3D braided composites. The analysis is based on idealized geometric Representative Unit Cell (RUC). The analysis consists of identifying the geometrical RUC for braided composite and finding out the exact jamming condition. Once the jamming condition is achieved the possibility of introducing the axial fibres are explored. The geometric details of the above RUC are worked out and solved using analytical methods for estimating the thermomechanical properties.

4.3.2 Geometric modeling

The braided preforms are constructed by intertwining of yarns to form an integral structure. The preform consists of a system of braider yarns and axial yarns with spatial distribution of yarns in many directions. The exact distribution and orientation of the yarns depend on braiding procedure used and the consolidation of braided composites. The 3D braided preforms can be made by 2-step braiding, 4-step braiding or solid braiding.

Because of the inherent nature of the braiding process, the braided preform architecture would be repetitive in nature. For a typical braiding process representative unit cell (RUC) can be identified. The braider yarns would be oriented in all the 4 segments of the coordinate system. Schematic arrangement of different orientations of braider yarns in geometrical representative unit cell is shown in fig. 4.9. Here it can be noticed that the fibres are moving from one vertex to diagonally opposite vertex, representing 4-axis of braided composite. Important geometrical parameters defining the RUC are the orientation of braider

yarns, diameter of braider and axial yarns and the actual location of the braider yarns in the RUC. Identification of the geometric representative unit cell based on repetitive nature of the braiding process can be achieved as follows. A typical 3D 5-axes braided composite RUC is shown in fig. 4.10. The RUC is defined with respect to xyz coordinate system. The RUC is indicated by $(IJKL - I'J'K'L')$. This RUC is defined as RUC2, since for the analytical formulation RUC1 is defined later, which is at an angle of 45^0 to RUC2. The RUC consists of braider yarns, axial yarns and pure matrix regions. The RUC consists of inner compact region as indicated by $(ABCD - A'B'C'D')$ in fig 4.10 and the outer region. The inner compact region is termed as the subcell. A typical 3D 5-axis braided composite subcell is shown in fig 4.11. It consists of four braider yarns oriented at an angle θ_x with the braiding direction and the axial yarns. Such a configuration is termed as 3D 5-axes braided composite. The configuration without the axial yarns is termed as 3D 4-axes braided composite. The RUC defined based on the braider yarn diameter (d_b), the angle between the braider yarn and the braiding axis referred to as the braid angle (θ_x) and the axial yarn diameter (d_a), the dimensions of the subcell (Lx, Ly, Lz) can be determined.

The RUC can also be defined in $xy'z'$ coordinate system as shown in fig 4.10 and 4.12, and indicated by $(EFGH - E'F'G'H')$. In this RUC the braider yarns are parallel to the reference coordinate system and have only 2D orientation. This RUC is defined as RUC1. It may be noted that RUC1 would be oriented at an angle of 45^0 to RUC2 in yz plane. On the other hand, the braider yarns within the RUC2 $(IJKL - I'J'K'L')$ have 3D orientation (i.e; with spatially oriented yarns) with respect to the coordinate system xyz.

The angle the braider yarn makes with respect to the reference axis is termed as the braid angle (θ). The azimuth angle (β) is the angle between the projections of the braider yarn on a plane perpendicular to the reference axis, with a reference axis within the plane. Specifically, the braid angle (θ_x) is the angle made by the braider yarn with the x axis. The azimuth angle (β_x) is the angle between the projection of the braider yarn on yz plane and z axis. The braid angle (θ_x) is positive when the direction of rotation of braider yarn to the x axis is anticlockwise. The azimuth angle (β_x) is positive when the direction of rotation from braider yarn projection to z axis is clockwise. Using the geometrical parameters defining the RUC and the fiber volume fraction within the yarn (V_f^s), the overall fiber volume fraction (V_f^0)

of 3D braided composite can be determined. In the case of an ideal geometry of the RUC, where fibres are assumed straight, the angles (θ) and (β) are constant.

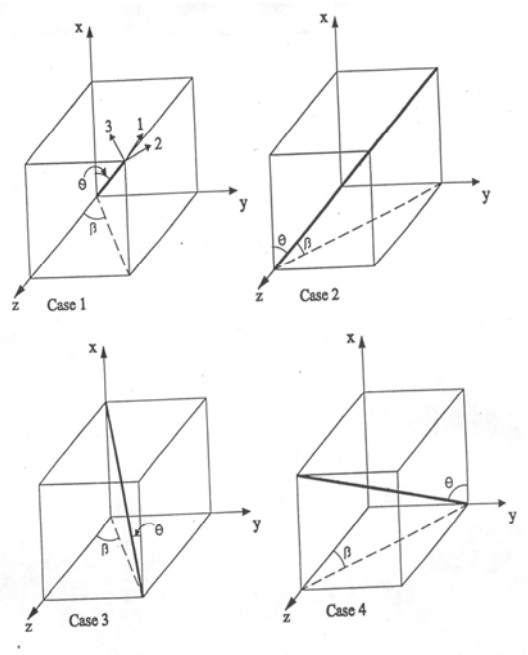

Fig 4.9 Different Orientations of Braider Yarns in Geometrical Representative Unit Cell

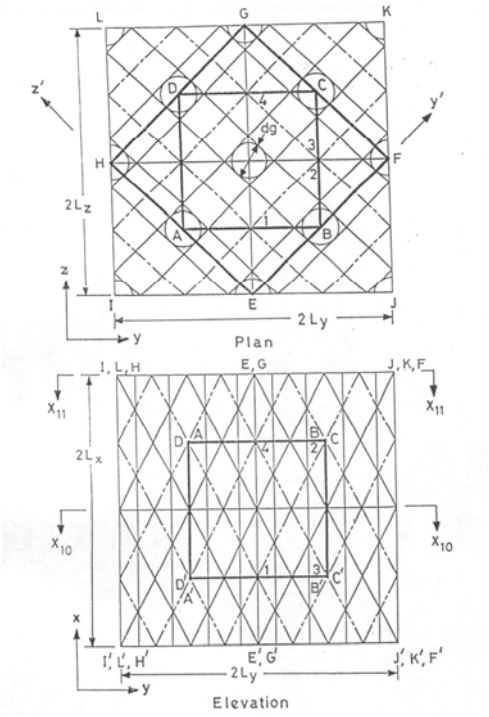

Fig 4.10 Identifying the Geometrical RUC: 3D 5-axes Braided Composite

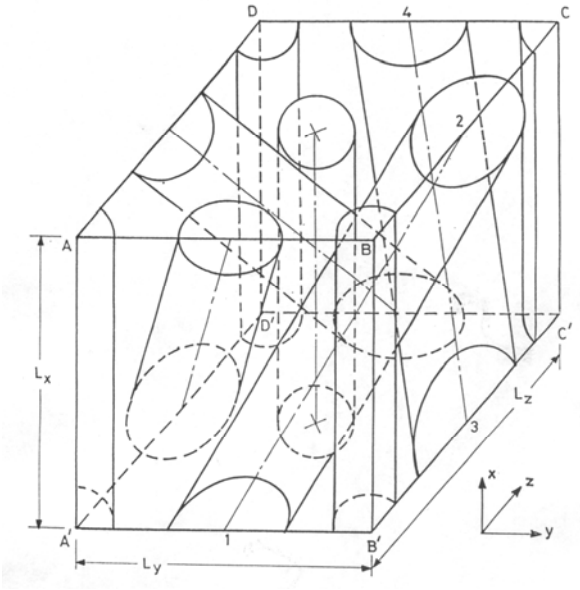

Fig 4.11 3D 5-axes Braided Composite Subcell

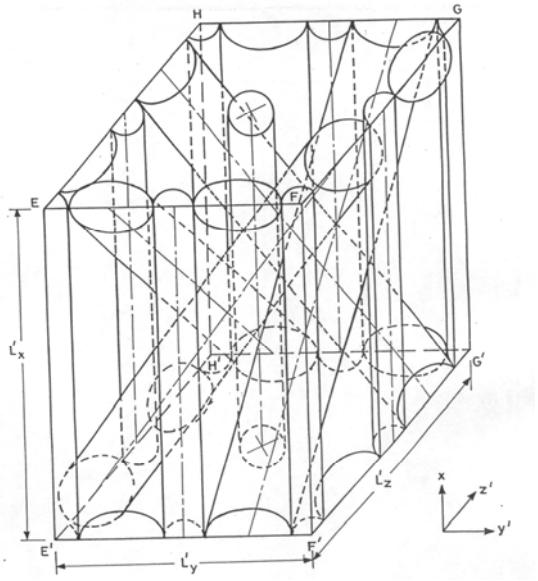

Fig 4.12 RUC1 for 5-axis Braided Composite

(Du and Ko 1993, Sun and Qiao 1997, Zuorong *et al.* 1999)

The braider yarn diameter (d_b) and the braid angle (θ_x) define the geometry of the RUC, i.e., L_x, L_y and L_z can be determined based on d_b and θ_x . or, d_b and θ_x can be calculated for given L_x, L_y, and L_z. For the subcell dimension of $L_x : L_y : L_z$ = 1 : 1 : 1 (fig 4.11), the dimensions of RUC1 ($EFGH - E'F'G'H'$) would be $L'_x : L'_y : L'_z = 2 : \sqrt{2} : \sqrt{2}$ (fig 4.12) and the dimensions of the RUC2 ($IJKL - I'J'K'L'$) would be $L^*_x : L^*_y : L^*_z$ = 2 : 2 : 2 (fig 4.10). Since both RUC1 and RUC2 represent the same 3D 5-axes braided composites, the thermomechanical properties would be the same whether RUC1 or RUC2 is considered. But the stress strain transformation matrices would be different. Here RUC1 is considered for the analysis.

4.3.2.1 Exact jamming condition

An important consideration in braiding technology is the exact jamming condition. The diameter of the braider yarn is worked out considering the jamming condition. An exact method based on the concept of shortest distance between two skewed lines is used to find out d_b using plane method.

The calculation details are given for a subcell (fig 4.11). The centre lines of two braider yarns (1-2 and 3-4) are two skewed lines. The shortest distance MN between these two skewed lines would be the diameter of the braider yarn d_b at jamming condition and is shown in fig 4.13. For the subcell dimension of (1:1:1), MN = 0.447. This can be calculated using eqn. 4.43 and 4.44.

$$MN = (L_y / 2)\sin\phi \tag{4.43}$$

$$\tan\phi = L_x /(L_y / 2) \tag{4.44}$$

There would be a gap between two adjacent braider yarns as shown in fig 4.10. The diameter of the circle inscribed in the gap (d_g) in the plan view can be determined using eqn. 4.45.

$$d_g = \left[1/2\sqrt{(L_y^2 + L_z^2)}\right] - d_b \tag{4.45}$$

If $d_a \le d_g$, the axial yarns can be placed within the gap region. If $d_a > d_g$, d_b can be calculated as,

$$d_b = \left[1/2\sqrt{(L_y^2 + L_z^2)} \right] - d_a \qquad (4.46)$$

Typical cross sections perpendicular to z' direction for RUC1 is shown in fig 4.14 and 4.15 at jamming condition. At jamming condition, two braiding yarns just touch to each other as shown in section x_2-x_2. The minor axis of the elliptical cross section is given by d_b whereas the major axis is given by (d_b / sin θ_x). Fig 4.16 shows elevation of 3D 5-axes braided composite for RUC1. If the sections are taken perpendicular to x axis of RUC1, the movement of braider yarns with respect to axial yarns can be observed and is represented in fig 4.17. It may be noted that there are four braider yarns and four axial yarns in each cross section. Fig 4.18 shows discretization of a typical section perpendicular to x axis into subelements for RUC1. The section consists of braider yarn subelements, axial yarn subelements and pure matrix subelements.

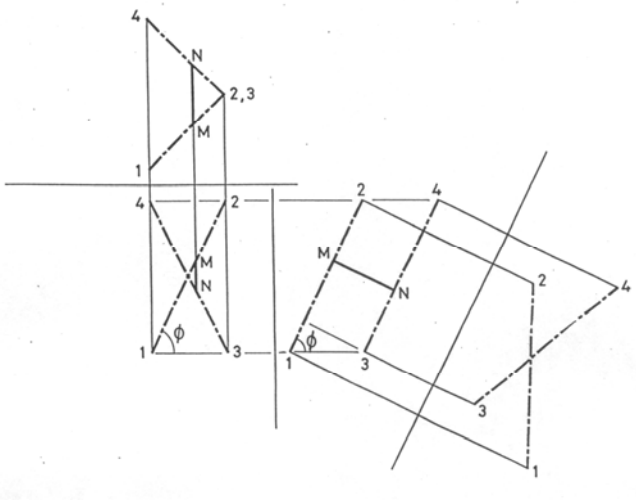

Fig 4.13 Braider Yarn Diameter at Jamming

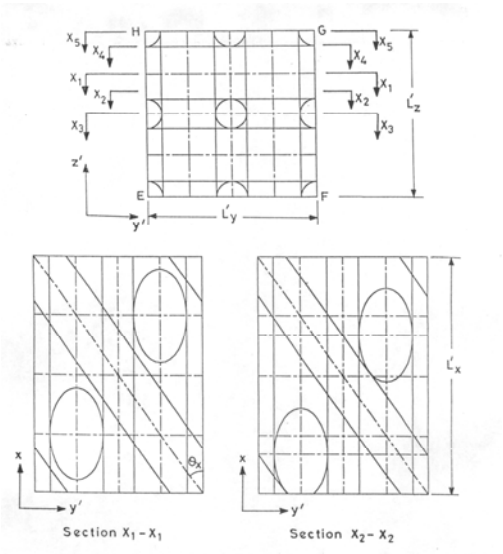

Fig 4.14 RUC1 for 5-axes Braided Composite: Sections Perpendicular to z' Direction

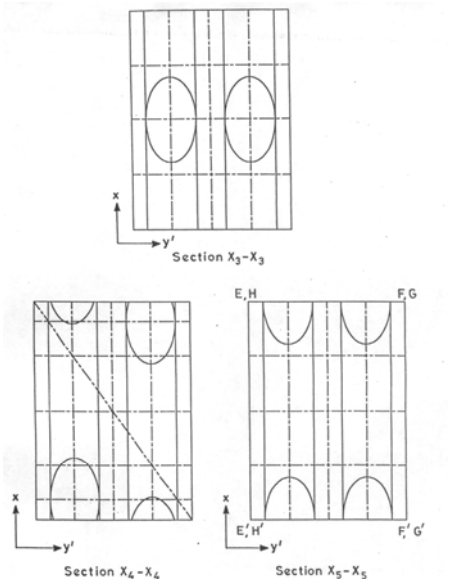

Fig 4.15 Sectional Views of RUC1

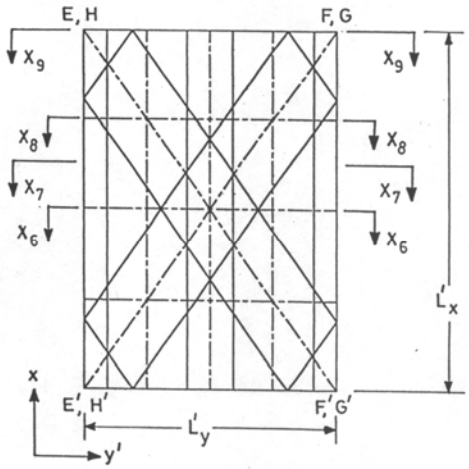

Fig 4.16 RUC1 for 3D 5-axes Braided Composite (Elevation)

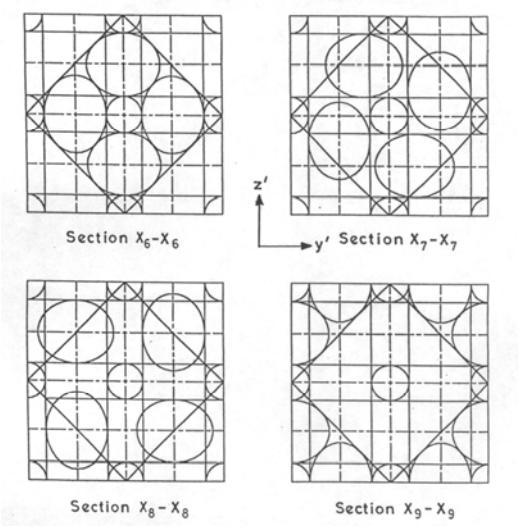

Fig 4.17 RUC1 for 3D 5-axes Braided Composite: Typical Sections Perpendicular to x axis

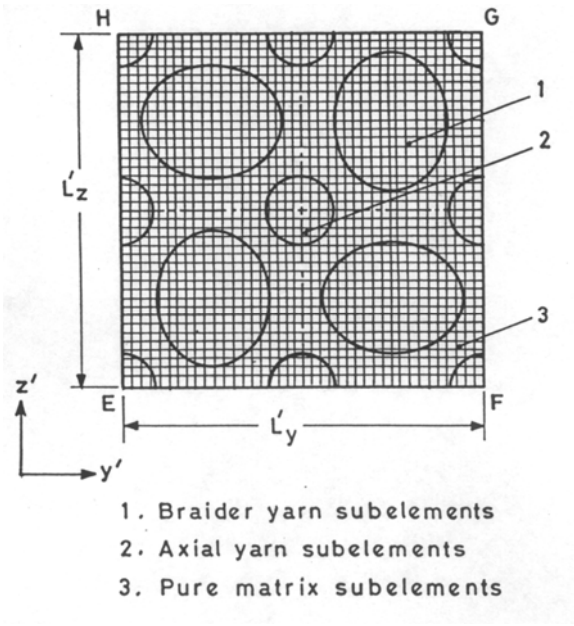

Fig 4.18 Discretization of a Typical Section Perpendicular to x axis into Subelements for RUC1

4.3.2.2 Analytical formulation

An analytical formulation for the prediction of thermoelastic and failure behavior of 3D braided composites is presented here. The RUC1 is discretized into sections and

subelements. Each subelement consists of braider yarn, axial yarn or pure matrix. Hence, the subelements provide the local behaviour of the braided composites. The failure can be predicted at subelements level. The details of the model are presented below.

The analysis methodology is based on orientation averaging of RUC for 3D braided composite. For the present analysis, an idealized geometry of the 3D braided composite is considered. The RUC is identified based on the geometrical symmetry shown in fig 4.10, 4.11 and 4.12. Since the entire 3D braided composite is obtained by the translation of the RUC, the properties of the 3D braided composite are the same as that of RUC. The parameters used for defining the 3D braided composite subcell geometry are the length (L_x), width (L_y *and* L_z) and the axial yarn diameter (d_a). Based on the above parameters using eqn. 4.43 to 4.46, braid angle (θ_x), azimuth angle (β_x) and the diameter of braider yarn (d_b) can be calculated.

The RUC is divided into sections perpendicular to the reference (axial) direction and then into subelements. The sections of the discretized RUC are represented in fig 4.17 for RUC1 and fig 4.19 for RUC2. The figures show the sections at different intervals. The cross sectional geometry of the braider yarns and axial yarns can be quasi square or even quasi rectangular depending on the processing conditions. It has been shown that for the same fiber content, the cross sectional geometry does not make significant effect on the predicted mechanical properties (Naik and Thuruthimattam 1998[2]). Considering the cross section of the yarns as circular, subelements has both impregnated yarns (braided and axial) and pure matrix regions. The discretization of typical sections into subelements is shown in fig 4.18 with respect to x direction for RUC1. The elastic properties of subelements can be determined by using the fiber properties, matrix properties and fiber volume fraction of the subelement using the Composite Cylinder Assemblage Model (Lei *et al.* 1992, Sun and Qiao 1997, Zuorong *et al.* 1999).

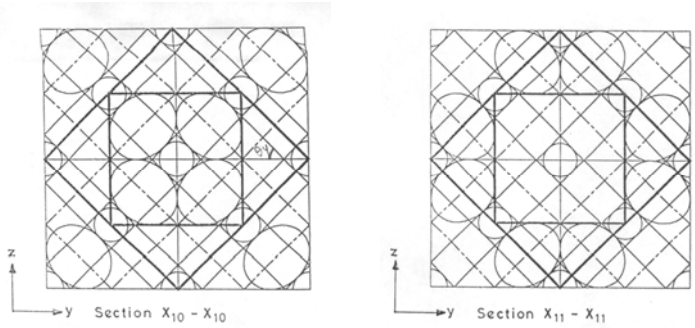

Fig 4.19 Typical Sections Perpendicular to x axis for RUC2

The coefficient of stiffness matrix of the subelements in their local coordinates can be described using eqn. 4.47 and 4.48, where E_i is the moduli of elasticity, v_{ij} and G_{ij} are the Poisson's ratio and shear moduli for the respective subelements. .

$$\left.\begin{aligned}
C_{11}^{sel} &= \frac{E_1(1-\upsilon_{23}\upsilon_{32})}{\Delta} & C_{12}^{sel} &= \frac{E_1(\upsilon_{21}+\upsilon_{23}\upsilon_{31})}{\Delta} \\
C_{22}^{sel} &= \frac{E_2(1-\upsilon_{13}\upsilon_{31})}{\Delta} & C_{23}^{sel} &= \frac{E_2(\upsilon_{32}+\upsilon_{12}\upsilon_{31})}{\Delta} \\
C_{13}^{sel} &= \frac{E_1(\upsilon_{31}+\upsilon_{21}\upsilon_{32})}{\Delta} & C_{33}^{sel} &= \frac{E_3(1-\upsilon_{12}\upsilon_{21})}{\Delta} \\
C_{44}^{sel} &= G_{23}\,, \quad C_{55}^{sel} = G_{13}\,, \quad C_{66}^{sel} = G_{12} \\
C_{21}^{sel} &= C_{12}^{sel}\,, \quad C_{32}^{sel} = C_{23}^{sel}\,, \quad C_{31}^{sel} = C_{13}^{sel}
\end{aligned}\right\} \qquad (4.47)$$

where $\Delta = 1-\upsilon_{12}\upsilon_{21}-\upsilon_{23}\upsilon_{32}-\upsilon_{31}\upsilon_{13}-2\upsilon_{21}\upsilon_{32}\upsilon_{13}$ (4.48)

Considering the impregnated strands to be transversely isotropic,

$$C_{12}^{sel} = C_{13}^{sel}\,,\ C_{22}^{sel} = C_{33}^{sel}\,,\ C_{55}^{sel} = C_{66}^{sel} \qquad (4.49)$$

The stiffness matrix can be represented in the matrix form as,

$$\left[C_{ij}^{sel}\right] \quad \text{i, j=1,.....6} \qquad (4.50)$$

After the determination of stiffness matrix of each subelement in its local coordinates, it is transformed to the global coordinate system. This transformation is not required for the pure matrix subelements, matrix being isotropic.

The transformed stiffness matrix can be written using eqn. 4.51.

$$\left[\bar{C}_{ij}^{sel}\right] = [T]^{-1}\left[C_{ij}^{sel}\right][T]^{-T} \quad \text{i, j = 1,....6} \qquad (4.51)$$

Here, $[T]$ is the transformation matrix given in appendix C.

For the fibres oriented along the y axis, transformation is carried out about z axis and for the fibres oriented along the z axis, transformation about z axis is carried out first, and then transformation about x axis is carried out.

In the present analysis two schemes viz., Compliance Averaging (CA) and Stiffness Averaging (SA) methods are used for the assembly of subelements into sections and sections into RUC. In the CA scheme, isostrain condition is considered in sections with respect to the reference direction, i.e., the section properties are obtained by stiffness averaging. Isostress condition is considered in RUC, i.e., compliance averaging scheme is used to obtain RUC properties starting with the section properties. In the SA scheme,

isostrain condition is considered in sections with respect to the reference direction, i.e., the section properties are obtained by stiffness averaging. The properties of RUC are obtained by stiffness averaging method starting with the section properties.

The extensional stiffness matrix of each section can be determined using eqn. 4.52 and 4.53 considering sections perpendicular to x direction.

$$\left[A_{ij}^{\sec}\right] = \frac{1}{L_y^{\sec} L_z^{\sec}} \int_0^{l_y^{sel}} \int_0^{l_z^{sel}} \left[\bar{C}_{ij}^{sel}\right] dydz \qquad \text{i,j = 1,….6} \tag{4.52}$$

This equation can also be represented in the discretized form as

$$\left[A_{ij}^{\sec}\right] = \frac{1}{L_y^{\sec} L_z^{\sec}} \sum_1^{ny^{sel}} \sum_1^{nz^{sel}} \left[\bar{C}_{ij}^{sel}\right] l_y^{sel} l_z^{sel} \qquad \text{i,j = 1,….6} \tag{4.53}$$

Where, ny^{sel} and nz^{sel} are the number of subelements in the section along y and z directions, respectively. The overall RUC dimensions for RUC1 can be written as $L_x' : L_y' : L_z'$ and for RUC2 it is $L^*_x : L^*_y : L^*_z$.

4.3.3 Elastic properties

Using ***stiffness averaging method*** the properties of the entire RUC can be determined integrating the properties of all the sections. The extensional stiffness matrix of the RUC can be determined using eqn. 4.54 and 4.55, where $nx^{\sec}$ is the number of sections along x direction.

$$\left[\bar{A}_{ij}\right] = \frac{1}{L_x} \int_0^{L_x} \left[A_{ij}^{\sec}\right] dx \qquad \text{i,j = 1,…..6} \tag{4.54}$$

$$\left[\bar{A}_{ij}\right] = \frac{1}{L_x} \sum_1^{nx^{\sec}} \left[A_{ij}^{\sec}\right] l_x^{\sec} \qquad \text{i,j = 1,….6} \tag{4.55}$$

The extensional compliance matrix of the RUC can be written using eqn. 4.56.

$$\left[\bar{a}_{ij}\right] = \left[\bar{A}_{ij}\right]^{-1} \text{i,j = 1,….6} \tag{4.56}$$

The elastic properties of the RUC/3D braided composite can be determined using eqn. 4.57.

$$\left.\begin{aligned} &E_x = \frac{1}{\bar{a}_{11}},\ E_y = \frac{1}{\bar{a}_{22}},\ E_z = \frac{1}{\bar{a}_{33}},\ G_{yz} = \frac{1}{\bar{a}_{44}},\ G_{xz} = \frac{1}{\bar{a}_{55}},\ G_{xy} = \frac{1}{\bar{a}_{66}} \\ &\upsilon_{xy} = -\frac{\bar{a}_{12}}{\bar{a}_{11}},\ \upsilon_{yz} = -\frac{\bar{a}_{23}}{\bar{a}_{22}},\ \upsilon_{yx} = -\frac{\bar{a}_{21}}{\bar{a}_{22}},\ \upsilon_{zx} = -\frac{\bar{a}_{31}}{\bar{a}_{33}},\ \upsilon_{zy} = -\frac{\bar{a}_{32}}{\bar{a}_{33}},\ \upsilon_{xz} = -\frac{\bar{a}_{13}}{\bar{a}_{11}} \end{aligned}\right\} \tag{4.57}$$

Using ***Compliance Averaging (CA) method*** the extensional compliance matrix of each section can be determined using eqn. 4.58.

$$\left[a_{ij}^{\sec}\right]=\left[A_{ij}^{\sec}\right]^{-1} \quad \text{i,j = 1,…6} \tag{4.58}$$

The extensional compliance matrix of the RUC can be determined using eqn. 4.59 and 4.60.

$$\left[\bar{a}_{ij}\right]=\frac{1}{L_x}\int_0^{L_x}\left[a_{ij}^{\sec}\right]dx \quad \text{i,j = 1,….6} \tag{4.59}$$

$$\left[\bar{a}_{ij}\right]=\frac{1}{L_x}\sum_1^{nx^{\sec}}\left[a_{ij}^{\sec}\right]l_x^{\sec} \quad \text{i,j = 1,…..6} \tag{4.60}$$

The extensional stiffness matrix of the RUC can be written as

$$\left[\bar{A}_{ij}\right]=\left[\bar{a}_{ij}\right]^{-1} \quad \text{i,j = 1,…6} \tag{4.61}$$

The elastic properties of the RUC/3D braided composite can be found out using eqn. 4.57 to 4.61.

4.3.4 Thermal expansion properties

Using the fibre and matrix properties and fibre volume fraction of the subelements, the coefficients of thermal expansion of the strand subelements are determined using Composite Cylinder Assemblage Model (Hashin 1972) and represented using eqn. 4.62.

$$\left\{\alpha_i^{sel}\right\} \quad \text{i= 1,…..6} \tag{4.62}$$

After the determination of the coefficients of thermal expansion of each subelement in its local coordinates, the properties are transformed to the global coordinate system. The transformed coefficients of thermal expansion of the subelements can be written using eqn. 4.63, where [T] is the 3D transformation matrix.

$$\left\{\bar{\alpha}_i^{sel}\right\}=[T]^{-1}\left\{\alpha_i^{sel}\right\} \quad \text{i = 1,…..6} \tag{4.63}$$

The thermal force resultants and coefficients of thermal expansion can be determined using CA and SA methods.

Using SA method the thermal force resultants of each section can be determined using eqn. 4.64 and 4.65, where $\left[\bar{C}_{ij}^{sel}\right]$ is described in eqn. 4.51.

$$\left\{N_i^{T\sec}\right\}=\frac{\Delta T}{L_yL_z}\int_0^{L_y}\int_0^{L_z}\left[\bar{C}_{ij}^{sel}\right]\left\{\bar{\alpha}_i^{sel}\right\}dydx \quad \text{i,j = 1,….6} \tag{4.64}$$

$$\left\{N_i^{T\sec}\right\}=\frac{\Delta T}{L_yL_z}\sum_1^{ny^{sel}}\sum_1^{nz^{sel}}\left[\bar{C}_{ij}^{sel}\right]\left\{\bar{\alpha}_i^{sel}\right\}l_y^{sel}l_z^{sel} \quad \text{i,j = 1,….6} \tag{4.65}$$

The thermal force resultants of the RUC can be determined using eqn. 4.66 and 4.67.

$$\left\{N_i^T\right\} = \frac{1}{L_x}\int_0^{L_x}\left\{N_i^{T\,\sec}\right\}dx \quad i = 1,\ldots.6 \tag{4.66}$$

$$\left\{N_i^T\right\} = \frac{1}{L_x}\sum_{1}^{nx^{\sec}}\left\{N_i^{T\,\sec}\right\}l_x^{\sec} \quad i = 1,..6 \tag{4.67}$$

The coefficients of thermal expansion of the RUC / 3D braided composite can be worked out using eqn. 4.68, where $\left[\bar{a}_{ij}\right]$ are obtained using eqn. 4.56.

$$\{\alpha_k\} = \frac{1}{\Delta T}\left[\bar{a}_{ij}\right]\left\{N_i^T\right\} \quad i,j = 1,\ldots6 \tag{4.68}$$

Where, α_k, *i.e.*, $\alpha_x, \alpha_y, \alpha_z, \alpha_{xy}, \alpha_{xz}$ and α_{yz} are the coefficients of thermal expansion for the 3D braided composite.

If thermal force resultants of each section are determined using eqn. 4.65, using CA method the coefficients of thermal expansion of each section can be worked out using eqn. 4.69, where $\left[a_{ij}^{\sec}\right]$ can be calculated using eqn. 4.58.

$$\left\{\alpha_i^{\sec}\right\} = \frac{1}{\Delta T}\left[a_{ij}^{\sec}\right]\left\{N_i^{T\sec}\right\} \quad i,j = 1,\ldots..6 \tag{4.69}$$

The coefficients of thermal expansion of the RUC / 3D braided composite can be determined using eqn. 4.70 and 4.71.

$$\{\alpha_k\} = \frac{1}{L_x}\int_0^{L_x}\left\{\alpha_i^{\sec}\right\}dx \quad i= 1,\ldots6 \tag{4.70}$$

$$\{\alpha_k\} = \frac{1}{L_x}\sum_{1}^{nx^{\sec}}\left\{\alpha_i^{\sec}\right\}l_x^{\sec} \quad i = 1,\ldots6 \tag{4.71}$$

where, α_k, *i.e.*, $\alpha_x, \alpha_y, \alpha_z, \alpha_{xy}, \alpha_{xz}$ and α_{yz} are the coefficients of thermal expansion of the 3D braided composite.

The flow sequence for evaluating the elastic and thermal properties is given in fig 4.20.

4.3.5 Thermal conductivity properties

The thermal conductivity of 4-axis and 5-axis composite can be found by the same thermal electrical analogy explained in section 4.2.4.

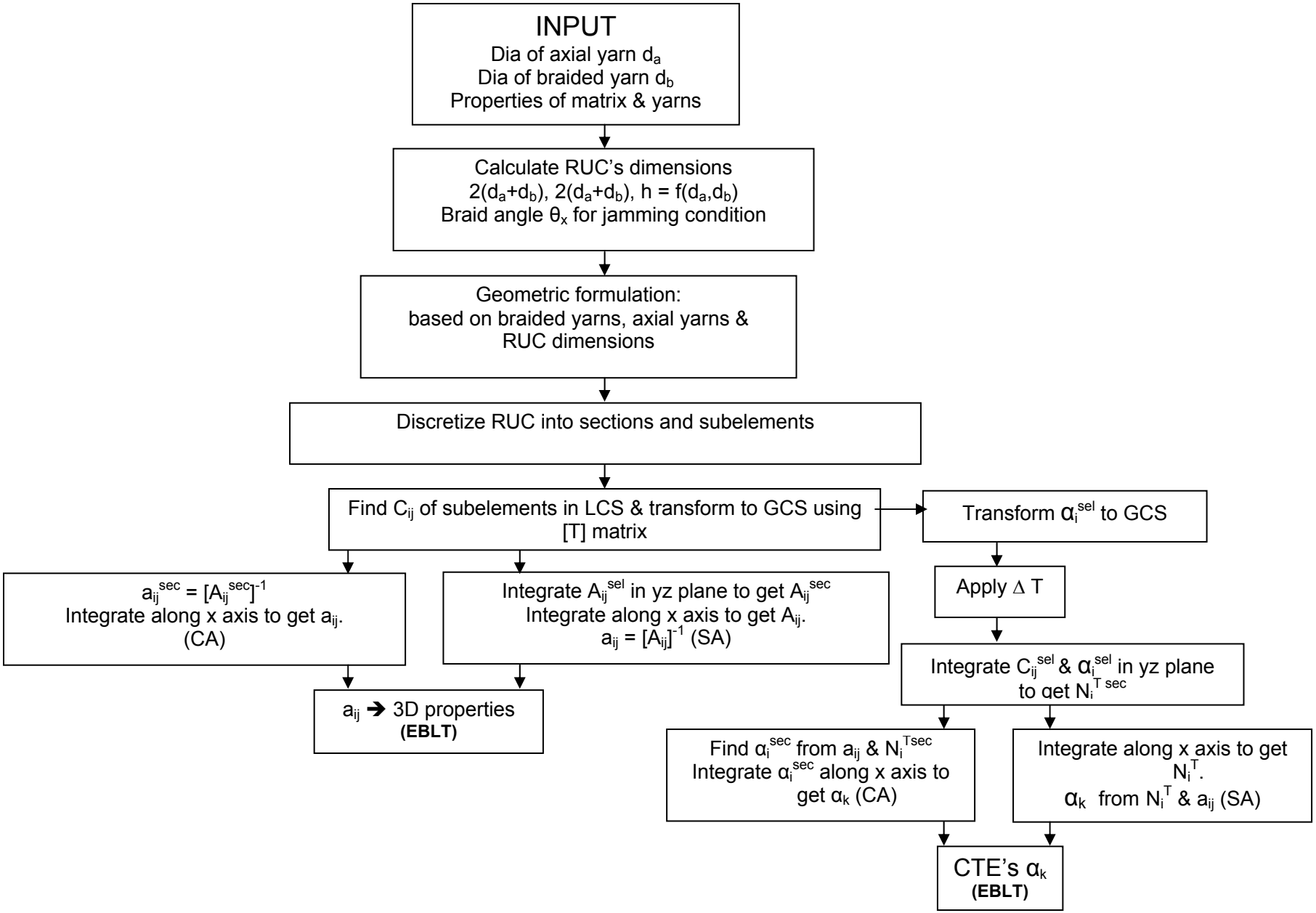

Fig 4.20. Schematic Diagram for Determination of Thermomechanical Properties of 4-axis / 5-axis Braided Composites

4.3.6 Strength analysis

4.3.6.1 Tensile strength

For the tensile strength analysis, the RUC is divided into sections perpendicular to the loading direction. The isostress assumption is made for calculating the stresses in each section. The sections are divided into subelements. The isostrain assumption is made for calculating the stresses in the subelements.

For loading along x direction, the transverse and shear strains for the RUC can be written using eqn. 4.72.

$$\varepsilon_y = \bar{a}_{21} N_x \qquad \gamma_{yz} = \bar{a}_{41} N_x \qquad \gamma_{xy} = \bar{a}_{61} N_x$$
$$\varepsilon_z = \bar{a}_{31} N_x \qquad \gamma_{zx} = \bar{a}_{51} N_x \tag{4.72}$$

Where, N_x is the load applied in x direction on the RUC per unit area.

The transverse and shear strains for all sections are assumed to be the same as the average transverse and shear strains for the RUC as described in eqn. 4.73, where the transverse strains for the RUC are given by eqn. 4.72.

$$\varepsilon_y^{sel} = \varepsilon_y^{\sec} = \varepsilon_y \qquad \gamma_{yz}^{\sec} = \gamma_{yz} \qquad \gamma_{zx}^{\sec} = \gamma_{zx} \tag{4.73}$$
$$\varepsilon_z^{sel} = \varepsilon_z^{\sec} = \varepsilon_z \qquad \gamma_{xy}^{\sec} = \gamma_{xy}$$

Since isostrain assumption is made within each section, the strain along the loading direction within the section and all the corresponding subelements would be the same, where ε_x^{sel} can be obtained using eqn. 4.74.

i.e; $$\varepsilon_x^{sel} = \varepsilon_x^{\sec} \tag{4.74}$$

From the above equations, the strains of each section along the loading direction can be determined using eqn. 4.75.

$$\varepsilon_x^{\sec} = \frac{N_x - A_{12}^{\sec}\varepsilon_y - A_{13}^{\sec}\varepsilon_z - A_{14}^{\sec}\gamma_{yz} - A_{15}^{\sec}\gamma_{zx} - A_{16}^{\sec}\gamma_{xy}}{A_{11}^{\sec}} \tag{4.75}$$

Average strain of the RUC along the loading direction can be determined using eqn. 4.76 and 4.77.

$$\varepsilon_x = \frac{1}{L_x}\int_0^{L_x} \varepsilon_x^{\sec} dx \tag{4.76}$$

$$\varepsilon_x = \frac{1}{L_x}\sum_{1}^{nx^{\sec}} \varepsilon_x^{\sec} l_x^{\sec} \tag{4.77}$$

The subelement strain is transformed to the subelement local coordinates using eqn. 4.78 where [T] is the transformation matrix.

$$\{\varepsilon\}_L = [T]\{\varepsilon\}_G \tag{4.78}$$

The subelement is assumed to have failed when the strain due to the applied load exceeds the failure strain of the corresponding subelement. When a subelement fails, degradation analysis is carried out. The RUC / 3D braided composite is assumed to have failed when all the subelements in a section have failed. The load at which the entire section fails corresponds to the failure strength of the RUC / 3D braided composite. The corresponding strain indicates the failure strain of the RUC / 3D braided composite. In a similar way, the failure behaviour of the 3D braided composite is characterized along the y and z directions considering the loading to be along the respective directions.

4.3.6.2 Shear strength

The shear strength is calculated assuming that the shear strain is the same for all the sections and subelements as that of the RUC / 3D braided composite.

$$\gamma_{yz}^{sel} = \gamma_{yz}^{\sec} = \gamma_{yz} \tag{4.79}$$

The shear strain is assumed to be constant within the RUC for the applied shear load N_{yz} and can be estimated using eqn. 4.80 and 4.81.

$$\tau_{yz} = \frac{N_{yz}}{L_y L_z} \tag{4.80}$$

$$\gamma_{yz} = \bar{a}_{44} N_{yz} \tag{4.81}$$

Similarly, the shear strains in the other directions can be determined using eqn. 4.82 and 4.83.

$$\tau_{xy} = \frac{N_{xy}}{L_x L_y} \qquad \gamma_{xy} = \bar{a}_{66} N_{xy} \tag{4.82}$$

$$\tau_{zx} = \frac{N_{zx}}{L_z L_x} \qquad \gamma_{zx} = \bar{a}_{55} N_{zx} \tag{4.83}$$

The subelement strain is transformed to the subelement local coordinates. If this shear strain is more than the failure strain of the subelement, the subelement is assumed to have failed. After all the subelements have failed in a section, the RUC / 3D braided composite is assumed to have failed. The corresponding shear stress / shear strain gives the shear strength / shear failure strain of the RUC / 3D braided composite. Considering the shear loading to be in xy plane and xz plane, the corresponding shear strengths and shear failure strains can be estimated. The flow sequence for evaluating the strength properties is given in fig 4.21.

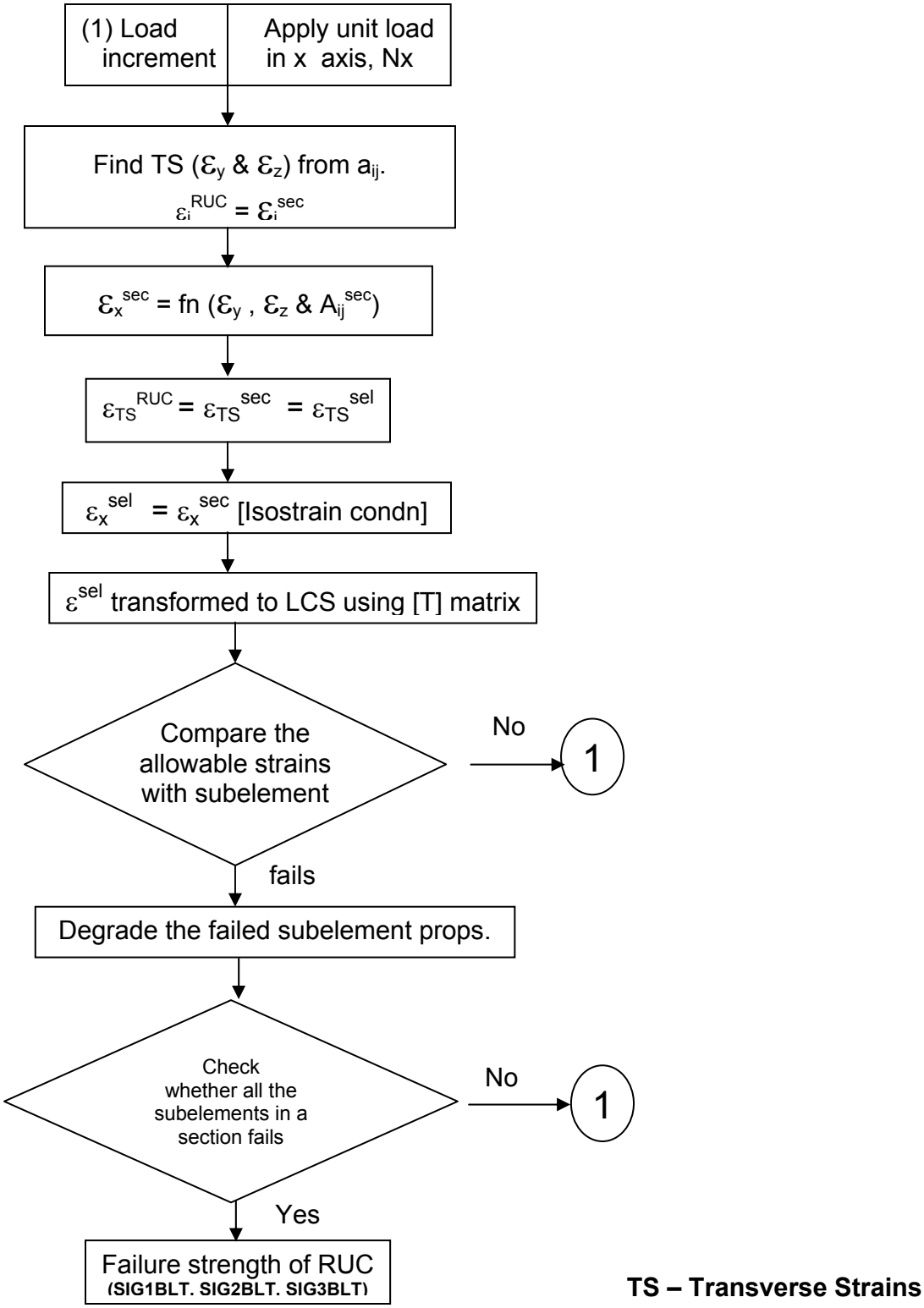

Fig 4.21. Schematic Diagram for Determination of Strength Properties for 4-axis/5-axis Braided Composites

4.3.7 Development of computer code

For generating the elastic, strength and thermal properties for braided composites, five separate codes have been written using MATLAB and the details of subroutines are described in subsequent subsection. The description and the source codes generated are described elsewhere (Santhosh 2010).

4.3.7.1 *EBLT*

This code generates the elastic and CTE constants for the 4-axis and 5-axis braided composites. The inputs required for the code are fibre details, elastic properties (nine elastic constants) and CTE's (three constants) of the fibre and matrix with respect to temperature and the geometrical parameters of the RUC's. The outputs from the code are the equivalent elastic properties (nine elastic constants) and CTE's (three constants) for all the respective RUC's.

4.3.7.2 *KBLT*

This code generates the thermal conductivity constants for the 4-axis and 5-axis braided composites. The inputs required for the code are fibre details, thermal conductivity properties (three constants) of the fibre and matrix with respect to temperature and the geometrical parameters of the RUC's. The outputs from the code are the equivalent conductivity properties (three constants) for all the respective RUC's.

4.3.7.3 *SIG1BLT*

This code generates the strength constants like σ_x and τ_{xy} for the 4-axis and 5-axis braided composites. The inputs required for the code are fibre details, elastic properties (nine elastic constants) and strength properties (six constants) of the fibre and matrix with respect to temperature and the geometrical parameters of the RUC's. The outputs from the code are the equivalent strength properties (σ_x and τ_{xy}) for all the respective RUC's.

4.3.7.4 SIG2BLT

This code generates the strength constants like σ_y and τ_{yz} for the 4-axis and 5-axis braided composites. The inputs required for the code are fibre details, elastic properties (nine elastic constants) and strength properties (six constants) of the fibre and matrix with

respect to temperature and the geometrical parameters of the RUC's. The outputs from the code are the equivalent strength properties (σ_y and τ_{yz}) for all the respective RUC's.

4.3.7.5 SIG3BLT

This code generates the strength constants like σ_z and τ_{zx} for the 4-axis and 5-axis braided composites. The inputs required for the code are fibre details, elastic properties (nine elastic constants) and strength properties (six constants) of the fibre and matrix with respect to temperature and the geometrical parameters of the RUC's. The outputs from the code are the equivalent strength properties (σ_z and τ_{zx}) for all the respective RUC's.

4.4 Results and Discussions

The properties of the various 3D composites have been evaluated based on the mathematical formulations given in sections 4.2 and 4.3 using the UD properties derived in section 3.4 and 3.5. Codes have been written in MATLAB for the evaluation of elastic and thermal properties of the 3D composites. The code has been further extended for the evaluation of the strength properties of the RUC configurations. Elastic, strength and thermal properties varying with temperature derived in the present study has been discussed in subsequent headings.

4.4.1 Validation

The code developed herein has been used to predict the elastic, strength and thermal properties of 3D woven and braided composites. From the available literature appropriate published work has been identified in which the properties of RUC's are determined through experimental studies. The geometric parameters of the 3D orthogonal woven composites for weave geometry 1 and 2 (WG1 and WG2) have been reported in table 4.1 (Cox *et al.* 1994[1], 1995, Cox and Dadkhah 1995). Similarly elastic and strength properties of the resin impregnated strands / elements (AS4 Carbon and E glass) from the same source have been given as tables 4.2 and 4.3 respectively.

Table 4.1 Geometry of 3D Orthogonal Woven Composites

Weave Geometry	n_x	d_s (mm)	d_f (mm)	d_w (mm)	V_f^s (%)	V_f^f (%)	V_f^w (%)	V_f^o (%)	Configuration
WG1	2	1.2	1.0	0.8	70	70	70	40.0	-ZOZ-
WG2	4	0.85	0.92	0.39	69	69	69	48.4	-ZOZ-

ZOZ – Warp weaver passes around two fillers before reversing. There exists a gap between the fillers due to warp weaver in the next unit cell.

Table 4.2 Elastic Properties of the Resin Impregnated Strands / Elements

Material		V_f^{str} (%)	E_1^{str} (GPa)	E_2^{str} (GPa)	G_{12}^{str} (GPa)	G_{23}^{str} (GPa)	v_{12}^{str}	v_{23}^{str}
AS4 carbon / epoxy	Material I	65	148	13.1	4.9	4.5	0.289	-
	Material II	69	156	14.4	5.5	5.2	0.285	
E-glass / epoxy		70	51	17.5	5.8	6.6	0.313	-

Table 4.3 Strength Properties of the Resin Impregnated Strands / Elements

Material		V_f^{str} (%)	X_t^{str}/ X_c^{str} (MPa)	Y_t^{str}/ Y_c^{str} (MPa)	S_{12}^{str} (MPa)	S_{23}^{str} (MPa)
AS4 carbon / epoxy	Material I	65	1654	51.9	105.1	100
	Material II	69	1720	52.5	111.6	100
E-glass / epoxy		70	1426	29.1	38.9	39

The input for the code (EWLT, KLT, SIG1LT, SIG2LT and SIG3LT) has been appropriated from the above tables and the volume fractions, the Young's modulus and Poisson's ratio of the 3D orthogonal composites have been evaluated and shown in table 4.4. Tensile strength of the above composite has been given in table 4.5.

Table 4.4 Comparison of Predicted and Experimental Values of Elastic Properties of AS4 Carbon / Epoxy (WG2, Material II)

Model		Weave Geometry	V_f^o (%)	E_x (GPa)	E_y (GPa)	E_z (GPa)	v_{xy}	v_{xz}
3D Composite Strength Model		Ideal geometry	48.4	36.6	46.8	10.3	0.040	0.210
		KNF and CR	48.4	30.6	45.7	6.1	0.032	0.367
Reported values (Cox)	Analytical	Ideal geometry	48.3	48.9	63.7	9.4	0.027	0.428
		KNF and CR	48.3	42.1	-	6.9	-	0.310
	Experimental		48.3 [±1]	30.0 [±2]	45.5 [±1.5]	7.0 [±1]	0.053	0.490
% deviation of analytical values for ideal geometry reported by author and Cox			0.2	25	26.5	9.5	48.1	50.9
% deviation of analytical values with KNF and CR reported by author and Cox			0.2	27.3	-	11.5	-	18.4
% deviation of analytical of author with KNF and CR and experiment of Cox			0.2	2	0.4	12.8	39.6	25.1
% deviation of analytical with KNF and CR and experiment of Cox			0	40.3	-	1.4	-	36.7

[ ] deviation in the experimental values as reported by Cox *et al.* (1994[1], 1995) & Cox and Dadkhah (1995) are given in brackets

It can be noted from table 4.4 that percentage deviation of analytical values for ideal geometry of author and Cox and percentage deviation of analytical values with KNF and CR of author and Cox are fairly close to each other except for the transverse Poisson's ratio. The above deviation gets reduced with KNF and CR. It can be further inferred that the analytical prediction of author is fairly close to the experimental results than the values predicted by Cox except for the transverse modulus, where the magnitude is low and if the scatter in the test is considered the percentage deviation is within the acceptable range. Similar observation has been noticed for the tensile strength and has been shown in table 4.5.

Table 4.5 Comparison of Predicted and Experimental Values of Tensile Strength of AS4 Carbon/Epoxy (WG2, Material I)

Model		X_t (MPa)
3D Composite Strength Model	Ideal Geometry	496
	KNF and CR	440
Experimental (Cox *et al.* 1994[1], 1995, Cox and Dadkhah 1995)		390 [$\pm$30]

4.4.2 E-glass epoxy

Strong recommendations made by Ishikawa *et al.* (1997) for using Compliance Averaging scheme for determination of modulus of elasticity and CTE and Stiffness Averaging scheme for moduli of rigidity and Poisson's ratio have been adopted in the present study.

UD composite / impregnated strand properties are derived using the 3D composite strength model, considering the filler and warp weaver dimensions to be tending to zero. These UD composite properties match well with properties obtained using the CCA model by Hashin (1972) and the method of cells by Aboudi (1991). Balanced symmetric crossply laminate properties are obtained using the 3D composite strength model considering the warp weaver dimensions to be tending to zero. Also, the fiber distributions along the stuffer and filler directions are considered to be the same for the crossply laminate.

Elastic properties of E-glass/epoxy composite for UD composite / impregnated strand, balanced symmetric crossply laminate, bidirectional woven fabric composite and 3D

orthogonally woven composite geometries evaluated using the code EWLT have been given in table 4.6. Comparison has been made with the values provided by Naik and Thuruthimattam (1998[2]) which are indicated in table appropriately. It can be observed that the deviation in the relevant values i.e, those predicted by author and those reported in literature, has been less than 1 %. Hence the methodology has been validated.

Strength properties of E-glass/epoxy composite for UD composite / impregnated strand, balanced symmetric crossply laminate, bidirectional woven fabric composite and 3D orthogonally woven composite geometries evaluated using the codes SIG1LT, SIG2LT and SIG3LT have been given in table 4.7. The comparison has been made with the values provided by Naik and Thuruthimattam (1998[2]) which are indicated in the appropriate table. It can be observed that the deviation in the relevant values i.e, those predicted by author and those reported in literature, has been less than 1 %. Hence the methodology has been accepted for practice confidently.

Table 4.6 Validation for Different E-glass/epoxy Composite Configurations from 3D to UD (Elastic properties)

Configurations		V_f^o (%)	V_f^{str} (%)	E_x (GPa)	E_y (GPa)	E_z (GPa)	ν_{xy}	ν_{yz}	ν_{xz}
UD Composite / Impregnated strand		40 (40)	-	30.9 (31)	8.39 (8.4)	8.39 (8.4)	0.325 (0.326)	0.446 (0.448)	0.325 (0.326)
		70 (70)	-	51.05 (51)	17.52 (17.5)	17.52 (17.5)	0.313 (0.313)	0.325 (0.326)	0.313 (0.313)
Balanced symmetric crossply laminate		40 (40)	-	19.8 (19.9)	19.8 (19.9)	8.2 (8.4)	0.133 (0.137)	0.398 (0.401)	0.398 (0.401)
Bidirectional woven fabric composite		40 [40]	65 [65-70]	16.05 [16-20]	16.05 [16-20]	-	0.169 [0.165-0.192]	-	-
WG1	Ideal geometry	40 (40)	70 (70)	19.98 (20.1)	19.64 (19.9)	14.21 (14.0)	0.204 (0.201)	0.312 (0.301)	0.288 (0.296)
	KNF and CR Cox [1995]	40 (40)	70 (70)	16.81 (16.9)	19.17 (19.5)	11.79 (11.7)	0.191 (0.193)	0.373 (0.362)	0.356 (0.360)

Values available from Naik and Thuruthimattam (1998[2]) are given in ordinary brackets and from Naik (1994) & Ganesh and Naik (1994) are given in square brackets respectively

Table 4.7 Validation for Different E-glass/epoxy Composite Configurations from 3D to UD (Strength properties)

Configurations		V_f, V_f^o (%)	X_t (MPa)	Y_t (MPa)	Z_t (MPa)
UD Composite / Impregnated strand		40 (40) 70 (70)	846 (857) 1418 (1426)	27 (28) 27.8 (29)	27 (28) 27.8 (29)
Balanced symmetric crossply laminate		40 (40)	428 (429)	428 (429)	26.8 (28)
Bidirectional woven Fabric composite		40 [40]	268 [255-390]	268 [255-390]	-
3D orthogonally woven composite (WG1)	Ideal geometry	40 (40)	357 (359)	338 (340)	81 (83)
	KNF and CR Cox (1995)	40 (40)	249 (253)	330 (333)	27 (28)

Values available from Naik and Thuruthimattam (1998[2]) are given in ordinary brackets and from Naik (1994) and Ganesh and Naik (1994) are given in square brackets respectively

The prediction of elastic, strength and thermal properties of 3D composites using the code developed for the purpose has been validated with the similar studies available in literature for the 3D composite. The code developed herein can be degraded for the UD, crossply and woven laminates. This utility code has been accepted for the generation of high temperature values in the further investigations.

4.4.3 Evaluation of high temperature properties for 3D woven composites

4.4.3.1 Elastic properties of 3D woven composites

High temperature properties of 3D woven composites has been determined based on the analytical investigations performed on the TTOW-1-1, TTOW-2-1, TTOW-1-2, TTOW-2-2, LLOW-1-1, LLOW-2-1, LLOW-1-2 and LLOW-2-2 geometries. The elastic properties for the 3D orthogonal woven composite have been derived for the various types of geometries at elevated temperatures, and are shown in tables 4.8, 4.9 and 4.10.

Table 4.8 Elastic Properties for Woven Composites at 293°K, 773°K, 1273°K, 1773°K

RUC Type	E_1 N/mm^2	E_2 N/mm^2	E_3 N/mm^2	v_{12}	v_{23}	v_{31}	G_{12} N/mm^2	G_{23} N/mm^2	G_{31} N/mm^2
TTOW-1-1	30085	39468	5153.8	0.0209	0.1892	0.0316	1976.9	1976.9	1976.9
TTOW-1-2	21673	39394	5043.2	0.0232	0.1876	0.0451	1919.7	1920.1	1919.9
TTOW-2-1	29598	38984	4698.1	0.0161	0.1829	0.0281	1827.2	1826.8	1826.8
TTOW-2-2	21166	38895	4577.3	0.0171	0.1757	0.0391	1786	1785.9	1785.7
LLOW-1-1	30253	39648	5378.3	0.0205	0.2012	0.0327	2045.4	2045	2045.3
LLOW-1-2	22085	39822	5526	0.023	0.1986	0.0471	2098.9	2098.8	2099
LLOW-2-1	29774	39169	4914.8	0.0163	0.1933	0.0293	1895.6	1895	1895.2
LLOW-2-2	21447	39189	4911.5	0.0174	0.1887	0.0413	1899.2	1898.7	1898.8

Table 4.9 Elastic Properties for Woven Composites at 2273°K

RUC Type	E_1 N/mm^2	E_2 N/mm^2	E_3 N/mm^2	v_{12}	v_{23}	N_{31}	G_{12} N/mm^2	G_{23} N/mm^2	G_{31} N/mm^2
TTOW-1-1	28593	37426	5159.3	0.022	0.1884	0.0331	1976.4	1976.4	1976.4
TTOW-1-2	20677	37351	5051.9	0.0244	0.1866	0.0471	1918.9	1919.6	1919.4
TTOW-2-1	28106	36942	4698.9	0.017	0.1824	0.0295	1826.9	1826.3	1826.3
TTOW-2-2	20171	36853	4579.8	0.018	0.1751	0.041	1785.6	1785.5	1785.2
LLOW-1-1	28764	37605	5381.1	0.0216	0.2005	0.0343	2044.9	2044.3	2044.7
LLOW-1-2	21094	37779	5531.1	0.0242	0.1977	0.0492	2098.3	2098.1	2098.4
LLOW-2-1	28285	37128	4914	0.0172	0.1929	0.0308	1895.4	1894.3	1894.6
LLOW-2-2	20457	37147	4911.9	0.0183	0.1881	0.0432	1898.8	1898.1	1898.3

Table 4.10 Elastic Properties for Woven Composites at 2773°K

RUC Type	E_1 N/mm^2	E_2 N/mm^2	E_3 N/mm^2	v_{12}	v_{23}	v_{31}	G_{12} N/mm^2	G_{23} N/mm^2	G_{31} N/mm^2
TTOW-1-1	27845	36405	5155.5	0.0226	0.1883	0.034	1976.2	1976.3	1976.4
TTOW-1-2	20178	36329	5047.9	0.0251	0.1863	0.0482	1918.7	1919.6	1919.4
TTOW-2-1	27359	35922	4695.8	0.0175	0.1823	0.0303	1826.8	1826.2	1829.3
TTOW-2-2	19673	35832	4576.7	0.0185	0.1749	0.0419	1785.5	1785.4	1785.2
LLOW-1-1	28017	36584	5377	0.0222	0.2003	0.0352	2044.8	2044.2	2044.7
LLOW-1-2	20595	36757	5526.5	0.0248	0.1975	0.0503	2098.1	2098	2098.4
LLOW-2-1	27538	36107	4910.6	0.0177	0.1927	0.0316	1895.3	1894.2	1894.6
LLOW-2-2	19958	36126	4908.3	0.0188	0.1879	0.0442	1898.7	1898	1898.3

The variation of Young's moduli (E_1, E_2, E_3) with respect to temperature for the woven composites are shown in fig 4.22 to 4.24. It can be seen from the graphs that, LLOW-1-1 gives the maximum E_1; it reduces to the level of TTOW-1-1 for E_2, but gives better E_3. For LLOW the warp weaver's bend across each filler resulting in increase of E_1 and E_2 and subsequently E_3 gets reduced. It can be seen that TTOW-2-1 and LLOW-2-2 gives the lowest E_1, where as LLOW-1-2 gives the maximum E_2 and E_3 due to the contribution of warp weavers in that direction. TTOW-2-2 gives the lowest E_3 among the configurations, but they have lower magnitudes of E_2 also.

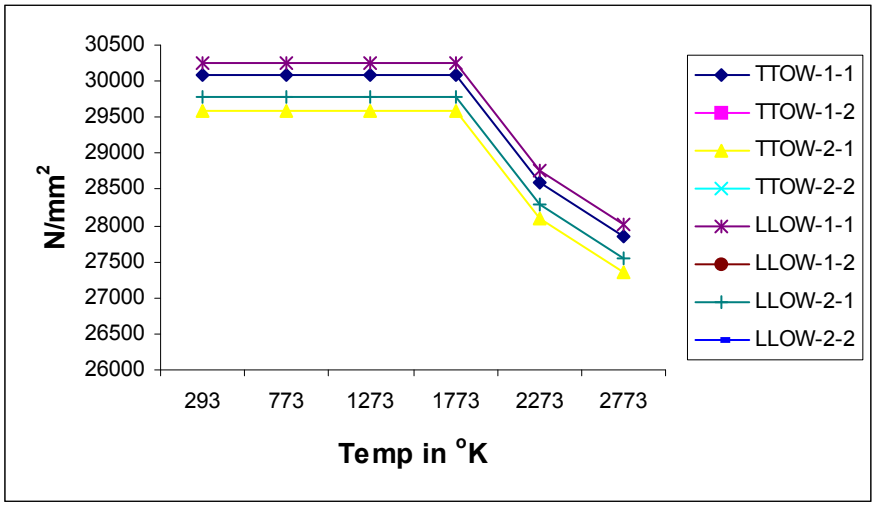

Fig 4.22 E_1 for Woven Composites

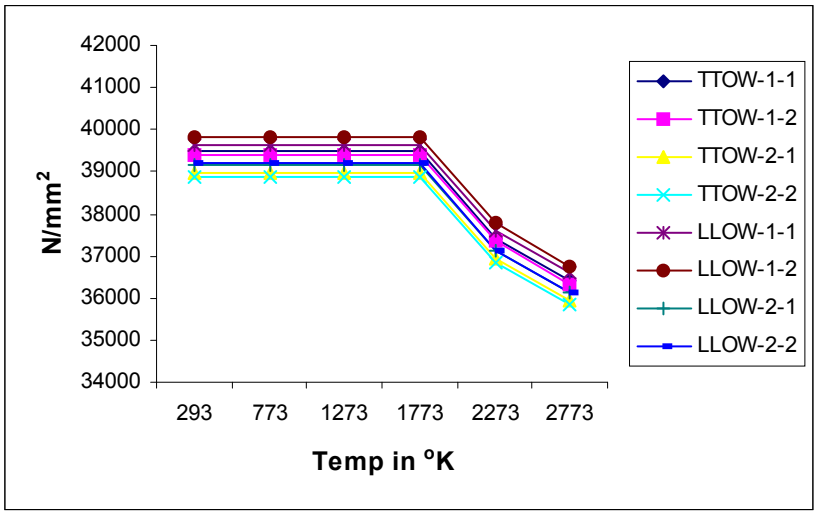

Fig 4.23 E_2 for Woven Composites

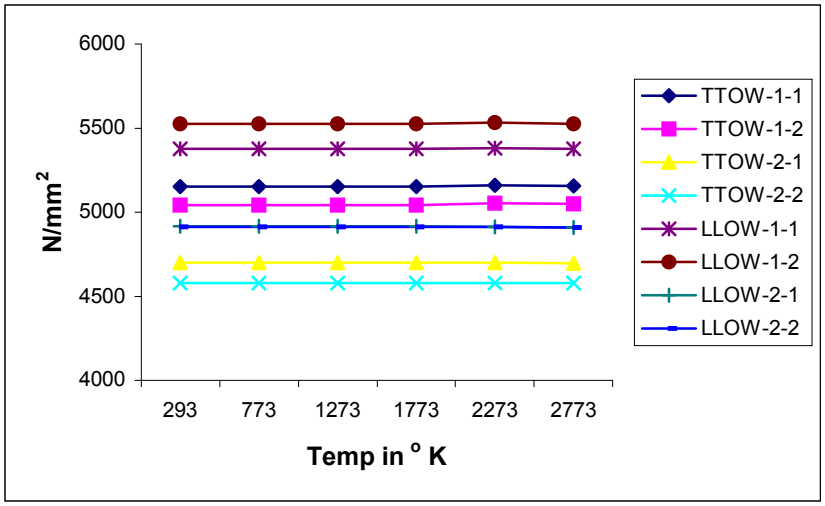

Fig 4.24 E_3 for Woven Composites

The variation of Poisson's ratio for woven composites is shown in fig 4.25 to 4.27. It can be noticed that the Poisson's ratio v_{12} and v_{31} increase after 1773°K and v_{23} remains constant for woven composites.

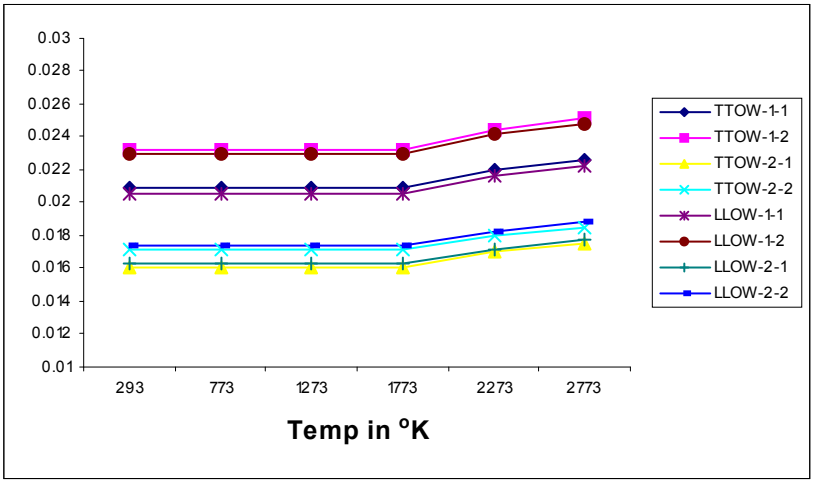

Fig 4.25 v_{12} for Woven Composites

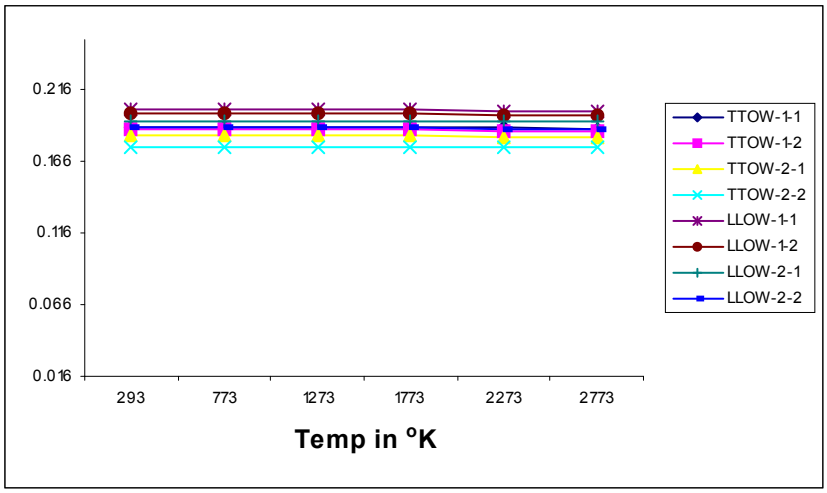

Fig 4.26 v_{23} for Woven Composites

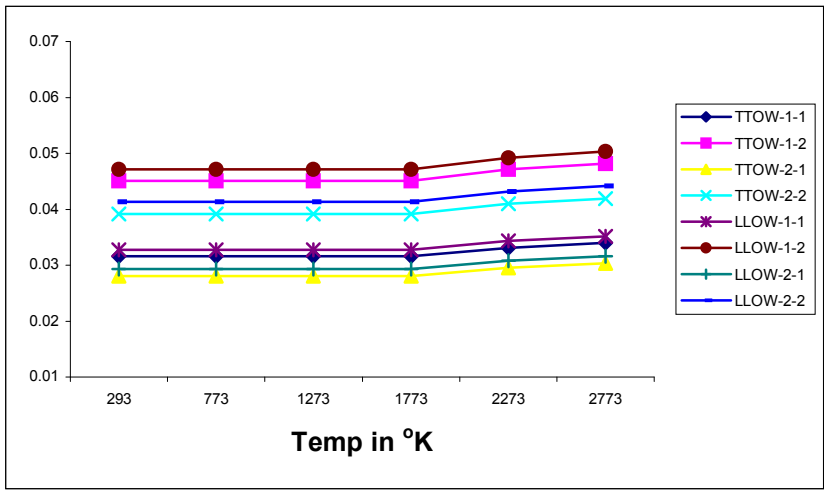

Fig 4.27 v_{31} for Woven Composites

The variation of shear modulus properties for woven composites is shown in fig 4.28 to 4.30. The variation of shear moduli (G_{12}, G_{23}, G_{31}) with temperature is identical for TTOW and the value reduces consistently for TTOW-1-1 to TTOW-2-2. From the above figures it can be noted that the values of all the shear moduli are fairly close to one other in both the cases of TTOW and LLOW.

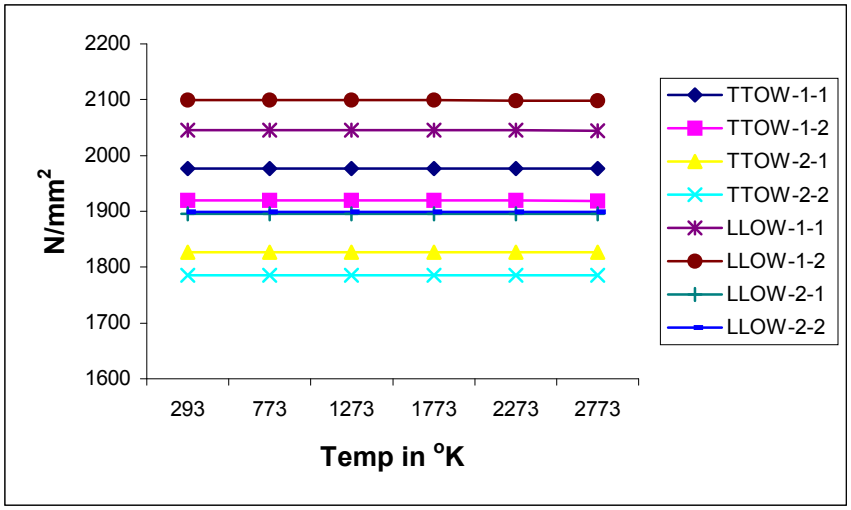

Fig 4.28 G_{12} for Woven Composites

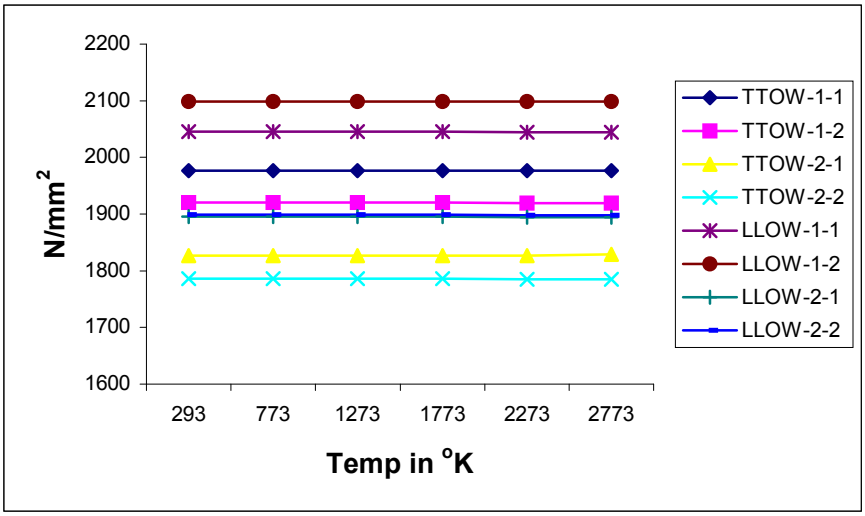

Fig 4.29 G_{31} for Woven Composites

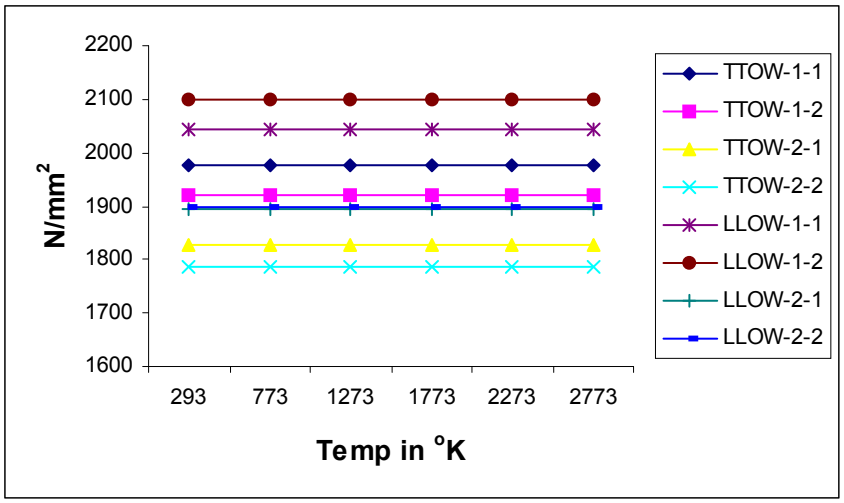

Fig 4.30 G_{23} for Woven Composites

4.4.3.2 Thermal properties of 3D woven composites

The thermal properties for the 3D orthogonal woven composites have been derived for the 8 different preforms for various temperatures and are shown in tables 4.11 to 4.16.

Table 4.11 Coefficient of Thermal Expansion for Woven Composites at 293 ^{o}K

RUC Type	α_1 /^{o}K	α_2 /^{o}K	α_3 /^{o}K
TTOW-1-1	1.47E-08	-2.24E-07	6.02E-06
TTOW-1-2	5.74E-07	-2.00E-07	5.52E-06
TTOW-2-1	-1.79E-07	-3.73E-07	6.51E-06
TTOW-2-2	2.45E-07	-3.81E-07	6.07E-06
LLOW-1-1	-5.88E-08	-1.97E-07	6.51E-06
LLOW-1-2	4.53E-07	-1.47E-07	6.08E-06
LLOW-2-1	-2.16E-07	-3.39E-07	6.85E-06
LLOW-2-2	1.77E-07	-3.31E-07	6.51E-06

Table 4.12 Coefficient of Thermal Expansion for Woven Composites at 773 ^{o}K

RUC Type	α_1 /^{o}K	α_2 /^{o}K	α_3 /^{o}K
TTOW-1-1	2.55E-06	2.40E-06	9.20E-06
TTOW-1-2	3.23E-06	2.46E-06	8.82E-06
TTOW-2-1	2.29E-06	2.21E-06	9.62E-06
TTOW-2-2	2.79E-06	2.22E-06	9.24E-06
LLOW-1-1	2.46E-06	2.44E-06	9.84E-06
LLOW-1-2	3.08E-06	2.52E-06	9.51E-06
LLOW-2-1	2.25E-06	2.25E-06	1.01E-05
LLOW-2-2	2.71E-06	2.28E-06	9.83E-06

Table 4.13 Coefficient of Thermal Expansion for Woven Composites at 1273 ^{o}K

RUC Type	α_1 /^{o}K	α_2 /^{o}K	α_3 /^{o}K
TTOW-1-1	3.84E-06	3.78E-06	1.15E-05
TTOW-1-2	4.63E-06	3.85E-06	1.11E-05
TTOW-2-1	3.54E-06	3.55E-06	1.19E-05
TTOW-2-2	4.11E-06	3.57E-06	1.15E-05
LLOW-1-1	3.74E-06	3.82E-06	1.22E-05
LLOW-1-2	4.45E-06	3.92E-06	1.19E-05
LLOW-2-1	3.49E-06	3.61E-06	1.25E-05
LLOW-2-2	4.02E-06	3.64E-06	1.22E-05

Table 4.14 Coefficient of Thermal Expansion for Woven Composites at 1773 ^{o}K

RUC Type	α_1 /^{o}K	α_2 /^{o}K	α_3 /^{o}K
TTOW-1-1	4.82E-06	4.79E-06	1.38E-05
TTOW-1-2	5.76E-06	4.87E-06	1.34E-05
TTOW-2-1	4.46E-06	4.52E-06	1.43E-05
TTOW-2-2	5.14E-06	4.54E-06	1.38E-05
LLOW-1-1	4.70E-06	4.84E-06	1.47E-05
LLOW-1-2	5.55E-06	4.95E-06	1.43E-05
LLOW-2-1	4.41E-06	4.58E-06	1.50E-05
LLOW-2-2	5.03E-06	4.62E-06	1.46E-05

Table 4.15 Coefficient of Thermal Expansion for Woven Composites at 2273 ^{o}K

RUC Type	α_1 /^{o}K	α_2 /^{o}K	α_3 /^{o}K
TTOW-1-1	6.32E-06	6.37E-06	1.61E-05
TTOW-1-2	7.41E-06	6.48E-06	1.56E-05
TTOW-2-1	5.90E-06	6.06E-06	1.66E-05
TTOW-2-2	6.68E-06	6.07E-06	1.61E-05
LLOW-1-1	6.18E-06	6.43E-06	1.71E-05
LLOW-1-2	7.16E-06	6.57E-06	1.67E-05
LLOW-2-1	5.84E-06	6.13E-06	1.74E-05
LLOW-2-2	6.55E-06	6.18E-06	1.70E-05

Table 4.16 Coefficient of Thermal Expansion for Woven Composites at 2773 ^{o}K

RUC Type	α_1 /^{o}K	α_2 /^{o}K	α_3 /^{o}K
TTOW-1-1	6.78E-06	6.90E-06	1.61E-05
TTOW-1-2	7.86E-06	7.01E-06	1.57E-05
TTOW-2-1	6.36E-06	6.59E-06	1.66E-05
TTOW-2-2	7.12E-06	6.60E-06	1.61E-05
LLOW-1-1	6.65E-06	6.96E-06	1.71E-05
LLOW-1-2	7.61E-06	7.09E-06	1.67E-05
LLOW-2-1	6.30E-06	6.66E-06	1.73E-05
LLOW-2-2	7.01E-06	6.71E-06	1.70E-05

The variation of thermal parameters, CTE (α_1, α_2, α_3) of the woven composites are shown in fig 4.31 to 4.33.

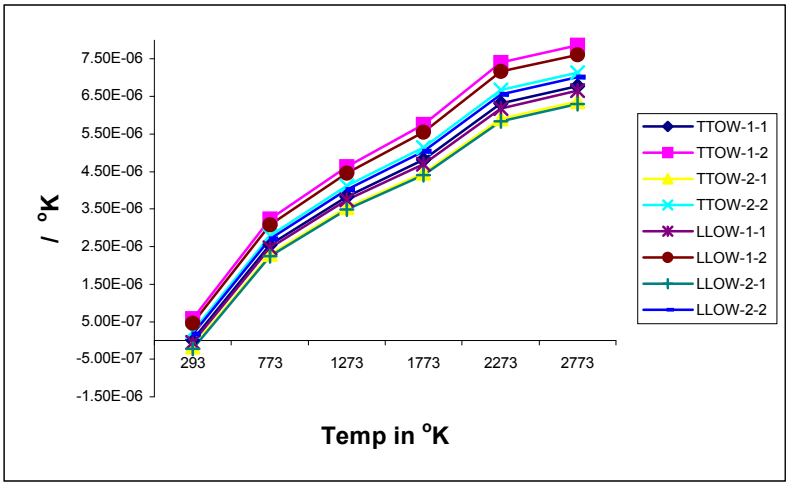

Fig 4.31 α_1 for Woven Composites

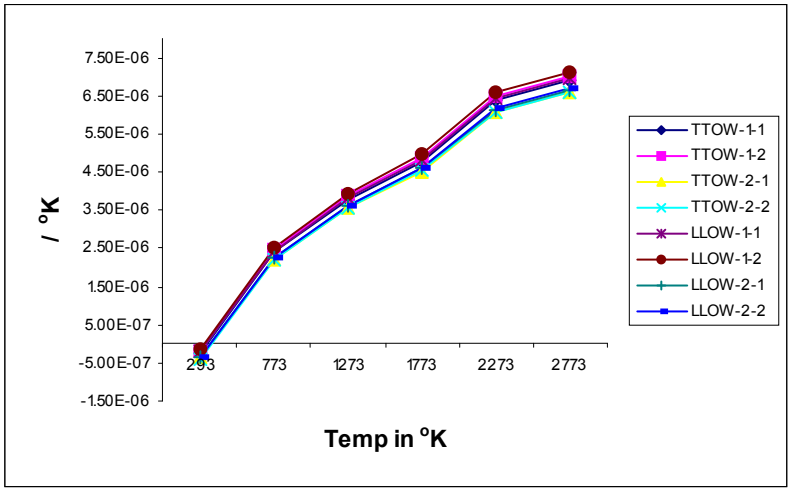

Fig 4.32 α_2 for Woven Composites

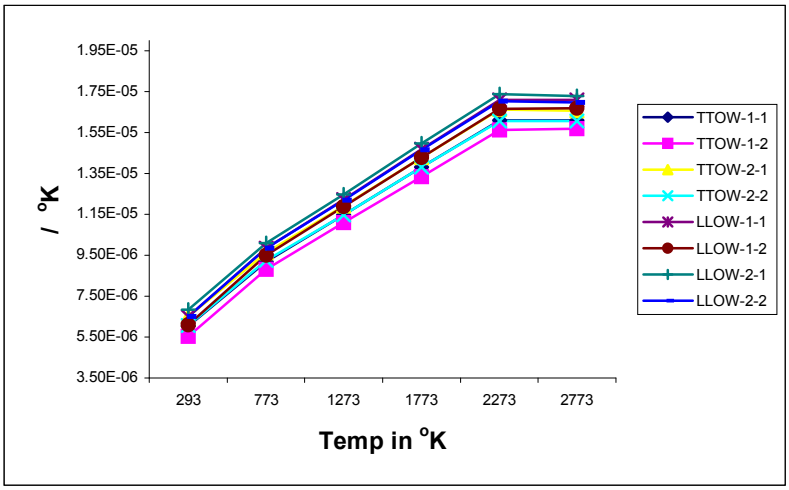

Fig 4.33 α_3 for Woven Composites

For woven composites irrespective of fibre architecture variations, CTE almost remains same. The thermal conductivity properties for the 3D orthogonal woven composites have been derived for the various preforms for various temperatures and are depicted in tables 4.17 to 4.22.

Table 4.17 Thermal Conductivity (W/m^{o}K) for Woven Composites at 293 ^{o}K

RUC Type	Kx	K_y	Kz
TTOW-1-1	9.87	9.96	10.12
TTOW-1-2	12.33	5.41	5.52
TTOW-2-1	8.96	8.63	8.49
TTOW-2-2	8.45	8.51	8.47
LLOW-1-1	10.63	15.69	10.03
LLOW-1-2	13.81	5.62	6.54
LLOW-2-1	9.79	8.89	8.57
LLOW-2-2	9.37	8.86	10.08

Table 4.18 Thermal Conductivity (W/m^{o}K) for Woven Composites at 773 ^{o}K

RUC Type	Kx	K_y	Kz
TTOW-1-1	12.31	12.42	12.62
TTOW-1-2	15.41	6.77	6.9
TTOW-2-1	11.18	10.77	10.64
TTOW-2-2	10.56	10.62	10.59
LLOW-1-1	13.22	19.55	12.51
LLOW-1-2	17.21	7.02	8.18
LLOW-2-1	12.19	11.1	10.74
LLOW-2-2	11.68	11.06	12.61

Table 4.19 Thermal Conductivity (W/m^{o}K) for Woven Composites at 1273 ^{o}K

RUC Type	Kx	K_y	Kz
TTOW-1-1	14.91	15.05	15.28
TTOW-1-2	18.71	8.22	8.37
TTOW-2-1	13.55	13.06	12.93
TTOW-2-2	12.82	12.88	12.86
LLOW-1-1	15.97	23.65	15.16
LLOW-1-2	20.84	8.53	9.94
LLOW-2-1	14.73	13.46	13.05
LLOW-2-2	14.15	13.41	15.33

Table 4.20 Thermal Conductivity (W/m^{o}K) for Woven Composites at 1773 ^{o}K

RUC Type	Kx	K_y	Kz
TTOW-1-1	17.54	17.7	17.98
TTOW-1-2	22.03	9.69	9.85
TTOW-2-1	15.94	15.37	15.23
TTOW-2-2	15.1	15.15	15.15
LLOW-1-1	18.78	27.82	17.84
LLOW-1-2	24.52	10.05	11.71
LLOW-2-1	17.32	15.84	15.38
LLOW-2-2	16.64	15.78	18.06

Table 4.21 Thermal Conductivity (W/m^{o}K) for Woven Composites at 2273 ^{o}K

RUC Type	Kx	K_y	Kz
TTOW-1-1	19.98	20.16	20.48
TTOW-1-2	25.11	11.05	11.23
TTOW-2-1	18.16	17.51	17.36
TTOW-2-2	17.21	17.27	17.27
LLOW-1-1	21.37	31.67	20.33
LLOW-1-2	27.92	11.46	13.35
LLOW-2-1	19.72	18.05	17.54
LLOW-2-2	18.96	17.98	20.6

Table 4.22 Thermal Conductivity (W/m^{o}K) for Woven Composites at 2773 ^{o}K

RUC Type	Kx	K_y	Kz
TTOW-1-1	22	22.2	22.54
TTOW-1-2	27.68	12.18	12.37
TTOW-2-1	20	19.28	19.15
TTOW-2-2	18.96	19.02	19.04
LLOW-1-1	23.49	34.85	22.38
LLOW-1-2	30.73	12.63	14.72
LLOW-2-1	21.68	19.87	19.35
LLOW-2-2	20.86	19.8	22.72

The variation of thermal conductivity parameters (K_1, K_2, K_3) are shown in fig 4.34 to 4.36 for woven composites. It can be seen from the graphs that TTOW-1-2 and LLOW-1-2 gives maximum conductivity along stuffer direction whereas TTOW-1-1 and LLOW-1-1 shows maximum conductivity along filler direction. It is interesting to note that TTOW-1-1, LLOW-1-1 and LLOW-2-2 shows almost same conductivity along warp direction (fig 4.36). The same phenomenon is observed for TTOW-2-1, TTOW-2-2 and LLOW-2-1 also.

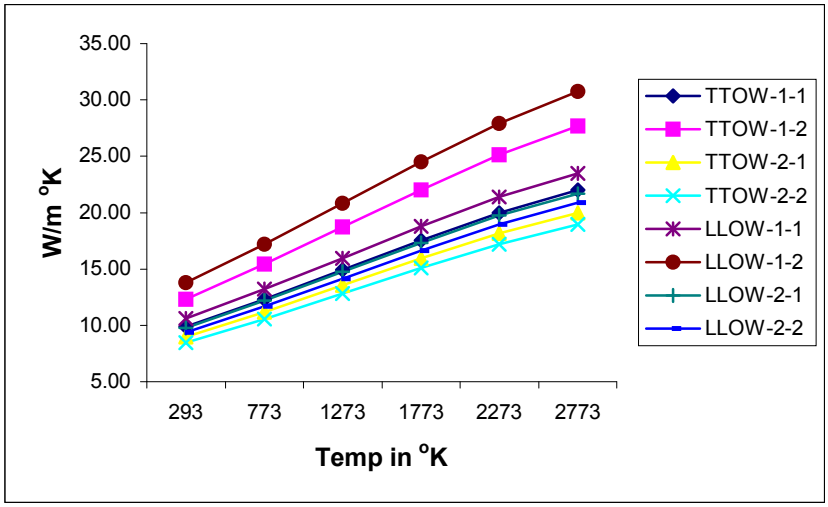

Fig 4.34 K_1 for Woven Composites

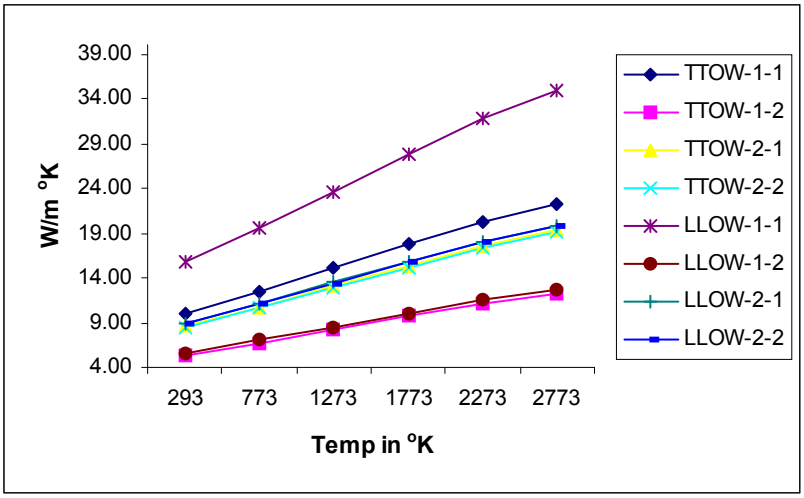

Fig 4.35 K_2 for Woven Composites

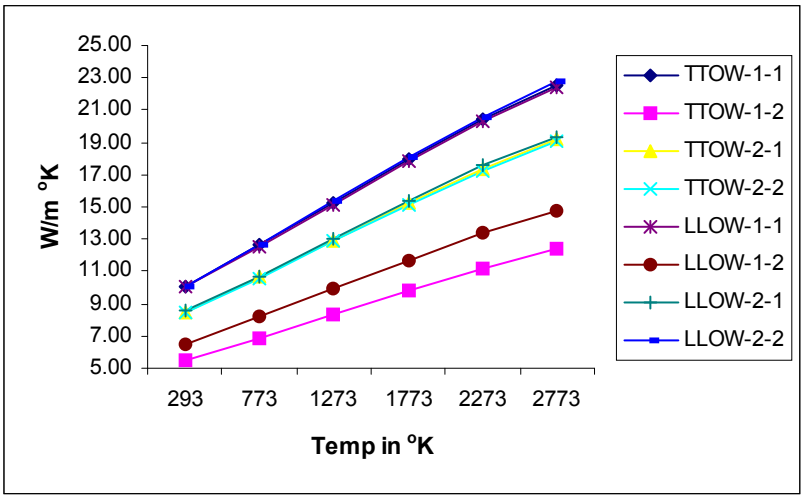

Fig 4.36 K_3 for Woven Composites

4.4.3.3 Strength properties of 3D woven composites

The strength properties have been generated for 3D woven composites for various RUC configurations for various temperatures and are shown in table 4.23 to 4.26. The variation of strength properties for woven composites is shown in fig 4.37 to 4.42.

Table 4.23 Strength Properties for Woven Composites at 293 °K, 773°K, 1273°K

RUC Type	σ_1	σ_2	$\sigma 3$	τ_{12}	τ_{23}	τ_{31}
	N/mm^2	N/mm^2	N/mm^2	N/mm^2	N/mm^2	N/mm^2
TTOW-1-1	66.7077	79.5077	17.6	5.6615	5.9077	19.2
TTOW-1-2	44.6359	53.0051	8.5333	5.0872	6.0718	8.5333
TTOW-2-1	66.7077	79.5077	8.8	5.6615	5.7846	9.6
TTOW-2-2	44.6359	79.5077	28.8	3.9385	6.0308	6.9333
LLOW-1-1	67.9385	79.5077	17.6	11.5692	6.4	19.2
LLOW-1-2	44.1436	53.0051	8.5333	6.4	5.5795	11.378
LLOW-2-1	67.939	79.508	9.6	11.569	6.0308	9.6
LLOW-2-2	45.621	79.508	6.4	5.4154	6.0308	10.667

Table 4.24 Strength Properties for Woven Composites at 1773 ^{o}K

RUC Type	σ_1	σ_2	$\sigma 3$	τ_{12}	τ_{23}	τ_{31}
	N/mm^2	N/mm^2	N/mm^2	N/mm^2	N/mm^2	N/mm^2
TTOW-1-1	77.7846	92.8	17.6	7.1385	7.3846	19.2
TTOW-1-2	52.1846	61.8667	8.5333	6.2359	7.5487	8.5333
TTOW-2-1	77.7846	92.8	8.8	6.8923	7.1385	9.6
TTOW-2-2	52.1846	92.8	33.6	4.9231	7.3846	7.4667
LLOW-1-1	79.2615	92.8	17.6	14.5231	7.6308	19.2
LLOW-1-2	51.5282	61.8667	8.5333	7.8769	6.8923	13.5111
LLOW-2-1	79.2615	92.8	9.6	14.5231	7.3846	9.6
LLOW-2-2	53.169	92.8	6.4	6.5641	7.3846	12.8

Table 4.25 Strength Properties for Woven Composites at 2273 ^{o}K

RUC Type	σ_1	σ_2	$\sigma 3$	τ_{12}	τ_{23}	τ_{31}
	N/mm^2	N/mm^2	N/mm^2	N/mm^2	N/mm^2	N/mm^2
TTOW-1-1	72.1231	86.1538	17.6	8.3692	8.6154	19.2
TTOW-1-2	48.4103	57.4359	8.5333	7.3846	9.0256	8.5333
TTOW-2-1	72.1231	86.1538	8.8	8.1231	8.6154	9.6
TTOW-2-2	48.4103	86.1538	31.4667	5.9077	8.8615	7.4667
LLOW-1-1	73.6	86.1538	17.6	16	8.1231	19.2
LLOW-1-2	47.9179	57.4359	8.5333	9.5179	7.8769	11.3778
LLOW-2-1	73.6	86.154	9.6	16	8.8615	9.6
LLOW-2-2	49.559	86.154	6.4	7.8769	8.8615	10.667

Table 4.26 Strength Properties for Woven Composites at 2773 ^{o}K

RUC Type	σ_1	σ_2	$\sigma 3$	τ_{12}	τ_{23}	τ_{31}
	N/mm^2	N/mm^2	N/mm^2	N/mm^2	N/mm^2	N/mm^2
TTOW-1-1	66.7077	79.5077	17.6	8.3692	8.6154	19.2
TTOW-1-2	44.8	53.0051	8.5333	7.3846	9.0256	8.5333
TTOW-2-1	66.7077	79.5077	8.8	8.1231	8.6154	9.6
TTOW-2-2	44.8	79.5077	28.8	5.9077	8.8615	7.4667
LLOW-1-1	68.1846	79.5077	17.6	16	8.1231	19.2
LLOW-1-2	44.3077	53.0051	8.5333	9.5179	7.8769	11.3778
LLOW-2-1	68.185	79.508	9.6	16	8.8615	9.6
LLOW-2-2	45.785	79.508	6.4	7.8769	8.8615	10.667

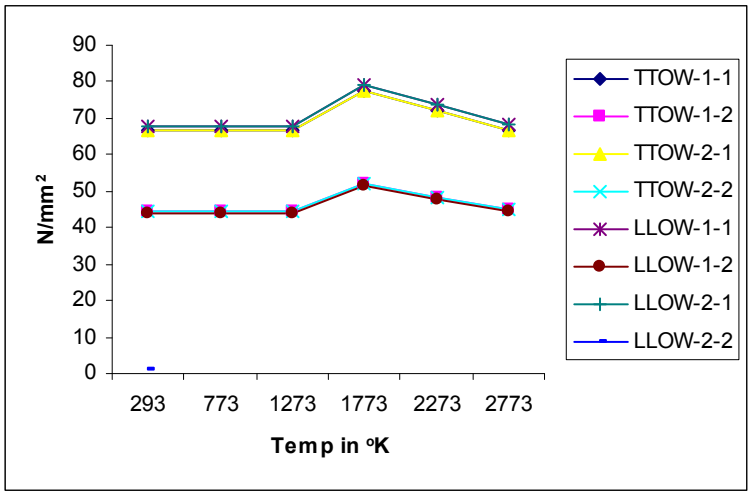

Fig 4.37 σ_1 for Woven Composites

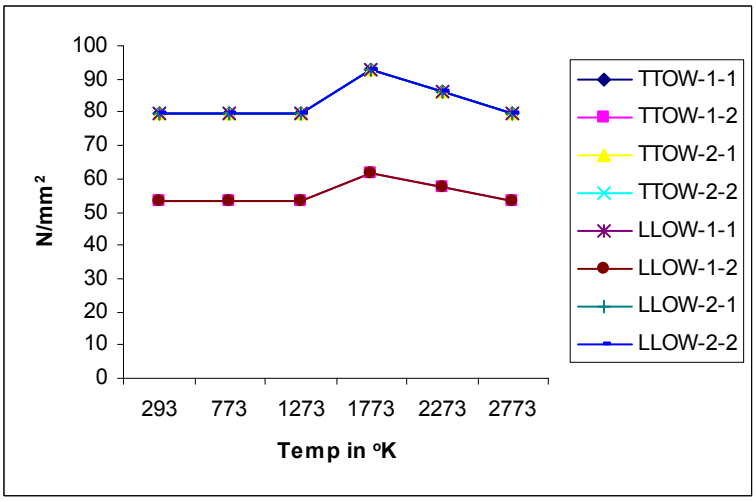

Fig 4.38 σ_2 for Woven Composites

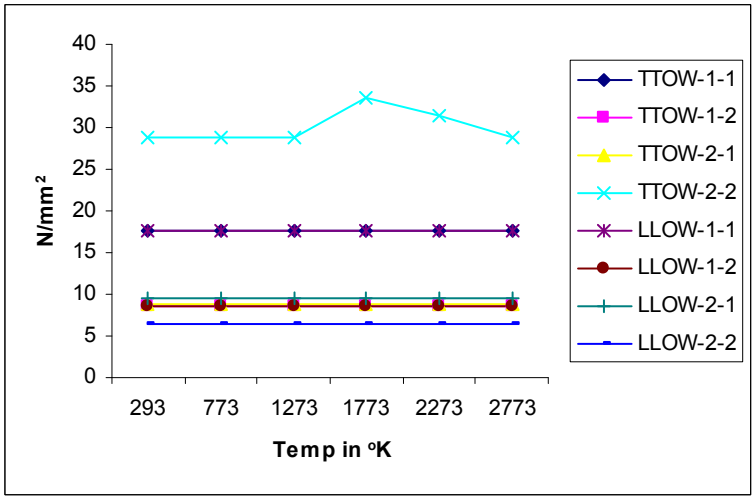

Fig 4.39 σ_3 for Woven Composites

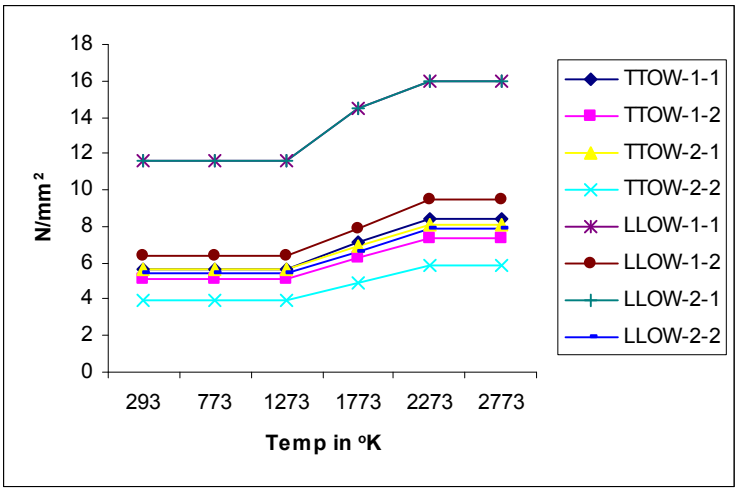

Fig 4.40 τ_{12} for Woven Composites

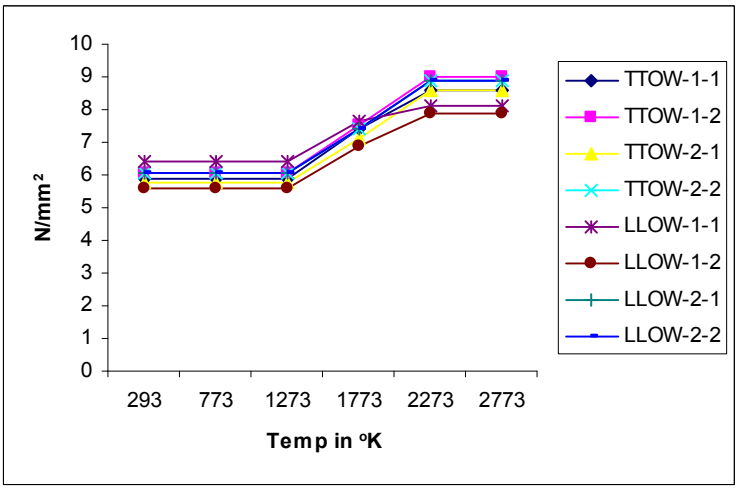

Fig 4.41 τ_{23} for Woven Composites

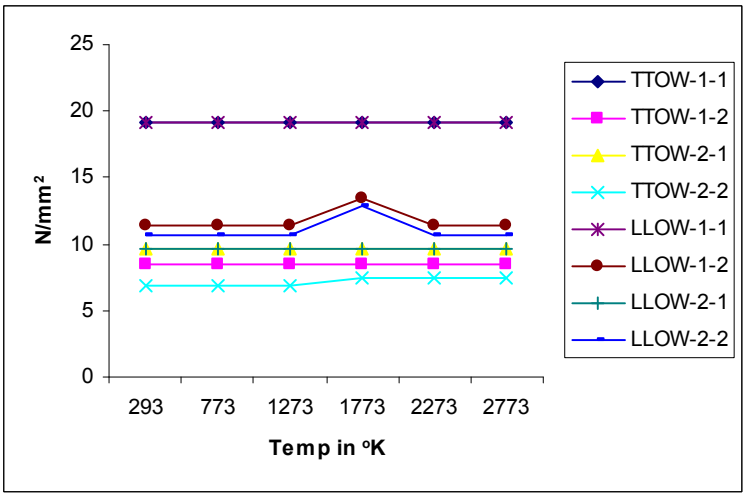

Fig 4.42 τ_{31} for Woven Composites

Eventhough σ_1 and σ_2 (inplane) are higher in magnitude for LLOW-2-1 and TTOW-2-1; σ_3 (thickness direction) is higher for TTOW-2-2. It is quite noticeable that all the stress components except σ_3 follow the same trend (fig 4.39). The failure is initiated at fibre level for TTOW-2-2 whereas for other preforms failures are initiated at matrix level. Similar stress distribution has been found for the shear stresses.

4.4.4 Evaluation of high temperature properties for 3D braided composites

4.4.4.1 Elastic properties of 3D braided composites

The elastic properties for the 3D braided composites have been derived for 4-axis/5-axis for various temperature ranges and are shown in tables 4.27, 4.28 and 4.29. The variation of Young's moduli (E_1, E_2, E_3) with respect to temperature for the braided composites are shown in fig 4.43 and 4.44.

Table 4.27 Elastic Properties for Braided Composites at 293 ^oK, 773 ^oK, 1273 ^oK, 1773 ^oK

RUC Type	E_1 N/mm^2	E_2 N/mm^2	E_3 N/mm^2	ν_{12}	ν_{23}	ν_{31}	G_{12} N/mm^2	G_{23} N/mm^2	G_{31} N/mm^2
4-axis 15^o	58431	4316	4316	0.4744	0.1874	0.035	3800	1744	3800
4-axis 30^o	28022	5254	5254	0.9262	-0.0467	0.1736	7844	1738	7844
4-axis 45^o	8334	7292	7292	0.6635	-0.3474	0.5806	9464	1710	9464
5-axis 15^o	71000	4660	4660	0.4454	0.2076	0.0292	3912	1856	3912
5-axis 30^o	44741	6036.4	6036.4	0.8582	0.0411	0.1158	7987.7	1881.8	7987.7
5-axis 45^o	32700	1.09E+04	1.09E+04	0.6244	-0.0587	0.2083	9.68E+03	1.93E+03	9680

Table 4.28 Elastic Properties for Braided Composites at 2273 ^oK

RUC Type	E_1 N/mm^2	E_2 N/mm^2	E_3 N/mm^2	ν_{12}	ν_{23}	ν_{31}	G_{12} N/mm^2	G_{23} N/mm^2	G_{31} N/mm^2
4-axis 15^o	5.53E+04	4.31E+03	4.31E+03	0.4534	0.1885	0.0353	3.68E+03	1.74E+03	3.68E+03
4-axis 30^o	2.70E+04	5.20E+03	5.20E+03	0.8915	-0.0358	0.1718	7.48E+03	1.74E+03	7.48E+03
4-axis 45^o	8.23E+03	7.18E+03	7.18E+03	0.651	-0.3297	0.5685	9.01E+03	1.71E+03	9.01E+03
5-axis 15^o	6.71E+04	4.65E+03	4.65E+03	0.4262	0.2085	0.0295	3.79E+03	1.85E+03	3.79E+03
5-axis 30^o	4.27E+04	5.95E+03	5.95E+03	0.8256	0.0486	0.1151	7.63E+03	1.88E+03	7.63E+03
5-axis 45^o	3.12E+04	1.06E+04	1.06E+04	0.6115	-0.0522	0.2069	9.22E+03	1.92E+03	9.22E+03

Table 4.29 Elastic Properties for Braided Composites at 2773 °K

RUC Type	E_1 N/mm^2	E_2 N/mm^2	E_3 N/mm^2	ν_{12}	ν_{23}	ν_{31}	G_{12} N/mm^2	G_{23} N/mm^2	G_{31} N/mm^2
4-axis 15°	5.37E+04	4.30E+03	4.30E+03	0.4429	0.1891	0.0355	3.62E+03	1.74E+03	3.62E+03
4-axis 30°	2.64E+04	5.17E+03	5.17E+03	0.8738	-0.0303	0.1708	7.30E+03	1.74E+03	7.30E+03
4-axis 45°	8.17E+03	7.13E+03	7.13E+03	0.6443	-0.3205	0.5621	8.78E+03	1.71E+03	8.78E+03
5-axis 15°	6.52E+04	4.65E+03	4.65E+03	0.4166	0.2089	0.0297	3.73E+03	1.85E+03	3.73E+03
5-axis 30°	4.17E+04	5.91E+03	5.91E+03	0.809	0.0524	0.1147	7.45E+03	1.88E+03	7.45E+03
5-axis 45°	3.05E+04	1.04E+04	1.04E+04	0.6047	-0.0487	0.2062	8.99E+03	1.92E+03	8.99E+03

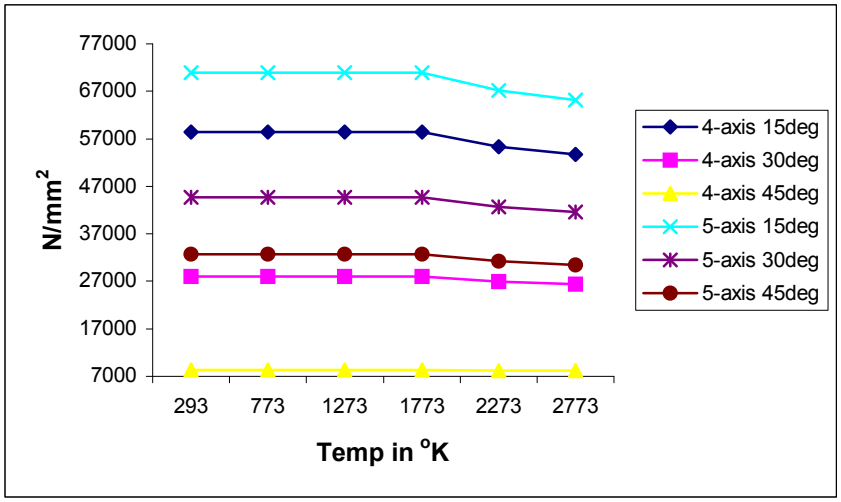

Fig 4.43 E_1 for Braided Composites

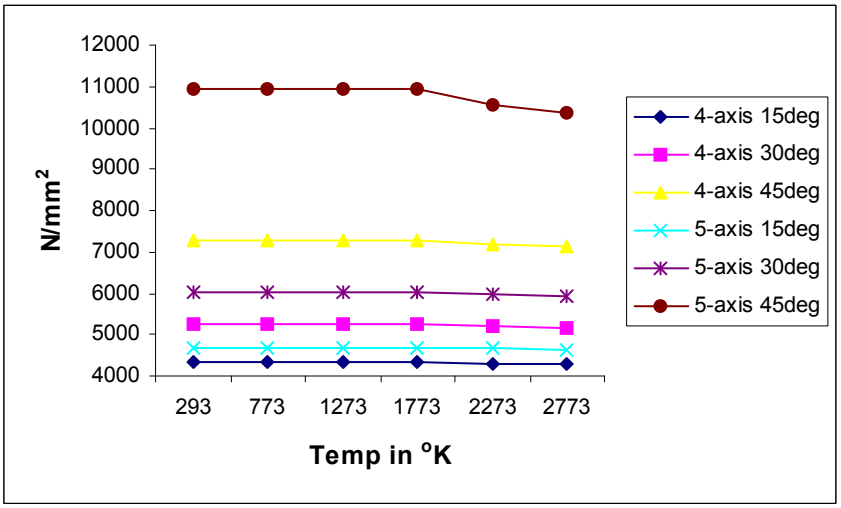

Fig 4.44 E_2 and E_3 for Braided Composites

The maximum E_1 and the lowest E_2 and E_3 are available for braided composites 5-axis 15° which is natural since this orientation coincides with that of the axis of the fibre. 4-axis 15° braided composites also exhibit the same trend. E_2 and E_3 increases with increase in theta whereas E_1 decreases with it (fig 4.43 and fig 4.44). It can be noted that the E_2 and E_3 are relatively higher for 5-axis 45° preform compared to other preforms. It may be noted that E_2 and E_3 of 4-axis 45° are nearly 2/3rd of that of the 5-axis 45°. This can be attributed to the transverse properties of the axial fibres of the 5-axis 45° preform.

The variation of Poisson's ratio for braided composites is shown in fig 4.45 to 4.47.

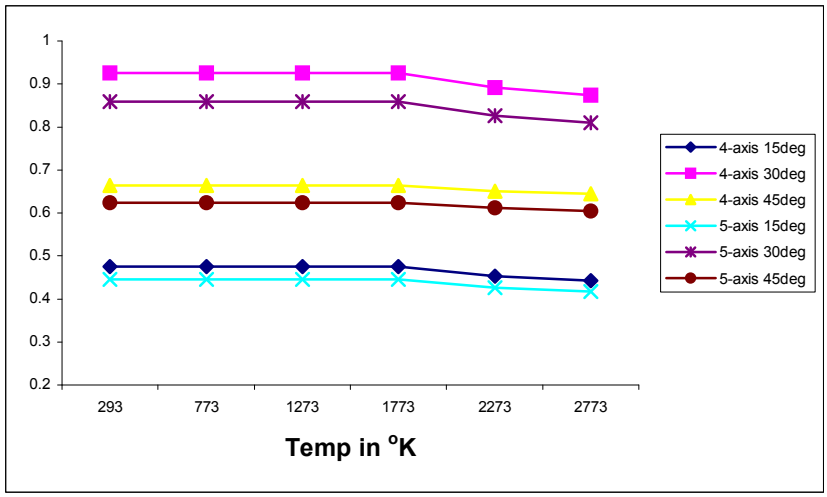

Fig 4.45 v_{12} for Braided Composites

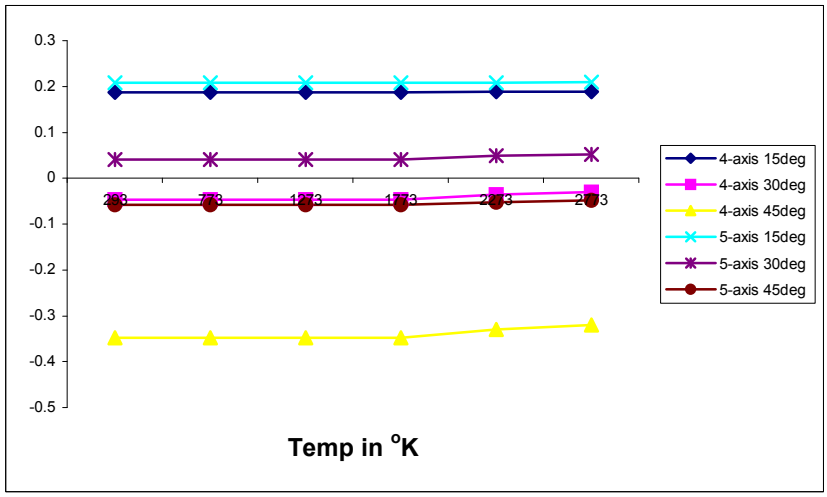

Fig 4.46 v_{23} for Braided Composites

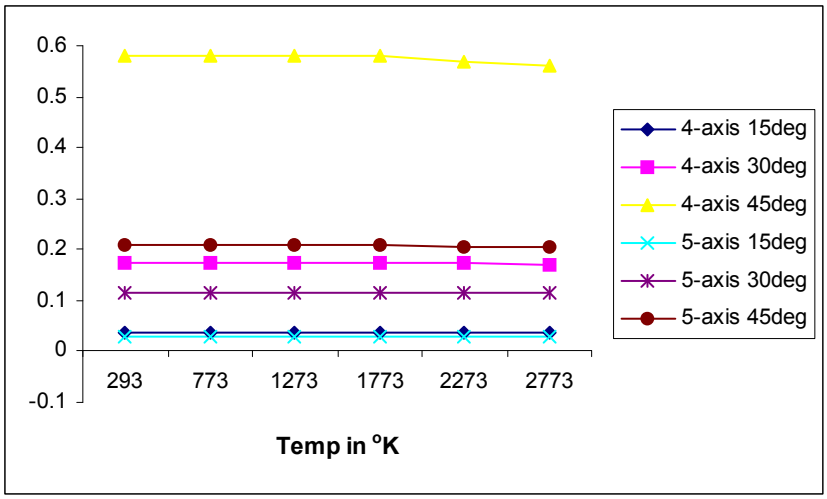

Fig 4.47 v_{31} for Braided Composites

For all the preforms of the braided composites the Poisson's ratio v_{12} remains almost constant upto 1773°K and later on upto 2773°K it shows reduction (fig 4.45). Whereas v_{23} and v_{31} almost remain constant for all the cases (fig 4.46 and 4.47).

The variation of shear moduli for braided composites is shown in fig 4.48 and 4.49.

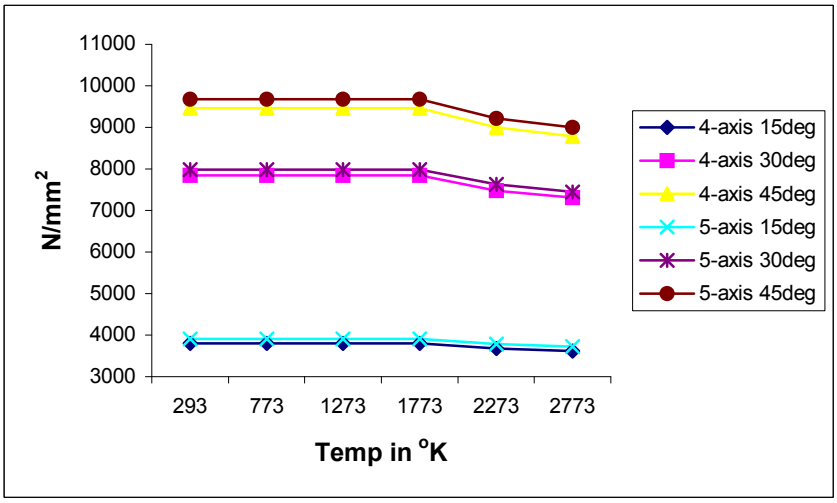

Fig 4.48 G_{31} and G_{12} for Braided Composites

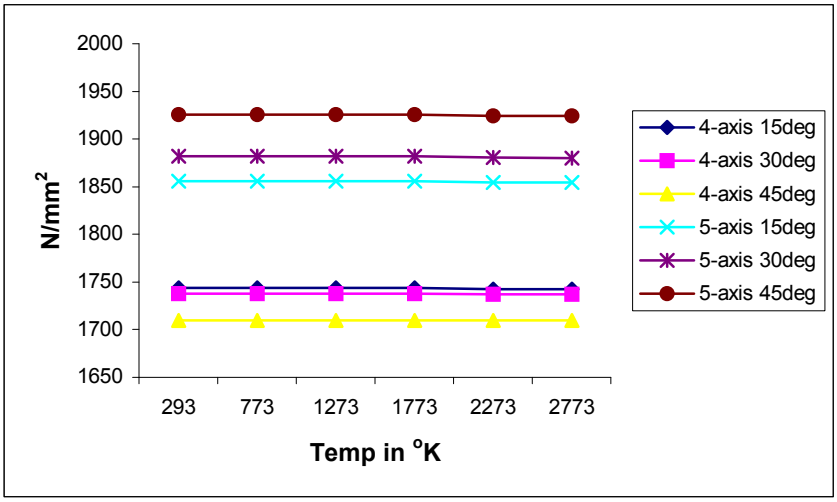

Fig 4.49 G_{23} for Braided Composites

It is evident form the relative values that G_{12} and G_{13} remains almost same for same theta irrespective of 4-axis or 5-axis (fig 4.48). The shear modulus G_{23} of 5-axis preforms increases with increase in theta whereas that of the 4-axis preform decreases with increase in theta (fig 4.49).

4.4.4.2 Thermal properties of 3D braided composites

The thermal properties for the 3D braided composites have been derived for 4-axis / 5-axis for various temperatures and are depicted in tables 4.30 to 4.35. For braided composites the transverse properties remains same (i.e; $\alpha_2 = \alpha_3$ and $K_2 = K_3$).

Table 4.30 Coefficient of Thermal Expansion and K for Braided Composites at 293 °K

RUC Type	α_1 /°K	α_2 /°K	K_1 (W/m°K)	K_2 (W/m°K)
4-axis 15°	-1.34E-06	5.80E-06	12.17	4.69E+00
4-axis 30°	-2.57E-06	5.19E-06	12.57	4.56E+00
4-axis 45°	-2.87E-06	2.64E-06	12.95	4.22E+00
5-axis 15°	-1.30E-06	6.05E-06	12.8	6.87E+00
5-axis 30°	-2.12E-06	5.13E-06	13.51	7.34E+00
5-axis 45°	-1.74E-06	2.42E-06	14.5692	8.42E+00

Table 4.31 Coefficient of Thermal Expansion and K for Braided Composites at 773 ^{o}K

RUC Type	α_1 /^{o}K	α_2 /^{o}K	K_1 (W/m^{o}K)	K_2 (W/m^{o}K)
4-axis 15^{o}	1.17E-06	9.30E-06	15.2402	5.88E+00
4-axis 30^{o}	-2.41E-07	8.61E-06	15.676	5.72E+00
4-axis 45^{o}	-5.69E-07	5.67E-06	16.0583	5.29E+00
5-axis 15^{o}	1.21E-06	9.71E-06	16.0286	8.60E+00
5-axis 30^{o}	2.63E-07	8.67E-06	16.8241	9.18E+00
5-axis 45^{o}	6.97E-07	5.54E-06	18.0225	1.05E+01

Table 4.32 Coefficient of Thermal Expansion and K for Braided Composites at 1273 ^{o}K

RUC Type	α_1 /^{o}K	α_2 /^{o}K	K_1 (W/m^{o}K)	K_2 (W/m^{o}K)
4-axis 15^{o}	2.39E-06	1.16E-05	18.5447	7.17E+00
4-axis 30^{o}	8.04E-07	1.08E-05	18.9977	6.97E+00
4-axis 45^{o}	4.37E-07	7.47E-06	19.3774	6.45E+00
5-axis 15^{o}	2.44E-06	1.21E-05	19.5002	1.05E+01
5-axis 30^{o}	1.37E-06	1.09E-05	20.3712	1.12E+01
5-axis 45^{o}	1.86E-06	7.37E-06	21.6982	1.27E+01

Table 4.33 Coefficient of Thermal Expansion and K for Braided Composites at 1773 ^{o}K

RUC Type	α_1 /^{o}K	α_2 /^{o}K	K_1 (W/m^{o}K)	K_2 (W/m^{o}K)
4-axis 15^{o}	3.17E-06	1.39E-05	21.8598	8.46E+00
4-axis 30^{o}	1.31E-06	1.30E-05	22.3583	8.23E+00
4-axis 45^{o}	8.79E-07	9.11E-06	22.7665	7.61E+00
5-axis 15^{o}	3.22E-06	1.45E-05	22.9844	1.23E+01
5-axis 30^{o}	1.96E-06	1.32E-05	23.9665	1.32E+01
5-axis 45^{o}	2.54E-06	9.01E-06	25.4703	1.50E+01

Table 4.34 Coefficient of Thermal Expansion and K for Braided Composites at 2273 ^{o}K

RUC Type	α_1 /^{o}K	α_2 /^{o}K	K_1 (W/m^{o}K)	K_2 (W/m^{o}K)
4-axis 15^{o}	4.56E-06	1.63E-05	24.9369	9.65E+00
4-axis 30^{o}	2.56E-06	1.53E-05	25.4748	9.39E+00
4-axis 45^{o}	2.16E-06	1.10E-05	25.9064	8.68E+00
5-axis 15^{o}	4.61E-06	1.70E-05	26.2182	1.41E+01
5-axis 30^{o}	3.24E-06	1.55E-05	27.2999	1.50E+01
5-axis 45^{o}	3.85E-06	1.11E-05	28.963	1.71E+01

Table 4.35 Coefficient of Thermal Expansion and K for Braided Composites at 2773 °K

RUC Type	α_1 /°K	α_2 /°K	K_1 (W/m°K)	K_2 (W/m°K)
4-axis 15°	5.15E-06	1.63E-05	27.5278	1.07E+01
4-axis 30°	3.27E-06	1.53E-05	28.0647	1.04E+01
4-axis 45°	2.93E-06	1.13E-05	28.4783	9.59E+00
5-axis 15°	5.21E-06	1.70E-05	28.9394	1.55E+01
5-axis 30°	3.90E-06	1.57E-05	30.0622	1.65E+01
5-axis 45°	4.47E-06	1.15E-05	31.8014	1.88E+01

The variation of thermal parameters, CTE (α_1, α_2, α_3) of the braided composites are shown in fig 4.50 and 4.51.

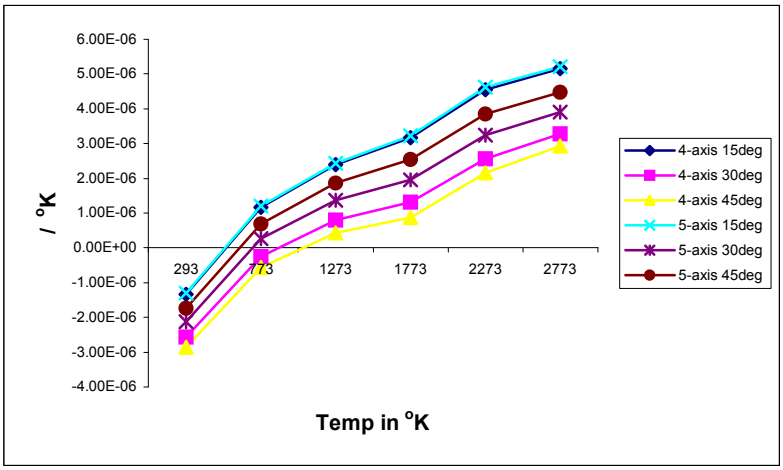

Fig 4.50 α_1 for Braided Composites

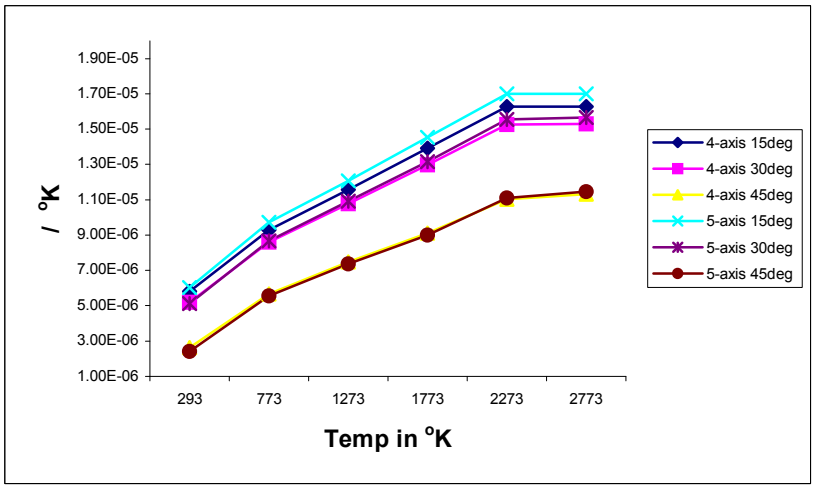

Fig 4.51 α_2 and α_3 for Braided Composites

It is evident from fig 4.50 that α_1 changes its sign from negative to positive in the range 400°K to 773°K for all the prefoms. For both the preforms of the braided composites α_1, α_2 and α_3 reduce as theta increases (fig 4.50 and 4.51). It may be noticed that for woven composites variations of CTE almost remained same in all the cases (fig 4.31 to 4.33).

The variation of thermal conductivity parameters (K_1, K_2, K_3) are shown in fig 4.52 to 4.53 for braided composites.

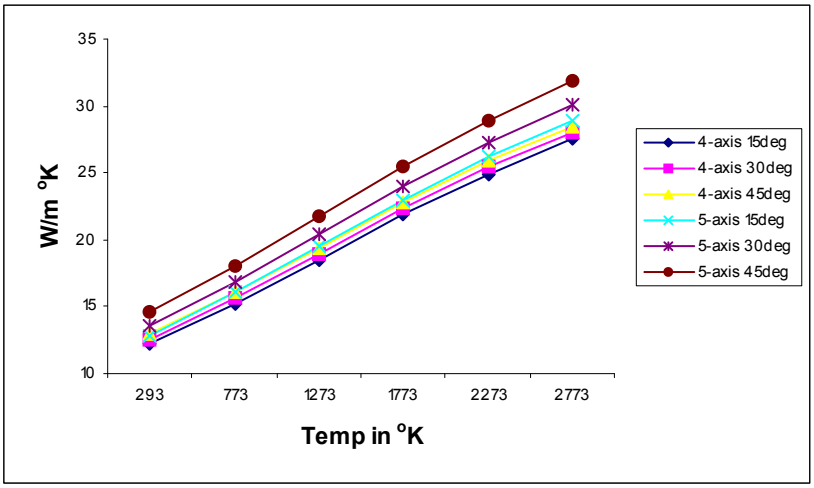

Fig 4.52 K_1 for Braided Composites

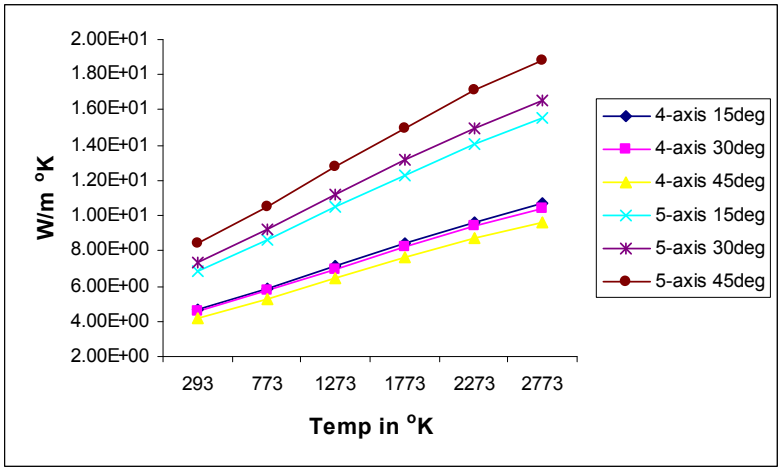

Fig 4.53 K_2 and K_3 for Braided Composites

For braided composites as theta increases conductivity increases in the longitudinal direction because of higher contribution of carbon matrix than the fibre (fig 4.52). Similar trend is seen in the transverse direction for 5-axis. Whereas conductivity remains same for all orientations of 4-axis (fig 4.53). Probably the fibre contribution is not playing a major role in defining the conductivity for 4-axis braided composites.

4.4.4.3 Strength properties of 3D braided composites

The tensile strengths and shear strengths for the 3D braided composites have been derived from codes in the respective axes for 4-axis / 5-axis for various temperature ranges and are depicted in tables 4.36 to 4.39. The variation of strength properties for braided composites is shown in fig 4.54 to 4.57.

Table 4.36 Strength Properties for Braided Composites at 293 ^oK, 773^oC, 1273^oC

RUC Type	σ_1 N/mm^2	$\sigma_2 = \sigma_3$ N/mm^2	$\tau_{12} = \tau_{13}$ N/mm^2	τ_{23} N/mm^2
4-axis 15^o	131.173	6.9444	17.3671	6.9444
4-axis 30^o	105.263	6.9252	16.7927	6.9252
4-axis 45^o	29.0659	7.9271	18.4965	7.9271
5-axis 15^o	143.519	6.9444	16.5401	6.9444
5-axis 30^o	105.263	6.9252	18.392	6.9252
5-axis 45^o	66.5874	6.8701	19.025	6.8701

Table 4.37 Strength Properties for Braided Composites at 1773 ^oK

RUC Type	σ_1 N/mm^2	$\sigma_2 = \sigma_3$ N/mm^2	$\tau_{12} = \tau_{13}$ N/mm^2	T_{23} N/mm^2
4-axis 15^o	152.778	7.716	20.6751	7.716
4-axis 30^o	122.576	8.3102	19.1917	8.3102
4-axis 45^o	34.8791	10.041	21.1389	10.041
5-axis 15^o	166.667	7.716	19.6413	7.716
5-axis 30^o	122.576	8.3102	21.9905	8.3102
5-axis 45^o	77.6853	8.4555	21.6673	8.4555

Table 4.38 Strength Properties for Braided Composites at 2273 ^oK

RUC Type	σ_1 N/mm^2	$\sigma_2 = \sigma_3$ N/mm^2	$\tau_{12} = \tau_{13}$ N/mm^2	τ_{23} N/mm^2
4-axis 15^o	141.975	9.2593	16.9536	9.2593
4-axis 30^o	114.266	10.3878	18.7919	10.3878
4-axis 45^o	29.0659	11.6264	20.0819	11.6264
5-axis 15^o	155.864	9.2593	16.1266	9.2593
5-axis 30^o	114.266	9.6953	25.1891	9.6953
5-axis 45^o	72.9291	10.041	20.6104	10.041

Table 4.39 Strength Properties for Braided Composites at 2773 °K

RUC Type	σ_1 N/mm^2	$\sigma_2 = \sigma_3$ N/mm^2	$\tau_{12} = \tau_{13}$ N/mm^2	τ_{23} N/mm^2
4-axis 15°	131.173	9.2593	16.7468	9.2593
4-axis 30°	105.263	10.3878	18.392	10.3878
4-axis 45°	29.0659	11.6264	19.5534	11.6264
5-axis 15°	143.519	9.2593	15.9198	9.2593
5-axis 30°	105.263	9.6953	23.9896	9.6953
5-axis 45°	67.6443	10.041	20.0819	10.041

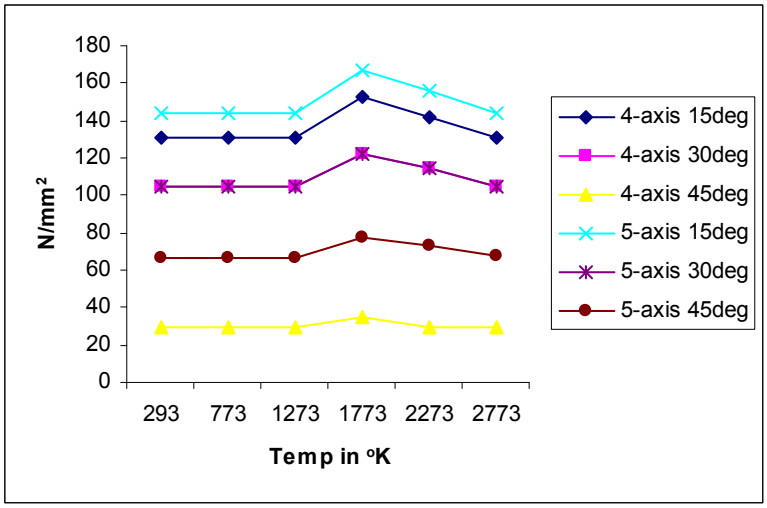

Fig 4.54 σ_1 for Braided Composites

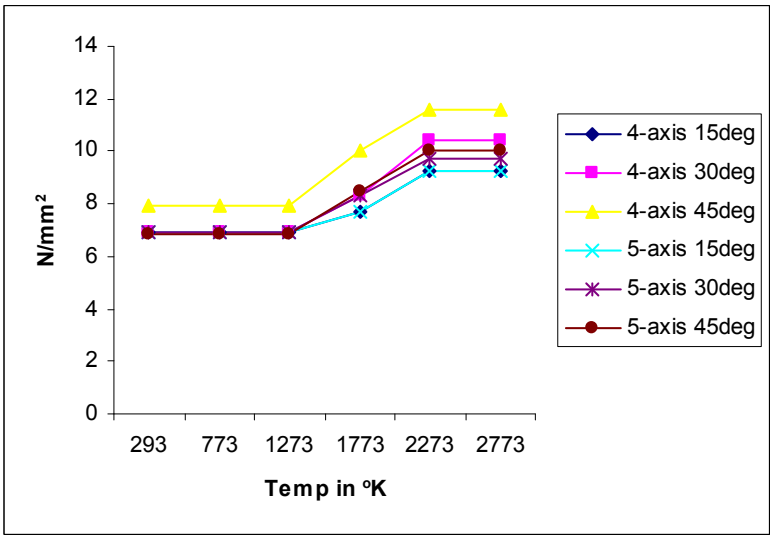

Fig 4.55 σ_2 for Braided Composites

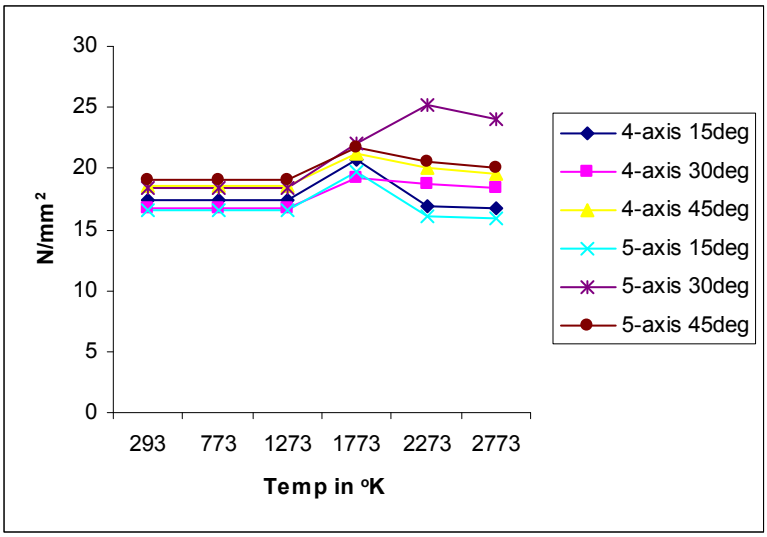

Fig 4.56 τ_{12} for Braided Composites

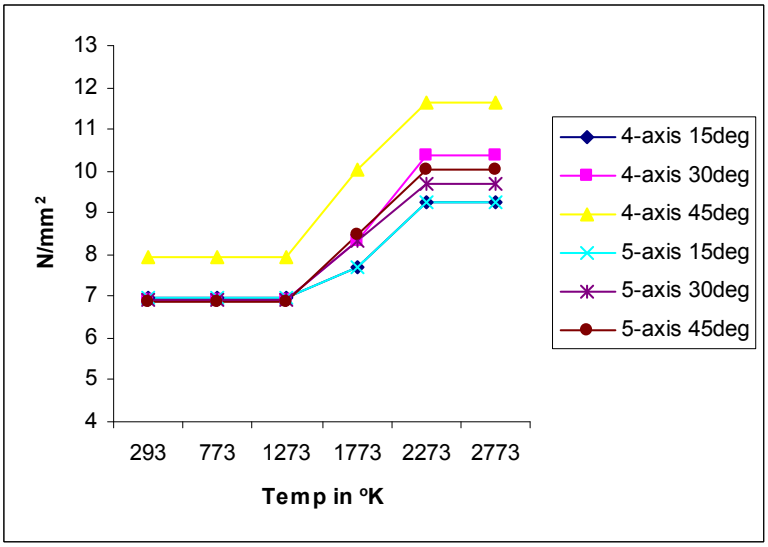

Fig 4.57 τ_{23} for Braided Composites

It can be noticed that 5-axis 15^0 gives the maximum axial capability as expected; whereas its lateral capability is less than the 45^0 inclined fibres. The shear strengths are more for the 45^0 inclined fibres than the axially oriented fibres as expected. Qualitative and quantitative description of high temperature profile (elastic, strength and thermal) of eight woven and six braided geometries of 3D composite have been described.

4.4.5 Identification of preform for hot structure application

The very purpose of the investigations on the determination and comparison of elastic, strength and thermal properties of woven and braided composites has been to identify the best preform for hot structure application. Such structure experiences both variable heat flux and variable pressure through out the mission. In structural sense it has to withstand both thermal and mechanical stresses simultaneously. The results presented in the preceding sections are critically assessed to achieve the above mentioned aim.

The properties are analytically estimated for the woven and braided composites. All the properties (elastic, strength and thermal) are estimated for 4 numbers of LLOW, 4 numbers of TTOW, 3 numbers of 4-axis and 3 numbers of 5-axis composites (total 14 numbers) at room temperature as well as at high temperatures (6 cases). Out of the 14 set of properties few have to be selected for the hot structure application and then the best preform has to be finalized for the fabrication of the Nosecap which is the hot structure of the present study.

Young's modulus, Poisson's ratio and shear modulus are the elastic properties which contribute to the stiffness capabilities of the structure. It is observed from the present study that the Poisson's ratio and shear modulus do not vary much for the material and geometric combinations of the 14 preforms studied. Hence the material and geometric combination with maximum value of Young's modulus have been preferred and recommended. The induced thermal stress will be minimum, for the material and geometric options with minimum CTE, and accordingly material and geometry combination with low CTE has been recommended. However it may be noted that the thermal stresses will be proportional to the product of Young's modulus and CTE. These may not be a compromise on higher value of Young's modulus, since that parameter contributes to stiffness which is the prime structural concern. Regarding the selection of thermal conductivity, the condition of uniform thermal gradient through thickness has been given importance. Subsequently material and geometry combination with maximum and uniform thermal conductivity have been recommended. As far as the strength criterion is concerned, the material and geometry combination with maximum strength margin has been recommended.

By the above process the following preform configurations are selected for woven composites and braided composites according to the order of preference and are shown in table 4.40 and 4.41.

Table 4.40 Order of Preference of 3D Woven Preforms

Choice	***Elastic***	***CTE***	***K***	***Strength***
1	**LLOW-1-1**	**LLOW-2-1**	**LLOW-1-1**	**LLOW-1-1**
2	**TTOW-1-1**	TTOW-2-1	**TTOW-1-1**	**LLOW-2-1**
3	**LLOW-2-1**	**LLOW-1-1**	**LLOW-2-1**	**TTOW-1-1**
4	TTOW-2-1	**TTOW-1-1**	TTOW-2-1	TTOW-2-1
5	LLOW-1-2	LLOW-2-2	LLOW-2-2	LLOW-2-2
6	TTOW-1-2	TTOW-2-2	TTOW-2-2	TTOW-2-2
7	LLOW-2-2	LLOW-1-2	LLOW-1-2	TTOW-1-2
8	TTOW-2-2	TTOW-1-2	TTOW-1-2	LLOW-1-2
Criteria	Maximum elastic values.	Minimum CTE values. The CTE values of TTOW-1-1 are fairly close to TTOW-2-1.	Maximum K values. LLOW-1-1 is having higher conductivity in Ky direction. For near uniform K values in three directions, LLOW-2-1 is also selected.	Maximum strength values.

Table 4.41 Order of Preference of 3D Braided Preforms

Choice	***Elastic***	***CTE***	***K***	***Strength***
1	**5-axis 15^o**	4-axis 45^o	**5-axis 45^o**	**5-axis 15^o**
2	**4-axis 15^o**	4-axis 30^o	5-axis 30^o	**4-axis 15^o**
3	5-axis 30^o	**4-axis 15^o**	**5-axis 15^o**	5-axis 30^o
4	**5-axis 45^o**	5-axis 30^o	4-axis 45^o	4-axis 30^o
5	4-axis 30^o	**5-axis 45^o**	4-axis 30^o	**5-axis 45^o**
6	4-axis 45^o	**5-axis 15^o**	**4-axis 15^o**	4-axis 45^o
Criteria	Maximum E value. 5-axis 45 also selected to see the effect of increase in transverse direction and reduction in axial direction (not only for elasticity but also for other properties).	Not considered since the values are small.	Maximum and uniform K value. The values are fairly close for all preforms except 5-axis 45^o.	Maximum Strength value. 5-axis 45^o for maximum shear capability.

Based on the order of preference 6 preforms are selected for the hot structure application (Nosecap) and are given in table 4.42.

Table 4.42 Selected Preforms for Numerical Studies

Woven	***Braided***
LLOW-1-1	5-axis 15^o
TTOW-1-1	4-axis 15^o
LLOW-2-1	5-axis 45^o

The generated properties of the above selected preforms of woven and braided composites are used for carrying out numerical investigations on Nosecap.

CHAPTER 5

NUMERICAL INVESTIGATIONS ON COMPOSITE SHELLS USING RUC

5.1 Introduction

Nosecap has been adopted as the structure for the analysis in the present study. The tip of the reusable launch vehicle is called Nosecap. The hot structures of a reusable launch vehicle are shown in fig 5.1 and a zoomed view of Nosecap is shown in fig 5.2. The typical cross section of the nosecap is a doubly curved conical shell. This nosecap experiences different loading conditions in the different regimes of the vehicle mission. These are to be designed for thermal as well as structural loads.

There are three trajectories for reusable launch vehicles for the aerodynamic loadings of the hot structures, viz., ascent flight, reentry flight, descent flight.

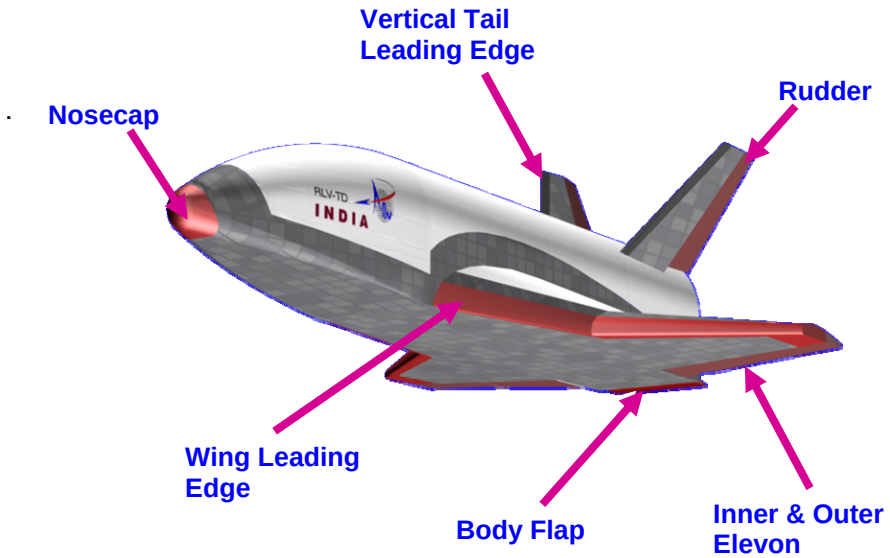

Fig 5.1 Hot structures of Reusable Launch Vehicle
(Courtsey: www.indianspaceweb.blogspot.com)

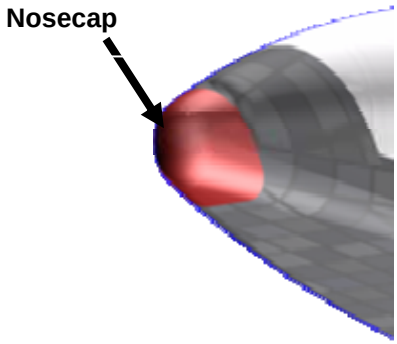

Fig 5.2 Zoomed view of Nosecap

5.1.1 Description of the structure

Nosecap considered for the present study has a spherical enclosure at the tip and it has a varying cross section with respect to height i.e; it forms a 'D' shape from the circular cross section at the spherical interface. It is connected to Titanium (Ti) end ring by Inconel brackets. The 3D model of the Nosecap is depicted in fig 5.3.

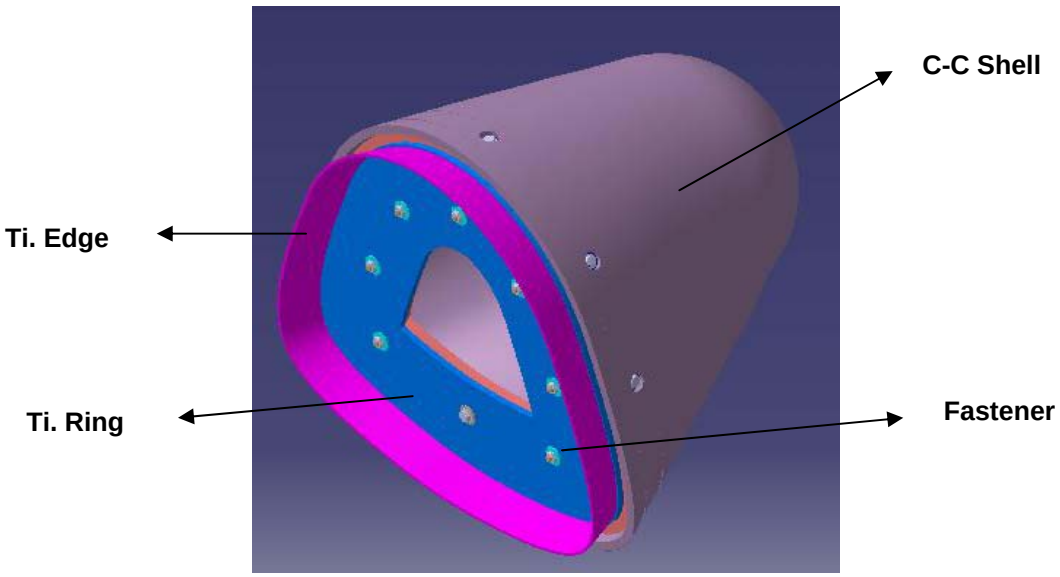

Fig 5.3 3D model of the Nosecap

The geometry of the Nosecap is 315mm height at one side and 418mm height at the other side. The maximum base length is 348mm. The Nosecap is placed with a tilt of 14 degrees and with a tip radius of 125mm. The overall geometry of the Nosecap is as shown in fig 5.4. The overall cross sectional view of the nosecap is as shown in fig 5.5.

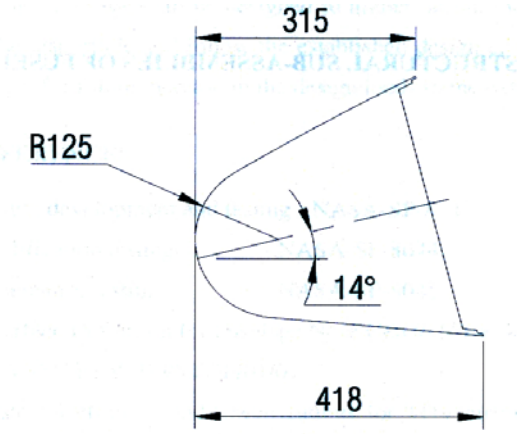

Fig 5.4 Overall Geometry of the Nosecap

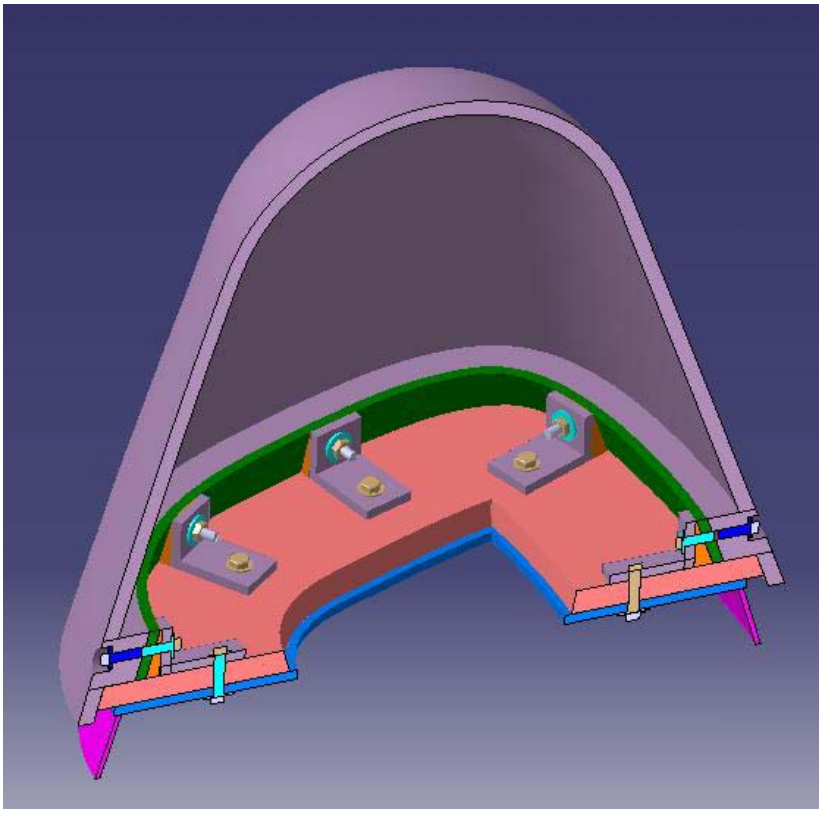

Fig 5.5 Cross Sectional View of Nosecap

The requirements of insulator material like Zirconia felt etc., will be decided based on the heat transfer analysis. The details of the Carbon-Carbon shell connection to the Titanium base plate is shown in fig 5.6 and 5.7. The Titanium base plate is shown in fig 5.8 and the interface fasteners connecting Inconel bracket is shown in fig 5.9.

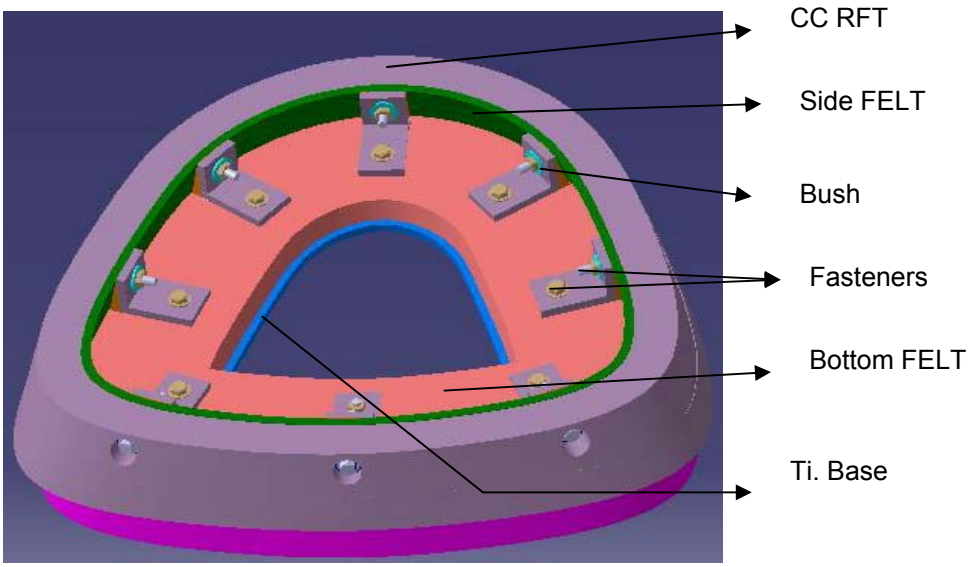

Fig 5.6 Details at the Nosecap to Ring joint

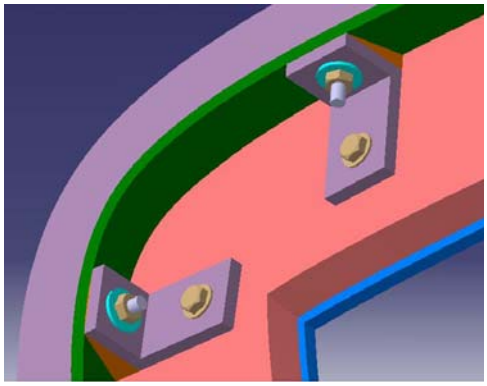

Fig 5.7 Details at the Nosecap to Ring joint (Local view)

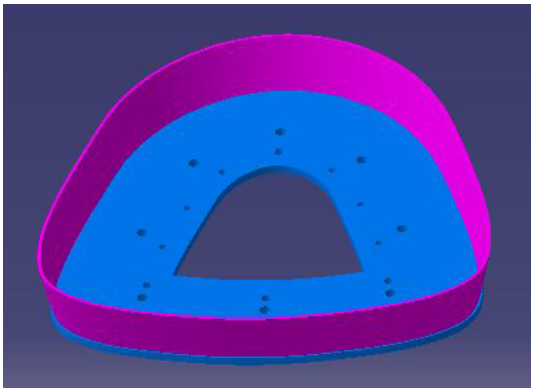

Fig 5.8 Titanium Base plate

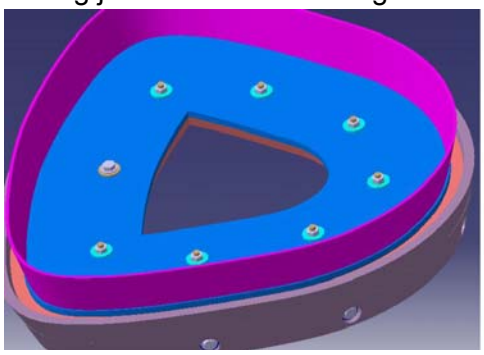

Fig 5.9 Titanium Base plate with Interface Fasteners

5.1.2 Trial dimensioning

The basic thickness parameters for the Nosecap is arrived based on a preliminary structural analysis carried out using general purpose software NISA (NISAII 1997). In the present analysis the structure has been made up of general isotropic materials like

Aluminium and Inconel which is modeled using 3D general shell element (NKTP20) and layered C-C composite which is modeled using 3D laminated composite general shell element (NKTP32). The material properties used in the analysis for C-C fabric composite, Inconel and Titanium are given in table 5.1.

Table 5.1 Mechanical Properties of C-C Fabric / Inconel / Titanium at RT

A. C-C Fabric Composite		**Unit**
Youngs modulus in warp and weft directions	70000	N/mm^2
Youngs modulus in thickness direction	24000	N/mm^2
Poisson's ratio	0.05	
In plane shear modulus	20000	N/mm^2
Tensile strength in warp and weft	120	N/mm^2
Compressive strength in warp and weft	90	N/mm^2
Inplane shear strength	25	N/mm^2
B. INCONEL		
Youngs modulus	209000	N/mm^2
Poisson's ratio	0.3	
Yield strength	1180	N/mm^2
Shear strength	590	N/mm^2
C. TITANIUM		
Youngs modulus	105000	N/mm^2
Poisson's ratio	0.3	
Ultimate tensile strength	980	N/mm^2
Shear strength	490	N/mm^2

A maximum external pressure of 141kPa is applied on the outer surface of the shell. The present analysis being of preliminary nature the variation of pressure throughout the depth and along the circumference has not been taken into account. The Titanium ring in the structure where it is getting interfaced with the neighboring main frame all the degrees of freedom are arrested. The finite element model is shown in fig 5.10 and the load along with boundary conditions are shown in fig 5.11.

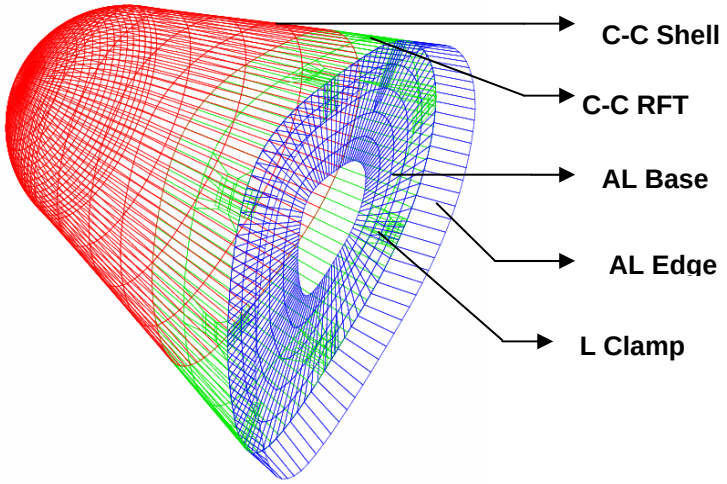

Fig 5.10 Finite Element Model

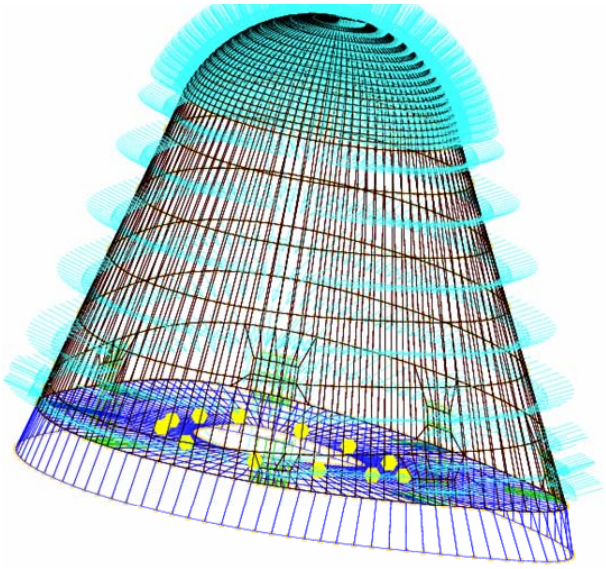

Fig 5.11 Finite Element Model with Loads and Boundary Conditions

The body portion made up of composites is assumed to be made out of a layup sequence of 0/+45/-45/90 combination (quasi isotropic) in the present analysis. From the analysis the overall displacements and stresses are found for each layer in its own principal material direction and compared with its corresponding allowables. The overall displacement is shown in fig 5.12 and 5.13. The displacement in the axial direction is as shown in fig 5.14. The resultant displacement of 2.73 mm is found in the Nosecap. The stresses in the fibre direction i.e; S_{XX} (warp), S_{YY} (weft) and S_{XY} (inplane shear) are shown in fig 5.15, 5.16 and 5.17 respectively. The unit of the stresses in the figures is N/m^2.

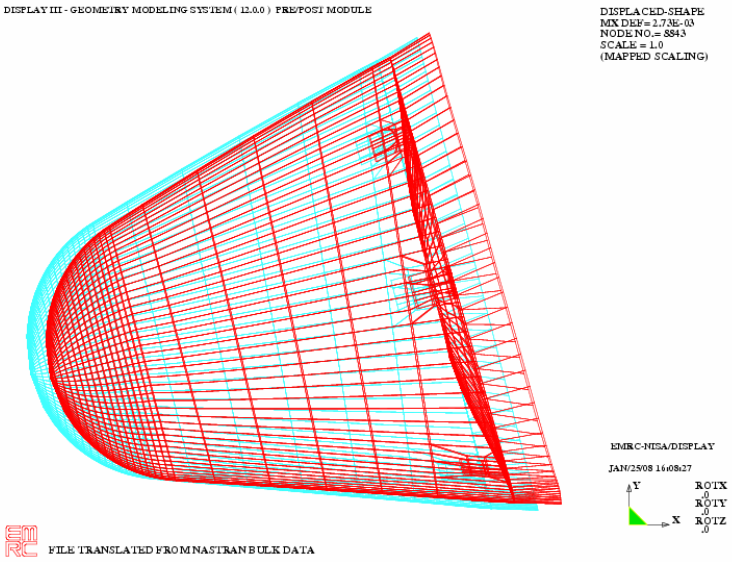

Fig 5.12 The Overall Displacement

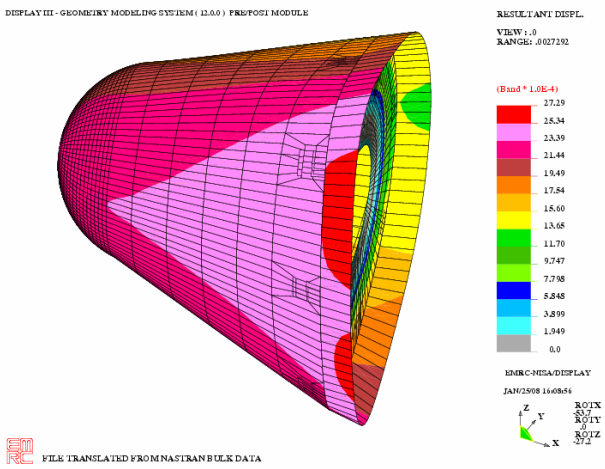

Fig 5.13 Overall Displacement – Shaded view

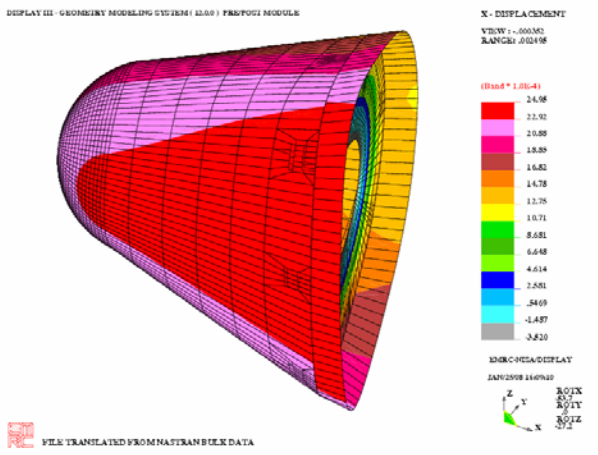

Fig 5.14 Displacement in Axial direction

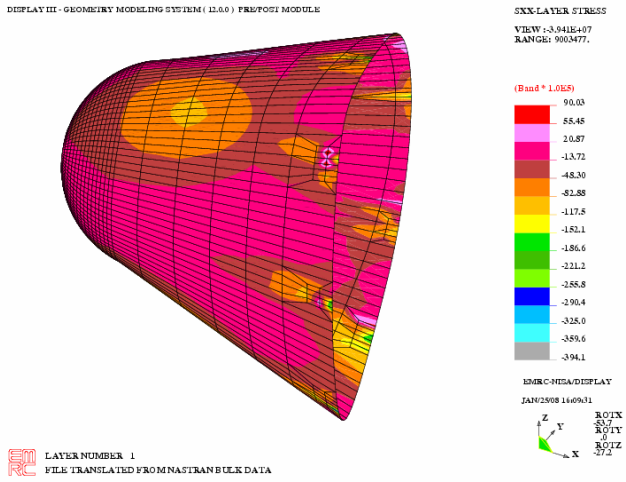

Fig 5.15 Fibre Stress along Warp direction

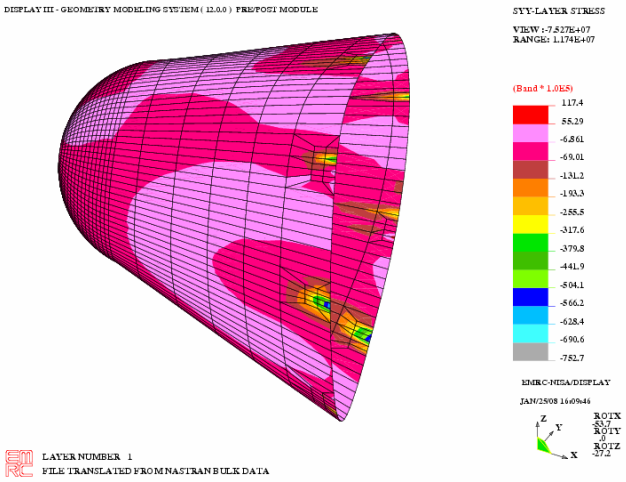

Fig 5.16 Fibre Stress along Weft direction

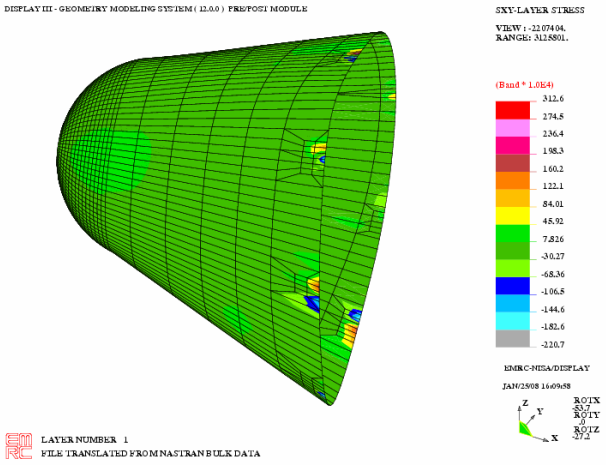

Fig 5.17 Inplane Shear Stress

The maximum fibre direction stress in longitudinal direction is 39.4 N/mm^2 and in the transverse direction is 75.2 N/mm^2 (allowable 90 N/mm^2). The maximum shear stress observed is 3.13 N/mm^2 (allowable 25 N/mm^2). The stresses and overall displacement are with in the allowable limit of Carbon-Carbon, Inconel and Titanium.

The layer numbers and their orientations are finalized and the corresponding geometric parameters arrived from the preliminary structural analysis are shown in table 5.2.

Table 5.2 Geometric Parameters of Nosecap

Sl. No	Components	Thickness (mm)
1	C-C Shell	8.96
2	C-C Edge Reinforcement	26.88
3	Clamp – Inconel	10
4	Titanium- Base	6
5	Titanium Edge	3
6	Displacement	2.73

5.2 3D Finite Element Modelling of Nosecap

For the application of Nosecap which is to be designed using 3D preform the following steps have to be carried out. 3D finite element model is generated to capture the through the thickness variations. Nonlinear transient thermal analysis and nonlinear transient thermo-structural analysis are performed to verify the margins available in the structure. Parametric studies are carried out on the Nosecap based on the 3D properties generated and the best performing composite will be selected for the application in the hardware. Steps involved in the thermo-structural analysis are briefly explained in fig 5.18.

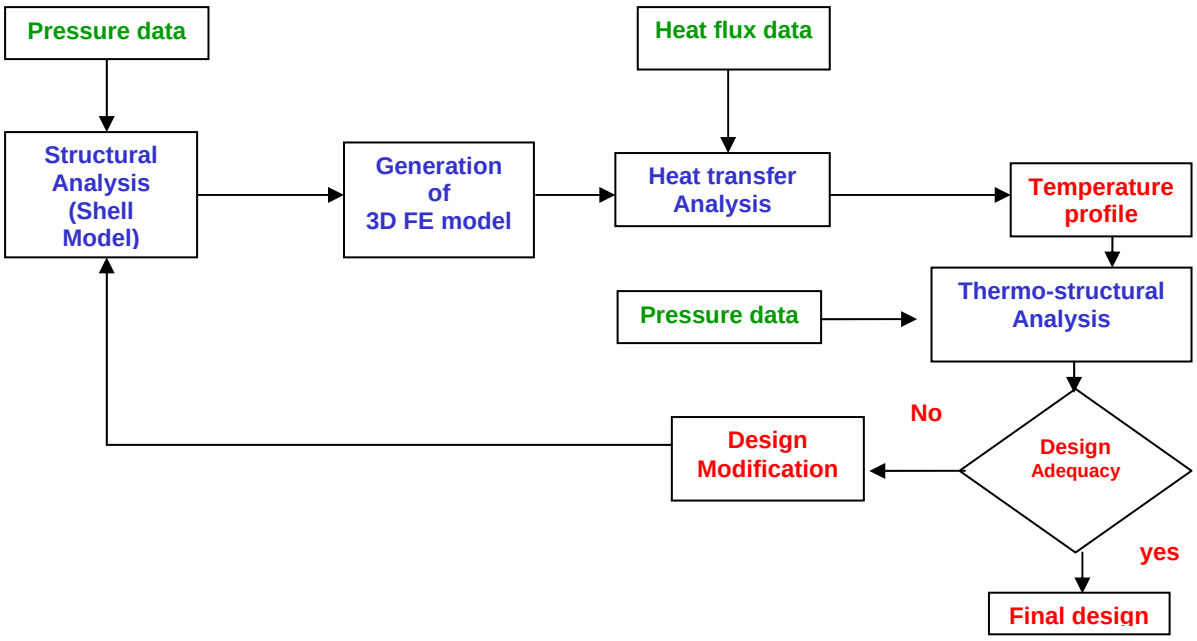

Fig 5.18 Flow Sequence for Thermo-structural Analysis

5.2.1 Finite element model generation

MSC NASTRAN software (Kilroy 1998) is used for carrying out the heat transfer and thermo-structural analysis. Owing to the complications in the generation of the finite element model with solid mesh, Hypermesh software has been used for that purpose. The NASTRAN deck is written from Hypermesh and further modified for the inputs required for carrying out analysis. The CPENTA and CHEXA elements available in NASTRAN are used for generating the finite element model. Nosecap have been modeled using 3D solid elements and the integrated finite element model of the Nosecap is shown in fig 5.19.

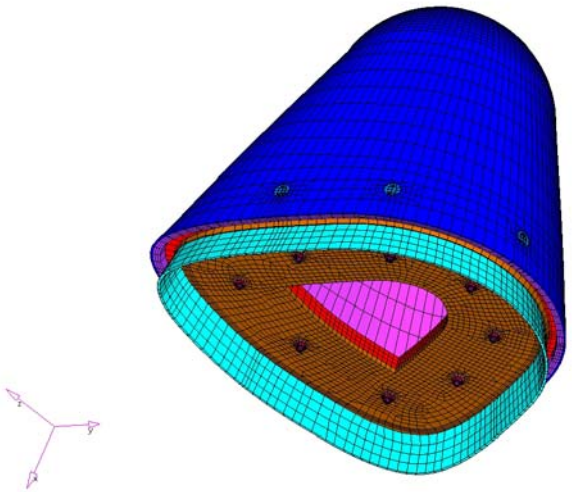

Fig 5.19 Integrated Finite Element Model

The outer surface of the Nosecap is connected to the Inconel brackets (8nos) by Carbon-Carbon bolts (M6). For thermal isolation of Inconel from C-C, Zirconia felt is used elsewhere and where it is connected by bolts Ceramic bush is used to connect C-C to Inconel brackets. The holes on the C-C nose skin for providing the bolts will be plugged by C-C material after the assembly and is essentially included in the finite element model. The C-C shell to the Inconel bracket joint is as shown in fig 5.20. The enlarged view of the C-C skin to Inconel bracket region is shown in fig 5.21, whereas the Inconel brackets are not shown.

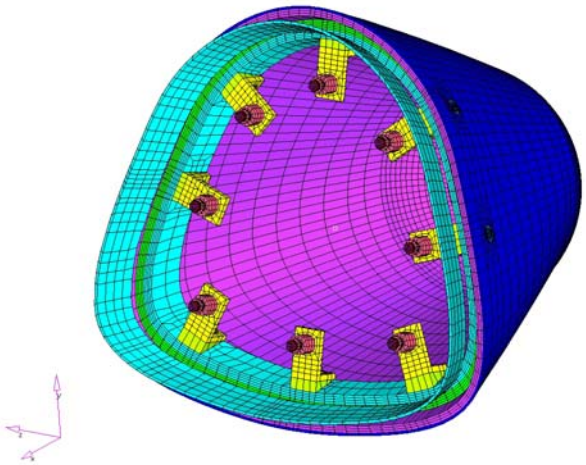

Fig 5.20 C-C Shell to Inconel Bracket Joint

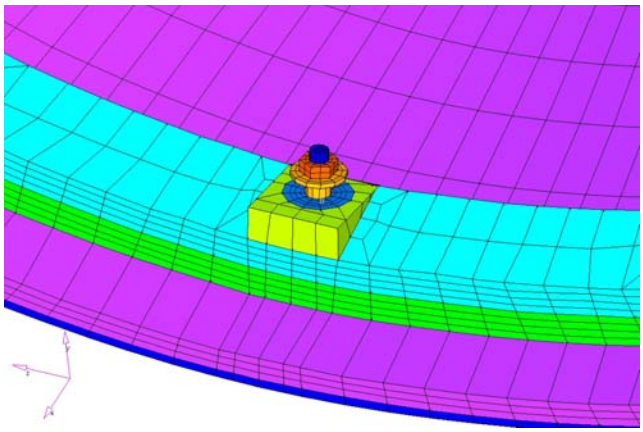

Fig 5.21 Enlarged View of C-C Skin to Inconel Bracket

The Inconel bracket to Titanium ring is connected by Inconel bolts and the ring is isolated by Zirconia felt material. The ring is connected to the Inconel bracket at the bolt location by Ceramic sleeves. Inconel bracket to C-C reinforcement is shown in fig 5.22 and Inconel bracket to Titanium ring joint is shown in fig 5.23. The enlarged view of the Inconel bracket connection to Titanium ring is shown in fig 5.24. The top and bottom cross sectional views of the interfaces are shown in fig 5.25 and 5.26.

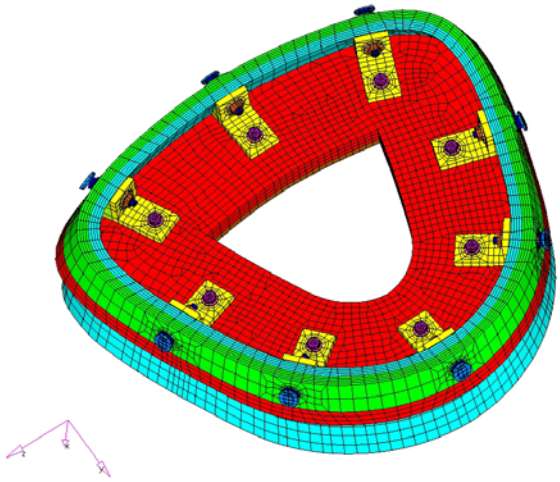

Fig 5.22 Inconel Bracket to C-C Reinforcement

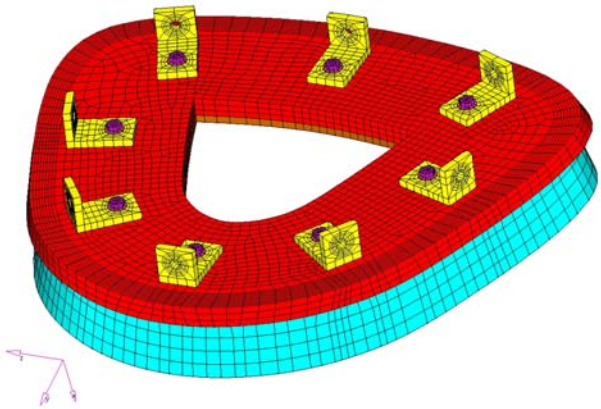

Fig 5.23 Inconel Bracket to Titanium Ring

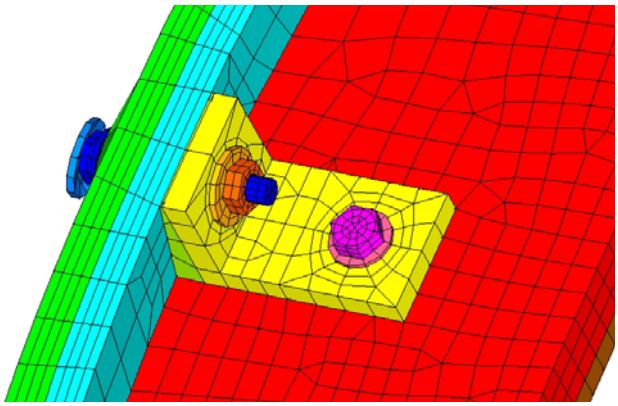

Fig 5.24 Enlarged View of Inconel Bracket Interface

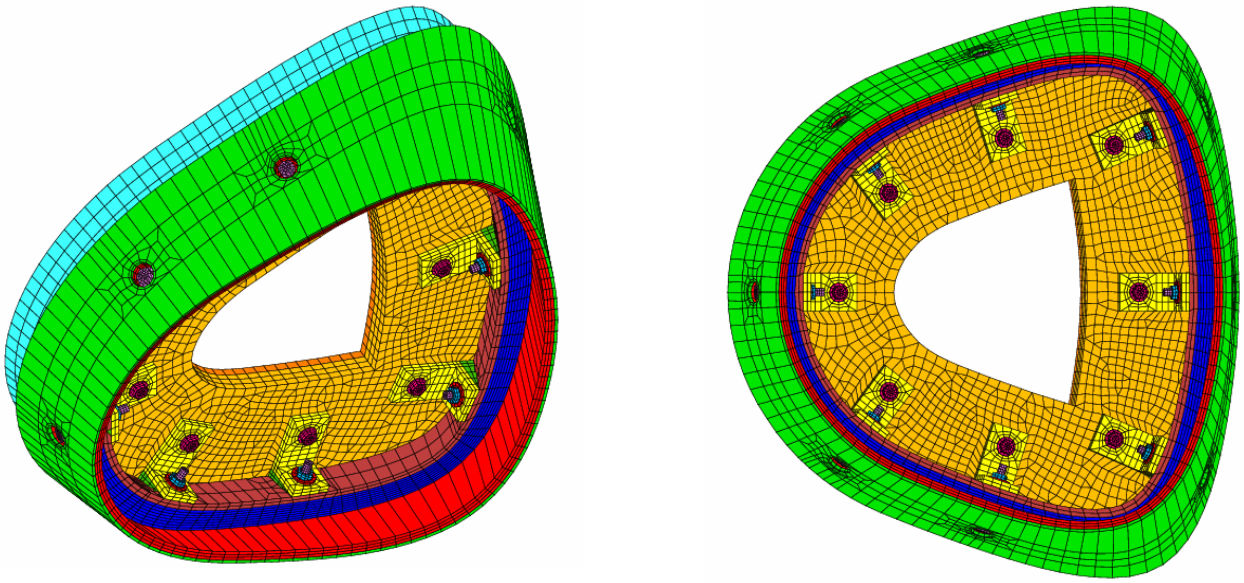

Fig 5.25 The Cross Sectional View (Top)

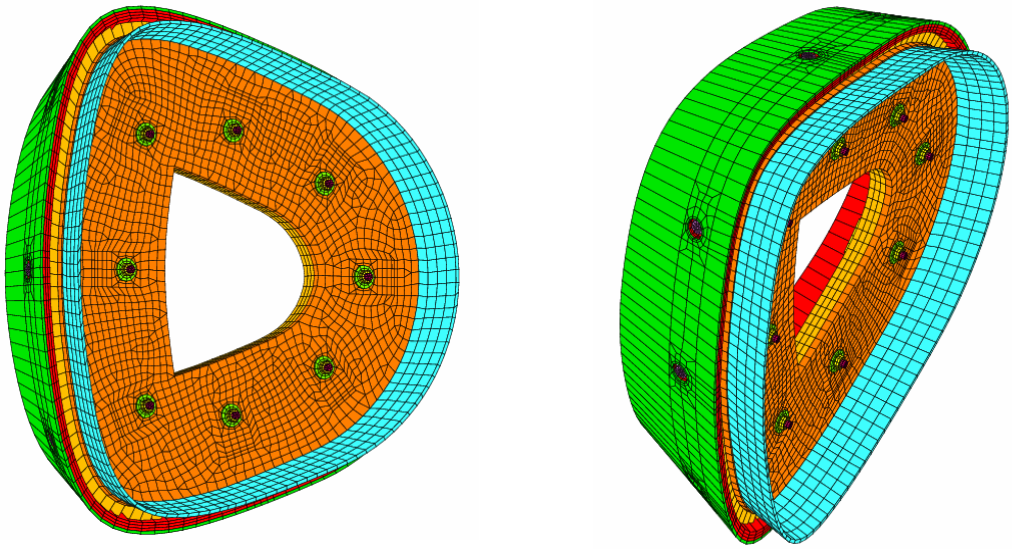

Fig 5.26 The Cross Sectional View (Bottom)

5.2.2 Estimation of loads

Based on the Computational Fluid Dynamics (CFD) analysis the heat flux and pressure loads have been arrived at, which is the input for the finite element analysis. Heat transfer analysis is then carried out using the heat flux load condition for the mission. The output of heat transfer analysis, which is the temperature load condition with respect to time, will be added with the corresponding pressure loads for carrying out the thermo-structural analysis of the structure.

5.2.2.1 Heat flux distribution on Nosecap

The heat flux on the Nosecap is estimated at three locations viz., nosecap stagnation point (X0), 210mm and 410mm away from the stagnation point. The heat flux histories at these locations are shown fig 5.27 and the maximum value is around 65 W/cm^2 at the stagnation point. The same heat flux is applied along the circumferential direction. The flux data with respect to temperature is given in section D.1 in Appendix D.

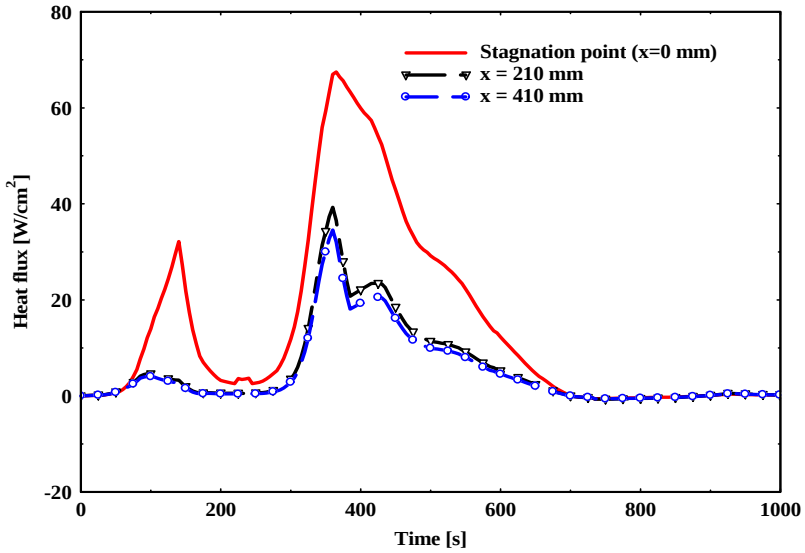

Fig 5.27 Heat Flux History on the Nosecap

The variation of flow parameter is shown in Fig. 5.28 and the data with respect to time is shown in section D.2 in Appendix D. Heat flux q and T_g are related by the equation $q = H (T_g - T_{amp})$, where T_{amp} is assumed as 303°K.

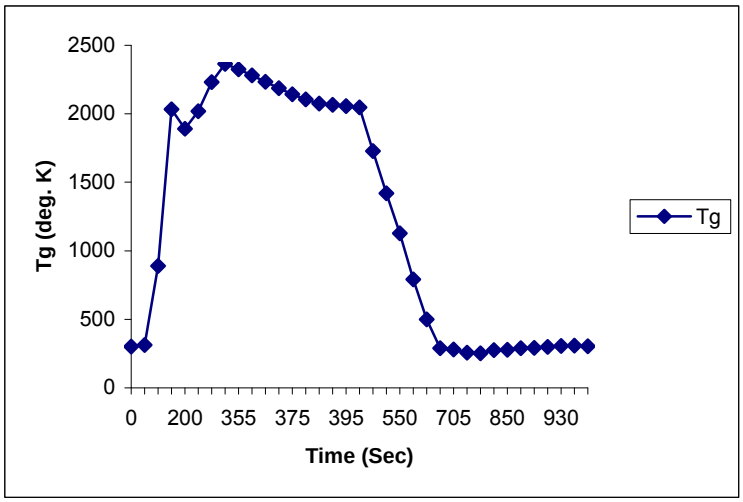

Fig 5.28 Variation of Flow Parameter T_g with Time

5.2.2.2 Pressure distribution on Nosecap

The Dynamic pressure (Cp) during the flight with respect to Mach number and time has been estimated and from these Cp values, the pressure has been evaluated and given in table 5.3. The variation of pressure with time for cap portion and cone area is shown in fig 5.29.

Table 5.3 The Pressure Data on the Cap tip and the Cone

Sl. No.	Flight Time (s)	Aerodynamic pressure (kPa) (with 20% margin)	
		Spherical Cap	Nose cone
1	100	96	30
2	350	34	21
3	400	26	16
4	700	62	25
5	1000	112	40

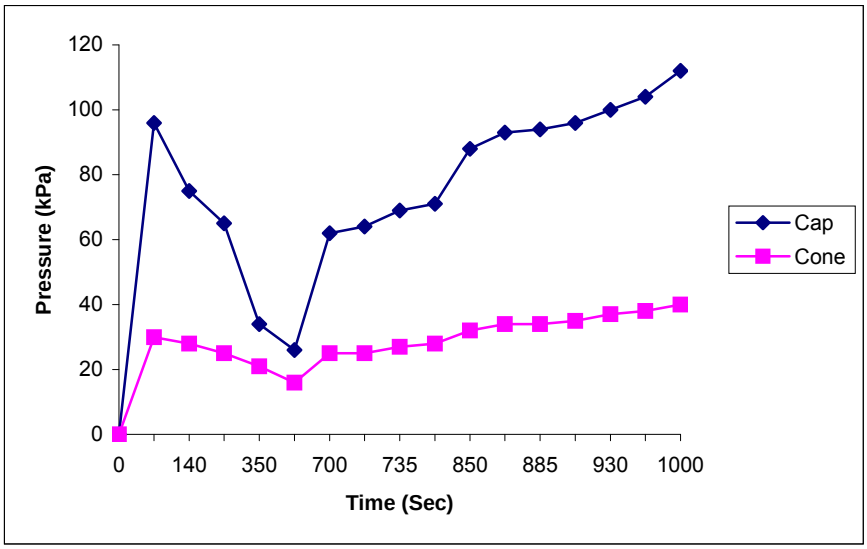

Fig 5.29 Variation of Pressure in Cap and Cone

5.3 Heat Transfer Analysis

5.3.1 Description of the model

Nonlinear transient heat transfer analysis has been carried out using the NASTRAN solver. The flux data variations available in section 5.2.2.1 have been implemented through 16 step incremental procedure.

The high temperature 3D composites properties generated from the computer codes developed as a part of the present study are used for analysis. The material properties have been assigned with respect to temperature and are given in tabulated form as necessitated by NASTRAN for C-C, Inconel, Ceramic Sleeve and Zirconia felt portions. The material property input as given in NASTRAN deck and the relevant boundary conditions are given in Annexure E for a typical preform. The properties are defined in MAT4 and MATT4 cards for materials like Titanium and Zirconium felt, whereas Inconel and C-C are defined in MAT5 and MATT5 cards where temperature dependent properties are defined. The C-C basic shell is defined in 34 cards from 101 to 134 where the orientations of the material is defined by local coordinate systems (34 numbers) and are referred in the element material cards. The axis definition on the Nosecap is as follows, x axis along the meridian, y axis along the circumference and z axis along the thickness direction.

The heat flux data and the flow parameter data are applied on the outer surface of Nosecap. The heat flux data is given in two tables in the required format of NASTRAN for

cap and cone regions. Radiation boundary condition is assumed to the exterior space from the outer surface of the Nosecap with an emissivity of 0.8 (Tested value of C-C). The radiation is defined in the solver as radiation boundary condition in 'RADBC' cards. Surface elements are defined in 'CHBDYG' cards and heat flux is applied on these surface elements. From the C-C surface there will be radiation to the interior and for that the view factor is defined using the radiation cavity 'RADCAV' and then the elements viewing each other are defined using the view factor concept by using 'VIEW3D' cards. The nonlinear transient thermal analysis of the nosecap has been carried out for six types of 3D multidirectionally reinforced composites that have been described in section 4.4.5.

5.3.2 Results and discussions

The output of the heat transfer analysis contains the temperature at each node for the total duration. In the present study the temperature has been considered at specified locations, viz., nosecap tip inside / outside, cap to cone junction inside / outside, nosecap bottom inside / outside, at all interfaces and brackets. The temperature distributions are shown in fig 5.30 to 5.41.

The temperature (inside and outside) near the nosecap tip is shown in fig 5.30 and 5.31 and near cap to cone junction is shown in fig 5.32 and 5.33. The temperature near the bottom of the nosecap (inside and outside) is shown in fig 5.34 and 5.35. The maximum temperature seen in C-C is 1540^{o}K, for Inconel it is 660^{o}K and for Titanium it is 520^{o}K for LLOW-1-1. Similar trend is seen for other performs as well. The temperature is reducing from C-C tip to base as expected. LLOW-1-1 gives the maximum temperature at cap to cone junction and the lowest is given by 4-axis 15^{o}, when the peak heat flux is prevailing. Similar trends are seen in Inconel bracket as shown in fig 5.36 to 5.38. The temperature in Inconel is at peak at the interface of C-C and Inconel and is shown in fig 5.37. The maximum temperature is within the allowable limits 1033^{o}K for Inconel. Similar behaviour is seen at various locations of Titanium ring as shown in fig 5.39 to 5.41 and the maximum temperature is within the allowable limit of 673^{o}K.

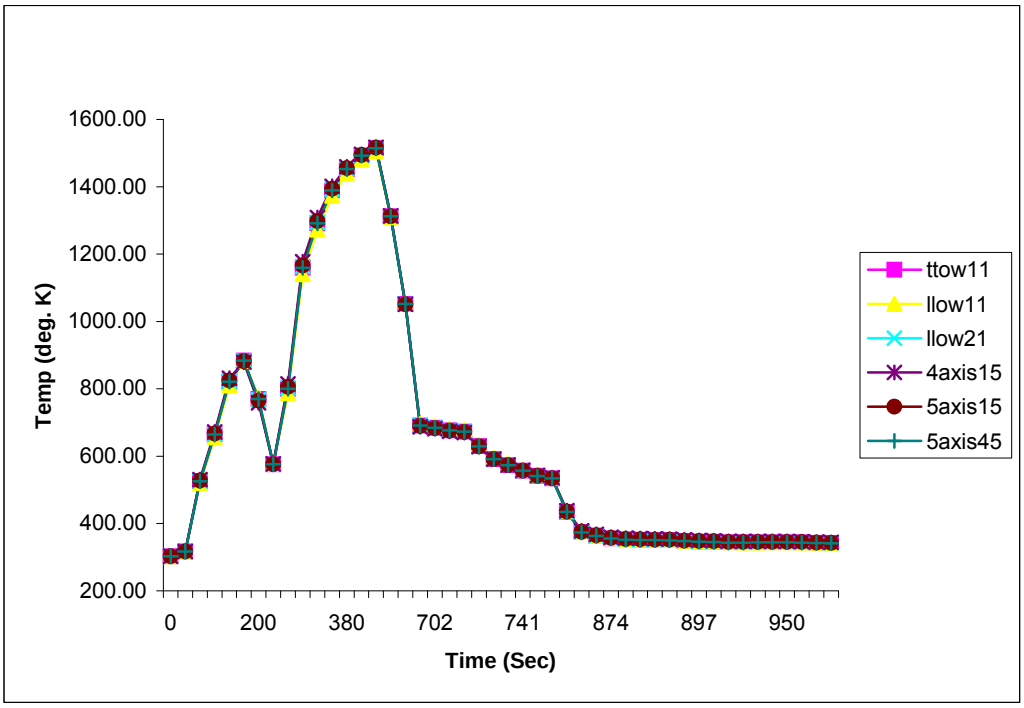

Fig 5.30 Temperature Distribution at Nosecap Tip – Outside

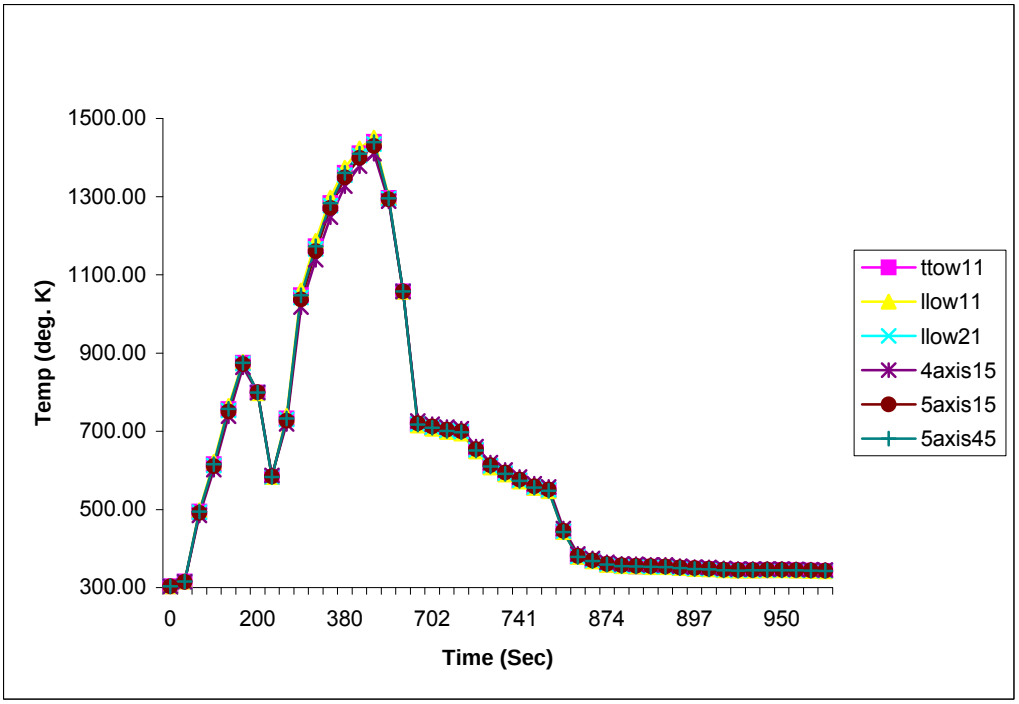

Fig 5.31 Temperature Distribution at Nosecap Tip – Inside

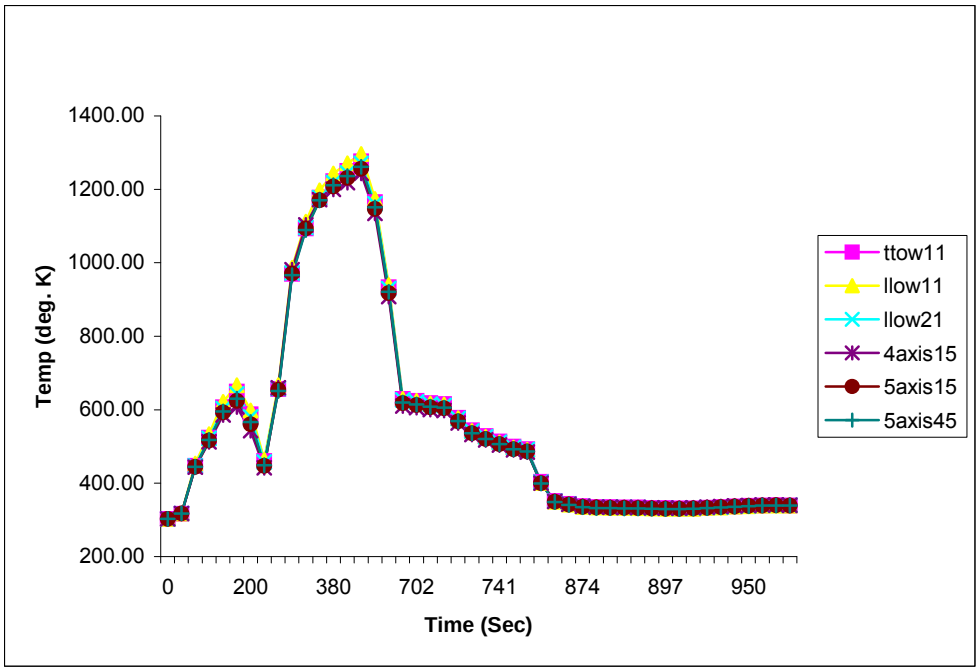

Fig 5.32 Temperature Distribution near Cap to Cone Junction – Outside

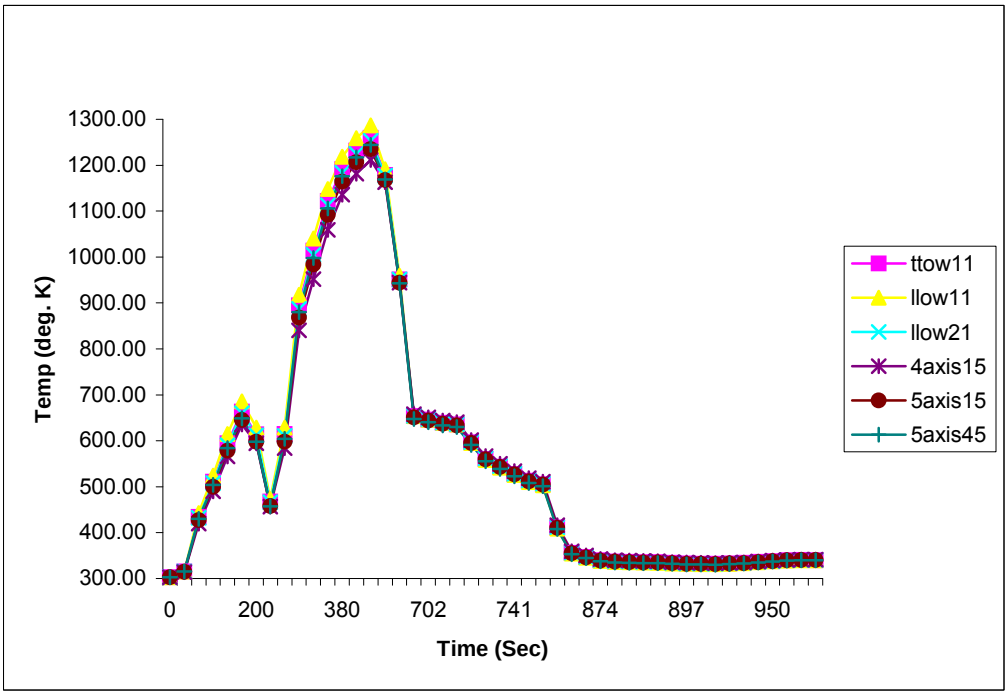

Fig 5.33 Temperature Distribution near Cap to Cone Junction – Inside

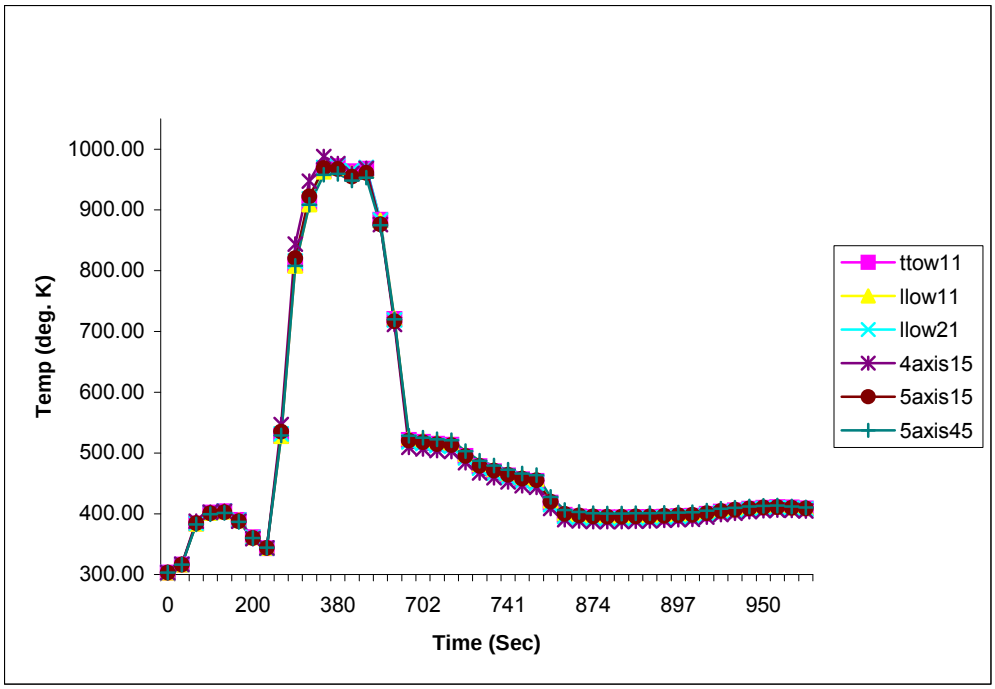

Fig 5.34 Temperature Distribution at Nosecap bottom – Outside

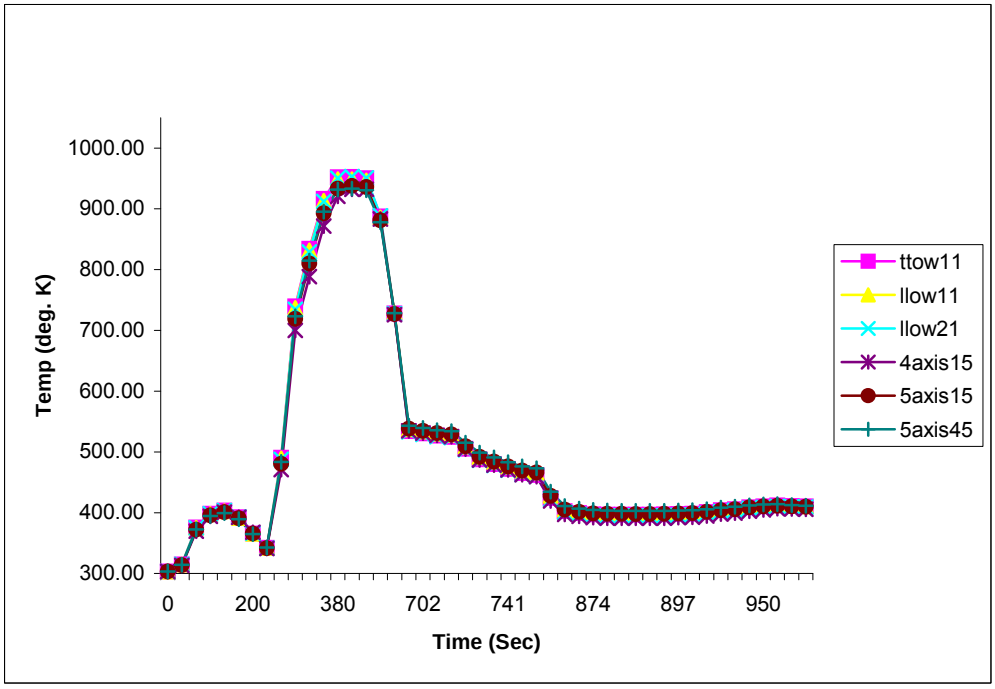

Fig 5.35 Temperature Distribution at Nosecap bottom – Inside

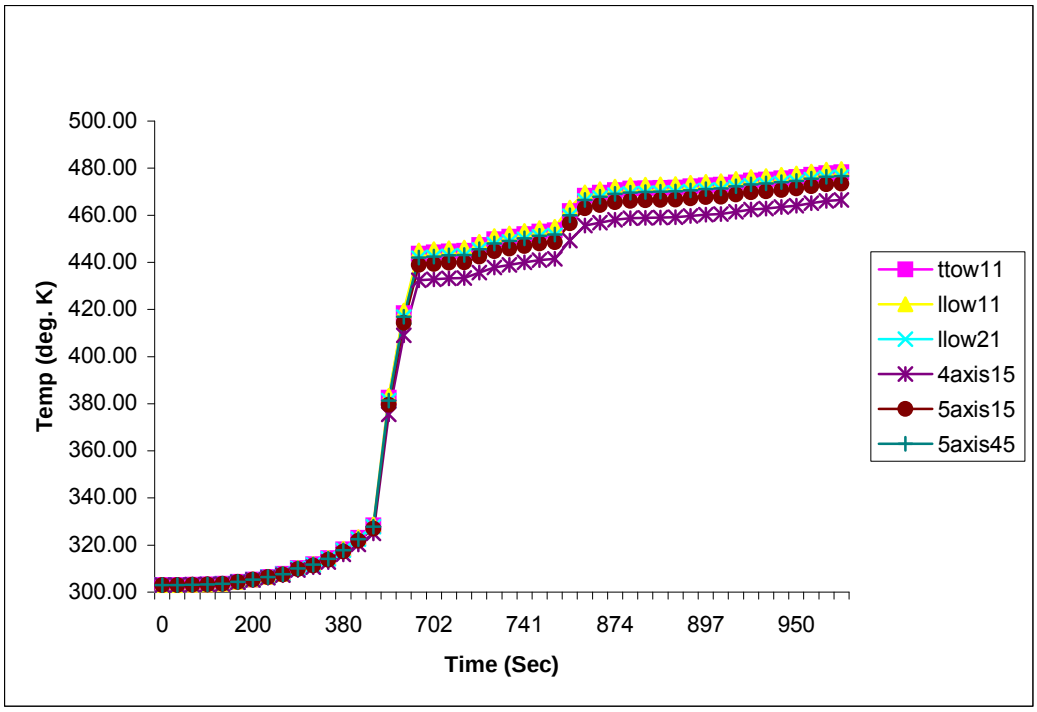

Fig 5.36 Temperature Distribution in Inconel Bracket - Inside Extreme end

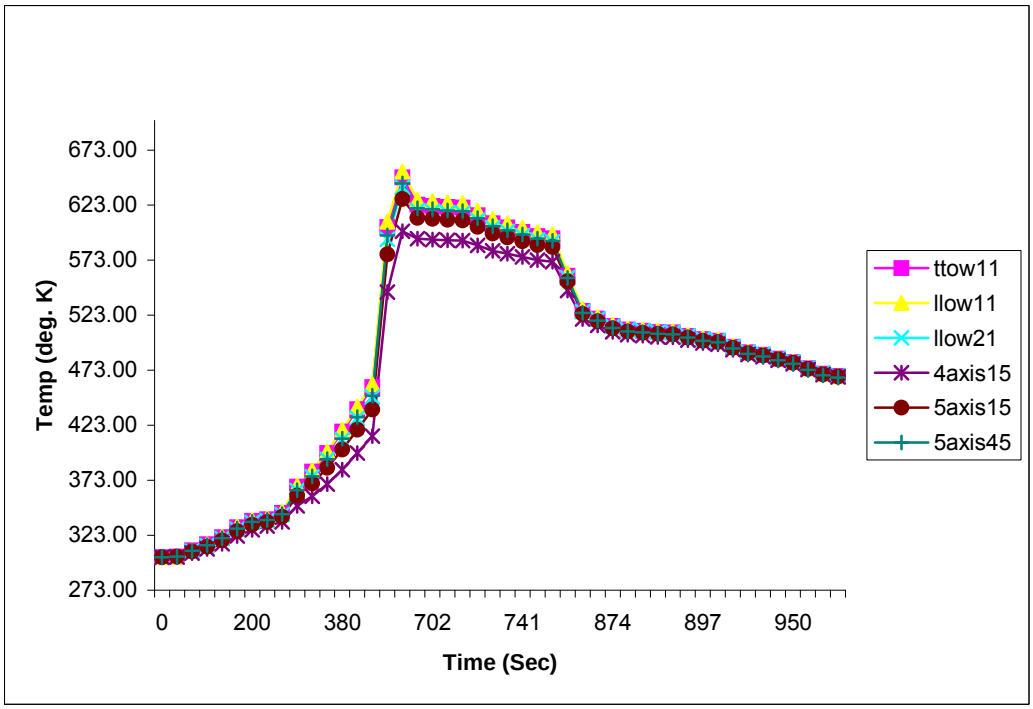

Fig 5.37 Temperature Distribution in Inconel Bracket at C-C Interface

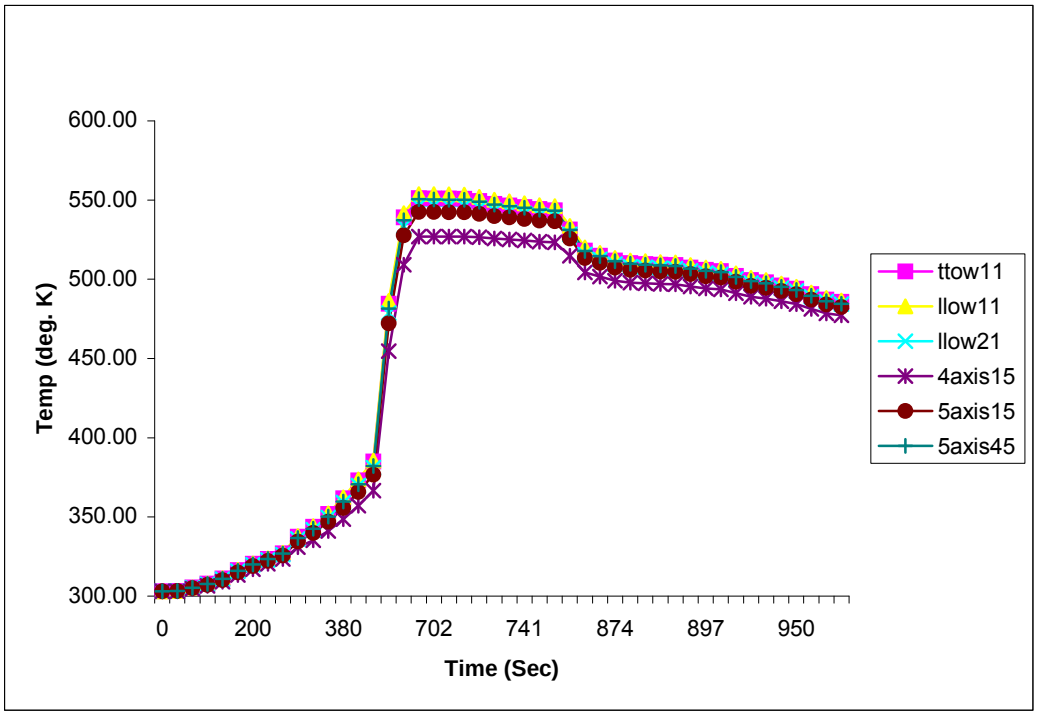

Fig 5.38 Temperature Distribution in Inconel Bracket - Inside near Web to Flange Junction

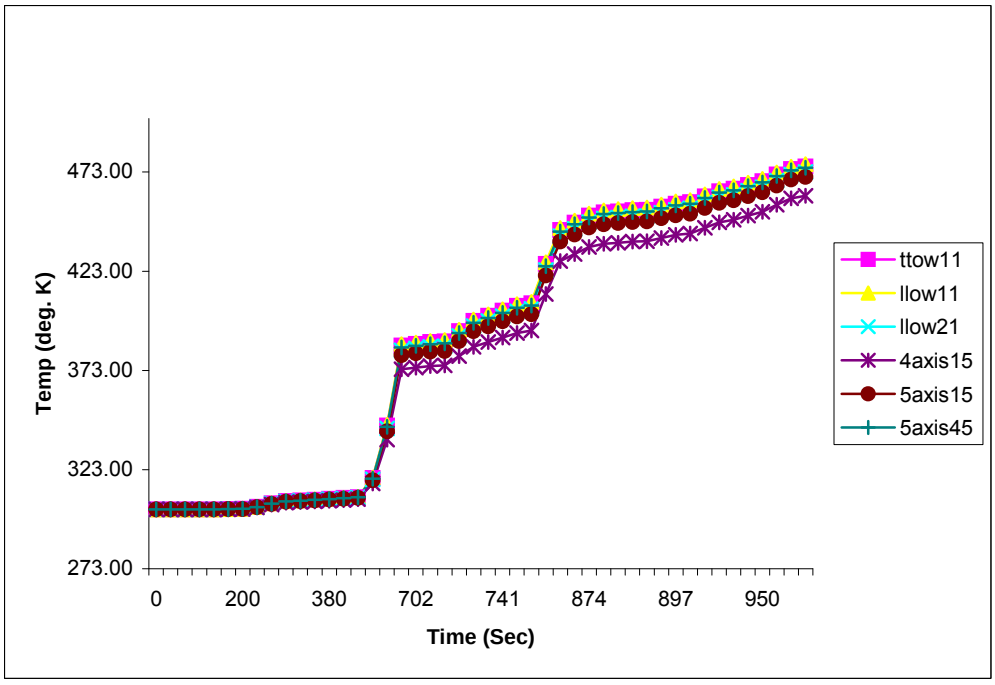

Fig 5.39 Temperature Distribution in Titanium Ring - Bottommost Point

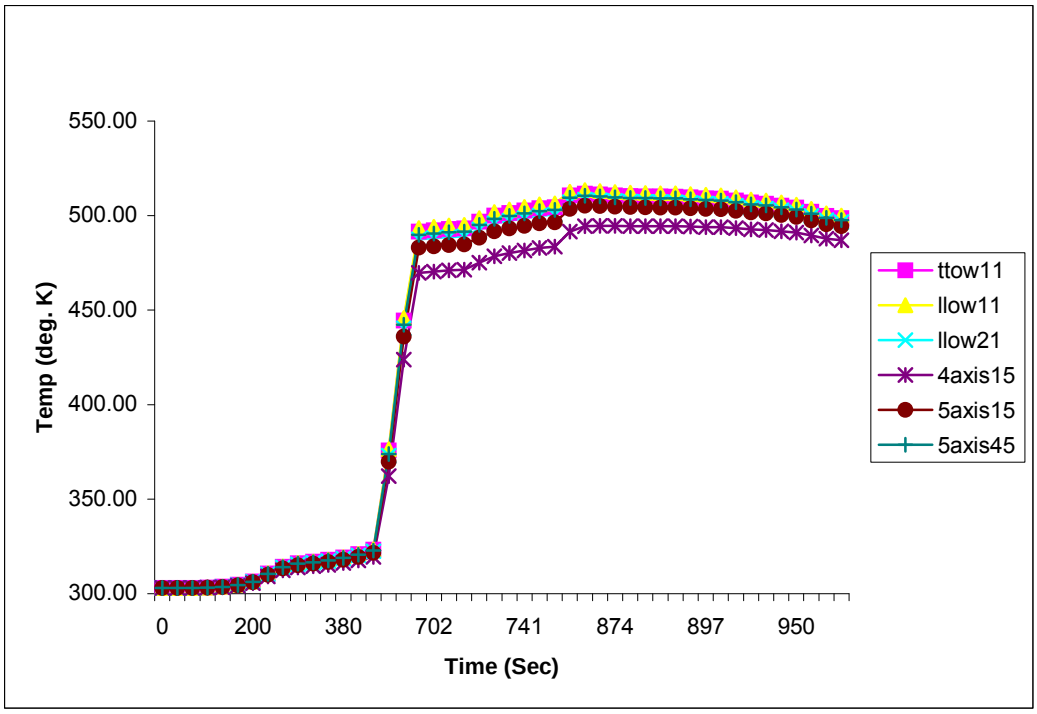

Fig 5.40 Temperature Distribution in Titanium ring - Near Bolt Top Surface

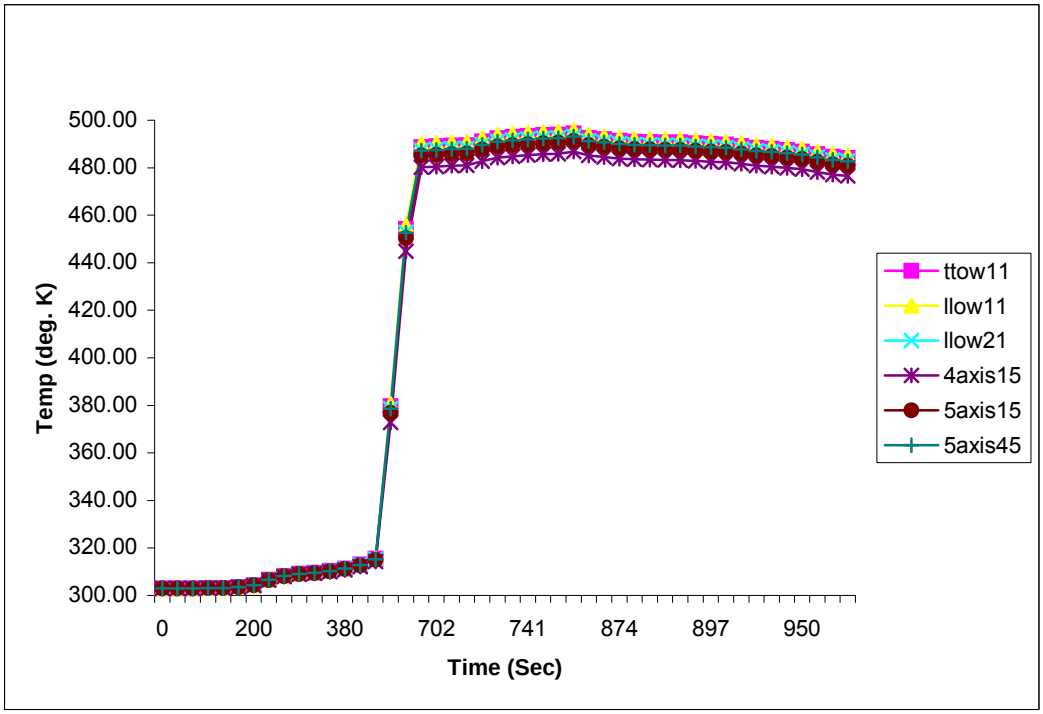

Fig 5.41 Temperature Distribution in Titanium ring - Away from Bolt Surface

The gradients of temperature at various locations have been estimated for all the six chosen materials. They are plotted to observe the temperature difference between the outside and inside surfaces. The typical plots for TTOW-1-1 woven composite and 5-axis

15^{o} braided composites are given in fig 5.42 to 5.47. The gradient at nosecap tip is shown in fig 5.42 and 5.43, the gradient at cap to cone junction is shown in fig 5.44 and 5.45 and the gradient near the nosecap bottom is shown in fig 5.46 and 5.47. It can be seen from these plots that both woven and braided composites show similar trend but the braided shows slightly higher gradient than woven composites.

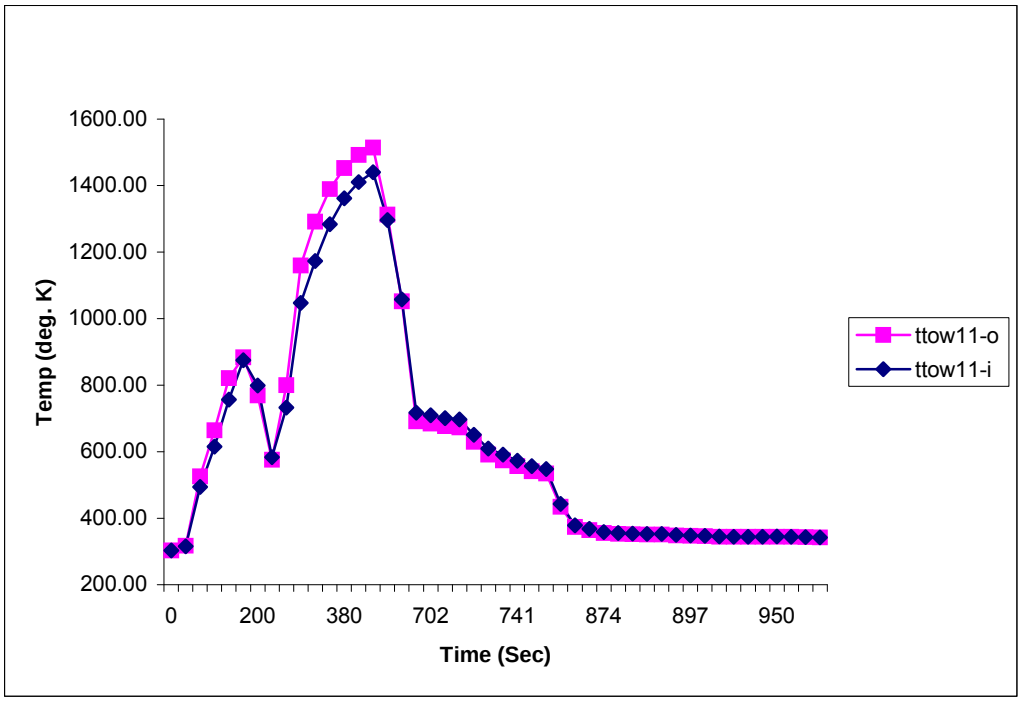

Fig 5.42 Temperature Gradient for Woven Composite at Nosecap Tip

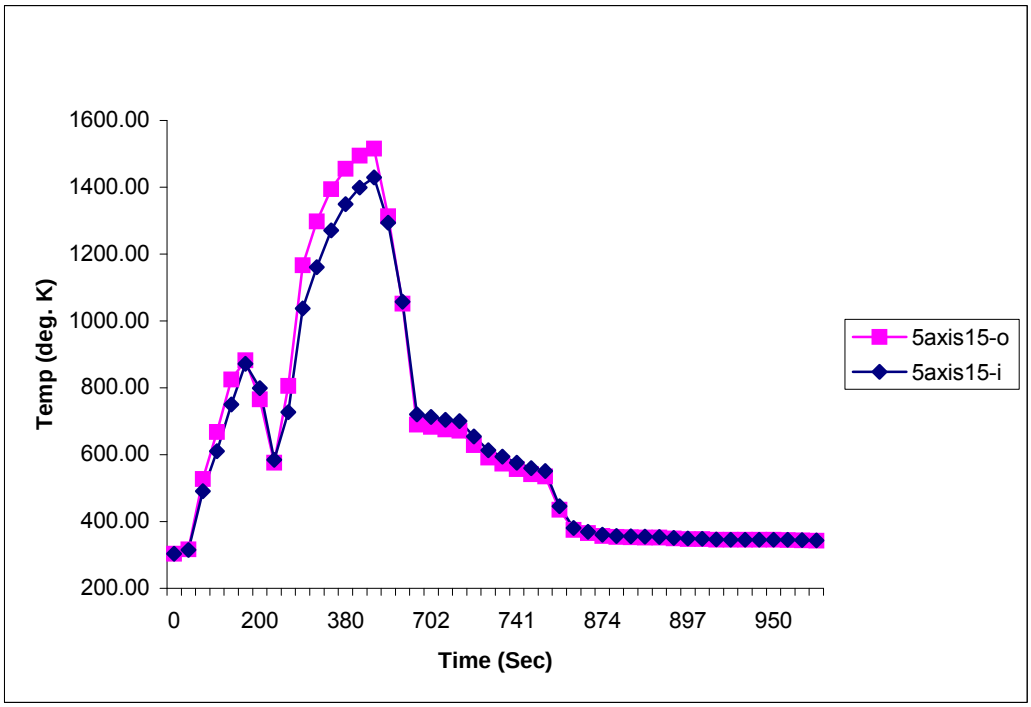

Fig 5.43 Temperature Gradient for Braided Composite at Nosecap Tip

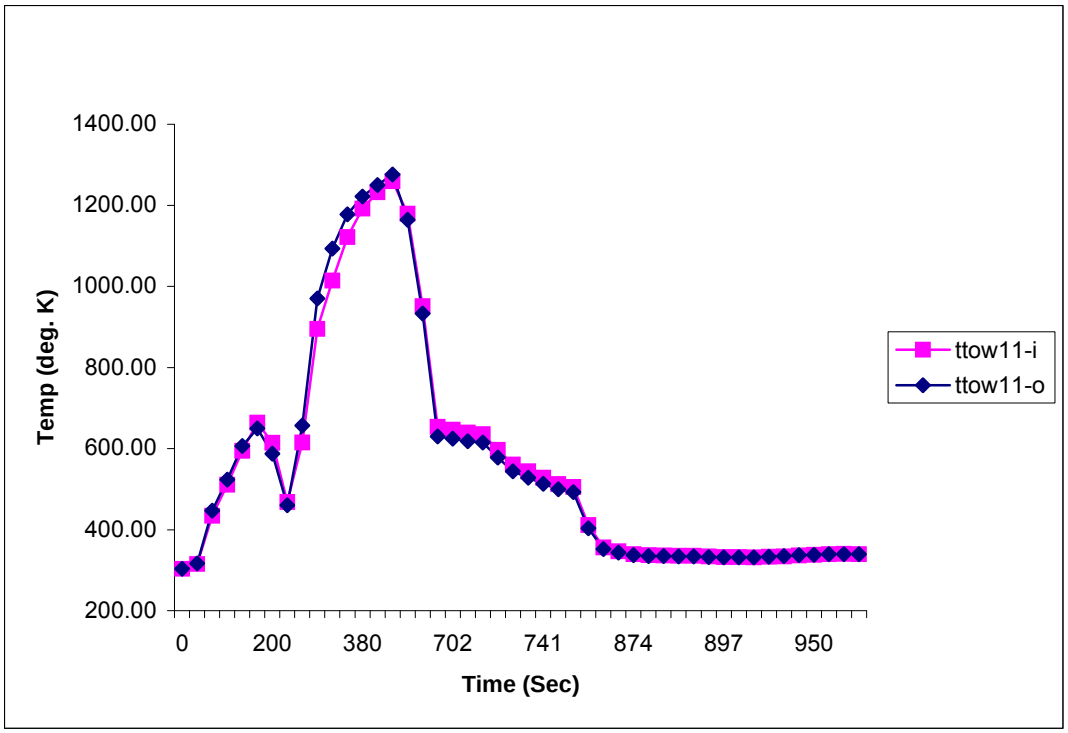

Fig 5.44 Temperature Gradient for Woven Composite at Nosecap to Cone Junction

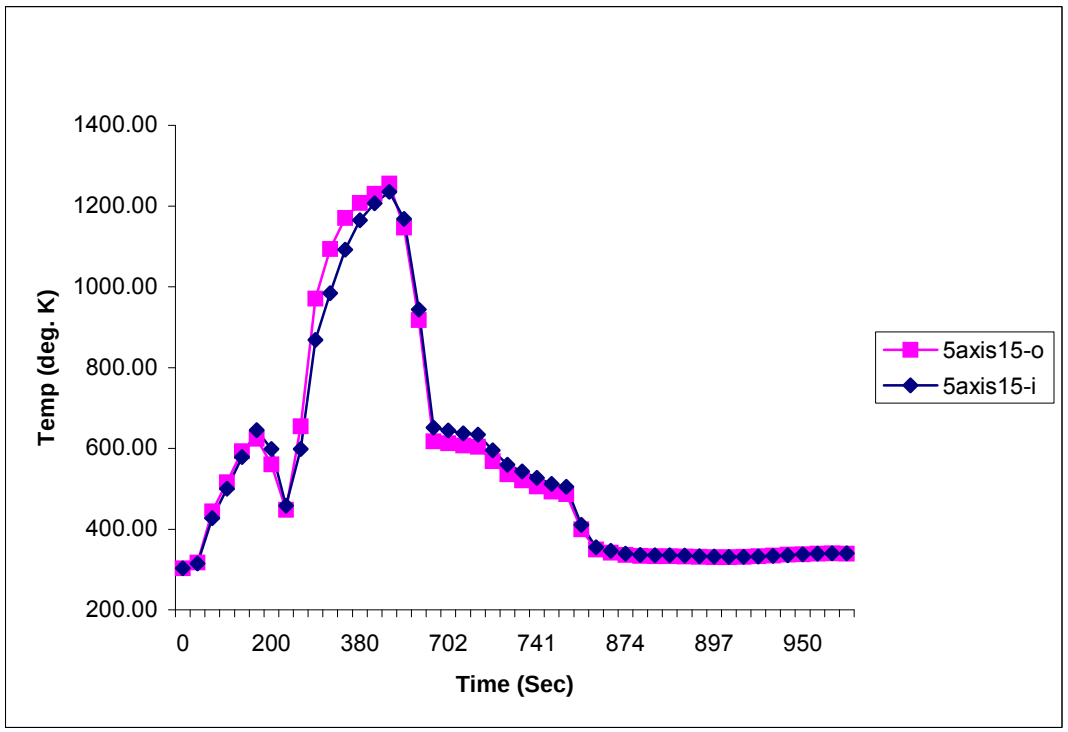

Fig 5.45 Temperature Gradient for Braided Composite at Nosecap to Cone Junction

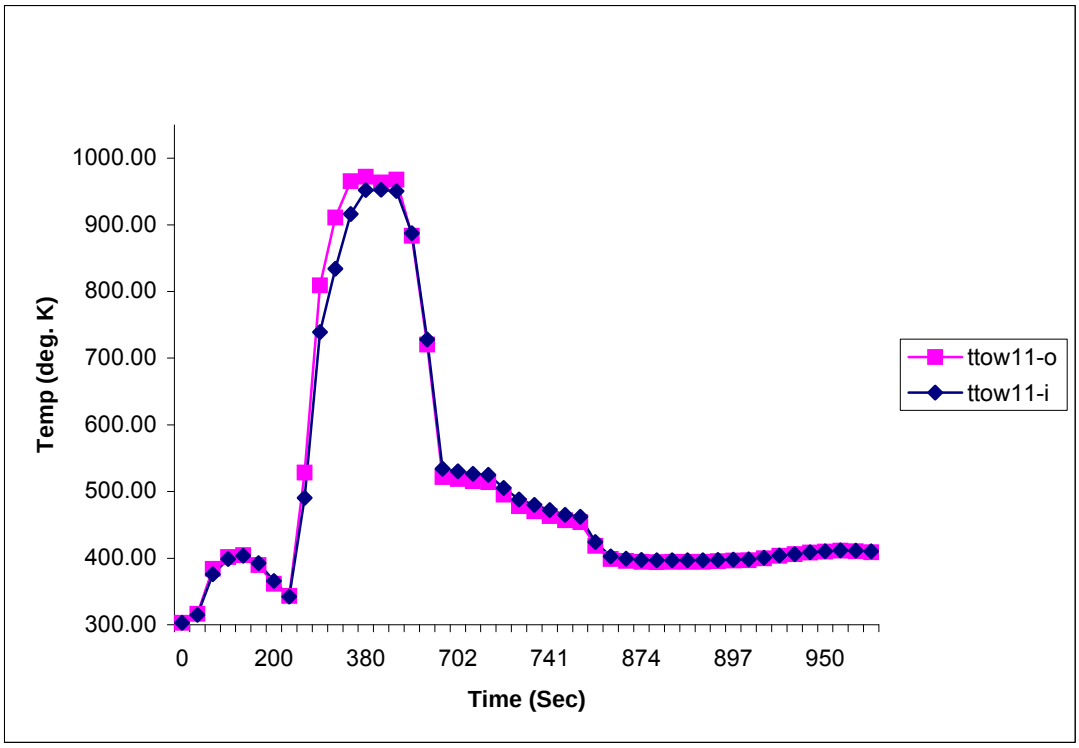

Fig 5.46 Temperature Gradient for Woven Composite at Nosecap Bottom

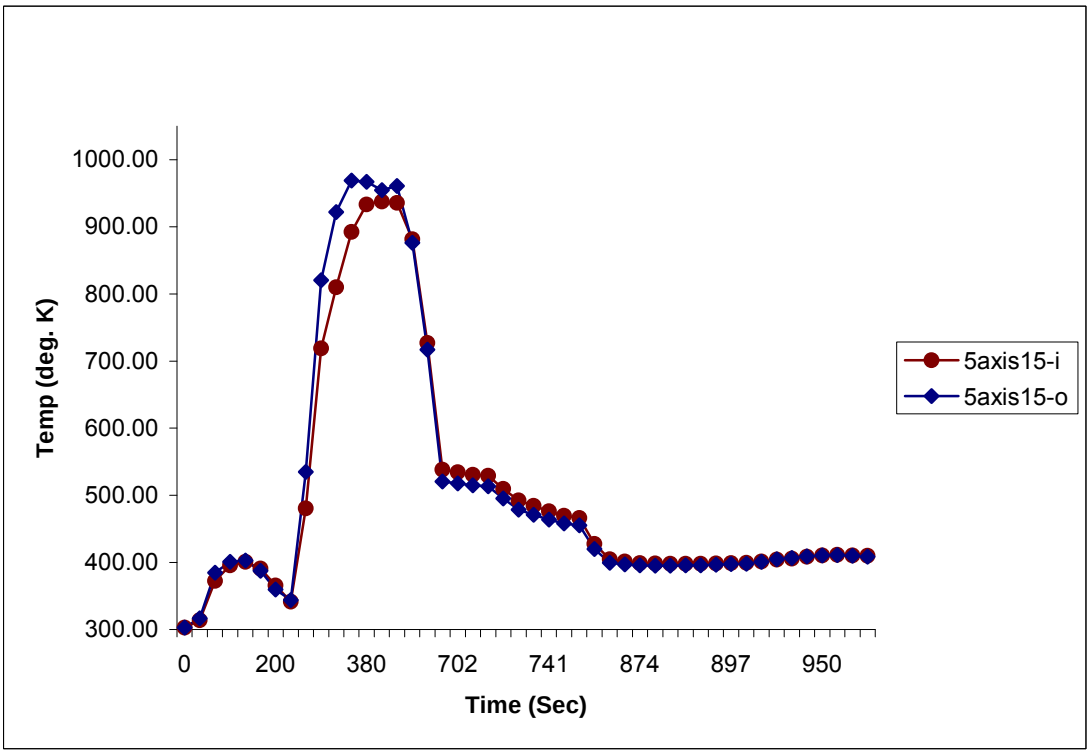

Fig 5.47 Temperature Gradient for Braided Composite at Nosecap Bottom

5.4 Thermo-structural Analysis

5.4.1 Description of the input and output

The results from the heat transfer analysis have been written into a file in the format required for nonlinear transient thermo-structural analysis. The temperature data have been written in the format such that all the nodal temperatures are sorted and segregated as a table applicable for NASTRAN solver. 16 tables have been identified for the input phase of the temperature loads and 2 tables for the corresponding pressures.

The isotropic and anisotropic materials cards has been defined for the analysis. NASTRAN has anisotropic material card as input not orthotropic. So the input values are entered as orthotropic in PATRAN which in turn writes the anisotropic cards for NASTRAN. The MAT9 and MATT9 cards have been written (34 numbers) in the format required for defining the temperature dependent inputs. 34 local coordinate systems have been used to define the material orientations of the structure. The above methodology has been adopted to define the temperature dependent material cards for all the identified preforms. The NASTRAN cards required for carrying out analysis are given in section E.2 of Appendix E for a typical preform.

5.4.2 Results and discussions

The stress field in the Nosecap has been studied based on the three locations viz., nosecap tip, cap to cone junction and nosecap bottom for all the identified preforms. Variation of stress with time has been plotted typically for TTOW-1-1 and is shown in fig 5.48 to 5.53. All the six stresses are compared at the three identified locations and it is found that the stresses are maximum at cap to cone junction. Similar behaviour is seen for other preforms also. Hence for comparison purpose, stresses have been taken at the cap to cone junction for identifying the preform with highest margin. The comparison of stresses of the six preforms is given in fig 5.54 to 5.59 and that of the displacements is shown in fig 5.60. The von-Mises stresses of the 6 preforms at the Inconel bracket and at Titanium ring are compared and are given in fig 5.61 and 5.62 respectively.

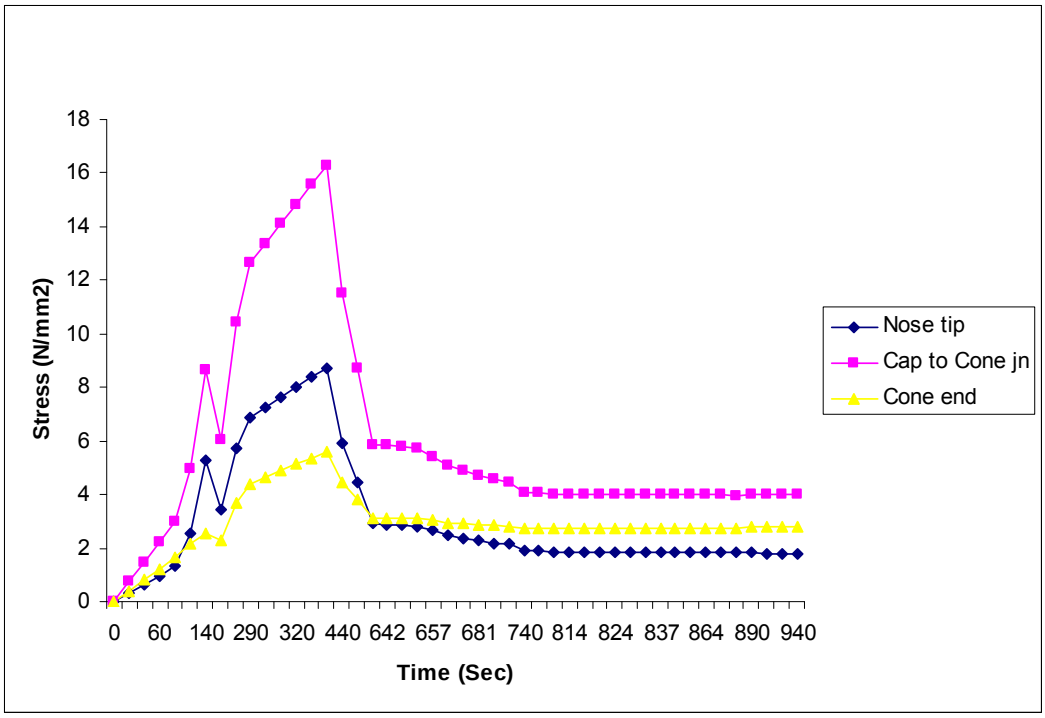

Fig 5.48 Variation of S_{XX} with Time at Three Critical Zones of Nosecap

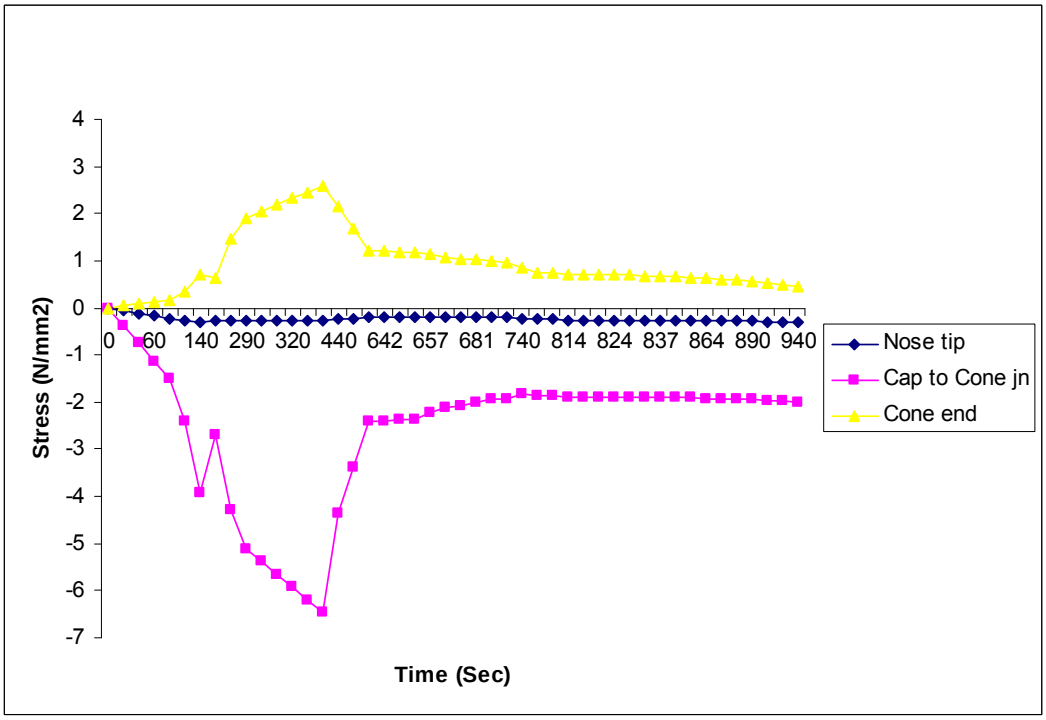

Fig 5.49 Variation of S_{YY} with Time at Three Critical Zones of Nosecap

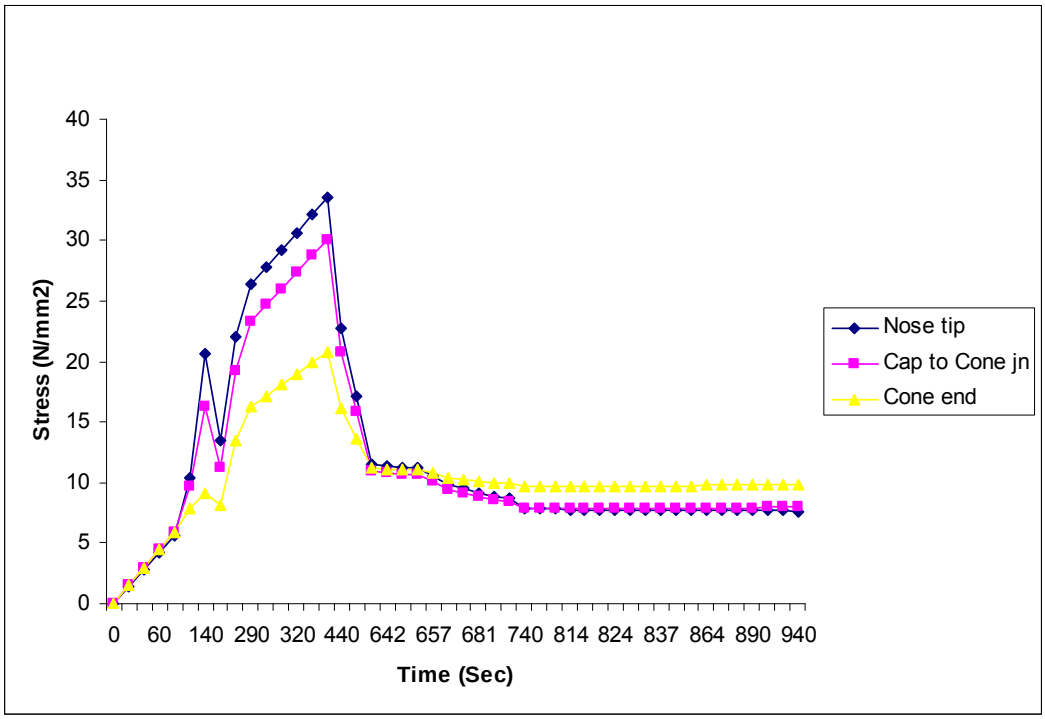

Fig 5.50 Variation of S_{ZZ} with Time at Three Critical Zones of Nosecap

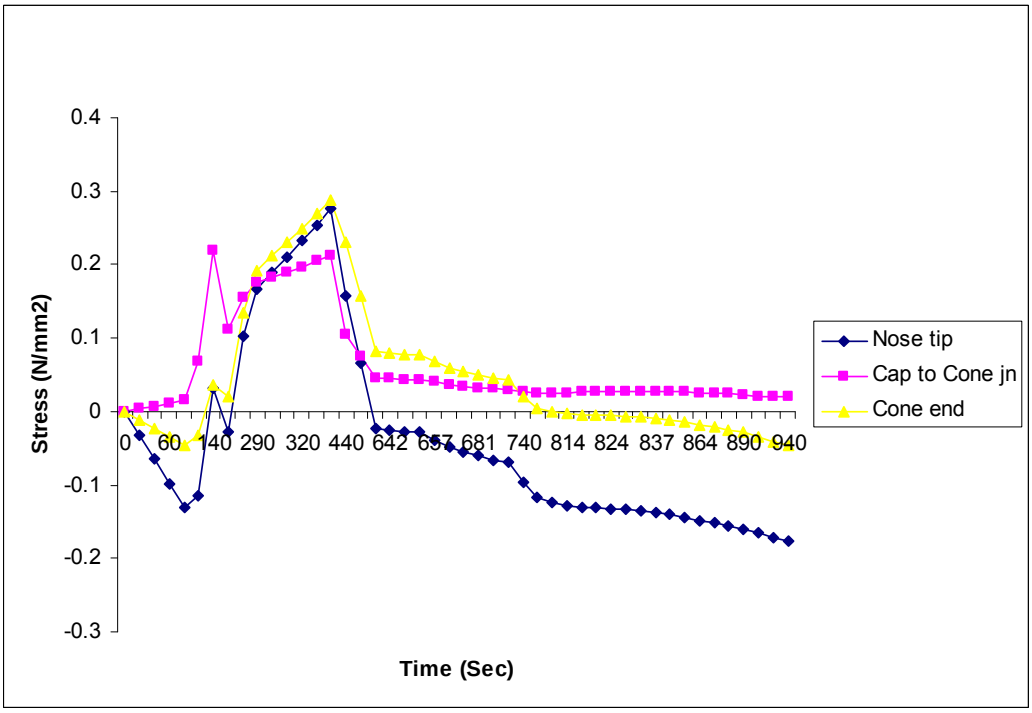

Fig 5.51 Variation of S_{XY} with Time at Three Critical Zones of Nosecap

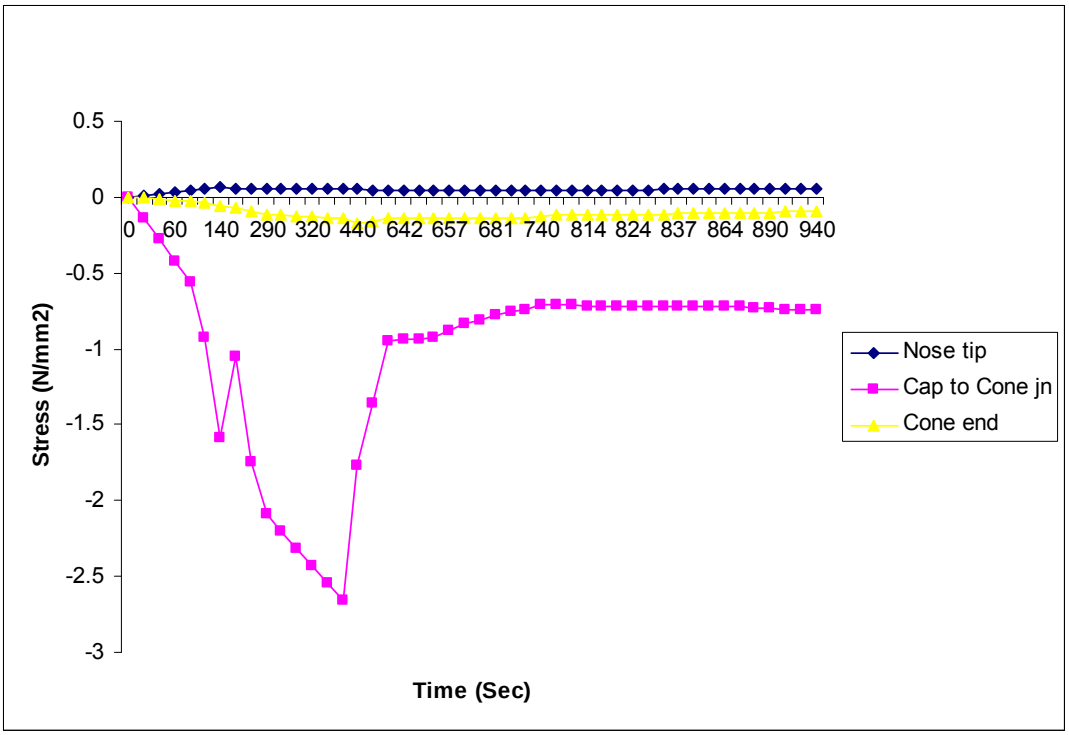

Fig 5.52 Variation of S_{YZ} with Time at Three Critical Zones of Nosecap

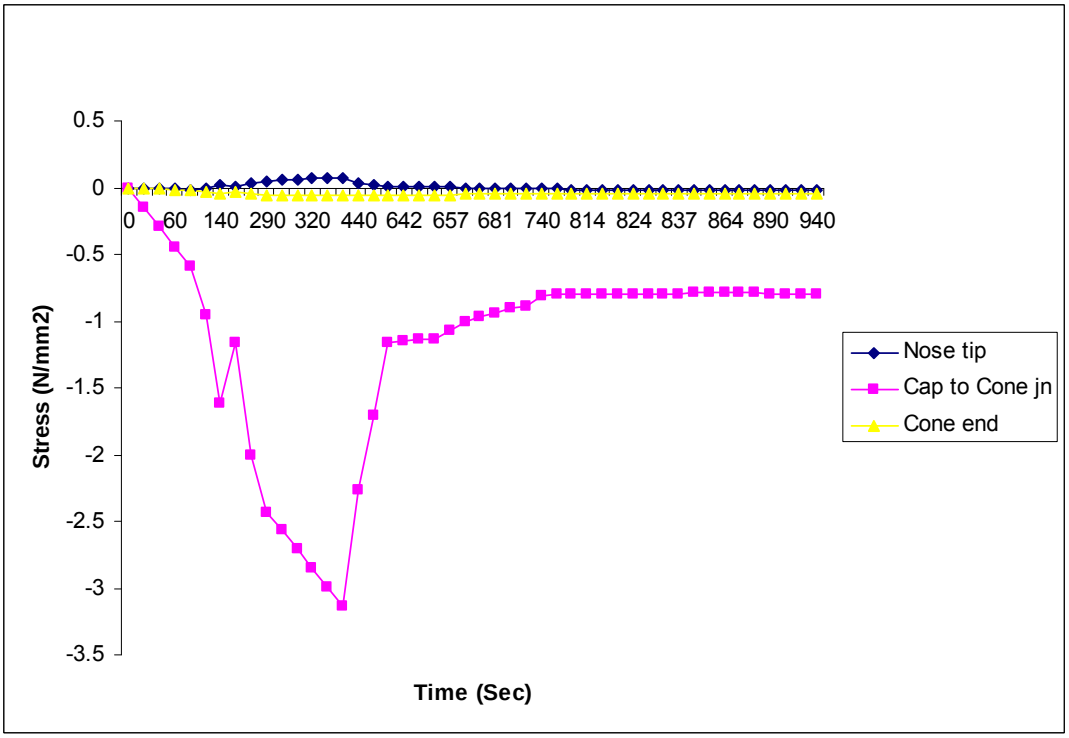

Fig 5.53 Variation of S_{ZX} with Time at Three Critical Zones of Nosecap

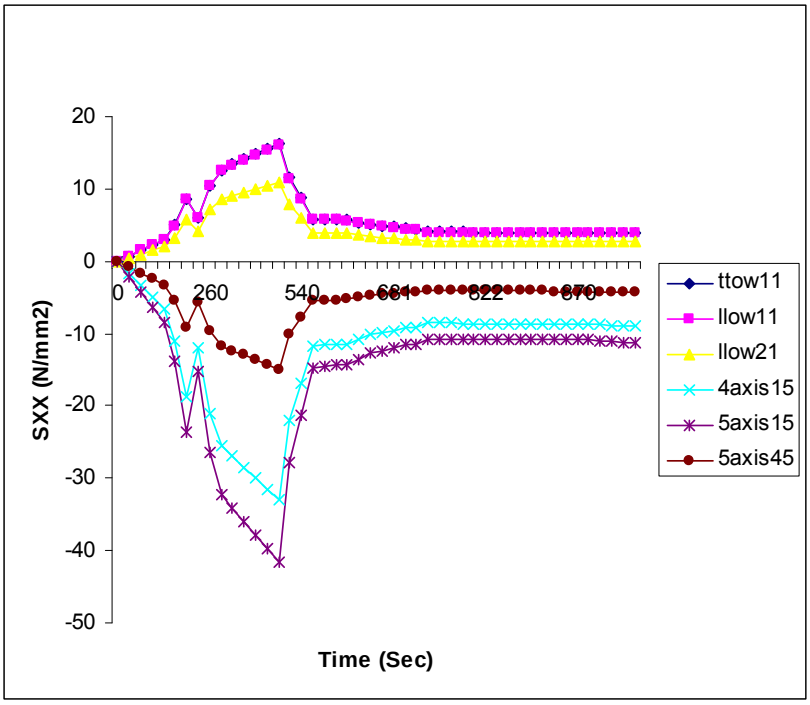

Fig 5.54 Variation of S_{XX} with Time for the Selected Preforms

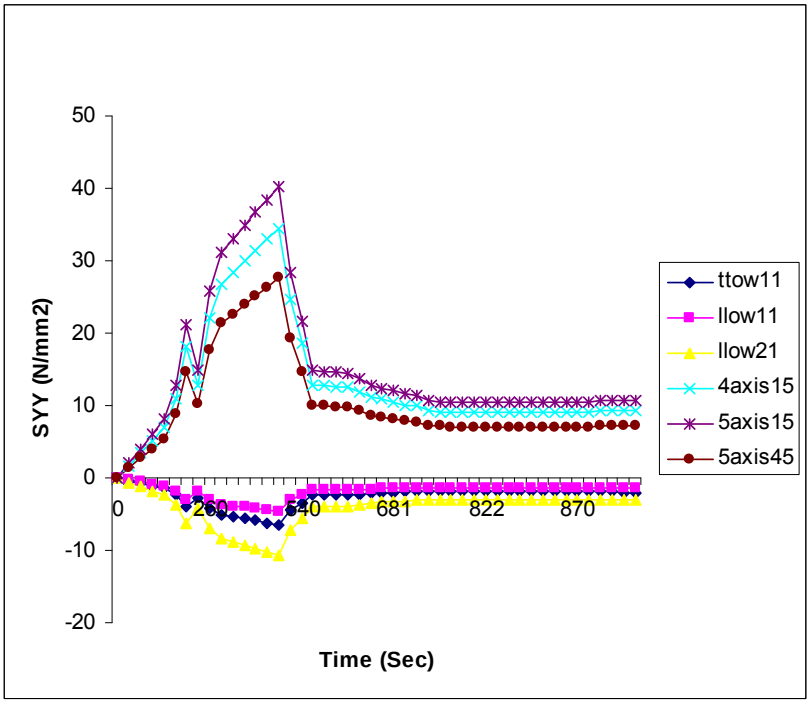

Fig 5.55 Variation of S_{YY} with Time for the Selected Preforms

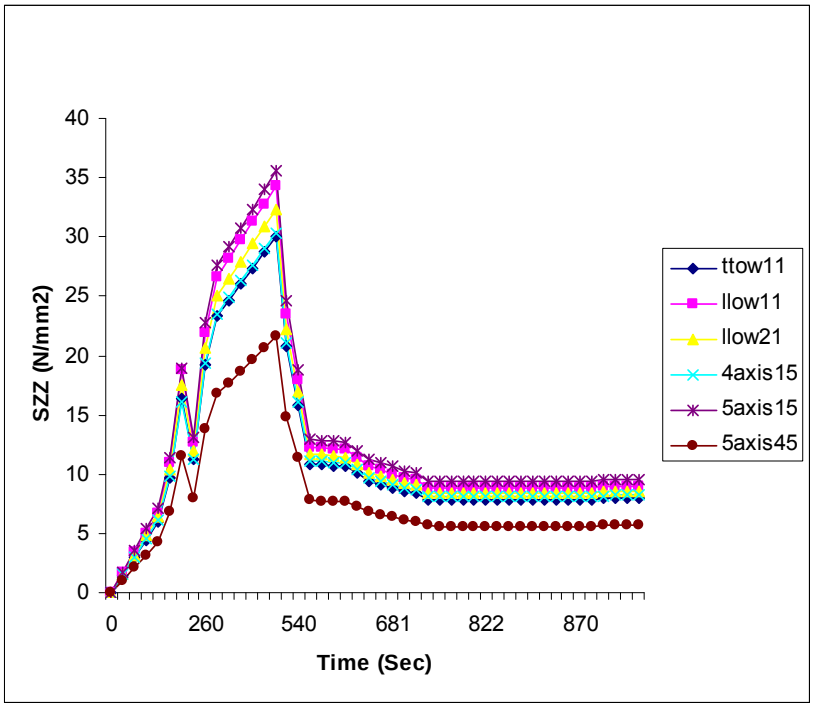

Fig 5.56 Variation of S_{ZZ} with Time for the Selected Preforms

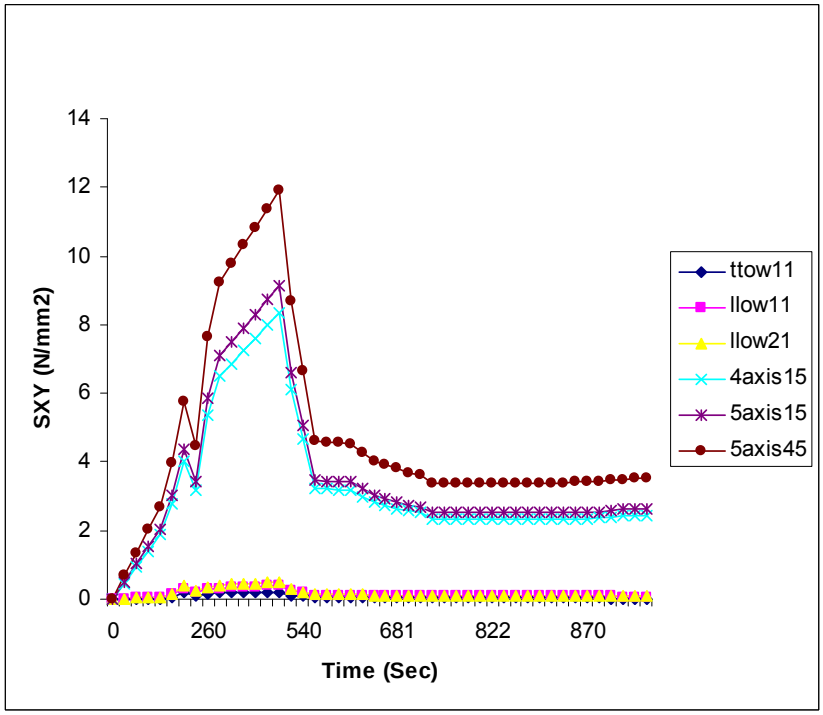

Fig 5.57 Variation of S_{XY} with Time for the Selected Preforms

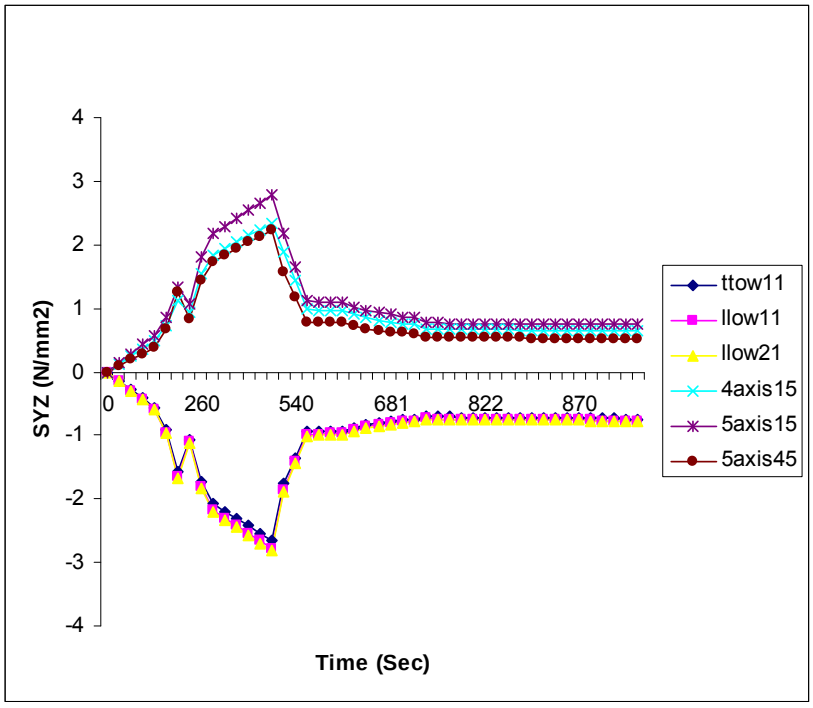

Fig 5.58 Variation of S_{YZ} with Time for the Selected Preforms

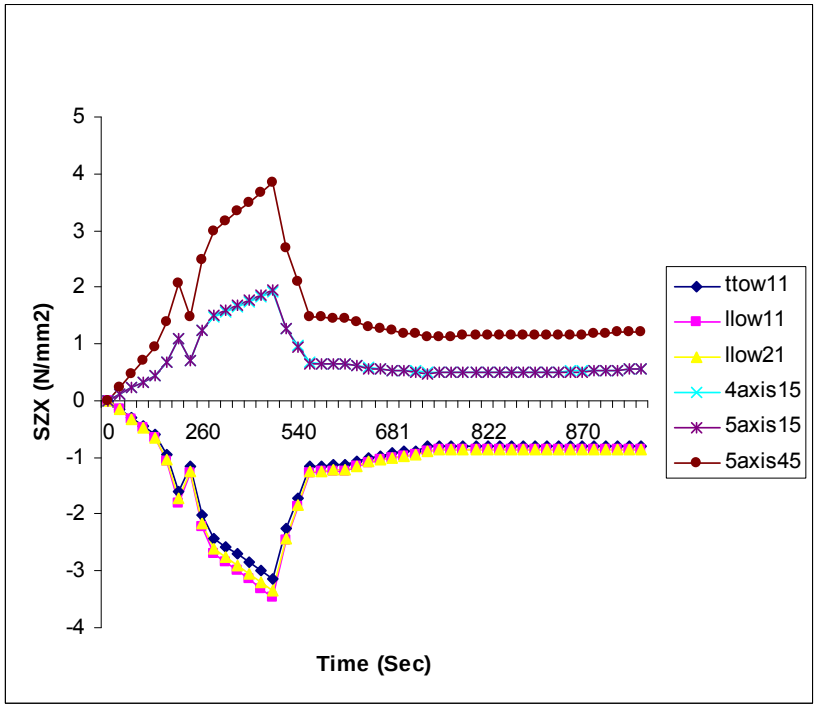

Fig 5.59 Variation of S_{ZX} with Time for the Selected Preforms

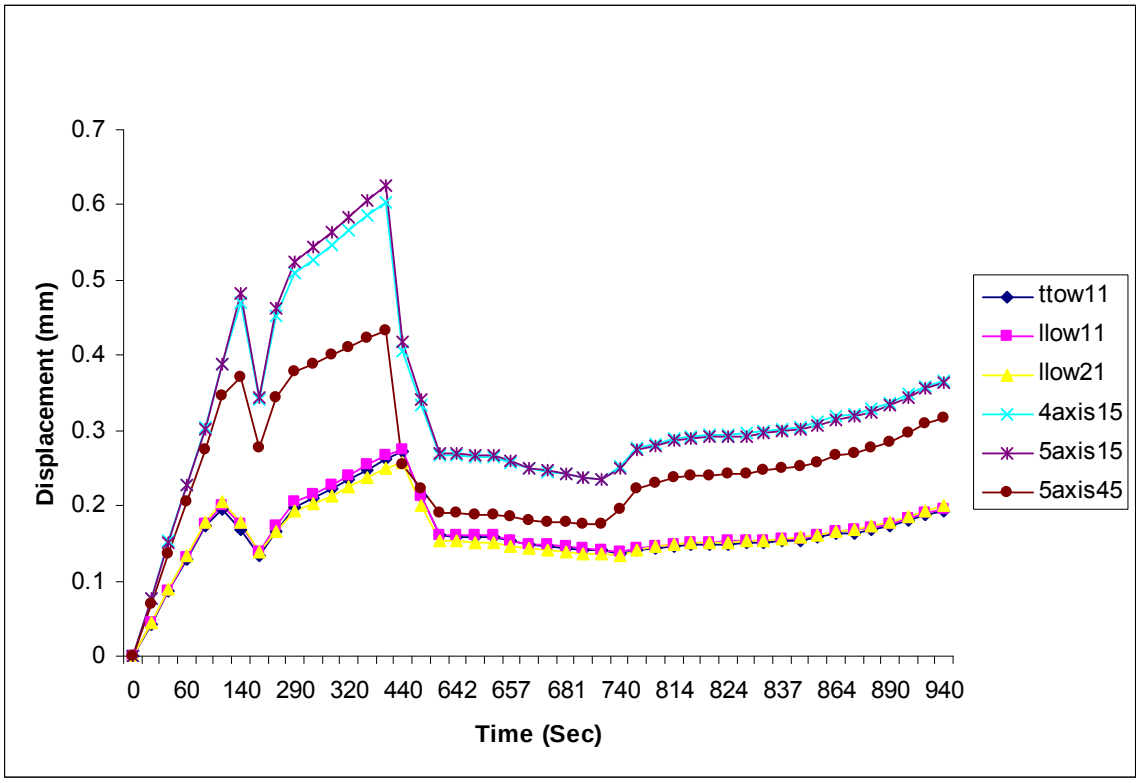

Fig 5.60 Variation of Displacement of 3D Composites with Time

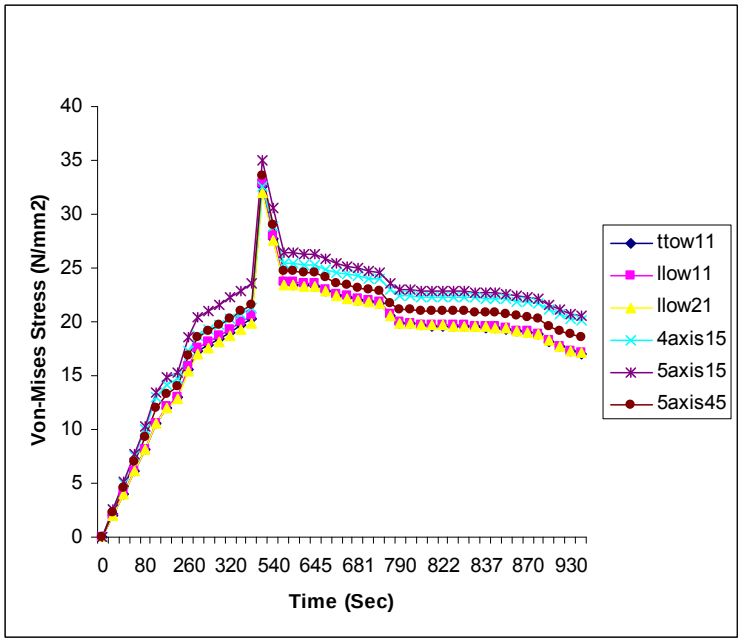

Fig 5.61 Variation of von-Mises Stress of Inconel Bracket with Time

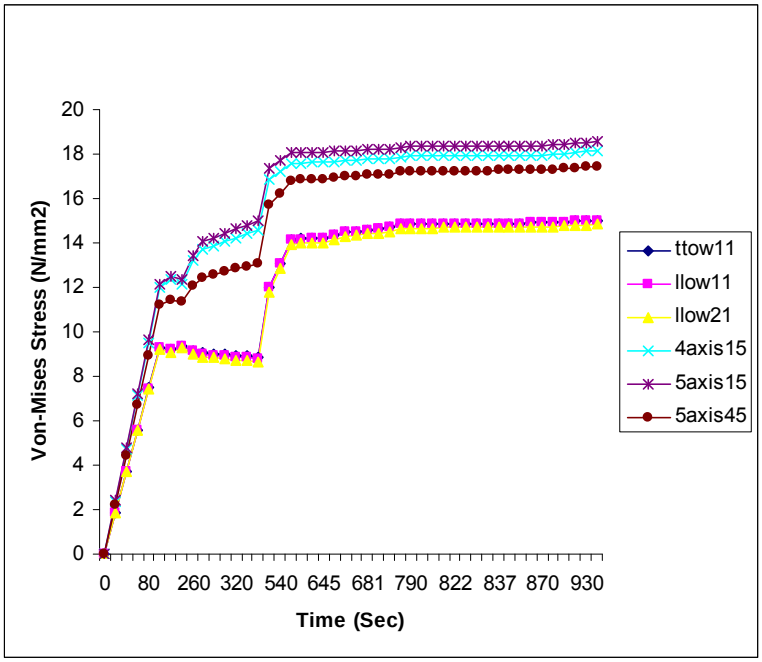

Fig 5.62 Variation of von-Mises Stress of Titanium Ring with Time

The first displacement peak occur 140 seconds and the second at 340 seconds. It comes down suddenly upto 690 seconds and gradually increases upto touchdown. The above phenomenon is attributed to the combined effect of thermal and structural loads. The maximum displacement of 0.63mm is noticed at 340 seconds on 5-axis 15^{o}. Whereas LLOW-2-1 gives a minimum displacement of 0.248mm at 340 seconds. Almost $3/4^{th}$ order of the above value is seen at the touchdown instant. It can be observed from the displacement profile that the maximum stiffness of the structure is available when made out of LLOW-2-1 for woven composites and 5-axis 45^{o} for braided composites. The overall deflections are within the acceptable allowable limits (5 mm).

It can be seen from the above stress plots that first stress peak occur at 140 seconds and the second one at 340 seconds. From this peak it suddenly reduces upto 640 seconds and subsequently decreases upto 880 seconds and then stabilizes further up to touchdown. It can be observed from the heat flux and the resulting thermal profile on the Nosecap that the peaks in the thermal loads appear approximately at 140 and 340 seconds. The maximum stress in all the 3D preforms has been noticed at 340 seconds accordingly. Stresses slightly increase from the nominal value towards the end of the mission due to the increase in pressure load towards the end of the mission. The stresses of the nosecap are more dominated by the thermal loads than the pressure loads. Stress components are

compared at cap to cone junction for the 6 preforms and the maximum stress values are shown in table 5.4.

Table 5.4 Comparison of Stresses at Cap to Cone Junction

Stress	Maximum		Time (Sec)
	Preform type	Value (N/mm^2)	
S_{xx}	5-axis 15°	-41.66	340
S_{yy}	5-axis 15°	40.26	340
S_{zz}	5-axis 15°	35.59	340
S_{xy}	5-axis 45°	11.9	340
S_{yz}	LLOW-2-1	-2.81	340
S_{zx}	5-axis 45°	3.83	340
von-Mises Inconel	5-axis 15°	35.06	440
von-Mises Titanium	5-axis 15°	18.53	touchdown

The stresses in Inconel and Titanium are within the allowable limits of the materials and can readily be used in the design. Both the peak stresses which may be taken as the design stress as well as the allowable stress for each of the six materials differ. Hence the selection of the best 3D composite material can be made only after applying a suitable failure criterion.

5.5 Failure Analysis

5.5.1 Tsai- Hill failure theory

Simple failure theory for an isotropic material is based on finding the principal normal stresses and the maximum shear stresses. These maximum stresses, if greater than any of the corresponding ultimate strengths, indicate failure of the material. In 3D composites, the failure theories are neither based on principal stresses nor based on maximum shear stresses, but on the stresses in the material or local axes. 3D failure theory has to be employed to predict the failure index of RUC of a 3D composite.

Tsai-Hill failure theory is a unified theory which considers the interaction between the strength parameters, unlike other failure theories. This theory is based on the distortion energy failure theory of von-Mises distortional energy yield criterion for isotropic materials as applied to anisotropic materials (Jones 1979). Distortion energy is actually a part of the total strain energy in a body. The strain energy in a body consists of two parts - one due to a change in volume and is called the dilation energy and the second due to change in shape and is called the distortion energy. It is assumed that the failure in the material takes place only when the distortion energy is greater than the failure distortion energy of the material. Based on the distortion energy theory, the failure of a lamina has been identified by the following criterion.

$$(G_2 + G_3)\sigma_1^{2-} + (G_1 + G_3)\sigma_2^2 + (G_1 + G_2)\sigma_3^2 - 2\,G_3\,\sigma_1\,\sigma_2 - 2\,G_2\,\sigma_1\,\sigma_3 - 2\,G_1\,\sigma_2\,\sigma_3 + 2\,G_4\,I_{23}^2 + 2\,G_5\,I_{13}^2 + 2\,G_6\,I_{12}^2 < 1 \quad (5.1)$$

The components G_1, G_2, G_3, G_4, G_5 and G_6 of the strength criterion depend on the failure strengths. The LHS equation is called failure index.

When σ_1, σ_2, σ_3 and τ_{12} are equal to X, Y, Z and S, eqn. 5.1 reduces to $G_2 + G_3 = 1/X^2$, $G_1 + G_3 = 1/Y^2$, $G_1 + G_2 = 1/Z^2$ and $2\,G_6 = 1/S^2$ respectively.

It can further be simplified and put as,

$$\begin{aligned} 2\,G_1 &= \frac{1}{Y^2} + \frac{1}{Z^2} - \frac{1}{X^2} \\ 2\,G_2 &= \frac{1}{X^2} + \frac{1}{Z^2} - \frac{1}{Y^2} \\ 2\,G_3 &= \frac{1}{X^2} + \frac{1}{Y^2} - \frac{1}{Z^2} \end{aligned} \quad (5.2)$$

5.5.2 Results and discussions

The failure index of the RUC's of the six 3D composite preforms studied herein have been plotted against time and shown in fig 5.63.

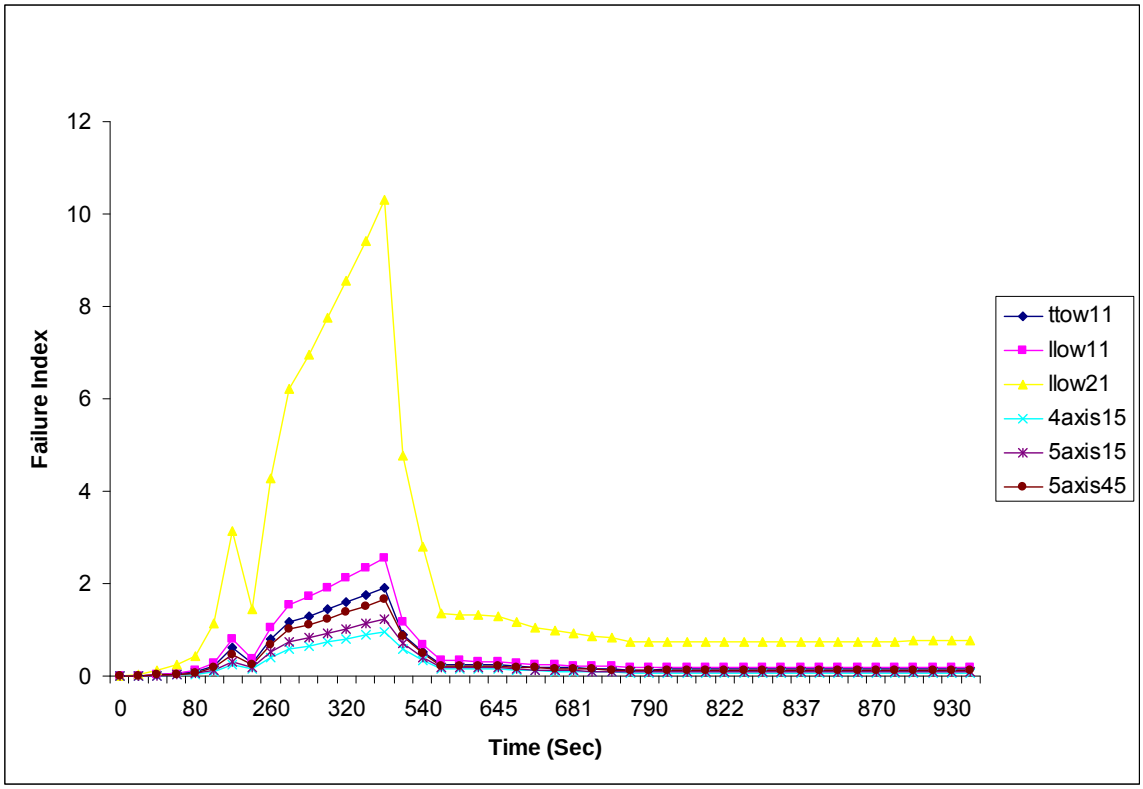

Fig 5.63 Failure Indices of 3D Composites

It can be noted from the failure index graph that the failure index is the lowest for the 4-axis 15^{o} braided composite and hence this is the best material for the selected application. The second best is 5-axis 15^{o} braided composite. It can be clearly made out from the index curves that the woven composites are not the suitable candidates since their index curves are not satisfying the failure criteria. The best among woven composite is TTOW-1-1 which gives the second best overall stiffness.

CHAPTER 6

SUMMARY AND CONCLUSIONS

6.1 Summary

The generic unidirectional properties are derived from the fabric properties using analytical methods for Carbon-Carbon material and the procedure is validated using the available data. Formulations for generating 3D thermomechanical properties for woven and braided composites are developed. The results from the formulations are validated using the data available in literature. Properties are generated as a function of temperature for 3D woven and braided composites considering 8 different types of woven composites and 6 different types of braided composites. From the above predicted data 6 preforms have been identified for carrying out analysis for application in a Nosecap. Nonlinear transient thermal and nonlinear transient thermo-structural analysis have been carried out for all the 6 materials and the stresses and displacements are estimated. The failure indices have been estimated for the 6 cases and it is seen that 4-axis 15^{o} braided composite is the best candidate for the application of Nosecap.

6.2 Conclusions

The major findings and conclusions of the present study are as follows,

- A methodology has been established to generate elastic, strength and thermal properties of 3D composites from the unidirectional properties using 3D constitutive equations. Computer code has been developed for this purpose, validated and is operational in PC environment to generate the thermomechanical properties of the RUC.
- High temperature material properties of unidirectional Carbon-Carbon material are determined from the Carbon-Carbon fabric properties using the analytical methods, viz., Composite Cylinder Assemblage Model and Method of Cells.

- Mathematical formulations are developed based on “3D Composite Strength Model” to generate 3D composite thermomechanical properties from Representative Unit Cells (RUC’s) based on constitutive equations for 3D composites.
- Computer code has been generated using MATLAB and validated using the data from the experimental investigations available in literature. The code is used to generate the 3D composite properties which can be used for the analysis and design of hot structures.
- Procedure for the structural design of hot structures made of 3D Carbon-Carbon composites has been established through the numerical investigations on a Nosecap. Selection criteria have been formulated and 6 preforms are identified from among the 14 preforms investigated, which are generally recommended for Nosecap application.
- Nonlinear transient thermal and nonlinear transient thermo-structural analysis on the Nosecap have been carried out and based on the stresses and displacements and subsequent application of the 3D failure theory the best preform for the Nosecap has been identified as 4-axis 15^{o} braided composite.

6.3 Scope for Future Work

- Validation of the 3D property generation computer code using the test results of specimens generated for the specific application.
- Improvement of the analytical model for predicting thermomechanical properties by providing Knock down and Crimp Reduction factors from experimental investigations.
- Development of finite elements for the analysis of 3D composites.

REFERENCES

1. **Aboudi, J.** (1991) *Mechanics of composite materials, a unified micromechanical approach*. Elsevier publications.
2. **Bigaud, D., L. Dreano.** and **P. Hamelin** (2005) Models of interactions between process, microstructure and mechanical properties of composite materials a study of the interlock layer-to-layer braiding technique., *Composite Structures;* 67:99-114.
3. **Bogdanovich, A. E.** and **C. M. Pastore** (1996) Theory of anisotropic elastic media. *Mechanics of textile and laminated composites*; London: Chapman & Hall, pp. 507-508.
4. **Boisse, P., A. Gasser.** and **G. Hivet** (2001) Analyses of fabric tensile behavior: determination of the biaxial tension strain surfaces and their use in forming simulations. *Composites Part A*; 32:1395 414.
5. **Byun, J. H.** and **T. W. Chou** (1989) Modelling and characterization of textile structural composites: a review. *J Strain Anal*; 4:253.
6. **Byun, J. H.** and **T. W. Chou** (1996) Process microstructure relationships of 2-step and 4-step braided composites. *Composites Science and Technology*; 56:235-251.
7. **Byun, J. H.** (2000) The analytical characterization of 2D braided textile composites. *Composites Science and Technology*; 60:705-716.
8. **Chen, B.** and **T. W. Chou** (1999) Compaction of woven fabric preforms in liquid composite molding processes: single layer deformation. *Composites Science and Technology*; 59:1519-26.
9. **Chen, L., X. M. Tao.** and **C. L. Choy** (1999[1]) On the microstructure of three-dimensional braided preforms. *Composites Science and Technology*; 59:391-404.
10. **Chen, L., X. M. Tao.** and **C. L. Choy** (1999[2]) Mechanical analysis of 3D braided composites by the finite multiphase element method. *Composites Science and Technology*; 59:2383-91.
11. **Chen, B.** and **T. W. Chou** (2000) Compaction of woven fabric performs: nesting and multilayer deformation. *Composites Science and Technology*; 60:2223-31.
12. **Chen, B., A. H. D. Cheng.** and **T. W. Chou** (2001) A nonlinear compaction model for fibrous performs. *Composites Part A*; 32:701-707.
13. **Chou, T. W.** and **F. K. Ko** (1989) *Textile structural composites*. Amsterdam: Elsevier.
14. **Chou, T. W.** (1992) Three dimensional textile structural composites. *Microstructural design of fiber composites*. Cambridge, U.K.: Cambridge University Press.
15. **Clayton, W. A.** (1971) Constituent and composite thermal conductivities of phenolic-carbon and phenolic-graphite ablators. *AIAA*; Paper no. 71-380.

16. **Cox, B. N., M. S. Dadkhah, W. L. Morris.** and **J. G. Flintoff** (1994[1]) Failure mechanisms of 3D woven composites in tension, compression and bending. *Acta Metallurgica et Materialia*, 42:3967-3984.
17. **Cox, B. N., W. C. Carter.** and **N. A. Fleck** (1994[2]) A binary model of textile composites I. Formulation. *Acta Metallurica et Materialia*, 42:3463-3479.
18. **Cox, B. N.** (1995[1]) Modelling the properties of 3D woven composites. *Mechanics of Textile Composites Conference*, NASA CP 3311, Part 1, pp. 55-59.
19. **Cox, B. N.** (1995[2]) *Failure Models for Textile Composites*, NASA CR 4686.
20. **Cox, B. N.** and **M. S. Dadkhah** (1995) The Macroscopic Elasticity of 3D Woven Composites. *Journal of Composite Materials*; 29:785-819.
21. **Cox, B. N., J. Xu, M. A. McGlockton.** and **W. C. Carter** (1995) A binary Model of Textile Composites II. The Elastic Regime. *Acta Metallurgica et Materialia*, 43:3511-3524.
22. **Dasgupta, A.** and **R. K. Agarwal** (1992) Orthotropic thermal conductivity of plain weave fabric composites using a homogenization technique. *Journal of Composite Materials*; 26:2736-2758.
23. **De Boer, H., F. V. Keulen.** and **R. Wever** (1998) Simulating forming processes of fabric reinforced composites by applying optimisation. *AIAA*-98-4842.
24. **Du, G. W., P. Popper.** and **T. W. Chou** (1991) Analysis of 3D textile preforms for multidirectional reinforcement of composites. *Journal of Material Science;* 26:3438-48.
25. **Du, G. W.** and **F. K. Ko** (1993) Unit cell geometry of 3D braided structures. *Journal of Reinforced Plastics and Composites*; 12:752-768.
26. **Falzon, P. J.** and **I. Herszbergl** (1998) Mechanical performance of 2D braided carbon/epoxy composites. *Composites Science and Technology*; 58:253-265.
27. **Ganesh, V. K.** and **N. K. Naik** (1994) Thermal expansion coefficients of plain weave fabric laminates. *Composites Science and Technology*; Vol. 51, pp.387-408.
28. **Ganesh. V. K.** and **N. K. Naik (**1996[1]) Failure behavior of plain weave fabric laminates under on-axis uniaxial tensile loading: I – Laminate Geometry. *Journal of Composite materials*; 30:1748-1778.
29. **Ganesh. V. K.** and **N. K. Naik** (1996[2]) Failure behavior of plain weave fabric laminates under on-axis uniaxial tensile loading: II – Analytical predictions. *Journal of Composite materials*; 30:1779-1822.
30. **Ganesh, V. K.** and **N. K. Naik** (1996[3]) Failure behavior of plain weave fabric laminates under on-axis uniaxial tensile loading: III – Effect of fabric geometry. *Journal of Composite Materials*; Vol. 30:1823-1856.
31. **Glaessgen, E. H., C. M. Pastore, O. H. Griffin.** and **A. Birger** (1996) Geometrical and finite element modelling of textile composites. *Composites Part B*; 27B:43-50.

32. **Harri, K.** and **Helsinki** (1998) Structural and Thermal Analysis of Carbon Composite Electronics Housing for a Satellite, Timo Brander & Markus Wallin, Helsinki University of Technology, Laboratory of Lightweight Structures, Espoo, Finland.
33. **Harte, A. M.** and **N. A. Fleck** (2000) Deformation and failure mechanisms of braided composite tubes in compression and torsion. *Acta Materialia*; 48:1259-1271.
34. **Hartranft, D., A. P. Majidi.** and **T. W. Chou (**1995) Modeling and characterization of through the thickness properties of 3D woven composites. *Mechanics of Textile Composites Conference*, NASA CP 3311, Part 2, pp. 251-313.
35. **Hashin, Z.** (1972) *Theory of Fibre Reinforced Materials*, NASA CR 1974.
36. **Hofstee, J.** and **F. V. Keulen (**2001) 3D geometric modelling of a draped woven fabric. *Composite Structures*; 54:179-95.
37. **Hu, J.** and **A. Newton** (1997) Low load lateral compression behavior of woven fabrics. *J. Text. Inst. Part 1*; 88:242-54.
38. **Huang, Z. M.** (2000) The mechanical properties of composites reinforced with woven and braided fabrics. *Composites Science and Technology*; 60:479-498.
39. **Ishikawa, T., N. Watanabe, K. Bansaku.** and **Y. Ono** (1997) Closed Form Predictions of Macroscopic Thermomechanical Properties of Orthogonal 3 D Woven Fabric Composites. *Proceedings of the Eleventh International Conference on Composite Materials*, Volume V, M. L. Scott, ed, Woodhead Publishing Limited, Cambridge, UK, pp. V.189 V.200.
40. **Jones, R. M.** (1979) *Mechanics of composite materials*.
41. **Kalidindi, S. R.** and **A. Abusafieh** (1996) Longitudinal and transverse moduli and strength of low angle 3D braided composites. *Journal of Composite Materials*; 30:885-905.
42. **Kamiya, R., B. A. Cheeseman, P. Popper.** and **T. W. Chou** (2000) Some recent advances in the fabrication and design of three dimensional textile performs: a review. *Composites Science and Technology*; 60:33-47.
43. **Kilroy, K.** (1998) MSC/NASTRAN Version 70.5 Quick Reference Guide, MacNeal Schwendler Corporation, USA.
44. **Ko, F. K.** (1982) Three dimensional fabrics for composites - An introduction to the Magnaweave structure. Proc. ICCM-4, Japan Soc. *Composite Materials*, Tokyo, Japan, p. 1609.
45. **Ko, F. K.** (1986) Tensile strength and modulus of a three dimensional braid. *Composite materials testing and design (seventh conference)*, ASTM STP, vol. 893; p. 392.
46. **Ko, F. K.** (1989) Three Dimensional Fabrics for Composites. *Textile Structural Composites*; T.W. Chou and F. K. Ko, eds, Elsevier, Amsterdam, pp. 129-171.

47. **Ko, F. K.** (1999) 3D textile reinforcements in composite materials. *In: Miravate A, editor. 3D textile reinforcements in composite materials*. Cambridge, UK: Woodhead Publishing Limited, pp. 9-42.
48. **Kostar, T. D.** and **T. W. Chou** (1992) Design and automated fabrication of 3D braided preforms for advanced structural composites. *Composite Materials Technology III*; Elsevier Science Publishers, p. 63.
49. **Kostar, T. D.** and **T. W. Chou** (1999) Braided structures. In: *Miravete A, editor. 3D textile reinforcements in composite materials*. Cambridge, UK: Woodhead Publishing Limited, 1999. pp. 217-240.
50. **Kumar, S.** and **Y. Wang** (1997) *Fibers, fabrics and fillers*. In: Mallick PK, editor. Composites engineering handbook. New York: Marcel Dekker, Inc., pp. 78-100.
51. **Kuo, W. S.** (1995) Elastic behavior and damage of three dimensional woven fabric composite. *Proceedings of the Tenth International Conference on Composite Materials*, Volume IV, A. Poursatip and K. Street, eds, Wodhead Publishing Limited, Cambridge, UK, pp. IV.301 IV.308.
52. **Kuo, W. S.** and **H. I. Chin** (1997) Fabrication and micro geometry of two-step braided composites incorporating pultruded rods. *Composites Science and Technology*; 57:1457-1467.
53. **Kuo, W. S., T. H. Ko.** and **H. I. Chin** (1998) Elastic moduli and damage mechanisms in 3D braided composites incorporating pultruded rods. *Composites Part A*; 29A:681-692.
54. **Lei, C., Y. J. Cai,** and **F. K. Ko** (1992) Finite element analysis of 3D braided composites. *Advances Engineering Software and Workstations*. Elsevier Science Publishers, p. 187.
55. **Li, W.** (1990) *On the structural mechanics of 3D braided preforms for composites*. PhD Thesis, North Carolina State University, USA, March.
56. **Li, W.** and **A. Shiekh** (1998) The effect of processes and processing parameters on 3D braided preforms for composites. *SAMPE Quart*., 19-22.
57. **Lomov, S. V., G. Huysmans, Y. Luo, R. S. Parnas, A. Prodromou.** and **I. Verpoest** (2001) Textile composites: modelling strategies. *Composites Part A*; 32:1379-94.
58. **Mattioni, F., A. Gatto, P. M. Weaver, M. I. Friswell.** and **K. D. Potter** (1998) The application of residual stress tailoring of snap-through composites for variable sweep wings. University of Bristol, Bristol, BS8 1TR, UK.
59. **Miravete, A., J. M. Bielsa, A. Chiminelli, J. Cuartero, S. Serrano, N. Tolosana.** and **R. G. D. Villoria** (2006) A 3D mesomechanical analysis of three-axial braided composite materials. *Composites Science and Technology*; 66:2954-2964.

60. **Mohajerjasbi, S.** (1998) Fiber architecture of three dimensional braided composites. *AIAA Journal*; 36:613-617.
61. **Mouritz, A. P., M. K. Bannister, P. J. Falzon.** and **K. H. Leong** (1999) Review of applications for advanced three dimensional fiber textile composites. *Composites: Part A*; 30:1445-1461.
62. **Nagai, K., A. Yokoyama, Z. Maekawa.** and **H. Hamada** (1994) The stress analysis method for three dimensional composite materials. *Applied Composite Materials*; 1:197-216.
63. **Naik, N. K.** (1994) *Woven Fabric Composites*, Technomic publishing co. Inc., Lancaster, PA.
64. **Naik, N. K.** and **B. J. Thuruthimattam** (1998[1]) Mechanical characterization of hybridized 3D orthogonally woven composites. *Proceedings of the 39th AIAA/ASME/ASCE/AHS/ASC Structures*, Structural Dynamics and Materials Conference, Part 2, AIAA 98 1809, pp. 953-961.
65. **Naik, N. K.** and **B. J. Thuruthimattam** (1998[2]) Behavior of 3D orthogonally woven composites under tensile loading, *Technical Report No. IITB/AE/ISRO/3D/TR/98/01*, IIT, Mumbai.
66. **Naik, N. K.** and **B. J. Thuruthimattam** (1999) Behavior of 3D orthogonally woven composites under tensile loading. *Journal of Composites Technology & Research*; 21:153-163.
67. **Naik, N. K.** and **N. M. Azad** (2001) Stress and failure analysis of 3D orthogonal / angle interlock woven composites under tensile loading. *Technical report, IITB/AE/ISRO/3D/TR/2001/02*, Aerospace engineering department, IIT Bombay.
68. **Naik, N. K.** and **E. Sridevi** (2001) An analytical method for thermoelastic analysis of 3D orthogonal interlock woven composites. *Technical report, IITB/AE/ISRO/3D/TR/2001/03*, Aerospace engineering department, IIT Bombay.
69. **Naik[b], R. A., P. G. Ifju.** and **J. E. Masters (**1994) Effect of fiber architecture and parameters on deformation fields and elastic moduli of 2D braided composites. *Journal of Composite Materials*; 28:656-681.
70. **Naik[b], R. A.** (1995) Failure analysis of woven and braided fabric reinforced composites. *Journal of Composite Materials*; 29:2334-2363.
71. **Ning, Q. G.** and **T. W. Chou** (1995) Closed form solutions of the inplane effective thermal conductivities of woven fabric composites. *Composites science and technology*; 55:41-48.
72. **Ning, Q. G.** and **T. W. Chou** (1998) A general analytical model for predicting the transverse effective thermal conductivities of woven fabric composites. *Composites Part A*; 29A:315-322.

73. **NISA II** Users Manual (1997) EMRC, INDIA.
74. **Paley, M.** and **J. Aboudi** (1992) Micromechanical analysis of composites by the generalized cells model. *Mechanics of Materials*; 14:127-139.
75. **Pandey, R.** and **H. T. Hahn** (1996[1]) Designing with 4-step braided fabric composites. *Composites Science and Technology*; 56:623-634.
76. **Pandey, R.** and **H. T. Hahn** (1996[2]) Visualization of representative volume elements for three dimensional four-step braided composites. *Composites Science and Technology*; 56:161-170.
77. **Ramesh, K. R.** (2004) Thermo-structural analysis of composite structures. *Banarus International Conference,* Calcutta.
78. **Robitaille, F.** and **R. Gauvin** (1998) Compaction of textile reinforcements for composites manufacturing. I: Review of experiments results. *Polymer Composites*; 19:198-216.
79. **Sagar, T. V., P. Potluri.** and **J. W. S. Hearle** (2003) Textile Composites Group. Mesoscale modelling of interlaced fiber assemblies using energy method. *Comput Mater Sci*; 28:49-62.
80. **Sankar, B. V.** and **R. V. Marrey** (1997[1]) Analytical method for Micromechanics of textile composites. *Composites Science and Technology*; 57:707-713.
81. **Sankar, B. V.** and **R. V. Marrey** (1997[2]) A Micromechanical model for textile composite plates. *Journal of Composite Materials*; 31:1187-1213.
82. **Santhosh, B.** (2010) *Codes for Thermomechanical analysis of 3D composites*. *Technical Report,* DST/CUSAT/PHD/CODE/01, Department of Ship Technology, CUSAT.
83. **Senthil, S. V.** (2002) Three-dimensional analysis of transient thermal stresses In functionally graded plates. R.C. Batra, Department of Engineering Science and Mechanics, Virginia Polytechnic Institute and State University, Blacksburg, USA.
84. **Shanahan, W. J.** and **J. W. S. Hearle** (1978) An energy method for calculations in fabric mechanisms. Part II: Examples of applications of the method to woven fabrics. *J. Text Inst*; 69:92-100.
85. **Stuart, M. L.** (1990) Braiding. In: Stuart ML, editor. *Encyclopedia of composites*. New York: VCH Publisher, pp. 130-147.
86. **Sun, H. Y.** and **X. Qiao** (1997) Prediction of the mechanical properties of three dimensionally braided composites. *Composites Science and Technology*; 57:623-9.
87. **Tan, P., L. Tong.** and **G. P. Steven** (1997) A three dimensional modelling technique for predicting the linear elastic property of opened packing woven fabric unit cell. *Composite Structures*; 38:261-271.

88. **Tan, P., L. Tong.** and **G. P. Steven** (1998) Modeling approaches for 3D orthogonal woven composites. *Journal of Reinforced Plastics and Composites*; 17:545-577.
89. **Tan, P., L. Tong.** and **G. P. Steven** (1999) Micromechanics models for mechanical and thermomechanical properties of 3D through the thickness angle interlock woven composites. *Composites: Part A*; 30A:637-648.
90. **Tang, Z. X.** and **R. Postle** (2000) Mechanics of three dimensional braided structures for composite materials- part-I: fabric structure and fiber volume fraction. *Composite Structures*; 49:451-459.
91. **Tang, Z. X.** and **R. Postle** (2001) Mechanics of three dimensional braided structures for composite materials- part-II: prediction of elastic moduli. *Composite Structures*; 51:451-7.
92. **Tang, Z. X.** and **R. Postle** (2002) Mechanics of three dimensional braided structures for composite materials- part-III: nonlinear finite element analysis. *Composite Structures*; 55:307-17.
93. **Tao, Z., L. Wu.** and **L. Guo** (2004[1]) Predicting the nonlinear response and failure of 3D braided composites. *Materials Letters*, 58:3237-3241.
94. **Tao, Z., L. Wu.** and **L. Guo** (2004[2]) A finite element model for failure analysis of 3D braided composites. *Materials Science and Engineering* A; 366:144-151.
95. **Tarnopolskii, Y. M., I. G. Zhigun.** and **V. A. Polyakov** (1992) *Spatially Reinforced Composites*, Technomic Publishing Company, Inc., Lancaster, PA.
96. **Thomas, C. M., S. Gajbir.** and **G. V. Rao** (1992) Thermal buckling of cross ply composite laminates. *Composite and Structures*; Vol42, No.2, pp, 281-287.
97. **Wang, Y. Q.** and **A. S. D. Wang** (1995[1]) Geometric mapping of yarn structures due to shape change in 3D braided composites. *Composites Science and Technology*; 54:359-370.
98. **Wang, Y. Q.** and **A. S. D. Wang** (1995[2]) On the topological yarn structure of 3D rectangular and tubular braided preforms. *Composites Science and Technology*; 51:575-586.
99. **Wang, Y.** and **X. Sun** (2001) Digital element simulation of textile processes. *Composites Science and Technology*; 61(2):311-9.
100. **Whitney, T. J.** and **T. W. Chou** (1989) Modelling of 3D angle interlock textile structural composite materials. *Journal of composite Materials*; 23:890 911.
101. **William, L. K., D. Q. Robert.** and **G. Leslie** (1986) Finite element reentry heat transfer analysis of space shuttle orbiter. Ames Research Center, Dryden Flight Research Facility, Edwards, California, *NASA Technical Paper* 2657.

102. **William, L. K.** and **H. J. Raymond** (1991) Thermal behavior of a Titanium honeycomb core sandwich panel, Ames Research Center, Dryden Flight Research Facility, Edwards, California, National Aeronautics and Space Administration, Ames Research Center, Dryden Flight Research Facility Edwards, California 93523-0273.
103. **William, L. K.** (1997) Thermo-structural behavior of a hypersonic aircraft sandwich panel subjected to heating on one side, Dryden Flight Research Center, Edwards, California, *NASA Technical Memorandum 4769*.
104. **William, L. K.** (1998) Mechanical and thermal-buckling behavior of rectangular plates with different central cutouts, Dryden Flight Research Center,Edwards, California National Aeronautics and Space Administration, Dryden Flight Research Center Edwards, California 93523-0273.
105. **William, L. K.** and **G. Leslie** (2001) Thermo-structural analysis of unconventional wing structures of a Hyper-X hypersonic flight research vehicle for the Mach 7 mission, NASA Dryden Flight Research Center, Edwards, California.
106. **Wu, D. L.** (1996) Three-cell model and 5D braided structural composites. *Composites Science and Technology*; 56:225-33.
107. **Yang, J. M., C. L. Ma.** and **T. W. Chou** (1986) Fiber inclination model of three-dimensional textile structural composites. *Journal of Composites Materials*; 20:472-484.
108. **Zuorong, C., Z. Dechao, M. Lu.** and **L. Ye** (1999) Evaluation of elastic properties of 3D (4-step) regular braided composites by a homogenization method. *Composite Structures*; 47:477-482.

Appendix A

Composite Cylinder Assemblage Model (CCA)

The Composite Cylinder Assemblage (CCA) model gives simple closed form analytical expressions for the effective composite moduli E_L, G_{LT}, ν_{LT} and k, while the moduli G_{TT} and E_T are bracketed by close bounds. Here, the UD composite cylinder consists of the inner circular fibre and the outer concentric matrix shell. The fibre and matrix are considered to be transversely isotropic.

The transverse bulk modulus of the UD composite is given by

$$k = \frac{k^m\left(k^f + G_{TT}^m\right)\left(1-V_f\right) + k^f\left(k^m + G_{TT}^m\right)V_f}{\left(k^f + G_{TT}^m\right)\left(1-V_f\right) + \left(k^m + G_{TT}^m\right)V_f} \tag{A.1}$$

Where

$$\frac{1}{k^f} = \frac{4}{E_{TT}^f} - \frac{4\nu_{LT}^{f^2}}{E_L^f} - \frac{1}{G_{TT}^f} \tag{A.2}$$

$$\frac{1}{k^m} = \frac{4}{E_{TT}^m} - \frac{4\nu_{LT}^{m^2}}{E_L^m} - \frac{1}{G_{TT}^m} \tag{A.3}$$

The longitudinal Young's modulus of the UD composite is given by eqn. A.4.

$$E_L = E_L^f V_f + E_L^m V_m + \frac{4(\nu_{LT}^f - \nu_{LT}^m)^2 V_m V_f}{V_m/k^f + V_f/k^m + 1/G_{TT}^m} \tag{A.4}$$

The longitudinal Poisson's ratio and shear modulus are given by eqn. A.5 and A.6.

$$\nu_{LT} = \nu_{LT}^f V_f + \nu_{LT}^m V_m + \frac{(\nu_{LT}^f - \nu_{LT}^m)^2 (1/k^m - 1/k^f) V_f V_m}{V_m/k^f + V_f/k^m + 1/G_{TT}^m} \tag{A.5}$$

$$G_{LT} = G_{LT}^m + \frac{G_{LT}^m V_m + G_{LT}^f (1+V_f)}{G_{LT}^m (1+V_f) + G_{LT}^f V_m} \tag{A.6}$$

The transverse shear modulus and the transverse young's modulus are bracketed by close bounds. The bounds of G_{TT} are given by eqn. A.7 to A.11.

$$G_{TT(-)} = G_{TT}^m + \frac{V_f}{1/(G_{TT}^f - G_{TT}^m) + (k^m + 2G_{TT}^m)V_m / 2G_{TT}^m(k^m + G_{TT}^m)} \tag{A.7}$$

$$G_{TT(+)} = G_{TT}^{m} + \left\{ 1 + \frac{(1+\beta_1)V_f}{\rho - V_f\,(1+(3\beta_1^2 V_m^2)/(\alpha V_f^3 + 1)} \right\} \qquad \text{(A.8)}$$

when

$G_{TT}^{f} > G_{TT}^{m}$ and $k^{f} > k^{m}$

Whereas

$$G_{TT(+)} = G_{TT}^{m} + \frac{V_f}{1/(G_{TT}^{f} - G_{TT}^{m}) + (k^{m} + 2G_{TT}^{m})V_m / 2G_{TT}^{m}(k^{m} + G_{TT}^{m})} \qquad \text{(A.9)}$$

$$G_{TT(-)} = G_{TT}^{m} + \left\{ 1 + \frac{(1+\beta_1)V_f}{\rho - V_f\,(1+(3\beta_1^2 V_m^2)/(\alpha V_f^3 - \beta_1)} \right\} \qquad \text{(A.10)}$$

when

$G_{TT}^{f} < G_{TT}^{m}$ and $k^{f} < k^{m}$

Here

$$\alpha = \frac{\beta_1 - \gamma\beta_2}{1+\gamma\beta_2}; \quad \rho = \frac{\gamma+\beta_1}{\gamma-1} \qquad \text{(A.11)}$$

$$\beta_1 = \frac{k^{m}}{k^{m} + 2G_{TT}^{m}}; \quad \beta_2 = \frac{k^{f}}{k^{f} + 2G_{TT}^{f}}$$

$\gamma = G_{TT}^{f} / G_{TT}^{m}$ $\qquad V_m = 1 - V_t$

The bounds of E_T are given by eqn. A.12.

$$E_{T(\pm)} = \frac{4kG_{TT(\pm)}}{k + mG_{TT(\pm)}} \qquad \text{(A.12)}$$

Where,

$$m = 1 + \frac{4kv_{LT}^2}{E_L}$$

The longitudinal thermal expansion coefficients of the composite with transversely isotropic fibres and isotropic matrix are given by following equations.

$$\alpha_L = \alpha_m + \left(\alpha_L^f - \alpha^m\right)\left[P_{11}\left(S_{11}^* - S_{11}\right) + 2P_{12}\left(S_{12}^* - S_{12}\right)\right] + 2\left(\alpha_T^f - \alpha^m\right)$$
$$\times\left\{P_{12}\left(S_{11}^* - S_{11}\right) + \left(P_{22} + P_{23}\right)\left[S_{12}^* - S_{12}\right]\right\} \quad \text{(A.13)}$$

$$\alpha_T = \alpha_m + \left(\alpha_L^f - \alpha^m\right)\left[P_{11}\left(S_{12}^* - S_{12}\right) + 2P_{12}\left(S_{22}^* + S_{23}^* - (S_{22} + S_{23})\right)\right] + 2\left(\alpha_T^f - \alpha^m\right)$$
$$\times\left\{P_{12}\left(S_{12}^* - S_{12}\right) + 0.5\left(P_{22} + P_{23}\right)\left[S_{22}^* + S_{23}^* - \left(S_{22} + S_{23}\right)\right]\right\} \quad \text{(A.14)}$$

where,

$$P_{11} = \left(\Delta S_{22} + \Delta S_{23}\right)/D;\ P_{12} = -\Delta S_{12}/D;\ P_{22} + P_{23} = \Delta S_{11}/D \quad \text{(A.15)}$$

$$D = \Delta S_{11}\left(\Delta S_{22} + \Delta S_{23}\right) - 2\Delta S_{12}^2 \quad \text{(A.16)}$$

$$\Delta S_{11} = 1/E_L^f - S_{11};\ \Delta S_{12} = -\nu_{LT}^f/E_L^f - S_{12} \quad \text{(A.17)}$$

$$\Delta S_{22} + \Delta S_{23} = 1/2\left(1/k^f + 4\nu_{LT}^{f\,2}/E_L^f\right) - \left(S_{22} + S_{23}\right) \quad \text{(A.18)}$$

$$S_{11} = 1/E_m;\ S_{12} = -\nu^m/E^m;\ S_{22} + S_{23} = \left(1 - \nu^m\right)/E^m \quad \text{(A.19)}$$

$$S_{11}^* = 1/E_L;\ S_{12}^* = -\nu_{LT}/E_L \quad \text{(A.20)}$$

$$S_{22}^* + S_{23}^* = 0.5\left(1/k + 4\nu_{LT}^2\right)/E_L \quad \text{(A.21)}$$

Appendix B

Micromechanical Analysis of Composite Materials by Method of Cells (Aboudi's method)

B.1 Introduction

The method of cells relies on the assumption that the two phase composite has a periodic structure. Here the reinforcing material fiber is arranged in a periodic manner, forming a periodic array. Here the representative element is analysed rather than the whole composite and the representative element is defined as the building block. Here for the representative element, displacement and traction continuity is imposed at the interfaces of the element as well as at the interfaces of the neighboring elements in conjunction with equilibrium conditions. Here the relations between average stress and strain are obtained assuming both fiber and resin as elastic materials, from which the elastic properties can be determined.

For simplicity purpose assumed the array having four subcells, one will be fiber and the other three matrices. Here fiber is assumed as a square cross section. The actual geometry of the fiber can be traced if the number of cells is increased (fig B1) and this method is called Generalized Method of Cells (GMC).

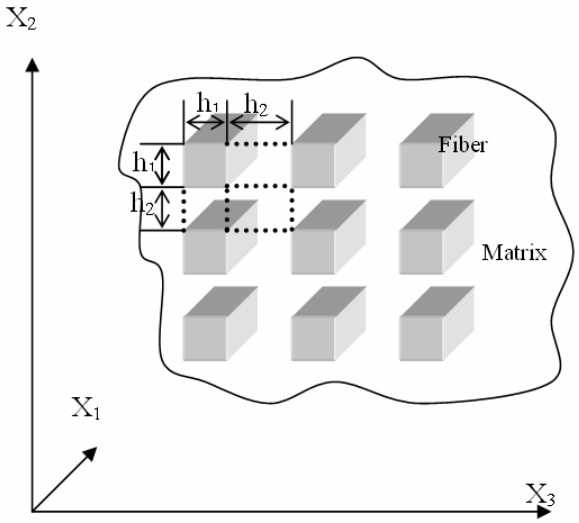

Fig B1 Periodic Array of Fibers in Matrix

Once the overall properties are extracted from the model, a transformation is employed which provides the effective transversely isotropic behavior of the unidirectional fiber composite. It provides all the independent constants, if the fiber and matrix constants and reinforcement volume fraction is known and vice versa. The same theory can be extended to predict the failure surfaces of the UD fiber composites. Here the stresses at the fiber and matrix are examined for a given system of loading.

The Repeating Unit Cell is divided into N_γ divisions in the x_3 direction and N_β divisions in the x_2 direction i.e; it is divided into N_γ x N_β subcells each having different material properties. Let 'l' and 'h' be the dimensions of the cells in the x_3 and x_2 directions and the corresponding dimensions of the subcells are h_γ and h_β respectively. x_1 axis is assumed to be the loading direction (i.e; fibers are directed in this direction). Here the displacement continuity and traction continuity are applied at the boundaries of each subcell and periodic boundary conditions at the boundaries of the unit cell.

B.2 Assumptions

1. Let the displacement vector be $u = \{u_1, u_2, u_3\}^T$.

   $$\nabla u^{(\beta v)} = \nabla u^{(\beta v)} \tag{B.1}$$

   The gradient of displacement vector in a subcell is constant and is equal to its value at the center of each unit cell.
2. Assumed uniform deformation field 'w' in the RUC and displacement gradient Δw is uniform through out the RUC.
3. Displacement gradient in the subcells are such that,

   $$\frac{\partial u_1^{(\beta\gamma)}}{\partial x_1} = \frac{\partial w_1}{\partial x_1} \text{ for all values of } \beta, \gamma \tag{B.2}$$

   $$u_{i_{x_{2=h}}} = u_{i_{x_{2=0}}} + \frac{\partial w_i}{\partial x_2}.h \tag{B.3}$$

   $$u_{i_{x_{3=l}}} = u_{i_{x_{3=0}}} + \frac{\partial w_i}{\partial x_3}.l \tag{B.4}$$

Now from assumption 1 (constant gradient) B.3 & B.4 can be written as.

$$u_{i_{x_{2=h}}} = u_{i_{x_{2=0}}} + \sum_{\beta}^{N_\beta} \frac{\partial u_i^{\beta\gamma}}{\partial x_2} h_\beta \tag{B.5}$$

$$u_{i_{x_{3=l}}} = u_{i_{x_{3=0}}} + \sum_{\gamma}^{N_\gamma} \frac{\partial u_i^{\beta\gamma}}{\partial x_3} l_\gamma \tag{B.6}$$

from B.3 and B.5

$$\sum_{\beta}^{N_\beta} h_\beta \frac{\partial u_i^{\beta\gamma}}{\partial x_2} = \frac{\partial w_i}{\partial x_3} h \text{ for } \gamma = 1, N_\gamma \tag{B.7}$$

from B.4 and B.6

$$\sum_{\gamma}^{N_\gamma} l_\gamma \frac{\partial u_i^{\beta\gamma}}{\partial x_3} = \frac{\partial w_i}{\partial x_3} l \text{ for } \beta = 1, N_\beta \tag{B.8}$$

equations B.7 and B.8 satisfies the displacement continuity condition.

B.3 Effective average strain

The average strain for the unit cell is,

$$\bar{\varepsilon}_{ij} = \frac{1}{hl} \sum_{\gamma}^{N_\gamma} \sum_{\beta}^{N_\beta} h_\beta . l_\gamma . \varepsilon_{ij}^{(\beta\gamma)} \tag{B.9}$$

where subcell strains are,

$$\varepsilon_{ij}^{(\beta\gamma)} = \frac{1}{2}\left(\frac{\partial u_i^{\beta\gamma}}{\partial x_j} + \frac{\partial u_j^{\beta\gamma}}{\partial x_i} \right) \tag{B.10}$$

Following equations shows that the continuity conditions are satisfied.

From B.9 and B.10 and using B.2

$$\bar{\varepsilon}_{11} = \frac{\partial w_1}{\partial x_1} \tag{B.11}$$

$$\bar{\varepsilon}_{12} = \frac{1}{hl} \sum_{\gamma}^{N_\gamma} \sum_{\beta}^{N_\beta} \frac{1}{2}\left(\frac{\partial u_1^{(\beta\gamma)}}{\partial x_2} + \frac{\partial u_2^{(\beta\gamma)}}{\partial x_1} \right) h_\beta . l_\gamma \tag{B.12}$$

$$\bar{\varepsilon}_{12} = \frac{1}{hl} \sum_{\gamma}^{N_\gamma} \sum_{\beta}^{N_\beta} \frac{1}{2}\left(h_\beta . \frac{\partial u_i^{(\beta\gamma)}}{\partial x_2} + h_\beta . \frac{\partial u_2^{(\beta\gamma)}}{\partial x_1} \right) . l_\gamma \tag{B.13}$$

Using eqn. B.7

$$\bar{\varepsilon}_{12} = \frac{1}{l} \sum_{\gamma}^{N_\gamma} \frac{1}{2}\left(\frac{\partial w_1}{\partial x_2} + \frac{\partial w_2}{\partial x_1} \right) . l_\gamma \tag{B.14}$$

or

$$\bar{\varepsilon}_{12} = \frac{1}{2}\left(\frac{\partial w_1}{\partial x_2} + \frac{\partial w_2}{\partial x_1} \right) \tag{B.15}$$

in a similar manner it can be shown that,

$$\bar{\varepsilon}_{13} = \frac{1}{2}\left(\frac{\partial w_1}{\partial x_3} + \frac{\partial w_3}{\partial x_1} \right) \tag{B.16}$$

$$\bar{\varepsilon}_{22} = \frac{\partial w_2}{\partial x_2} \tag{B.17}$$

$$\bar{\varepsilon}_{23} = \frac{1}{2}\left(\frac{\partial w_2}{\partial x_3} + \frac{\partial w_3}{\partial x_2} \right) \tag{B.18}$$

$$\bar{\varepsilon}_{33} = \frac{\partial w_3}{\partial x_3} \tag{B.19}$$

The equations in terms of subcell and effective strain components defines subcell and global strains in matrix form.

From eqn. B.2 and B.11

$$\bar{\varepsilon}_{11} = \varepsilon_{11}^{(\beta\gamma)} \text{ for all } \beta, \gamma \tag{B.20}$$

From eqn. B.7 and B.17

$$\bar{\varepsilon}_{22}.h = \sum_{\beta}^{N_\beta} \varepsilon_{22}^{(\beta\gamma)}.h_\beta \text{ for } \gamma = i, \ldots N_\gamma \tag{B.21}$$

From eqn. B.7 and B.15 and using B.2

$$\bar{\varepsilon}_{12}.h = \frac{1}{2}\left(\sum_{\beta}^{N_\beta}.h_\beta . \frac{\partial u_1^{(\beta\gamma)}}{\partial x_2} + \sum_{\beta}^{N_\beta}.h_\beta . \frac{\partial u_2^{(\beta\gamma)}}{\partial x_1} \right) \tag{B.22}$$

$$\bar{\varepsilon}_{12}.h = \sum_{\gamma}^{N_\gamma} \varepsilon_{12}^{(\beta\gamma)}.h_\beta, \qquad \gamma = 1, \ldots N_\gamma \tag{B.23}$$

Similarly from eqn. B.8

$$\bar{\varepsilon}_{33}.l = \sum_{\gamma}^{N_\gamma} \varepsilon_{33}^{(\beta\gamma)}.l_\gamma, \qquad \beta = 1, \ldots N_\beta \tag{B.24}$$

and

$$\bar{\varepsilon}_{13}.l=\sum_{\gamma}^{N_\gamma}\varepsilon_{13}^{(\beta\gamma)}.l_\gamma, \qquad \beta=1,\ldots N_\beta \tag{B.25}$$

Now applying definition of average strain to $\bar{\varepsilon}_{23}$ yields

$$\bar{\varepsilon}_{23}.hl=\sum_{\beta}^{N_\beta}\sum_{\gamma}^{N_\gamma}\varepsilon_{23}^{(\beta\gamma)}.h_\beta.l_\gamma, \tag{B.26}$$

Equations B.20, B.21, B.23, B.24, B.25 and B.26 can be written in matrix form as

$$A_G\,\varepsilon_s=J\,\bar{\varepsilon} \tag{B.27}$$

Where, $\varepsilon_s=\left\{\varepsilon^{11},\varepsilon^{12},.....,\varepsilon^{N_\beta N_\gamma}\right\}^T$ contains the subcell strains.

$\bar{\varepsilon}=\left\{\bar{\varepsilon}_{11},\bar{\varepsilon}_{22},\bar{\varepsilon}_{33},2\bar{\varepsilon}_{23},2\bar{\varepsilon}_{13},2\bar{\varepsilon}_{12}\right\}^T$ contains effective average strains. A_G and J are matrices which contains geometric information of the subcell and unit cell respectively.

Now applying ***Traction Continuity Conditions***

From the fig B1, it can be written as,

$$\sigma_{22}^{(\beta\gamma)}=\sigma_{22}^{(\beta+1,\gamma)}\text{, for } \beta=1\text{ to }N_\beta-1\text{ and }\gamma=1\text{to }N_\gamma \tag{B.28}$$

Eqn. B.27 yields a system of $2\left(N_\beta+N_\gamma\right)+N_\beta N_\gamma+1$ containing the $6\,N_\beta\,N_\gamma$ unknown subcell strains. The remaining $5N_\beta N_\gamma-2\left(N_\beta+N_\gamma\right)-1$ equations are provided by the traction continuity conditions at the subcell interface. So $\left(N_\beta-1\right)\text{x}\,N_\gamma$ number of equations exists for traction continuity.

Similarly,

$$\sigma_{33}^{(\beta\gamma)}=\sigma_{33}^{(\beta,\gamma+1)}\text{, for } \beta=1\text{ to }N_\beta\text{ and }\gamma=1\text{to }N_\gamma-1 \tag{B.29}$$

$$\sigma_{23}^{(\beta\gamma)}=\sigma_{23}^{(\beta+1,\gamma)}\text{, for } \beta=1\text{ to }N_\beta-1\text{ and }\gamma=1\text{to }N_\gamma \tag{B.30}$$

$$\sigma_{32}^{(\beta\gamma)}=\sigma_{32}^{(\beta,\gamma+1)}\text{, for } \beta=N_\beta\text{ and }\gamma=1\text{to }N_\gamma-1 \tag{B.31}$$

i.e; 1 x $N_\gamma-1$ number of equations.

$$\sigma_{21}^{(\beta\gamma)}=\sigma_{21}^{(\beta+1,\gamma)}\text{, for } \beta=1\text{to }N_\beta-1\ \ \gamma=1\text{to }N_\gamma \tag{B.32}$$

$$\sigma_{31}^{(\beta\gamma)} = \sigma_{31}^{(\beta,\gamma+1)} \text{, for } \beta = 1 \text{ to } N_\beta \text{ and } \gamma = 1 \text{ to } N_\gamma - 1 \quad \text{(B.33)}$$

By using elasticity relationships,

$$\sigma^{(\beta\gamma)} = C^{(\beta,\gamma)}.\varepsilon^{(\beta,\gamma)} \quad \text{(B.34)}$$

Where, $C^{(\beta\gamma)}$ is the elasticity stiffness matrix of subcell (β,γ) and $\varepsilon^{(\beta\gamma)} = \{\varepsilon_{11}, \varepsilon_{22}, \varepsilon_{33}, 2\varepsilon_{23}, 2\varepsilon_{13}, 2\varepsilon_{12}\}^T$

From B.34 and using B.29, B.30, B.31, B.32, and B.33, another set of equations like B.27 are obtained.

$$A_M \varepsilon_s = 0 \quad \text{(B.35)}$$

Where, A_M is matrix containing entries of the individual elastic stiffness matrices of all subcells.

Eqn. B.27 and B.35 can be combined into

$$A \varepsilon_s = k.\bar{\varepsilon} \quad \text{(B.36)}$$

$$\text{where } A = \begin{bmatrix} A_M \\ A_G \end{bmatrix} \quad \text{(B.37)}$$

$$\text{and } k = \begin{bmatrix} O \\ J \end{bmatrix} \quad \text{(B.38)}$$

From eqn. B.36

$$\varepsilon_s = A_s.\bar{\varepsilon} \quad \text{(B.39)}$$

Where, $A_s = A^{-1} k$, is the ***concentration Matrix***.

Similar to B.39 we have analogous equation,

$$\varepsilon^{(\beta\gamma)} = A^{(\beta\gamma)}.\bar{\varepsilon} \quad \text{(B.40)}$$

It can be written as, $C^{(\beta\gamma)} \times \varepsilon^{(\beta\gamma)} = C^{(\beta\gamma)} \times A_s^{(\beta\gamma)}.\bar{\varepsilon}$

$$\sigma^{(\beta\gamma)} = C^{(\beta\gamma)}.A_s^{(\beta\gamma)}.\bar{\varepsilon} \quad \text{(B.41)}$$

and definition of average stress gives,

$$\bar{\sigma} = \frac{1}{hl}\sum_{\beta}^{N_\beta}\sum_{\gamma}^{N_\gamma} .h_\beta.l_\gamma.C^{(\beta\gamma)}.A_s^{(\beta\gamma)}.\bar{\varepsilon} \quad \text{(B.42)}$$

$$\bar{\sigma} = \bar{C}\ \bar{\varepsilon}$$

i.e; $$\bar{C} = \frac{1}{hl} \sum_{\beta}^{N_\beta} \sum_{\gamma}^{N_\gamma} .h_\beta .l_\gamma .C^{(\beta\gamma)} .A_s^{(\beta\gamma)} \quad \text{(B.43)}$$

Once $[\bar{C}]$ is obtained compliance matrix $[\bar{S}]$ can be obtained and then the elastic properties can be calculated from the following equations.

$$E_{11} = 1/\bar{S}_{11}, \nu_{12} = -\bar{S}_{12}/\bar{S}_{11}, E_{22} = 1/\bar{S}_{22}$$

$$\nu_{23} = -\bar{S}_{23}/\bar{S}_{22}; E_{33} = 1/\bar{S}_{33}, G_{23} = 1/\bar{S}_{44}\ G_{13} = 1/\bar{S}_{55}\ \ G_{12} = 1/\bar{S}_{66} \quad \text{(B.44)}$$

B.4 Reformulation of Aboudi's Method

The original formulation of GMC evaluates Hill's strain concentration matrices which relate average composite strains to $6N_\alpha N_\beta N_\gamma$ average subcell strains. The composites macroscopic behavior is defined by subcell strains. The strain concentration matrices are obtained by solving $6N_\alpha N_\beta N_\gamma$ x $6N_\alpha N_\beta N_\gamma$ system of equations constructed by applying continuity of displacements and tractions between the individual subcells, in an average sense, using a linear representation of the displacement field in each subcell. The number of subcells in the repeating unit cell will be large for three dimensional composites. i.e; the number of unknown ($6N_\alpha N_\beta N_\gamma$) subcell strains increases to a large extend.

The above defined problem is tackled by first reformulating the displacement continuity equations from the original formulation of GMC in terms of the subcell stress components using the subcell constitutive equations, and then directly imposing traction continuity conditions across the interfaces between individual subcells.

$$\sum_{\alpha} d_\alpha \varepsilon_{11}^{(\alpha\beta\gamma)} = d\bar{\varepsilon}_{11}, \quad \beta = 1,,,N_\beta, \quad \gamma = 1,,,,,N_\gamma \quad \text{(B.45)}$$

$$\sum_{\beta} d_\beta \varepsilon_{22}^{(\alpha\beta\gamma)} = h\bar{\varepsilon}_{22}, \quad \alpha = 1,,,N_\alpha, \quad \gamma = 1,,,,,N_\gamma \quad \text{(B.46)}$$

$$\sum_{\gamma} d_\gamma \varepsilon_{33}^{(\alpha\beta\gamma)} = l\bar{\varepsilon}_{33}, \quad \alpha = 1,,,N_\alpha, \quad \beta = 1,,,N_\beta \quad \text{(B.47)}$$

$$\sum_{\beta} \sum_{\gamma} h_\beta l_\gamma \varepsilon_{23}^{(\alpha\beta\gamma)} = hl\bar{\varepsilon}_{23}, \quad \alpha = 1,,,N_\alpha \quad \text{(B.48)}$$

$$\sum_{\alpha}\sum_{\gamma} d_{\alpha} l_{\gamma} \varepsilon_{13}^{(\alpha\beta\gamma)} = dl\bar{\varepsilon}_{13}, \quad \beta = 1,,, N_{\beta} \tag{B.49}$$

$$\sum_{\alpha}\sum_{\beta} d_{\alpha} h_{\beta} \varepsilon_{12}^{(\alpha\beta\gamma)} = dh\bar{\varepsilon}_{12}, \quad \gamma = 1,,, N_{\gamma} \tag{B.50}$$

The piecewise uniform character of the stress field throughout the repeating unit cell allows to relate the interfacial traction components to the average subcell stresses directly, thereby significantly reducing the number of unique unknown subcell stresses. Hence the displacement continuity equations are reformulated in terms of subcell traction components whose number is smaller than the number of unknown subcell strain components, thereby eliminating the traction continuity equations as an additional set of equations. Finally a set of mixed concentration equations that relate the unknown subcell traction components to the macroscopic composite strains and average subcell strains are obtained.

The anisotropic constitutive equations for an individual subcell considering the cells as heterogeneous can be written as,

$$\varepsilon^{(\alpha\beta\gamma)} = S^{(\alpha\beta\gamma)}\sigma^{(\alpha\beta\gamma)} + \alpha^{(\alpha\beta\gamma)}\Delta T + \varepsilon^{p(\alpha\beta\gamma)} \tag{B.51}$$

where, $S^{(\alpha\beta\gamma)} and\ \alpha^{(\alpha\beta\gamma)}$ are the anisotropic subcell compliance matrix and thermal expansion coefficient vector, and $\varepsilon^{(\alpha\beta\gamma)}$, $\sigma^{(\alpha\beta\gamma)}$, $and\ \varepsilon^{p(\alpha\beta\gamma)}$ are the subcell total strain, stress and the plastic strain vectors respectively and ΔT is the change in temperature from the reference temperature. The subcell traction continuity conditions require that at subcell and unit cell interfaces, the tractions be continuous. Since the unit cell and the subcells are parallelepipeds (fig B2), each such interface is normal to one coordinate axis.

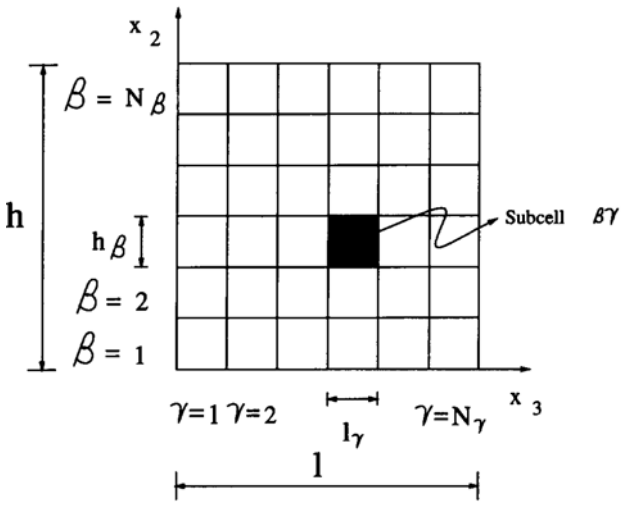

Fig B2 Discretization of the RUC

Thus, each unit normal vector for each interface is parallel to one coordinate axis, and particular subcell stress components, which are constant within a subcell are equal to traction components.

Traction components $t_i^{(n)}$ at the interfaces are,

$t_i^{(n)} = \sigma_{ij} n_j = \sigma_{ij}$, when ($n_j$ =1) and 0, when (n_j =0). (B.52)

The above equation allows each traction condition to be written in terms of one subcell component. The traction continuity conditions, which are applicable to normal subcell stress components, require that each normal stress component be constant through all subcells along the coordinate direction coincident with that subcell stress component. For example, $\sigma_{11}^{(\alpha\beta\gamma)}$ is constant when following a row of subcells through the unit cell as shown in fig B.2 in the x direction. The condition can be expressed as,

$$\sigma_{11}^{(1\beta\gamma)} = \sigma_{11}^{(2\beta\gamma)} = ... = \sigma_{11}^{(N_\alpha\beta\gamma)} = T_{11}^{(\beta\gamma)}, \quad \beta = 1,....., N_\beta, \quad \gamma = 1,....., N_\gamma \tag{B.53}$$

where $T_{11}^{(\beta\gamma)}$ denotes there is unique 11 stress component in each row of subcells along the x_1 direction. Similarly for other normal subcell stress components,

$$\sigma_{22}^{(\alpha 1\gamma)} = \sigma_{22}^{(\alpha 2\gamma)} = ... = \sigma_{22}^{(\alpha N_\beta\gamma)} = T_{22}^{(\alpha\gamma)}, \quad \alpha = 1,....., N_\alpha, \quad \gamma = 1,....., N_\gamma \tag{B.54}$$

$$\sigma_{33}^{(\alpha\beta 1)} = \sigma_{33}^{(\alpha\beta 2)} = ... = \sigma_{33}^{(\alpha\beta N_\gamma)} = T_{33}^{(\alpha\beta)}, \quad \alpha = 1,....., N_\alpha, \quad \beta = 1,....., N_\beta \tag{B.55}$$

Due to the symmetry of two traction continuity conditions for the shear stress components, two traction continuity conditions affect each subcell shear stress component. $\sigma_{23}^{(\alpha\beta\gamma)}$ is constant along x_2 direction and $\sigma_{32}^{(\alpha\beta\gamma)}$ is constant along x_3 direction. Since $\sigma_{23}^{(\alpha\beta\gamma)} = \sigma_{32}^{(\alpha\beta\gamma)}$, the 23 subcell stress component must be constant in each layer of subcells that has a constant value of α. They are expressed as,

$$\begin{matrix} \sigma_{23}^{\alpha 1\gamma} = \sigma_{23}^{\alpha 2\gamma} = ...\sigma_{23}^{\alpha N_\beta\gamma} \\ \sigma_{32}^{\alpha\beta 1} = \sigma_{32}^{\alpha\beta 2} = ...\sigma_{32}^{\alpha\beta N_\gamma} \end{matrix} ==> \sigma_{23}^{\alpha\beta\gamma} = \sigma_{32}^{\alpha\beta\gamma} = T_{23}^{\alpha}, \quad \alpha = 1,.....N_\alpha \tag{B.56}$$

where $T_{23}^{(\alpha)}$ denotes 23 stress component in each layer of subcells along the x_2 or x_3 directions. Similarly,

$$\begin{matrix} \sigma_{13}^{1\beta\gamma} = \sigma_{13}^{2\beta\gamma} = ...\sigma_{13}^{N_\alpha\beta\gamma} \\ \sigma_{31}^{\alpha\beta 1} = \sigma_{31}^{\alpha\beta 2} = ...\sigma_{31}^{\alpha\beta N_\gamma} \end{matrix} ==> \sigma_{13}^{\alpha\beta\gamma} = \sigma_{31}^{\alpha\beta\gamma} = T_{13}^{\beta}, \quad \beta = 1,.....N_\beta \tag{B.57}$$

$$\begin{matrix} \sigma_{12}^{1\beta\gamma} = \sigma_{12}^{2\beta\gamma} = ...\sigma_{12}^{N_\alpha\beta\gamma} \\ \sigma_{21}^{\alpha 1\gamma} = \sigma_{21}^{\alpha 2\gamma} = ...\sigma_{21}^{\alpha N_\beta\gamma} \end{matrix} ==> \sigma_{12}^{\alpha\beta\gamma} = \sigma_{21}^{\alpha\beta\gamma} = T_{12}^{\gamma}, \quad \gamma = 1,.....N_\gamma \tag{B.58}$$

Here the number of equations reduces to $N_\beta N_\gamma + N_\alpha N_\gamma + N_\alpha N_\beta + N_\alpha + N_\beta + N_\gamma$ unique subcell stress components, which is denoted as T_{ij}^{*}. Thus subcell stress components rather

than the $6N_\alpha N_\beta N_\gamma$ subcell strain components are employed as basic unknowns, the number of unknown quantities are reduced substantially. This increases the computational efficiency of the model.

Substituting for the subcell stress components in the subcell constitutive eqn. B.51 using eqn. B.53 to B.58, solving for the subcell total strains, and substituting into the displacement continuity eqn. B.45 to B.50 yields,

$$\sum_\alpha d_\alpha S_{11}^{(\alpha\beta\gamma)} T_{11}^{(\beta\gamma)} + \sum_\alpha d_\alpha S_{12}^{(\alpha\beta\gamma)} T_{22}^{(\alpha\gamma)} + \sum_\alpha d_\alpha S_{11}^{(\alpha\beta\gamma)} T_{33}^{(\alpha\beta)} + \sum_\alpha d_\alpha S_{14}^{(\alpha\beta\gamma)} T_{23}^{(\alpha)} + \sum_\alpha d_\alpha S_{15}^{(\alpha\beta\gamma)} T_{13}^{(\beta)}$$
$$+ \sum_\alpha d_\alpha S_{16}^{(\alpha\beta\gamma)} T_{12}^{(\gamma)} = d\bar{\varepsilon}_{11} - \sum_\alpha d_\alpha \alpha_{11}^{(\alpha\beta\gamma)} \Delta T - \sum_\alpha d_\alpha \varepsilon_{11}^{p(\alpha\beta\gamma)}, \quad \beta = 1,....N_\beta; \quad \gamma = 1,.....N_\gamma$$

(B.59)

$$\sum_\beta h_\beta S_{12}^{(\alpha\beta\gamma)} T_{11}^{(\beta\gamma)} + \sum_\beta h_\beta S_{22}^{(\alpha\beta\gamma)} T_{22}^{(\alpha\gamma)} + \sum_\beta h_\beta S_{23}^{(\alpha\beta\gamma)} T_{33}^{(\alpha\beta)} + \sum_\beta h_\beta S_{24}^{(\alpha\beta\gamma)} T_{23}^{(\alpha)} + \sum_\beta h_\beta S_{25}^{(\alpha\beta\gamma)} T_{13}^{(\beta)}$$
$$+ \sum_\beta h_\beta S_{26}^{(\alpha\beta\gamma)} T_{12}^{(\gamma)} = h\bar{\varepsilon}_{22} - \sum_\beta h_\beta \alpha_{22}^{(\alpha\beta\gamma)} \Delta T - \sum_\beta h_\beta \varepsilon_{22}^{p(\alpha\beta\gamma)}, \quad \alpha = 1,....N_\alpha; \quad \gamma = 1,.....N_\gamma$$

(B.60)

$$\sum_\gamma l_\gamma S_{13}^{(\alpha\beta\gamma)} T_{11}^{(\beta\gamma)} + \sum_\gamma l_\gamma S_{23}^{(\alpha\beta\gamma)} T_{22}^{(\alpha\gamma)} + \sum_\gamma l_\gamma S_{33}^{(\alpha\beta\gamma)} T_{33}^{(\alpha\beta)} + \sum_\gamma l_\gamma S_{34}^{(\alpha\beta\gamma)} T_{23}^{(\alpha)} + \sum_\gamma l_\gamma S_{35}^{(\alpha\beta\gamma)} T_{13}^{(\beta)}$$
$$+ \sum_\gamma l_\gamma S_{36}^{(\alpha\beta\gamma)} T_{12}^{(\gamma)} = l\bar{\varepsilon}_{33} - \sum_\gamma l_\gamma \alpha_{33}^{(\alpha\beta\gamma)} \Delta T - \sum_\gamma l_\gamma \varepsilon_{33}^{p(\alpha\beta\gamma)}, \quad \alpha = 1,....N_\alpha; \quad \beta = 1,....N_\beta$$

(B.61)

$$\sum_\beta \sum_\gamma h_\beta l_\gamma S_{14}^{(\alpha\beta\gamma)} T_{11}^{(\beta\gamma)} + \sum_\beta \sum_\gamma h_\beta l_\gamma S_{24}^{(\alpha\beta\gamma)} T_{22}^{(\alpha\gamma)} + \sum_\beta \sum_\gamma h_\beta l_\gamma S_{34}^{(\alpha\beta\gamma)} T_{33}^{(\alpha\beta)} + \sum_\beta \sum_\gamma h_\beta l_\gamma S_{44}^{(\alpha\beta\gamma)} T_{23}^{(\alpha)}$$
$$+ \sum_\beta \sum_\gamma h_\beta l_\gamma S_{45}^{(\alpha\beta\gamma)} T_{13}^{(\beta)} + \sum_\beta \sum_\gamma h_\beta l_\gamma S_{46}^{(\alpha\beta\gamma)} T_{12}^{(\gamma)} = 2h l\bar{\varepsilon}_{23} - 2\sum_\beta \sum_\gamma h_\beta l_\gamma \alpha_{23}^{(\alpha\beta\gamma)} \Delta T$$
$$- 2\sum_\beta \sum_\gamma h_\beta l_\gamma \varepsilon_{23}^{p(\alpha\beta\gamma)}, \quad \alpha = 1,....N_\alpha \qquad \text{(B.62)}$$

$$\sum_\alpha \sum_\gamma d_\alpha l_\gamma S_{15}^{(\alpha\beta\gamma)} T_{11}^{(\beta\gamma)} + \sum_\alpha \sum_\gamma d_\alpha l_\gamma S_{25}^{(\alpha\beta\gamma)} T_{22}^{(\alpha\gamma)} + \sum_\alpha \sum_\gamma d_\alpha l_\gamma S_{35}^{(\alpha\beta\gamma)} T_{33}^{(\alpha\beta)} + \sum_\alpha \sum_\gamma d_\alpha l_\gamma S_{45}^{(\alpha\beta\gamma)} T_{23}^{(\alpha)}$$
$$+ \sum_\alpha \sum_\gamma d_\alpha l_\gamma S_{55}^{(\alpha\beta\gamma)} T_{13}^{(\beta)} + \sum_\alpha \sum_\gamma d_\alpha l_\gamma S_{56}^{(\alpha\beta\gamma)} T_{12}^{(\gamma)} = 2d l\bar{\varepsilon}_{13} - 2\sum_\alpha \sum_\gamma d_\alpha l_\gamma \alpha_{13}^{(\alpha\beta\gamma)} \Delta T$$
$$- 2\sum_\alpha \sum_\gamma d_\alpha l_\gamma \varepsilon_{13}^{p(\alpha\beta\gamma)}, \quad \beta = 1,....N_\beta \qquad \text{(B.63)}$$

$$\sum_{\alpha}\sum_{\beta} d_\alpha h_\beta S_{16}^{(\alpha\beta\gamma)} T_{11}^{(\beta\gamma)} + \sum_{\alpha}\sum_{\beta} d_\alpha h_\beta S_{26}^{(\alpha\beta\gamma)} T_{22}^{(\alpha\gamma)} + \sum_{\alpha}\sum_{\beta} d_\alpha h_\beta S_{36}^{(\alpha\beta\gamma)} T_{33}^{(\alpha\beta)} + \sum_{\alpha}\sum_{\beta} d_\alpha h_\beta S_{46}^{(\alpha\beta\gamma)} T_{23}^{(\alpha)}$$
$$+ \sum_{\alpha}\sum_{\beta} d_\alpha h_\beta S_{56}^{(\alpha\beta\gamma)} T_{13}^{(\beta)} + \sum_{\alpha}\sum_{\beta} d_\alpha h_\beta S_{66}^{(\alpha\beta\gamma)} T_{12}^{(\gamma)} = 2dh\bar{\varepsilon}_{12} - 2\sum_{\alpha}\sum_{\beta} d_\alpha h_\beta \alpha_{12}^{(\alpha\beta\gamma)} \Delta T$$
$$- 2\sum_{\alpha}\sum_{\beta} d_\alpha h_\beta \varepsilon_{12}^{p(\alpha\beta\gamma)}, \quad \gamma = 1,....N_\gamma \qquad \text{(B.64)}$$

These equations can be assembled into a global equation in matrix form as,

$$\tilde{G}T = f^m - f^p - f^t \Delta T \qquad \text{(B.65)}$$

where, $\tilde{G}$ is an $N_\beta N_\gamma + N_\alpha N_\gamma + N_\alpha N_\beta + N_\alpha + N_\beta + N_\gamma$ order square matrix containing subcell dimensions and subcell compliance components. T, f^m, f^p and f^t are $N_\beta N_\gamma + N_\alpha N_\gamma + N_\alpha N_\beta + N_\alpha + N_\beta + N_\gamma$ order vectors containing the unknown subcell stresses, cell dimensions and global strains, subcell dimensions and subcell plastic strain components, and subcell dimensions and subcell coefficients of thermal expansion respectively. The $\tilde{G}$ matrix consists of 36 submatrices, out of which 12 are fully populated.

Eqn. B.65 can be written in terms of subcell stress components and by inverting, it gives the subcell mixed concentration equation of the form,

$$\begin{bmatrix} T_{11}^{(\beta\gamma)} \\ T_{22}^{(\alpha\gamma)} \\ T_{33}^{(\alpha\beta)} \\ T_{23}^{(\alpha)} \\ T_{13}^{(\beta)} \\ T_{12}^{(\gamma)} \end{bmatrix} = \begin{bmatrix} A_{11}^{(\beta\gamma)} & B_{11}^{(\beta\gamma)} & X_{11}^{(\beta\gamma)} & \Lambda_{11}^{(\beta\gamma)} & \Omega_{11}^{(\beta\gamma)} & \Psi_{11}^{(\beta\gamma)} \\ A_{22}^{(\alpha\gamma)} & B_{22}^{(\alpha\gamma)} & X_{22}^{(\alpha\gamma)} & \Lambda_{22}^{(\alpha\gamma)} & \Omega_{22}^{(\alpha\gamma)} & \Psi_{22}^{(\alpha\gamma)} \\ A_{33}^{(\alpha\beta)} & B_{33}^{(\alpha\beta)} & X_{33}^{(\alpha\beta)} & \Lambda_{33}^{(\alpha\beta)} & \Omega_{33}^{(\alpha\beta)} & \Psi_{33}^{(\alpha\beta)} \\ A_{23}^{(\alpha)} & B_{23}^{(\alpha)} & X_{23}^{(\alpha)} & \Lambda_{23}^{(\alpha)} & \Omega_{23}^{(\alpha)} & \Psi_{23}^{(\alpha)} \\ A_{13}^{(\beta)} & B_{13}^{(\beta)} & X_{13}^{(\beta)} & \Lambda_{13}^{(\beta)} & \Omega_{13}^{(\beta)} & \Psi_{13}^{(\beta)} \\ A_{12}^{(\gamma)} & B_{12}^{(\gamma)} & X_{12}^{(\gamma)} & \Lambda_{12}^{(\gamma)} & \Omega_{12}^{(\gamma)} & \Psi_{12}^{(\gamma)} \end{bmatrix} X \begin{bmatrix} \bar{\varepsilon}_{11} \\ \bar{\varepsilon}_{22} \\ \bar{\varepsilon}_{33} \\ \bar{\varepsilon}_{23} \\ \bar{\varepsilon}_{13} \\ \bar{\varepsilon}_{12} \end{bmatrix} + \begin{bmatrix} \Gamma_{11}^{(\beta\gamma)} \\ \Gamma_{22}^{(\alpha\gamma)} \\ \Gamma_{33}^{(\alpha\beta)} \\ \Gamma_{23}^{(\alpha)} \\ \Gamma_{13}^{(\beta)} \\ \Gamma_{12}^{(\gamma)} \end{bmatrix} \Delta T + \begin{bmatrix} \Phi_{11}^{(\beta\gamma)} \\ \Phi_{22}^{(\alpha\gamma)} \\ \Phi_{33}^{(\alpha\beta)} \\ \Phi_{23}^{(\alpha)} \\ \Phi_{13}^{(\beta)} \\ \Phi_{12}^{(\gamma)} \end{bmatrix} \qquad \text{(B.66)}$$

To obtain the components of the macroscopic thermoelastic constitutive equation for the woven composite's behavior, the definitions for the macroscopic composite stress components are given in terms of the volume averaged subcell stress components,

$$\sigma_{ij} = \frac{1}{dhl} \sum_{\alpha}\sum_{\beta}\sum_{\gamma} d_\alpha h_\beta l_\gamma \sigma_{ij}^{(\alpha\beta\gamma)} \qquad \text{(B.67)}$$

for the reformulated GMC in 3D is as follows,

$$\bar{\sigma}_{11} = \frac{1}{hl} \sum_{\beta}\sum_{\gamma} h_\beta l_\gamma T_{11}^{(\beta\gamma)}, \quad \bar{\sigma}_{22} = \frac{1}{dl} \sum_{\alpha}\sum_{\gamma} d_\alpha l_\gamma T_{22}^{(\alpha\gamma)}$$

$$\overline{\sigma}_{33} = \frac{1}{dh}\sum_{\alpha}\sum_{\beta} d_{\alpha} h_{\beta} T_{33}^{(\alpha\beta)} \ , \quad \overline{\sigma}_{23} = \frac{1}{d}\sum_{\alpha} d_{\alpha} T_{23}^{(\alpha)} \tag{B.68}$$

$$\overline{\sigma}_{13} = \frac{1}{h}\sum_{\beta} h_{\beta} T_{13}^{(\beta)} \ , \quad \overline{\sigma}_{12} = \frac{1}{l}\sum_{\gamma} l_{\gamma} T_{12}^{(\gamma)}$$

Substitute for expressions for T_{ij}^{*} from eqn. B.66 into eqn. B.68.

$$\overline{\sigma} = C^{*}(\overline{\varepsilon} - \overline{\varepsilon}^{p} - \alpha^{*}\Delta T) \tag{B.69}$$

The above results are compared with the macroscopic or effective constitutive equation for the composite, represented by the three dimensional unit cell, to yield closed form expressions for the cell effective stiffness matrix, C^{*}, the cell effective coefficients of thermal expansion, α_{ij}^{*}, and the cell effective plastic strain components, $\overline{\varepsilon}_{ij}^{p}$.

Appendix C

Transformation Matrices

The 3D transformation matrix [T] is given by,

$$[T]=\begin{bmatrix} l_1^2 & m_1^2 & n_1^2 & 2m_1n_1 & 2l_1n_1 & 2l_1m_1 \\ l_2^2 & m_2^2 & n_2^2 & 2m_2n_2 & 2l_2n_2 & 2l_2m_2 \\ l_3^2 & m_3^2 & n_3^2 & 2m_3n_3 & 2l_3n_3 & 2l_3m_3 \\ l_2l_3 & m_2m_3 & n_2n_3 & m_2n_3+m_3n_2 & l_2n_3+l_3n_2 & l_2m_3+l_3m_2 \\ l_3l_1 & m_3m_1 & n_3n_1 & m_3n_1+m_1n_3 & l_3n_1+l_1n_3 & l_3m_1+l_1m_3 \\ l_1l_2 & m_1m_2 & n_1n_2 & m_1n_2+m_2n_1 & l_1n_2+l_2n_1 & l_1m_2+l_2m_1 \end{bmatrix} \quad \text{(C.1)}$$

The direction cosines of the fibre with θ, β orientations can be written as,

$l_1 = \cos\theta$, $l_2 = \sin\theta\cos\beta$, $l_3 = \sin\theta\sin\beta$,

$m_1 = 0$, $m_2 = \sin\beta$, $m_3 = \cos\beta$,

$n_1 = \sin\theta$, $n_2 = \cos\theta\cos\beta$, $n_3 = \cos\theta\sin\beta$.

Where θ is the angle made by fibre with respect to x axis and β is the angle made by projection of fibre in the yz plane with respect to y axis.

For stress and strain transformation matrices under rotation about z axis, the stress transformation matrix G and the strain transformation matrix Q can be written as eqn. C.2 and C.3.

$$[G]=\begin{bmatrix} \cos^2\theta & \sin^2\theta & 0 & 0 & 0 & 2\sin\theta\cos\theta \\ \sin^2\theta & \cos^2\theta & 0 & 0 & 0 & -2\sin\theta\cos\theta \\ 0 & 0 & 1 & 0 & 0 & 0 \\ 0 & 0 & 0 & \cos\theta & -\sin\theta & 0 \\ 0 & 0 & 0 & \sin\theta & \cos\theta & 0 \\ -\sin\theta\cos\theta & \sin\theta\cos\theta & 0 & 0 & 0 & \cos^2\theta-\sin^2\theta \end{bmatrix} \quad \text{(C.2)}$$

$$[Q] = \begin{bmatrix} \cos^2\theta & \sin^2\theta & 0 & 0 & 0 & \sin\theta\cos\theta \\ \sin^2\theta & \cos^2\theta & 0 & 0 & 0 & -\sin\theta\cos\theta \\ 0 & 0 & 1 & 0 & 0 & 0 \\ 0 & 0 & 0 & \cos\theta & -\sin\theta & 0 \\ 0 & 0 & 0 & \sin\theta & \cos\theta & 0 \\ -2\sin\theta\cos\theta & 2\sin\theta\cos\theta & 0 & 0 & 0 & \cos^2\theta - \sin^2\theta \end{bmatrix} \quad \text{(C.3)}$$

In case of rotation about the x axis, stress transformation [T_x] takes the form,

$$[T_x] = \begin{bmatrix} 1 & 0 & 0 & 0 & 0 & 0 \\ 0 & \cos^2\theta & \sin^2\theta & 2\sin\theta\cos\theta & 0 & 0 \\ 0 & \sin^2\theta & \cos^2\theta & -2\sin\theta\cos\theta & 0 & 0 \\ 0 & -\sin\theta\cos\theta & \sin\theta\cos\theta & \cos^2\theta - \sin^2\theta & 0 & 0 \\ 0 & 0 & 0 & 0 & \cos\theta & -\sin\theta \\ 0 & 0 & 0 & 0 & \sin\theta & \cos\theta \end{bmatrix} \quad \text{(C.4)}$$

In case of rotation about the y axis, stress transformation [T_y] takes the form,

$$[T_y] = \begin{bmatrix} \cos^2\theta & 0 & \sin^2\theta & 0 & 2\sin\theta\cos\theta & 0 \\ 0 & 1 & 0 & 0 & 0 & 0 \\ \sin^2\theta & 0 & \cos^2\theta & 0 & -2\sin\theta\cos\theta & 0 \\ 0 & 0 & 0 & \cos\theta & 0 & -\sin\theta \\ -\sin\theta\cos\theta & 0 & \sin\theta\cos\theta & 0 & \cos^2\theta - \sin^2\theta & 0 \\ 0 & 0 & 0 & \sin\theta & 0 & \cos\theta \end{bmatrix} \quad \text{(C.5)}$$

Appendix D

Load Details of Nosecap

D.1 Heat Flux Data for Nosecap

The heat flux data at different locations on the Nosecap are as given below,

Time (s)	X* 0 mm	X 210mm	X 410mm
0	0.02	0.00	0.00
5	0.07	0.06	0.06
10	0.08	0.10	0.09
15	0.10	0.13	0.11
20	0.12	0.16	0.14
25	0.15	0.20	0.18
30	0.17	0.21	0.19
35	0.24	0.30	0.26
40	0.36	0.42	0.38
45	0.54	0.60	0.54
50	0.79	0.83	0.74
55	0.92	1.20	1.08
60	1.35	1.53	1.37
65	1.99	1.92	1.71
70	2.81	2.31	2.06
75	4.09	2.81	2.50
80	5.49	3.43	3.05
85	7.72	4.15	3.69
90	9.81	4.46	3.95
95	12.15	4.62	4.08
100	13.95	4.59	4.03
105	16.46	4.47	3.91
110	18.17	4.22	3.66
115	20.31	3.98	3.44
120	22.14	3.76	3.22
125	24.34	3.59	3.05
130	26.89	3.44	2.89
135	29.52	3.36	2.80
140	32.17	3.32	2.74
145	27.27	2.59	2.11
150	21.81	1.93	1.56
155	17.38	1.44	1.14
160	13.76	1.04	0.81
165	10.76	0.77	0.59
170	8.31	0.61	0.46
175	7.00	0.65	0.49
180	6.07	0.68	0.51
185	5.18	0.67	0.51
190	4.42	0.65	0.49
195	3.77	0.61	0.46
200	3.21	0.57	0.42
205	3.02	0.58	0.43
210	2.86	0.58	0.43
215	2.71	0.58	0.42
220	2.57	0.58	0.42
225	3.63	0.57	0.41
230	3.43	0.55	0.40
235	3.53	0.57	0.41
240	3.70	0.59	0.43
245	2.60	0.62	0.45
250	2.72	0.64	0.47
255	2.86	0.67	0.49
260	3.11	0.72	0.53
265	3.55	0.82	0.62
270	4.06	0.97	0.74
275	4.63	1.12	0.87
280	5.27	1.30	1.01
285	6.41	1.63	1.29
290	7.84	2.07	1.66
295	9.68	2.70	2.20
300	11.84	3.50	2.87
305	14.37	4.56	3.77
310	17.53	6.00	5.01
315	21.85	8.10	6.83
320	26.97	10.79	9.17
325	32.45	14.06	12.03
330	38.81	18.22	15.70
335	44.58	22.37	19.39
340	50.71	27.37	23.84
345	55.95	31.40	27.44
350	59.32	34.25	29.99
355	63.18	37.30	32.72
360	66.98	39.27	34.54
365	67.50	36.53	32.08
370	66.45	32.15	28.18
375	65.64	27.98	24.47
380	64.35	23.86	20.82

385	63.30	20.76	18.08
390	62.18	21.25	18.52
395	60.98	21.66	18.89
400	59.93	22.10	19.28
405	58.95	22.57	19.71
410	58.24	22.96	20.07
415	57.39	23.41	20.49
420	55.79	23.46	20.55
425	54.06	23.41	20.52
430	52.32	23.35	20.47
435	49.91	22.59	19.81
440	47.42	21.17	18.55
445	45.02	19.82	17.37
450	42.94	18.47	16.17
455	40.62	17.18	15.03
460	38.43	15.98	13.98
465	36.36	14.87	12.99
470	34.83	14.07	12.29
475	33.40	13.33	11.64
480	32.00	12.64	11.04
485	31.12	12.27	10.71
490	30.40	11.98	10.46
495	29.95	11.68	10.20
500	29.17	11.37	9.93
505	28.68	11.26	9.84
510	28.21	11.16	9.75
515	27.68	11.01	9.63
520	27.19	10.90	9.53
525	26.47	10.69	9.35
530	25.79	10.50	9.19
535	25.05	10.29	9.02
540	24.20	10.02	8.79
545	23.43	9.59	8.41
550	22.24	9.15	8.02
555	21.13	8.75	7.67
560	19.95	8.30	7.27
565	18.73	7.80	6.84
570	17.58	7.33	6.43
575	16.46	6.88	6.03
580	15.44	6.48	5.68
585	14.48	6.11	5.35
590	13.58	5.88	5.15
595	13.12	5.52	4.83
600	12.26	5.22	4.57
605	11.48	4.95	4.33
610	10.68	4.66	4.08
615	9.92	4.35	3.81
620	9.16	4.09	3.58

625	8.40	3.82	3.34
630	7.61	3.53	3.09
635	6.85	3.24	2.84
640	6.10	2.96	2.59
645	5.39	2.67	2.34
650	4.70	2.35	2.05
655	4.08	2.08	1.82
660	3.62	1.81	1.58
665	3.11	1.56	1.36
670	2.54	1.31	1.14
675	2.01	1.05	0.92
680	1.54	0.82	0.71
685	1.13	0.60	0.53
690	0.75	0.39	0.34
695	0.41	0.18	0.16
700	0.14	0.01	0.01
705	-0.06	-0.12	-0.10
710	-0.20	-0.22	-0.19
715	-0.28	-0.28	-0.24
720	-0.34	-0.32	-0.28
725	-0.37	-0.35	-0.30
730	-0.40	-0.34	-0.29
735	-0.58	-0.67	-0.58
740	-0.56	-0.67	-0.58
745	-0.54	-0.67	-0.58
750	-0.53	-0.66	-0.58
755	-0.51	-0.65	-0.57
760	-0.49	-0.64	-0.56
765	-0.47	-0.63	-0.55
770	-0.45	-0.62	-0.54
775	-0.43	-0.60	-0.53
780	-0.42	-0.58	-0.52
785	-0.40	-0.57	-0.50
790	-0.39	-0.55	-0.49
795	-0.37	-0.54	-0.48
800	-0.36	-0.53	-0.47
805	-0.35	-0.51	-0.45
810	-0.33	-0.49	-0.44
815	-0.32	-0.47	-0.42
820	-0.31	-0.46	-0.41
825	-0.29	-0.44	-0.39
830	-0.28	-0.42	-0.37
835	-0.27	-0.40	-0.36
840	-0.26	-0.39	-0.34
845	-0.25	-0.37	-0.33
850	-0.22	-0.34	-0.30
855	-0.19	-0.30	-0.27
860	-0.16	-0.26	-0.23

865	-0.13	-0.22	-0.19
870	-0.09	-0.17	-0.16
875	-0.06	-0.13	-0.11
880	-0.02	-0.08	-0.07
885	0.01	-0.02	-0.02
890	0.05	0.03	0.03
895	0.09	0.09	0.08
900	0.13	0.15	0.13
905	0.17	0.21	0.19
910	0.22	0.28	0.25
915	0.26	0.35	0.31
920	0.31	0.43	0.39
925	0.37	0.53	0.47
930	0.38	0.54	0.48
935	0.35	0.50	0.45

940	0.33	0.47	0.42
945	0.31	0.44	0.39
950	0.29	0.41	0.37
955	0.27	0.39	0.34
960	0.26	0.36	0.32
965	0.24	0.34	0.30
970	0.23	0.32	0.28
975	0.22	0.30	0.27
980	0.21	0.28	0.25
985	0.20	0.26	0.23
990	0.19	0.25	0.22
995	0.18	0.23	0.21
999.1	0.17	0.22	0.19

* Distance measured from the origin)

D.2 Flow Parameters

From the flow parameters during the flight the Tg value has been evaluated and is given below.

time	Tg
0	300.7
5	300.7
10	300.5
15	300.1
20	299.8
25	299.4
30	299.4
35	300.5
40	303.1
45	306.9
50	312.5
55	320.5
60	331.6
65	347
70	368.8
75	402.2
80	462.7
85	543.1
90	639.8
95	754.4
100	889.1
105	1015.9
110	1190.4
115	1392.6
120	1613.8
125	1804.1
130	1958.8
135	2009.3
140	2032.6
145	2017.1
150	2001.3
155	1984
160	1964.9
165	1945.7
170	1931.7
175	1921.6
180	1882.7
185	1877.3
190	1877.6
195	1882.6
200	1891
205	1901.8
210	1916.8
215	1940
220	1967.8

$Tg/Ts = 1 + ((r-1)/2)\ M^2$

Ts = Static Temperature from ATM table

r = gamma

M = Mach Number

225	2000.1	510	1363.7	795	274.2
230	2013.6	515	1334.4	800	276
235	2016.4	520	1304.8	805	277.1
240	2017	525	1273.6	810	277.7
245	2018.2	530	1269.5	815	278
250	2020.3	535	1235.4	820	278
255	2023.8	540	1200.1	825	277.7
260	2028.6	545	1163.5	830	277.3
265	2034.8	550	1126.5	835	276.9
270	2043.4	555	1089.8	840	276.7
275	2055.1	560	1053.3	845	276.6
280	2070.8	565	1017.3	850	276.8
285	2088.6	570	982.3	855	277.6
290	2174.4	575	948.2	860	278.9
295	2205.7	580	914.7	865	280.7
300	2232	585	882.5	870	283
305	2270.1	590	851.7	875	285.7
310	2304.6	595	821.7	880	288.4
315	2343.7	600	791.9	885	291.2
320	2388.2	605	762.6	890	293.9
325	2420.3	610	732.9	895	296.6
330	2450.5	615	703.4	900	299.2
335	2461.3	620	673.5	905	301.5
340	2438.4	625	643.9	910	303.2
345	2397.9	630	614.4	915	304.5
350	2365.7	635	585.1	920	305.6
355	2324.2	640	556	925	306.3
360	2279.8	645	527.7	930	306.7
365	2234.2	650	500.1	935	307
370	2186.5	655	477.7	940	307.3
375	2142	660	450.6	945	307.8
380	2104.6	665	425.4	950	308.5
385	2074.6	670	402	955	308.5
390	2065.7	675	379.2	960	307.3
395	2056.3	680	357.4	965	305
400	2046.6	685	337.5	970	302.5
405	2029.4	690	318.9	975	300.9
410	2009.1	695	301.9	980	300.5
415	1982.6	700	289	985	301.3
420	1949.8	705	279.2	990	302.4
425	1915.3	710	272.1	995	303
430	1879.9	715	267.3	999.11	302.9
435	1843	720	264.6		
440	1802	725	262.4		
445	1762.8	730	259.5		
450	1726.7	735	256.5		
455	1689.5	740	254.1		
460	1653.6	745	252.6		
465	1619.8	750	252.1		
470	1587.9	755	252.9		
475	1557.7	760	254.6		
480	1528.5	765	257		
485	1500.1	770	260.1		
490	1473	775	263.3		
495	1446.4	780	266.5		
500	1419.2	785	269.5		
505	1391.5	790	272.1		

Appendix E

NASTRAN Cards for Heat Transfer and Thermo-structural Analysis

E.1 Heat Transfer Analysis

The NASTRAN cards used for carrying out heat transfer analysis is described in this section. Analysis has been carried out in 16 subcases. The time steps defined and the material definition cards are given below.

```
TSTEPNL  1       2      50.      1       ADAPT   2       -10     U
        .01
                 0
----------------------------
TSTEPNL  16      1      50      2       ADAPT   2       -10     U
        .01
                 0

$ Referenced Material Records
$ Material Record : Inconel
MAT5     6      1.                      1.              1.      1.
        8220.
MATT5    6       1                       1               1       2
$ Material Record : C-C
MAT5     2      1.                      1.              1.      1.
        1500.
MATT5    2       3                       4               5       6
$ Material Record : Zirconium
MAT4,4,2.,452.1,6000.
$ Material Record : Titanium
MAT4,3,6.7,526.3,4400.
$ Material Record : cc-isotropic
MAT4,1,1.,1.,1500.
MATT4    1       7       6
$ Material Tables ( No Conversions Needed )
MAT5,101,1.,,,1.,,1.,1.,+
+,1500.
MATT5,101,3,,,4,,5,6

MAT5 and MATT5 are defined for 34 local co-ordinate systems to define
the orthotropic material directions of the Nosecap.
MAT5,134,1.,,,1.,,1.,1.,+
+,1500.
MATT5,134,3,,,4,,5,6

$ Temperature Dependent Material Table : Kx-cc-iso
TABLEM1  7
        293.    8.5     773.    10.     1273.   11.5    1773.   13.25
        2273.   14.85   2773.   15.9     ENDT
$ Temperature Dependent Material Table : Cp-cc
TABLEM1  6
        293.    670.    773.    1590.   1273.   1920.   1773.   2020.
        2273.   2090.   2773.   2130.    ENDT
```

```
$ Temperature Dependent Material Table : Kx-cc
TABLEM1  3
        293.    9.87    773.    12.31   1273.   14.91   1773.   17.54
        2273.   19.98   2773.   22.0     ENDT
$ Temperature Dependent Material Table : Ky-cc
TABLEM1  4
        293.    9.96    773.    12.42   1273.   15.05   1773.   17.70
        2273.   20.16   2773.   22.20    ENDT
$ Temperature Dependent Material Table : Kz-cc
TABLEM1  5
        293.    10.12   773.    12.62   1273.   15.28   1773.   17.98
        2273.   20.48   2773.   22.54    ENDT
$ Temperature Dependent Material Table : Cp-Inconel
TABLEM1  2
        300.    385.    513.    410.    605.    458.    715.    516.
        738.    528.    833.    578.    901.    613.    1035.   683.
        1138.   736.    1573.   985.     ENDT
$ Temperature Dependent Material Table : K-Inconel
TABLEM1  1
        303.    11.     373.    11.9    473.    13.6    573.    15.2
        673.    16.9    773.    18.5    873.    20.2    973.    21.8
        1073.   23.5    1573.   31.5     ENDT
```

The heat flux and the flow parameter data are given on the outer surface of Nosecap as boundary conditions. The above data is given in two tables for cap and cone and is given in tabular form as shown below.

```
$ Dynamic Load Table : heatflux1 - for the cone region 12 & 11 and cap
10 and 9
TABLED1  12
        -99.89  .02e4   .1      .02e4   50.     .79e4   100.    13.95e4
        140.    32.17e4 200.    3.21e4  250.    2.72e4  300.    11.84e4
        350.    59.32e4 355.    63.18e4 360.    66.98e4 365.    67.5e4
        370.    66.45e4 375.    65.64e4 380.    64.35e4 385.    63.3e4
        390.    62.18e4 395.    60.98e4 400.    59.93e4 450.    42.94e4
        500.    29.17e4 550.    22.24e4 600.    12.26e4 650.    4.7e4
        700.    .14e4   705.    -.6e4   735.    -.58e4  750.    -.53e4
        800.    -.36e4  850.    -.22e4  880.    -.02e4  885.    .01e4
        900.    .13e4   930.    .38e4   950.    .29e4   1000.   .17e4
        1099.99 .17e4    ENDT

$ Dynamic Load Table : FlowparameterH1
TABLED1  11
       -99.89  -0.009e4.1      -0.009e450.     0.0832e4100.    0.0238e4
       140.    0.0186e4200.    0.002e4 250.    0.0016e4300.    0.0061e4
       350.    0.0288e4355.    0.0313e4360.    0.0339e4365.    0.0350e4
       370.    0.0353e4375.    0.0357e4380.    0.0357e4385.    0.0357e4
       390.    0.0353e4395.    0.0348e4400.    0.0344e4450.    0.0302e4
       500.    0.0261e4550.    0.0270e4600.    0.0251e4650.    0.0238e4
       700.    -0.01e4 705.    0.0025e4735.    0.0125e4750.    0.0104e4
       800.    0.0133e4850.    0.0084e4880.    0.0014e4885.    -8e-4
       900.    -0.034e4930.    0.1027e4950.    0.0527e41000.   -1.7e4
       1099.99 -1.70e4  ENDT
```

```
$ Dynamic Load Table : heatflux2
TABLED1  10
        -99.89  .02e4   .1      .02e4   50.     .83e4   100.    4.590e4
        140.    3.320e4 200.    0.57e4  250.    0.64e4  300.    3.500e4
        350.    34.25e4 355.    37.30e4 360.    39.27e4 365.    36.53e4
        370.    32.15e4 375.    27.98e4 380.    23.66e4 385.    20.76e4
        390.    21.25e4 395.    21.66e4 400.    22.10e4 450.    18.47e4
        500.    11.37e4 550.    9.150e4 600.    5.220e4 650.    2.35e4
        700.    .01e4   705.    -.12e4  735.    -.67e4  750.    -.66e4
        800.    -.53e4  850.    -.34e4  880.    -.08e4  885.    .02e4
        900.    .15e4   930.    .54e4   950.    .41e4   1000.   .22e4
        1099.99 .22e4    ENDT

$ Dynamic Load Table : FlowparameterH2
TABLED1  9
       -99.89  -0.009e4.1      -0.009e450.     0.0832e4100.    0.0238e4
       140.    0.0186e4200.    0.002e4 250.    0.0016e4300.    0.0061e4
       350.    0.0288e4355.    0.0313e4360.    0.0339e4365.    0.0350e4
       370.    0.0353e4375.    0.0357e4380.    0.0357e4385.    0.0357e4
       390.    0.0353e4395.    0.0348e4400.    0.0344e4450.    0.0302e4
       500.    0.0261e4550.    0.0270e4600.    0.0251e4650.    0.0238e4
       700.    -0.01e4 705.    0.0025e4735.    0.0125e4750.    0.0104e4
       800.    0.0133e4850.    0.0084e4880.    0.0014e4885.    -8e-4
       900.    -0.034e4930.    0.1027e4950.    0.0527e41000.   -1.7e4
       1099.99 -1.70e4  ENDT
```

E.2 Thermo-structural Analysis

The NASTRAN cards used for carrying out thermo-structural analysis is described in this section. The load tables for thermal and pressure loads are shown below.

```
INCLUDE 'llow21.pch'
TLOAD1,1,2,,,1
TLOAD1,2,6,,,2
TLOAD1,3,8,,,3
TLOAD1,4,15,,,4
TLOAD1,5,17,,,5
TLOAD1,6,32,,,6
TLOAD1,7,34,,,7
TLOAD1,8,36,,,8
TLOAD1,9,38,,,9
TLOAD1,10,39,,,10
TLOAD1,11,40,,,11
TLOAD1,12,42,,,12
TLOAD1,13,43,,,13
TLOAD1,14,44,,,14
TLOAD1,15,45,,,15
TLOAD1,16,46,,,16
TLOAD1,1001,333,,,1001
TLOAD1,1002,444,,,1002
DLOAD,2001,1.,1.,1,1.,2,1.,3,+
+,1.,4,1.,5,1.,6,1.,7,+
+,1.,8,1.,9,1.,10,1.,11,+
+,1.,12,1.,13,1.,14,1.,15,+
+,1.,16,1.,1001,1.,1002
```

TABLED1: 16 tables are given as an input for NASTRAN for reading the corresponding temperature tables at the specified time.

```
$ Dynamic Load Table : Temperature from punch cards
TABLED1  1
        -99.89  0.0     .1      0.0     100.    1.0     140.    0.0
        200.    0.0     350.    0.0     400.    0.0     700.    0.0
        705.    0.0     735.    0.0     750.    0.0     850.    0.0
        880.    0.0     885.    0.0     900.    0.0     930.    0.0
        950.    0.0     1000.   0.0     1099.99 0.0      ENDT
------------------------------------------------------------------------
TABLED1  16
        -99.89  0.0     .1      0.0     100.    0.0     140.    0.0
        200.    0.0     350.    0.0     400.    0.0     700.    0.0
        705.    0.0     735.    0.0     750.    0.0     850.    0.0
        880.    0.0     885.    0.0     900.    0.0     930.    0.0
        950.    0.0     1000.   1.0     1099.99 0.0      ENDT
```

The tables described below are used for defining the pressure data for cap and cone.

```
TABLED1  1001
        -99.89  0.0     .1      0.0     100.    9.6E+4  140.    7.5E+4
        200.    6.5E+4  350.    3.4E+4  400.    2.6E+4  700.    6.2E+4
        705.    6.4E+4  735.    6.9E+4  750.    7.1E+4  850.    8.8E+4
        880.    9.3E+4  885.    9.4E+4  900.    9.6E+4  930.    1.0E+5
        950.    1.04E+5 1000.   1.12E+5 1099.99 0.0      ENDT
TABLED1  1002
        -99.89  0.0     .1      0.0     100.    3.0E+4  140.    2.8E+4
        200.    2.5E+4  350.    2.1E+4  400.    1.6E+4  700.    2.5E+4
        705.    2.5E+4  735.    2.7E+4  750.    2.8E+4  850.    3.2E+4
        880.    3.4E+4  885.    3.4E+4  900.    3.5E+4  930.    3.7E+4
        950.    3.80E+4 1000.   4.00E+4 1099.99 0.0      ENDT
```

The table described below is used for defining the displacement constraints.

```
SPCADD   3001    1
$ Displacement Constraints of Load Set : bc
SPC1     1       123     12843   12853   12867   12888   12949   12999
         13058   13074   13081   13229   13230   13274   13320   13322
         13447   13453   13626   13627   13628   13632   13662   13663
         13751   13874
```

The isotropic and anisotropic materials cards are defined for the analysis as shown below. NASTRAN has anisotropic material card as input not orthotropic. So the inputs are entered as orthotropic in PATRAN which in turn writes the anisotropic cards for NASTRAN as shown below.

```
$Direct Text Input for Bulk Data
$ Referenced Material Records
$ Material Record : inconel - brackets and inconcel bolts and sleeve
$to connect to the titanium material
MAT1,6,2.076+11,,.3,8190.,1.2973-5
MATT1,6,13,,,,14
```

```
$ Material Record : C-C
MAT1,2,7.000+10,,.05,1500.,-0.350-6
MATT1,2,15,,,,16
$ Material Record : Zirconium - insulator
MAT1,4,100.,,0.2,6000.
$ Material Record : Titanium
MAT1,3,10500E+7,,0.3,4400.
$ Material Record : cc-isotropic - instead of ceramic sleeve
$cc- bolt and cc-sleeve is used in contact with c-c skin
MAT1,1,7.000+10,,.05,1500.,-0.350-6
MATT1,1,15,,,,16
$ Material Record : orthoc-c
$ Material Tables ( No Conversions Needed )-cc-101 to 134
MAT9     101    2.995+108.1559+88.9722+8                        3.938+10
        9.7894+8                        4.9648+9
        1.8956+9                1.895+9         1.8952+91700.   -1.646-7
        -2.851-76.9177-6
MATT9    101     7       8       9                               10
         11                              12
         1                       2               3               4
         5       6
```

The MAT9 and MATT9 cards are defined from 101 to 134 in the format required for temperature dependent inputs for defining the orthotropic properties of the preform.

```
MAT9     134    2.995+108.1559+88.9722+8                        3.938+10
        9.7894+8                        4.9648+9
        1.8956+9                1.895+9         1.8952+91700.   -1.646-7
        -2.851-76.9177-6
MATT9    134     7       8       9                               10
         11                              12
         1                       2               3               4
         5       6
```

The temperature dependent material cards are entered for each preform / material and for a typical case it is shown below.

```
$ Material Tables ( No Conversions Needed )
$ Material Tables ( No Conversions Needed )
$ Temperature Dependent Material Table : cc-G12
TABLEM1  1
        293.    1.8956+9773.    1.8956+91273.   1.8956+91773.
1.8956+9
        2273.   1.8954+92773.   1.8953+9 ENDT
$ Temperature Dependent Material Table : cc-G23
TABLEM1  2
        293.    1.895+9 773.    1.895+9 1273.   1.895+9 1773.   1.895+9
        2273.   1.8943+92773.   1.8942+9 ENDT
$ Temperature Dependent Material Table : cc-G31
TABLEM1  3
        293.    1.8952+9773.    1.8952+91273.   1.8952+91773.
1.8952+9
        2273.   1.8946+92773.   1.8946+9 ENDT
$ Temperature Dependent Material Table : cc-alpha1
TABLEM1  4
        293.    -2.16-7 773.    2.25-6  1273.   3.49-6  1773.   4.41-6
        2273.   5.84-6  2773.   6.3-6    ENDT
$ Temperature Dependent Material Table : cc-alpha2
```

```
TABLEM1  5
        293.    -3.39-7 773.    2.25-6  1273.   3.61-6  1773.   4.58-6
        2273.   6.13-6  2773.   6.66-6   ENDT
$ Temperature Dependent Material Table : cc-alpha3
TABLEM1  6
        293.    6.85-6  773.    1.01-5  1273.   1.25-5  1773.   1.5-5
        2273.   1.74-5  2773.   1.73-5   ENDT
$ Temperature Dependent Material Table : inconel-E
TABLEM1  13
        293.    2.08+11 366.    2.05+11 477.    2.02+11 589.    1.94+11
        700.    1.86+11 811.    1.79+11 922.    1.72+11 1033.   1.62+11
        1144.   1.27+11 1227.   7.8+10   ENDT
$ Temperature Dependent Material Table : inconel-alpha
TABLEM1  14
        293.    1.3-5   366.    1.28-5  477.    1.35-5  589.    1.42-5
        700.    1.44-5  811.    1.51-5  922.    1.6-5   1033.   1.62+11
         ENDT
$ Temperature Dependent Material Table : cc-iso-E
TABLEM1  15
        293.    7.00+10 773.    7.00+10 1273.   7.00+10 1773.   7.00+10
        2273.   6.60+10 2773.   6.40+10  ENDT
$ Temperature Dependent Material Table : cc-iso-alpha
TABLEM1  16
        293.    -0.35-6 773.    0.55-6  1273.   1.00-6  1773.   1.30-6
        2273.   1.80-6  2773.   2.0-6    ENDT
$ Material Tables ( Converted by pat3nas )
$ Temperature Dependent Material Table : CALCULATED 3D STIFFNESS TERM
11
TABLEM1  7
        293.    2.995+10773.    2.995+101273.   2.995+101773.
2.995+10        2273.   2.846+102773.   2.771+10 ENDT
$ Temperature Dependent Material Table : CALCULATED 3D STIFFNESS TERM
12
TABLEM1  8
        293.    8.1559+8773.    8.1559+81273.   8.1559+81773.
8.1559+8        2273.   8.1597+82773.   8.1651+8 ENDT
$ Temperature Dependent Material Table : CALCULATED 3D STIFFNESS TERM
13
TABLEM1  9
        293.    8.9722+8773.    8.9722+81273.   8.9722+81773.
8.9722+8        2273.   8.9738+82773.   8.9714+8 ENDT
$ Temperature Dependent Material Table : CALCULATED 3D STIFFNESS TERM
22
TABLEM1  10
        293.    3.938+10773.    3.938+101273.   3.938+101773.
3.938+10        2273.   3.734+102773.   3.632+10 ENDT
$ Temperature Dependent Material Table : CALCULATED 3D STIFFNESS TERM
23
TABLEM1  11
        293.    9.7894+8773.    9.7894+81273.   9.7894+81773.
9.7894+8        2273.   9.8028+82773.   9.8035+8 ENDT
$ Temperature Dependent Material Table : CALCULATED 3D STIFFNESS TERM
33
TABLEM1  12
        293.    4.9648+9773.    4.9648+91273.   4.9648+91773.
4.9648+9        2273.   4.9667+92773.   4.9647+9 ENDT
```

PUBLICATIONS BASED ON THE RESEARCH WORK

1. Santhosh, B., S. Sundararajan. and C. G. Nandakumar., Elastic properties of 3D woven and braided composites for hot structure applications. (Communicated to Journal of Composite Materials).
2. Santhosh, B., S. Sundararajan. and C. G. Nandakumar., Thermal properties of 3D woven and braided composites for hot structure applications. (Communicated to Journal of Aeronautical Engineering).
3. Santhosh, B., S. Sundararajan. and C. G. Nandakumar., Strength properties of 3D woven and braided composites for hot structure applications. (Communicated to Journal of Composites Science and Technology).
4. Santhosh, B., S. Sundararajan. and C. G. Nandakumar., Thermo-structural analysis of 3D composite for reusable applications. (Communicated to Journal of Materials Science and Engineering).
5. Santhosh, B. and C. G. Nandakumar., Thermo-structural analysis of Nosecap. (Communicated to 2nd International Conference on Materials for the Future (ICMF), 23rd to 25th February 2011, Thrissur).